

DOT/FAA/TC-22/45

Federal Aviation Administration
William J. Hughes Technical Center
Aviation Research Division
Atlantic City International Airport
New Jersey 08405

Probabilistic Integrity and Risk Assessment of Turbine Engines, Phase II

Revised 2023

Final report



U.S. Department of Transportation
Federal Aviation Administration

NOTICE

This document is disseminated under the sponsorship of the U.S. Department of Transportation in the interest of information exchange. The U.S. Government assumes no liability for the contents or use thereof. The U.S. Government does not endorse products or manufacturers. Trade or manufacturers' names appear herein solely because they are considered essential to the objective of this report. The findings and conclusions in this report are those of the author(s) and do not necessarily represent the views of the funding agency. This document does not constitute FAA policy. Consult the FAA sponsoring organization listed on the Technical Documentation page as to its use.

This report is available at the Federal Aviation Administration William J. Hughes Technical Center's Full-Text Technical Reports page: actlibrary.tc.faa.gov in Adobe Acrobat portable document format (PDF).

Form DOT F 1700.7 (8-72)

Reproduction of completed page authorized

1. Report No. DOT/FAA/TC-44/67		2. Government Accession No.		3. Recipient's Catalog No.			
4. Title and Subtitle Probabilistic Integrity and Risk Assessment of Turbine Engines, Phase II				5. Report Date Lwpg 2023			
				6. Performing Organization Code			
7. Author(s) R. Craig McClung* James C. Sobotka* Bradley J. Robinson† Michael P. Enright* Vikram Bhamidipati* Rajiv Sampath†† Yi-Der Lee* Colin Thomas** Michael E. McClure††† Jonathan P. Moody* Benjamin Guseman** Brijesh Kumar††††				8. Performing Organization Report No. 18-21473			
9. Performing Organization Name and Address * Southwest Research Institute® †† GE Aviation 6220 Culebra Road San Antonio, TX 78238-5166 ** Elder Research, Inc. ††† Pratt & Whitney 300 West Main Street #301 Charlottesville, VA 22903 † Rolls-Royce Corporation †††† Honeywell 450 South Meridian Street Indianapolis, IN 46225				11. Contract or Grant No. 15-G-016			
				12. Sponsoring Agency Name and Address U.S. Department of Transportation Federal Aviation Administration Policy & Standards Division Engine & Propulsion Section, AIR-625		13. Type of Report and Period Covered Final Report September 2015 – May 2021	
				14. Sponsoring Agency Code AIR-625			
15. Supplementary Notes The FAA William J. Hughes Technical Center Aviation Research Division COR was David Galella, ANG-E282.							
16. Abstract This grant supported the efforts of the Federal Aviation Administration (FAA) to develop an enhanced life management process, based on probabilistic damage tolerance principles, to address the threat of material or manufacturing anomalies in high-energy rotating components of aircraft engines. Major research products included formal verification and validation of Design Assessment of Reliability With INspection (DARWIN®) stress-intensity factor solutions; enhanced DARWIN capabilities for manual and automatic fracture mechanics modeling, probabilistic methods, and fleet risk methods. Substantial improvements in the speed and robustness of DARWIN for large finite element (FE) models; streamlined methods for deterministic life calculations; a DARWIN Python module to facilitate scripting of multiple DARWIN runs; options to specify or limit optional features or default values available in DARWIN; new advanced visualization capabilities enabling users to define and manipulate regions within three-dimensional FE models; multiple new versions of the DARWIN computer code for technology transfer to industry and the FAA, and a large DARWIN training workshop are also included. The efforts facilitate implementation of official advisory material for axial blade slots, titanium hard alpha anomalies, and circular holes, while also developing improved analysis methods for other applications of deterministic and probabilistic damage tolerance to engine safety.							
17. Key Words Aircraft gas turbine engines, Disks, Rotors, Low cycle fatigue, Fracture mechanics, Probabilistic damage tolerance, Risk assessment, DARWIN			18. Distribution Statement This document is available to the U.S. public through the National Technical Information Service (NTIS), Springfield, Virginia 22161. This document is also available from the Federal Aviation Administration William J. Hughes Technical Center at actlibrary.tc.faa.gov .				
19. Security Classif. (of this report) Unclassified		20. Security Classif. (of this page) Unclassified		21. No. of Pages 324	22. Price		

ACKNOWLEDGEMENTS

Successful completion of this large, multidisciplinary research project would not have been possible without the significant contributions and assistance of many different people. Some are named as authors on this report, and many others deserve special mention.

Special appreciation is extended to the FAA employees and consultants who provided sustained support, encouragement, and guidance throughout the project. Heartfelt thanks go to Tim Mouzakis of the Technical Policy Branch (AIR-620), David Galella of the William J. Hughes Technical Center, and FAA consultant Jon Bartos.

The entire project was motivated and guided by the Rotor Integrity Steering Committee of the Aerospace Industries Association, led during nearly all of the project term by chair Nick Denton (GE Aviation, now retired).

Direct leadership was provided by the industry Steering Committee comprising representatives from the four partner companies: GE Aviation, Honeywell, Pratt & Whitney (P&W), and Rolls-Royce Corporation (RRC). Committee members during this grant were chair Mike McClure (P&W), Brad Robinson (RRC), Brijesh Kumar (Honeywell), and Rajiv Sampath (GE Aviation).

General DARWIN[®] development at Southwest Research Institute[®] (SwRI[®]) was led by Michael Enright with substantial support from Jonathan Moody and James Sobotka. Yi-Der Lee, James Sobotka, and Ghadir Haikal developed, maintained, and verified the Flight_Life fracture mechanics module and its stress intensity factor solutions. Vikram Bhamidipati developed and maintained the DARWIN Computational Engine (DCE) and Python Module (DPM) with assistance from Yasin Zaman and John McClure. Jonathan Moody led the DARWIN testing and verification activities with assistance from Liz Housley, Yasin Zaman, and John McClure.

DARWIN graphical user interface development was performed at Elder Research, Inc. The effort was led by Ben Guseman (formerly at Elder) and Colin Thomas. Contributors included Zach Brown, William Proffitt, Jovon Packard, and former Elder staff Brigham Bangerter, Jennifer Markee, Bill Aldrich, and Keith Council.

The partner companies provided extensive evaluation and testing of new DARWIN releases throughout the program. Key contributors included Rajiv Sampath, Michael Krauss, Matthew Oakland, and John Vandike (GE Aviation); Brijesh Kumar and Alonso Peralta (Honeywell); Brad Robinson and David Mills (RRC); and Mike McClure (P&W).

Test engineer John Pape, Lead Technician Daniel Werner, and Life Prediction Engineer Mary Sue Gilbert made significant contributions to the thermo-mechanical fatigue (TMF) crack-

growth test activity at GE Aviation. Ted Asare, Allan Gorneault, Gary Galarneau, Deborah Fletcher, and Lesley Dawag played key roles on the nickel anomaly fatigue testing at P&W. Carl Popelar led the benchmark test program at SwRI.

Birdie Matthews (SwRI) provided superlative clerical assistance in preparing this large final report.

Contents

1	Introduction	1
2	Advanced fracture methods	6
2.1	New SIF solution for surface cracks on a hollow cylinder	7
2.2	Revisions to SIF geometry limits and transitioning algorithms	8
2.3	Constraint loss model	10
2.4	Verification of SIF solutions	11
2.5	Benchmark fatigue crack growth experiments	15
2.6	Experiments to support high temperature FCG modeling	15
2.7	Nickel (Ni) anomaly fatigue testing	16
3	Advanced methods for residual stress analysis	17
3.1	Incorporate local residual stress into bivariant SIF solutions	17
4	Advanced probabilistic methods	18
4.1	Enhance Gaussian Process importance sampling	19
4.2	Fleet risk module enhancements	20
5	Further development of auto-modeling methods	23
5.1	Incorporate additional SIF solutions into auto-modeling	24
5.1.1	Enhanced bivariant plates	24
5.1.2	Shakedown enhancement for bivariant plates	26
5.2	Add Autoplate functionality to 3D manual mode	27
5.3	View and export fracture plates for life and risk contours	29
5.4	Maturation of auto-modeling capabilities for production use	31
5.4.1	Improved support for large finite element models	32
5.4.2	FE2NEU finite element model triage algorithm	33
5.4.3	Speed enhancements for user-defined cracks	35
5.4.4	GUI interaction with FE models speedup	36
5.4.5	DARWIN results file import speed enhancement	36
5.4.6	Autoplate speed improvement enabled by FE2NEU enhancement	37

6	Improved user interfaces.....	37
6.1	Zoneless deterministic analysis	38
6.2	Scriptable input	42
6.3	Allow user or superuser to control default settings.....	49
6.3.1	File-based capability to customize the GUI environment.....	49
6.3.2	User-defined project rules defined via special template files	51
6.4	GUI visualization improvements	55
7	Direct DARWIN support for Advisory Circulars.....	61
7.1	New DARWIN analysis mode to support new AC on attachment slots.....	62
7.2	Modifications to existing DARWIN analysis modes to support AC updates	69
7.2.1	Hard alpha AC revisions	69
7.2.2	Security features for anomaly distribution and POD data	70
8	DARWIN testing and evaluation.....	72
8.1	DARWIN code releases	72
8.1.1	DARWIN 9.0	73
8.1.2	DARWIN 9.1	73
8.1.3	DARWIN 9.2	74
8.1.4	DARWIN 9.3	75
8.1.5	DARWIN 9.4	75
8.1.6	DARWIN 10.0	77
8.2	DARWIN internal verification testing	77
8.2.1	Modular code development and verification	77
8.2.2	Incremental code releases	78
8.2.3	Automated verification procedure	78
8.3	Steering Committee evaluation	78
8.3.1	Design guidance for new features.....	79
8.3.2	Numerical verification	79
8.3.3	Evaluation for production use.....	79

9	Technology transfer	79
9.1	Progress reports and review meetings	79
9.2	Conference presentations and journal articles.....	80
9.3	DARWIN commercial licensing	80
9.4	DARWIN training	81
9.5	Technology transfer to other U.S. government agencies	86
9.6	DARWIN spin-off projects	86
9.6.1	Minimum low cycle fatigue life.....	87
9.6.2	Hot corrosion	87
9.6.3	Additive manufacturing	88
9.6.4	Licensee-funded enhancements	92
10	Summary.....	93
11	References	100
A	Development and verification of a new Stress Intensity Factor solution for an external circumferential elliptical surface crack in a hollow cylinder	A-1
B	SIF solution verification	B-1
C	Benchmark fatigue crack growth testing.....	C-1
D	Thermo-mechanical fatigue crack growth testing	D-1
E	Wrought nickel anomaly low cycle fatigue testing.....	E-1
F	DARWIN® model quality checks.....	F-1
G	DARWIN® Python module usage cases	G-1
H	PIRATE/DARWIN® publications and presentations (2016–present).....	H-1

Figures

Figure 1. The FAA/RISC vision for an enhanced rotor life management process	6
Figure 2. Geometric parameterization of SC34 SIF solution	7
Figure 3. Revised geometrical validity limits for SC30 and SC31	9
Figure 4. DARWIN GUI access to legacy SIF transition criteria.....	10
Figure 5. Univariant residual stress field superimposed on bivariant crack model in DARWIN GUI	18
Figure 6. Selection of GPM probabilistic method in DARWIN GUI.....	20
Figure 7. Overview of inspection-based corrective actions enhancement to DARWIN FAM	21
Figure 8. Example fleet risk results for DARWIN FAM inspection-based corrective actions enhancement: (a) without inspection; (b) with inspection	22
Figure 9. Problematic geometries for bivariant plates in finite element models: (a) edge tolerancing; (b) far-field missing material; (c) internal holes, and (d) convex crack surface.....	25
Figure 10. Bivariant plate extending beyond boundaries of FE model	26
Figure 11. Models for verification of bivariant shakedown enhancement: (a) missing material at remote end; (b) additional missing material at remote end; (c) missing material at stress concentration.....	27
Figure 12. Initial crack on surface of 3D FE model at non-nodal location	28
Figure 13. GUI fracture model display for (a) Autoplate-defined plates with a green border; (b) user-defined plates with a white border	29
Figure 14. “Export Intermediate Nodal Results” selection in GUI preferences menu	30
Figure 15. Example fracture plate associated with a single node in a 2D FE model.....	31
Figure 16. New FE2NEU ‘Convert and Sign’ button to execute MQCs and store results and digital signature in *.fea file	35
Figure 17. Enhanced DARWIN GUI configuration menus: (a) life assessment, (b) risk assessment.....	39
Figure 18. Enhanced DARWIN optional features menu for deterministic life assessment.....	40
Figure 19. Enhanced GUI display for the Life @ Selected Points objective.....	41
Figure 20. Enhanced DARWIN Contour Models menu	42
Figure 21. Relationship among DPM, user-provided Python scripts, and DARWIN project file and executable program	44
Figure 22. Example Python script utilizing DPM to query a DARWIN project	46
Figure 23. Example Python script utilizing DPM to modify a DARWIN project.....	46
Figure 24. Example Python script utilizing DPM to create a DARWIN project.....	47

Figure 25. Example script utilizing DPM to create a DARWIN project (cont).	48
Figure 26. Example Python script utilizing DPM to execute a DARWIN project	48
Figure 27. Example GUI Configuration file	50
Figure 28. New preference menu field for optional specification of a GCF path	50
Figure 29. Overview of template mode, where super-users can set rules for fields	52
Figure 30. New project type prompt enabling users to specify use of template-based projects...	52
Figure 31. New GUI preferences menu field for the optional specification of a template directory path.....	54
Figure 32. Example of region definition by element number capability	56
Figure 33. Example of region definition via selection of elements by contour range	56
Figure 34. Example of region definition by selecting elements within a bounding box	57
Figure 35. Illustration of DARWIN capability to create view filters. In this filter, elements shown in Figure 32 were removed from the elements shown in Figure 33	58
Figure 36. Illustration of Toggle Edges GUI 3D visualization feature.....	59
Figure 37. Illustration of Clipping GUI 3D visualization feature (at three different clip depths)	60
Figure 38. Illustration of Clipping feature at different clip angles.	60
Figure 39. Illustration of Iso-Surfaces GUI 3D visualization feature (removing material above a selected threshold)	61
Figure 40. Illustration of iso-surfaces GUI 3D visualization feature (removing material below a selected threshold)	61
Figure 41. Selection of new axial blade slot analysis mode in DARWIN GUI	63
Figure 42. Defining a blade slot edge zone using the new axial blade slot capability	64
Figure 43. DARWIN GUI screen showing manufacturing process credits for axial blade slot...	65
Figure 44. Page 1 of the FAA report form generated via the DARWIN GUI for axial blade-slot damage tolerance assessment.....	67
Figure 45. Page 2 of the FAA report form generated via the DARWIN GUI for axial blade-slot damage tolerance assessment.....	68
Figure 46. New titanium HA anomaly analysis modes in DARWIN 9.4.....	70
Figure 47. Signed anomaly distribution (*.dist) file with hash signature highlighted.....	71
Figure 48. Candid photograph of participants in DARWIN workshop	81
Figure 49. Candid photograph of instructor and participants in DARWIN workshop.....	82
Figure 50. Candid photograph of instructors and participants in DARWIN workshop	82
Figure 51. Group photograph of instructors and participants in DARWIN workshop.....	83

Acronyms

Acronym	Definition
1D	one-dimensional
2D	two-dimensional
3D	three-dimensional
AC	Advisory Circular
AFLCMC	Air Force Life Cycle Management Center
AFRL	Air Force Research Laboratory
AIA	Aerospace Industries Association
ALA	as large as
AM	additive manufacturing
ASCII	American Standard Code for Information Exchange
ASTM	American Society for Testing and Materials
BCF	Beta correction factor
DARWIN [®]	Design Assessment of Reliability With INspection
CDF	cumulative distribution function
CICS	Critical Initial Crack Size
CLM	Constraint Loss Model
DARPA	Defense Advanced Research Projects Agency
DCE	DARWIN Computational Engine
DMLS	direct to metal laser sintering
DOE	design of experiment
DOF	degree of freedom
DPM	DARWIN Python module
DTR	design target reliability
ERI	Elder Research, Inc.
FAA	Federal Aviation Administration
FAM	Fleet Assessment Module
FE	finite element
FEA	finite element analysis
FCG	fatigue crack growth
GB	gigabyte
GCF	GUI Configuration File

Acronym	Definition
GP	Gaussian Process
GPM	Gaussian Process method
GRC	NASA Glenn Research Center
GUI	graphical user interface
HA	hard alpha
HPT	high pressure turbine
HS	high strength
LAF	Life Approximation Function
LHS	Latin Hypercube Sampling
LCF	low cycle fatigue
MC	Monte Carlo
min	Minimum
MQC	model quality check
MQM	model quality metrics
MSFC	NASA Marshall Space Flight Center
MTU	MTU Aero Engines
NDE	nondestructive evaluation
NASA	National Aeronautics and Space Administration
NAVAIR	Naval Air Systems Command
Ni	nickel
NSA	National Security Agency
OEM	original equipment manufacturer
P&W	Pratt & Whitney
PDRI	Probabilistic Design for Rotor Integrity
PDT	probabilistic damage tolerance
PIRATE	Probabilistic Integrity and Risk Assessment of Turbine Engines
POD	probability of detection
PWF	point weight function
PZS	plastic zone size
R&D	research and development
RAC	Risk Assessment Code
RAM	random access memory
RISC	Rotor Integrity Sub-Committee/Rotor Integrity Steering Committee
RRC	Rolls-Royce Corporation

Acronym	Definition
RS	residual stress
SBIR	Small Business Innovative Research
SI	International System
SIF	stress intensity factor
STTR	Small Business Technology Transfer
SwRI [®]	Southwest Research Institute [®]
TMF	thermo-mechanical fatigue
TRMD	Turbine Rotor Material Design
US	United States
UTS	ultimate tensile strength
V&V	verification and validation
YS	yield strength
WF	weight function

Executive summary

The Federal Aviation Administration (FAA) is working with the aircraft engine industry to develop an enhanced life management process, based on probabilistic damage tolerance principles, to address the threat of material or manufacturing anomalies in high-energy rotating components. The “Probabilistic Integrity and Risk Assessment of Turbine Engines, Phase 2” (PIRATE-2) research grant supported this effort by developing enhanced predictive tool capability and supplementary material/anomaly behavior characterization and modeling.

New DARWIN[®] (Design Assessment of Reliability With INspection) versions 9.0, 9.1, 9.2, 9.3, 9.4, and 10.0 were released to the FAA and industry. Twenty-two commercial DARWIN licenses were active at the end of this grant, including thirteen manufacturers of aircraft gas turbine engines.

A three-day DARWIN training workshop was conducted. Seventy-two persons from 37 organizations attended in person, and more than 60 others participated in the first day virtually. Four other two-day workshops were attended by 100 people from licensee organizations.

DARWIN was enhanced to provide direct support for specific FAA Advisory Circulars (ACs). A new analysis mode was implemented for risk assessment of axial blade slots in accordance with the forthcoming FAA AC 33.70-5. New analysis modes were developed to support the new titanium hard alpha anomaly distributions in AC 33.14-1 Change 1 (Federal Aviation Administration, 2001) and AC 33.70-3 (Federal Aviation Administration, 2023). A hash signature capability was added to DARWIN to prevent users from modifying standard anomaly distribution or probability of detection (POD) data files and attempting to use them in FAA certification assessments.

Several improvements were introduced to DARWIN fracture mechanics capabilities. A new bivariant stress intensity factor (SIF) solution for an external surface crack in a hollow cylinder was developed for cracks in shafts or casings. An alternative surface correction factor was implemented to address the free surface effect on part-through crack growth. DARWIN was enhanced to allow local univariant RS profiles to be applied to bivariant SIF solution for surface and corner cracks.

The accuracy of ten SIF solutions in DARWIN was verified by comparing DARWIN SIF results against high-fidelity SIF solutions from 3D finite element (FE) analyses. The verification matrix interrogated a wide range of crack sizes/shapes, cracked body dimensions, and applied stress gradients. The DARWIN SIF results for over 90% of the configurations considered were within 5% of the FE solutions. One new SIF solution with improved accuracy was developed.

A benchmarking study was conducted to perform validation of DARWIN SIF solutions and their use for FCG life predictions using Ti-6Al-4V. The SIF solutions were shown to provide accurate or conservative predictions of FCG lifetime under all test conditions considered.

A limited exploratory study investigated the interaction of thermo-mechanical fatigue (TMF) and shot-peening residual stress (RS) effects on crack growth in Inconel 718. One of the current DARWIN TMF models predicted the experimental results reasonably well.

A small test program was performed to attempt to define a low cycle fatigue debit due to a naturally occurring dirty white spot in Inconel 718. Unfortunately, the failure cracks initiated at carbides, so it was not possible to determine a fatigue life debit for the anomaly.

Probabilistic and fleet risk methods in DARWIN were improved. The Gaussian Process Importance Sampling probabilistic method was extended to include additional random variables. The DARWIN Fleet Assessment Module was enhanced to enable users to perform an inspection-based corrective action across an entire fleet of aircraft in accordance with AC 39-8.

Automatic fracture modeling (Autoplate) capabilities in DARWIN were enhanced. Autoplate functionality was extended to 3D manual fracture models. Users can now view and export fracture plates associated with life and risk contours. Bivariant plates are now allowed to extend outside the component model in several situations, facilitating future Autoplate use.

DARWIN auto-modeling was substantially matured. A new binary file format and other improvements in the GUI and FE2NEU have significantly reduced the time and memory required to load, display, and operate on large FE models. A new FE2NEU triage algorithm screens issues in the FE model that could prevent DARWIN from using the model. The time required to create user-defined cracks in large models was substantially reduced.

The original framework of DARWIN was focused on supporting zone-based probabilistic fracture risk calculations, but AC 33.70-1 (Federal Aviation Administration, Aug, 2009) advises deterministic damage tolerance analysis in some situations. DARWIN was enhanced to streamline setting up a deterministic life calculation.

Command line script programs can greatly reduce the amount of human time required to modify DARWIN input files to perform multiple runs. A Python script developed previously was enhanced to enable creation and/or modification of DARWIN input files without using the GUI.

DARWIN contains some optional features not needed/desired by all users. Some companies may wish to use different default settings. DARWIN was enhanced to enable an organization to specify the DARWIN features available to their users and to specify default values for selected inputs.

New DARWIN advanced visualization capabilities enable users to define and manipulate regions within 3D FE models. View filters enable users to visualize different parts of the geometry and can be combined using Boolean operations. New visualization features such as edge toggling, model clipping, and iso-surfaces were also implemented.

1 Introduction

The traditional design practice for high-energy aircraft gas turbine rotors, the so-called “safe-life” method, implicitly assumes that all material or manufacturing conditions that may influence the fatigue life of a rotor have been captured in laboratory coupon and full-scale component fatigue testing. In addition, the final design is based conservatively on minimum properties. This methodology provides a structured approach for design and life management that ensures high levels of safety. However, industry experience has shown that certain material and manufacturing anomalies can potentially degrade the structural integrity of high-energy rotors. These anomalies occur very rarely and, therefore, are not typically present in laboratory test articles. However, on those rare occasions when anomalies are present in manufactured products in service, they represent a significant departure from the assumed nominal conditions, and they can result in incidents such as the Sioux City accident in 1989.

As a result of Sioux City, the Federal Aviation Administration (FAA) requested that industry, through the Aerospace Industries Association (AIA) Rotor Integrity Sub-Committee (RISC), determine whether a damage tolerance approach could be introduced to produce a reduction in the rate of uncontained rotor events. The industry-working group concluded that additional enhancements to the conventional rotor-life management methodology could be developed that explicitly addressed anomalous conditions. During the development of this probabilistic damage tolerance (PDT) approach, it became apparent to RISC that the capabilities and effectiveness of the emerging technology could be significantly enhanced by further research and development. In 1995, Southwest Research Institute[®] (SwRI[®]), in partnership with four major U.S. engine manufacturers and with guidance from RISC, proposed a multiple-year research and development (R&D) program and was awarded an FAA grant to address identified shortfalls in technology and data. This program, titled “Turbine Rotor Material Design” (TRMD), developed enhanced predictive tool capability and supplementary material/anomaly characterization and modeling with a particular focus on hard alpha (HA) anomalies in titanium rotors.

One of the key outcomes of this work was a PDT computer code called DARWIN[®] (Design Assessment of Reliability With INspection). DARWIN integrates finite element (FE) models and stress analysis results, fracture mechanics models, material anomaly data, probability of anomaly detection, and uncertain inspection schedules with a user-friendly graphical user interface (GUI) to determine the probability-of-fracture of a rotor disk as a function of operating cycles with and without inspections. The DARWIN version developed under this program received an R&D100 Award in 2000 as one of the 100 most technologically significant new products of the year.

Other major accomplishments of the first grant included development of advanced probabilistic methods for risk assessment of components with rare material anomalies (Wu, Enright, & Millwater, 2002) three versions of DARWIN (Millwater, et al., 2000), and verification and validation (V&V) of DARWIN against industry software and experience. Additional accomplishments included generation of fatigue crack growth (FCG) data in vacuum for three titanium rotor alloys (McClung, et al., 1999), characterization of titanium HA properties (Chan, Perocchi, & Leverant, 2000; Chan, 2001), characterization of HA cracking in titanium alloy matrix material (McKeighan, Perocchi, Nicholls, & McClung, 1999), and development and validation of a forging microcode to predict the fracture and change of location and shape of HA during reduction from ingot to billet and from billet to final forged shape. Further details are available in the TRMD Final Report (Leverant, et al., 2000).

An incident at Pensacola, Florida in 1996 called attention to surface anomalies induced by manufacturing activities. With guidance from the FAA, RISC began to apply and extend the insights and methods developed for inherent material anomalies in titanium rotors to the broader problem of induced surface anomalies in all rotor materials. SwRI, in continuing collaboration with the industry, proposed and was awarded, a second FAA grant (“Turbine Rotor Material Design – Phase II”). This program began to address the surface anomaly challenge while completing the titanium HA work.

Major accomplishments of TRMD-II directly related to DARWIN included:

- new weight function (WF) stress intensity factor (SIF) solutions for select crack geometries under univariant and bivariant stressing (Enright, et al., 2003; Fitch, et al., 2004);
- advanced probabilistic methods to improve the efficiency and accuracy of risk computations (Wu, Enright, & Millwater, 2000; Enright & Millwater, 2002; Huyse & Enright, 2003; Enright, Millwater, & Huyse, 2006),
- a sophisticated GUI to facilitate analysis of fully three-dimensional (3D) models (Enright, et al., 2003);
- new DARWIN versions 4.x, 5.x, and 6.0 developed to implement these and other technology advances;
- V&V of each DARWIN version by comparison with engine company software and experience;

- and an infrastructure for software configuration management, code licensing, distribution, and user support, so that engine companies can employ DARWIN for official FAA and company purposes.

Additional technology resulting from TRMD-II included:

- a model and computer code for the diffusion of nitrogen or oxygen in titanium from an inclusion during manufacture;
- nondestructive evaluation (NDE) and metallography of forgings with HA anomalies to validate the HA forging microcode;
- experimental investigations of the effects of oxygen on tensile, fatigue, and dwell fatigue behavior of Ti-17;
- measurement of the coefficient of thermal expansion of bulk HA;
- evaluation of the effects of thermally-induced residual stresses on fatigue crack initiation and growth at HA inclusions (Laz, Chan, McClung, & Leverant, 2003);
- spin pit and coupon fatigue tests using material from the TRMD-Phase I forgings containing natural and synthetic HA anomalies;
- vacuum FCG data for one titanium rotor alloy and three nickel rotor alloys; thermo-mechanical FCG data for IN-718;
- and a comprehensive literature survey on the stability and significance of residual stresses in fatigue (McClung, 2007).

Further details are available in the TRMD-II Final Report (McClung, et al., 2008).

Additional work on surface damage and inherent anomalies was performed in a third grant (“Probabilistic Design for Rotor Integrity,” PDRI). Major accomplishments of PDRI included:

- new univariant and bivariant WF SIF solutions with significant speed improvements (Lee, McClung, & Chell, 2008);
- a new bivariant elastic-plastic shakedown method;
- new software to translate commercial FE models into DARWIN-compatible formats; new algorithms for thermo-mechanical FCG and time-dependent crack growth;
- a new analysis mode for surface damage on turned surfaces in two-dimensional (2D) models;

- new DARWIN capabilities that directly support certification calculations and reports for FAA advisory material on damage tolerance of hole features (Enright, et al., 2012);
- novel auto-modeling methods for material anomaly analysis in 2D models that substantially reduce total analysis time and significantly reduce the potential for user error and user-to-user variability (Moody, Millwater, & Enright, 2007; Enright, Liang, Moody, & Fitch, 2010; McClung, Lee, Liang, Enright, & Fitch, 2010);
- time-dependent FCG data for IN-718 to evaluate predictive methods;
- a comprehensive literature survey of small-crack effects in rotor alloys;
- new algorithms to calculate the service life associated with a user-specified probability of fracture;
- new capabilities to input user-supplied tabular SIF solutions;
- five new DARWIN versions to implement these and other technology advances;
- and V&V of each DARWIN version.

These accomplishments were documented in the PDRI Final Report (McClung, et al., [DOT/FAA/TC-18/6], 2018).

A fourth grant, entitled “Probabilistic Integrity and Risk Assessment of Turbine Engines” (PIRATE), supported new fracture and risk methods for surface damage and inherent anomalies as well as continued airworthiness assessment. Major accomplishments include:

- novel optimal autozoning methods for 2D and 3D FE models (McClung, Lee, Enright, & Liang, 2014; Moody, Enright, & Liang, 2013; Enright, Moody, & Sobotka, 2016);
- new DARWIN methods for superposition of residual stresses with service stresses;
- support for cracks on non-hoop principal planes in 2D models;
- new WF SIF solutions, including cracks at angled and chamfered corners;
- new risk assessment methods for anomalies that first appear at shop visits;
- new zoning techniques for attachment slots;
- new DARWIN methods for crack growth retardation;
- accommodation of cracks in 3D sector models;

- new software engineering advances to manage and visualize extremely large production FE models efficiently;
- and the development and verification of five new DARWIN versions to implement these and other technology advances.

These accomplishments were documented in the PIRATE Final Report (McClung, et al., [DOT/FAA/TC-17/15], 2018).

The FAA has addressed assessment methods for continued airworthiness issues through Advisory Circular (AC) 39-8 (Federal Aviation Administration, 2003). A DARWIN Fleet Assessment module was developed with funding from an engine company. It is available to all DARWIN users and addresses some of the provisions of AC 39-8. The PIRATE grant also developed new disk risk replacement capabilities for fleet risk assessments.

The broad FAA/RISC vision for enhanced life management of high-energy rotors is summarized in Figure 1. Here damage tolerance is a supplement to the existing safe life methodologies. The FAA/RISC vision embraces both inherent anomalies introduced during production of the rotor materials and induced surface anomalies introduced during manufacturing or maintenance of the rotors themselves. All rotor materials are addressed. The red check mark by “Titanium Hard Alpha” indicates that the methods to address that threat have been developed and are now defined in FAA AC 33.14-1 (Federal Aviation Administration, 2001) and AC 33.70-3 (Federal Aviation Administration, 2023). The check mark by “Circular holes” indicates the completion of that methodology and the release of FAA AC 33.70-2 (Federal Aviation Administration, Aug, 2009). Current RISC focuses include attachment slots and inherent anomalies in nickel alloys.

The previous grants mirrored this incremental realization of the FAA/RISC vision. TRMD-I supported AC 33.14 (Federal Aviation Administration, 2001) for titanium HA anomalies. The primary focus of TRMD-II was the development and implementation of probabilistic damage tolerance methods for induced surface anomalies at circular holes. The PDRI grant continued to support the advisory material for circular holes and the PDRI and PIRATE grants addressed surface damage at attachment slots and turned surfaces, while also developing enhanced methods for inherent anomalies in all materials.

A new grant, “Probabilistic Integrity and Risk Assessment of Turbine Engines, Phase 2” (PIRATE-2), was awarded in 2015 to continue this support of the FAA and the aircraft engine industry as they worked together to address the next steps in the comprehensive rotor integrity vision described in Figure 1. Four initiatives were pursued. One effort supported the continuing development of methods to treat surface anomalies at attachment slots and on turned surfaces for

all rotor materials. A second effort supported the enhancement of methods to treat inherent material anomalies in all rotor materials. A third effort developed new capabilities for fleet risk assessment and continued airworthiness. A fourth effort began expanding the scope of DARWIN to address life-limited engine parts other than rotors.

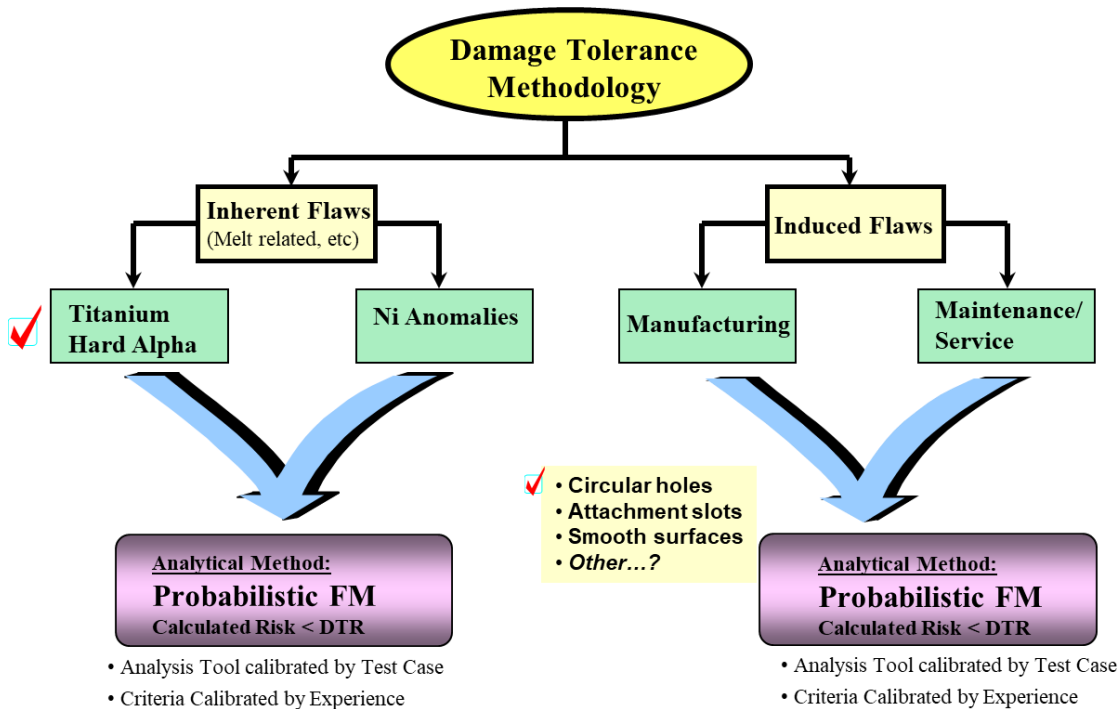


Figure 1. The FAA/RISC vision for an enhanced rotor life management process

Southwest Research Institute led the effort, and industry partners GE Aviation, Honeywell, Pratt & Whitney (P&W), and Rolls-Royce Corporation served as both major subcontractors and Steering Committee. Elder Research played an important subcontracting role in support of DARWIN development. RISC continued to provide oversight and guidance.

This document is a comprehensive final report of the investigations conducted and results obtained under the PIRATE-2 grant. The main body of the report is a summary of the major activities and key results from the grant. Some additional details are contained in appendices.

2 Advanced fracture methods

The most fundamental step in probabilistic damage tolerance analysis is calculation of the crack driving force and the resulting crack growth rate. Activities in this task advanced the state-of-the-art in computation of the safe remaining life of the component, including the generation of

numerical and experimental data to support model development, verification, and validation activities.

2.1 New SIF solution for surface cracks on a hollow cylinder

Previous development of DARWIN and its associated fracture mechanics capabilities focused exclusively on rotors, which are generally the most safety-critical components in an aircraft engine. However, FAA AC 33.70-1 (Federal Aviation Administration, Aug, 2009) addresses all engine life-limited parts, noting that their failure is likely to result in a hazardous engine effect, and directs that applicants should meet specific integrity requirements by executing a series of life management activities that include damage tolerance analysis. In this particular effort, a new engineering SIF solution was developed, verified, and implemented in DARWIN to address a surface crack in a hollow cylinder. This is one step in a planned expansion of DARWIN capabilities to address new classes of life-limited engine parts such as shafts and casings.

The new SIF solution for an external circumferential elliptical surface crack in a hollow cylinder is denoted SC34. Figure 2 shows the parametric idealization for this new SIF solution, based on four measurable dimensions. The new solution has geometric limits defined by $4 \leq D/t \leq 256$, $0 \leq a/t \leq 0.9$, and a wide range of a/c -ratios that depend on other parameters. The new crack case is a weight function solution that employs bivariant stress gradients.

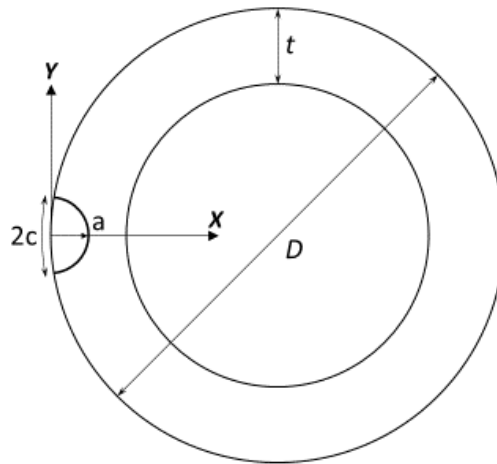


Figure 2. Geometric parameterization of SC34 SIF solution

Development of SC34 included several substantial steps. A new crack front parameterization was derived to enforce normality for the surface tip intersection with the cylinder surface while maintaining a part-elliptical shape. An existing bivariate weight function (WF) formulation was adapted and corresponding integration schemes were developed for several distinct regions of the geometrical solution space. More than 700 reference solutions to calibrate the WF were generated with high resolution 3D FE methods. Hundreds of additional FE solutions were generated to perform rigorous numerical verification of the solution and to identify needs for improvement. The final version of the SC34 solution was found to agree with the benchmark 3D FE solutions within 2.5% more than 90% of the time. Complete details of the derivation and verification of SC34 are given in Appendix A.

2.2 Revisions to SIF geometry limits and transitioning algorithms

DARWIN automatically transitions from one crack type to another as the crack grows and reaches a model boundary. For example, when an embedded crack reaches the surface, it changes to a surface crack and continues to grow until the next geometry transition, or until it reaches a failure condition. The criteria that determine exactly when the transition occurs are based on the verified geometry limits of the SIF solutions. Historically this also included an adjustment to the physical crack size based on the estimated size of the plastic zone at the crack tip. When the adjusted crack size exceeds the limit of the SIF solution, transition occurs.

DARWIN shares many SIF solutions with NASGRO[®], a widely used fracture mechanics-based life prediction tool developed and maintained by SwRI and the National Aeronautics and Space Administration (NASA) Johnson Space Center, with additional support from the FAA. However, some minor differences between NASGRO and DARWIN implementations of some SIF solutions have existed, especially in solution validity limits and crack transition criteria.

DARWIN has generally used the validity limits for individual SIF solutions that were established when the solutions were originally developed. Some of these validity limits were subsequently revised (usually extended) in NASGRO as the solutions themselves were studied further and, in some cases, revised, but these revisions had not always been carried over to DARWIN. As a result, some inconsistencies existed between the implementation and performance of nominally identical SIF solutions in the two codes.

In this effort, a comprehensive review of the then-current geometry limits enforced in DARWIN was conducted. This included a systematic comparison of the limits enforced in the same solutions in DARWIN and NASGRO and a systematic comparison of the limits enforced for related univariate and bivariate solutions corresponding to the same geometry. The goal of this

review was to ensure that the limits currently being enforced were consistent and represented the widest solution scope with adequate verification.

As a result of this review, the geometry limits for some SIF solutions were revised to eliminate some unnecessary over-conservatism. These changes may result in slightly longer calculated lifetimes, although the differences are expected to be small in most cases. In a few cases, minor changes were also made in NASGRO to maintain consistency. DARWIN and NASGRO should now give identical results for the same crack case with the same dimensions and same applied stresses.

For example, for the univariant and bivariant SIF solutions SC30 and SC31 for a semi-elliptical surface crack in a plate, the crack was previously not allowed to grow beyond 90% of various non-dimensional geometry limits for crack size, or beyond a normalized offset of 95%, as detailed in Figure 3. Here, the effective crack length includes an augmentation to the physical crack size based on the estimated size of the plastic zone at the crack tip (explained below). The revised limits enforce a uniform crack size limit of 95% for all tips and have no limit on the offset. The previous offset limit, in particular, could be highly over-conservative for larger offsets and smaller cracks. Other minor changes of a similar nature were implemented for crack cases CC11 and CC09, CC08 and CC10, and SC18 and SC29.

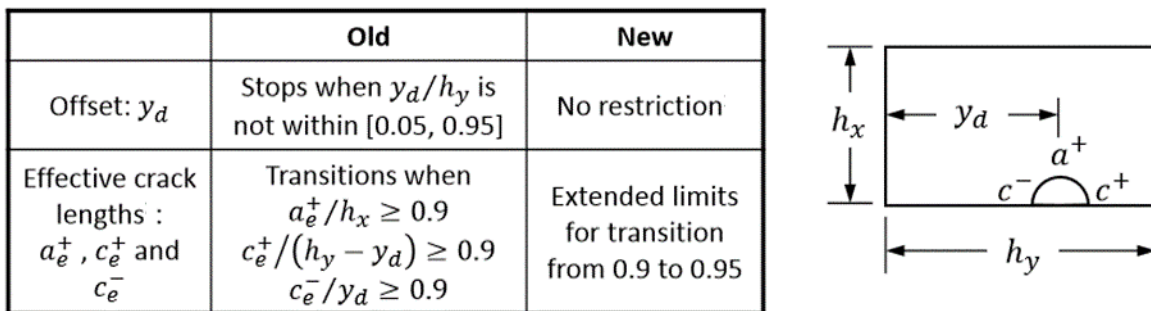


Figure 3. Revised geometrical validity limits for SC30 and SC31

Previous versions of DARWIN always enforced crack geometry transitions based on an effective crack size that adds the estimated crack tip monotonic plastic zone size (PZS) to the physical crack size. Adding the crack tip plastic zone size to the physical crack size has the net result of making the transition check more conservative, because the crack is forced to transition before the physical crack size reaches the SIF solution limit. This method was originally implemented in the very earliest years of DARWIN development to be cautious, before any user experience with DARWIN had been accumulated, and is now understood to be excessively conservative in

most cases. The NASGRO transition criteria for the same SIF solutions have never included the PZS augmentation.

In order to remove this excessive conservatism and to be consistent with NASGRO, an optional feature was added to DARWIN 9.1 that allowed users to turn off the PZS augmentation of crack size for crack transition purposes. At that time, the legacy transition method to include the PZS augmentation remained the default. Similarly, the new crack geometry limits described earlier were first implemented as an optional feature in DARWIN 9.1, with the previous geometry limits remaining the default. After accumulating a few years of successful user experience, the default DARWIN methods were changed in Version 9.3 Alpha to omit the PZS augmentation and to adopt the new geometry limits. However, users still have the option of using the legacy transition criterion and/or the legacy SIF geometry limits. To do so, they must provide the optional hidden feature keyword “legacySIFLimits” and then make appropriate choices in the GUI to select legacy SIF validity limits and/or the PZS correction to crack size, as shown in Figure 4.

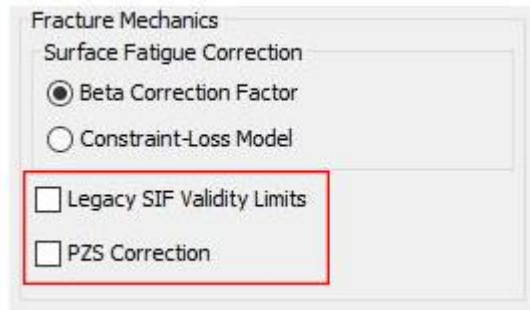


Figure 4. DARWIN GUI access to legacy SIF transition criteria

2.3 Constraint loss model

The computed shape of a growing fatigue crack is influenced by the values of the SIF around the perimeter of the crack front. To account for the observed effect of the free surface on the growth of the crack near the surface, correction factors are often applied to the SIF at the tips of part-through cracks where the crack intersects the surface (so-called surface-breaking tips) during crack growth calculations. DARWIN has always applied a so-called beta correction factor (BCF) to the value of the SIF range for surface-breaking tips. This BCF approach is identical to the method used in NASGRO and was originally based on research by Raju and Newman (Newman & Raju, 1984). The BCF generally reduces the value of the SIF at the surface about 10%, although there is also a dependence on the R value, where $R = K_{\min}/K_{\max}$ (the BCF is larger, and the reduction in SIF is slightly smaller, at high R).

An alternative surface correction factor method referred to as the Constraint-Loss Model (CLM) (Van Stone, Gilbert, Gooden, & Laflen, 1988) was first implemented in DARWIN 9.3 Alpha. CLM accounts for the region of constraint loss along the surface-breaking crack front when an applied stress approaches the elastic limit. This method modifies the SIF value for surface-breaking tips using an equation that is calibrated to test data for specific materials. The CLM equation is given by:

$$K = \frac{\sqrt{1 + 4\alpha\beta K_{el}^2} - 1}{2\alpha K_{el}}$$

where α and β are positive-valued material-dependent constants and K_{el} is the SIF value at the surface as calculated by the elastic solution.

The CLM method is provided as an alternative correction factor for surface-breaking tips in the Global Properties screen of the DARWIN GUI (see again Figure 4). When this option is selected, CLM is used to modify the SIF at surface-breaking tips of a crack during FCG analyses. Unlike the legacy BCF method, CLM is a material-dependent model. Accordingly, it requires the addition of the material-dependent constants α and β in the material properties file.

2.4 Verification of SIF solutions

The RISC requested that SwRI document its verification¹ of the SIF solutions in DARWIN. SIF solutions are used by the Flight_Life fracture mechanics module in DARWIN to compute FCG rates and fracture states. Over the past fifteen years, SwRI verified these solutions as they were developed and integrated into DARWIN. However, the results of the verification exercises had never been fully documented in a single summary. Upon further reflection, we determined that it was useful to perform new independent verification exercises for the DARWIN SIF library. Over the past few years, SwRI has substantially enhanced our internal capabilities to generate, execute, and post-process large numbers of high fidelity, FE analyses to obtain highly accurate SIF values. These new capabilities support cost-efficient verification exercises that can provide a much more comprehensive coverage of the DARWIN SIF solution space.

¹ Note that “verification” refers to independent confirmation that the calculations are being performed correctly; *i.e.*, that mathematics and software produce the same result. This is different from “validation”. Validation involves comparisons with experimental results. Selected experimental validation studies are planned in a separate subtask under the referenced grant.

The verification exercises conducted during PIRATE-2 featured the following characteristics:

- Semi-random determination of crack geometries using the Latin-Hypercube Sampling (LHS) method: LHS produces a design of experiment (DOE) for computational efforts that both span and fill the solution space. Analysts set the computational budget by setting the number of samples in the DOE. DOEs from LHS have more extreme combinations of geometric ratios than Monte Carlo (MC) Sampling, which often produces geometries clustered in the center of the solution space. This approach also ensures that the examined geometries are not limited to the geometries that define the reference cases.
- Application of multiple loadings: WF SIF solutions support arbitrary loadings. During the verification efforts, at least two loadings were imposed on each crack geometry to test the integration capabilities of the WF implementation. At a minimum, these loadings involve stresses characteristic of a remote force (constant stress) and moment (linearly varying stress), since these gradients reflect the major stresses during service. Higher-order polynomial stresses were imposed on certain crack front geometries to investigate the impact of residual stresses and local stresses triggered by geometric features.
- Computation of baseline SIF values using high-fidelity FE analyses built by automated processes: Here, Python scripting capabilities supported by Abaqus/CAE were used to generate, execute, and post-process large numbers of geometries. The scripting process enables consistent model definitions, better modeling techniques, and more exact modeling processes. SIF solutions from the FE analyses represent baseline values that are considered closest to an answer produced by a closed-form mathematical solution.
- Calculation of test SIF values using DARWIN-equivalent routines in NASGRO:DARWIN and NASGRO share routines for computing SIF values. NASGRO facilitates easy access to these routines through the NASSIF module that directly computes SIF values for a given crack type, geometry, and loading. This work exploits this relationship to produce SIF values for DARWIN using the NASGRO routine that serve as the test values.
- Definition of a credibility measure: The credibility measure indicates the error between the DARWIN solution and the Abaqus solution for one geometry, under one loading, and at the appropriate crack tip. The credibility measure has been described as a ratio of the DARWIN SIF to the FEA SIF, and it has been described as the percent error between these SIF values.

- Determination of a cumulative distribution function (CDF) of the credibility measure: A rank ordering of the credibility measure produces a CDF that provides a quantitative measurement of the overall solution quality. Tightly grouped CDFs about the FEA solution demonstrate a solution with excellent quality. Widely distributed CDFs suggest the opposite.

We refer to this process as formal verification of the solutions. It is more rigorous than earlier verification efforts associated with the development of these solutions. It tests the mathematical formulation, reference solutions, interpolation procedures, and integration processes of the WF SIF solution. It provides a quantifiable metric of the accuracy of the solution. It tests (as far as possible) the complete geometric solution space and many possible loading scenarios.

During this grant, SwRI completed verification for the following SIF solutions in DARWIN:

- CC09 – Quarter elliptical corner crack in plate – bivariate WF
- CC11 – Quarter elliptical corner crack in plate – univariate WF
- SC30 – Semi-elliptical surface crack (offset) in plate – univariate WF
- SC31 – Semi-elliptical surface crack (offset) in plate – bivariate WF
- EC04 – Elliptical embedded crack (offset) in plate – bivariate WF
- EC05 – Elliptical embedded crack (offset) in plate – univariate WF
- CC08 – Quarter elliptical corner cracks at hole (offset) in plate – univariate WF
- CC10 – Quarter elliptical corner cracks at hole (offset) in plate – bivariate WF
- CC12 – Quarter elliptical corner crack at chamfer in plate – bivariate WF
- SC34 – External surface crack in a hollow cylinder – WF solution

These solutions cover almost all analyses performed in DARWIN by most users. Automatic analyses that invoke automatic fracture modeling (so-called Autoplate) currently use the univariate crack-in-plate solutions CC11, SC30, and EC05 as the initial crack models.

Consequently, automatic assessments (optimal autozoning, crack growth contours, and critical initial crack size [CICS] contours) are largely covered by the verification efforts in PIRATE-2. The verified bivariate solutions CC09, SC31, and EC04 are in the process of being added to this automated functionality. The other verified crack models must be manually defined by the user in the GUI. SC34 is a special purpose solution for hollow shafts and casings that was developed in the current grant, and the verification of that solution was performed during development.

The verification of a few special purpose solutions remains to be completed using this formal process:

- CC18 – Part elliptical corner crack at angled corner – bivariant WF
- SC18 – Semi-elliptical surface crack (offset) at hole (offset) in plate – univariant WF
- SC29 – Semi-elliptical surface crack (offset) at hole (offset) in plate – bivariant WF
- TC13 – Through crack at hole (offset) in plate – univariant WF
- TC15 – Through crack at edge of variable-thickness plate – univariant WF

These solutions all require manual user intervention. The associated geometries are uncommon in DARWIN analyses. CC18 and TC15 are only available for manually zoned and user-defined cracks. TC13 is only available as a transition solution from CC08, CC10, SC18, and SC29, and it generally reflects the final cycles of crack growth. We plan to complete formal verification of these solutions in a subsequent grant.

For completeness, note two other simple through crack solutions used in DARWIN:

- TC01 – Offset internal through crack in a plate
- TC02 – Through crack at the edge of a plate

These solutions employ a slightly different formulation than the analogous solutions in NASGRO. However, these solutions are sufficiently simple and well established that comprehensive verification is unneeded. They are only available after transition from corner or surface cracks and usually have a very limited impact on total FCG lifetime.

In general, this effort revealed the fidelity of DARWIN SIF solutions to baseline FEA SIF solutions. Based on the CDFs, more than 90% of the DARWIN SIF solutions are within 5% of the FEA SIF solutions for most crack cases and loadings. In those rare situations when this accuracy criterion is not met, it usually reflects a slight conservative bias in the solution, very small SIF values that do not contribute towards FCG, or extreme and impractical regimes of the geometry solution space (*e.g.*, highly unusual crack sizes and shapes). Therefore, this verification exercise provides confidence in the accuracy of the DARWIN SIF solutions.

As a result of the verification studies of CC10, several opportunities were identified for minor improvements in solution accuracy. These improvements have been performed, and a revised solution CC26 was developed, verified, and documented. This revised solution will be implemented in DARWIN in a subsequent grant.

A more detailed documentation of this verification effort is provided in Appendix B. This documentation is also being incorporated into the DARWIN Crack Models manual to release to the DARWIN user community.

2.5 Benchmark fatigue crack growth experiments

Engineering SIF solutions are verified numerically through comparison with more sophisticated numerical solutions, as described in the previous section. However, experimental validation is also needed to confirm that these SIF solutions provide adequately accurate predictions of FCG rates and lifetimes. In this subtask, a reliable database of FCG data on a variety of specimen and crack geometries was generated for a carefully pedigreed rotor material to facilitate the validation of the Flight_Life fracture mechanics module in DARWIN. Details of this study are provided in Appendix C.

FCG experiments were performed using Ti-6Al-4V at room temperature. Six different crack model geometries were evaluated. Baseline FCG tests were performed with simple through crack tension geometries to develop high quality FCG properties. These baseline tests were analyzed statistically and shown to compare favorably with legacy FCG data for the same material source. Calculated FCG curves and lifetimes were compared with the baseline tests, as well as independent tests performed with the same geometries, in order to validate the baseline property models.

Additional benchmark FCG experiments were performed with four other common geometries as well as different loading configurations (bending versus tension). The FCG behavior of the benchmark experiments was predicted using the baseline properties. The predictions were highly accurate (within expected material scatter) or slightly conservative in all cases with tension loading. Some potential reasons for the conservatism were identified. The predictions for the bending tests were more conservative, and the reasons for this stronger bias are not yet understood. Additional studies are planned to explore other conditions.

2.6 Experiments to support high temperature FCG modeling

Aircraft turbine engine-components operate in a very complex thermo-mechanical fatigue (TMF) environment. Both temperatures and stresses change during a flight cycle, and typically these changes are not fully aligned. DARWIN includes several algorithms to determine and apply the appropriate temperature-dependent crack growth properties for each identified load pair.

Many aircraft turbine engine-components employ some surface treatment (*e.g.*, shot peening) that imparts a compressive residual stress (RS) layer on the surface. This practice generally

results in improved fatigue life. While previous studies have explored the TMF effect on crack growth or the RS effect on crack growth, very little effort has been spent to understand the complex interaction of RS and thermo-mechanical effects on FCG.

A very limited exploratory study was conducted in this grant to better understand the interaction of RS and TMF effects. The objective of this effort was not to fully characterize the complex interaction, but rather to build some limited understanding and key insights by performing a few appropriate experiments and evaluating the results with some existing models. The widely used high temperature, high-strength alloy Inconel 718 was chosen for this investigation. Specimens were machined from remnant material contributed by GE Aviation. All crack growth tests and analyses were performed by GE Aviation.

Isothermal FCG tests were performed on unpeened specimens at 450°F and 1200°F to establish baseline FCG rate properties, and isothermal residual life FCG tests were performed at the same two temperatures with specimens shot peened to a prescribed intensity. Residual life FCG tests were then performed using a representative out-of-phase TMF history between 450°F and 1200°F with both unpeened and peened specimens. Heat tinting to mark the fracture surface was performed to aid with interpretation and analysis of test results. The shot peening RS gradient was also measured. Finally, FCG lifetime was predicted for all TMF tests using several different TMF models in DARWIN, including RS effects as appropriate.

This limited exploratory study indicated that, for the single set of test conditions considered, the “average da/dN ” TMF method predicted experimental results reasonably well and was more accurate than the maximum temperature or temperature at maximum stress approaches. More details of the experiments and the analysis are provided in Appendix D.

2.7 Nickel (Ni) anomaly fatigue testing

Historically, wrought Ni alloy disk fractures from melt anomalies have had a very low incidence rate. However, the threat does exist. In October 2016, a wrought Ni high pressure turbine (HPT) disk fractured from a subsurface anomaly that was not detected by inspections performed at manufacture. This accident emphasized the need to develop enhanced melting, inspection, and design methods. As a result of this accident, the FAA has tasked RISC to develop a probabilistic assessment approach for nickel material anomalies in rotating engine hardware.

However, because the phenomenon is so rare, few data are available to understand tendencies for fatigue crack formation and growth at naturally occurring nickel anomalies. RISC made a request to member original equipment manufacturers (OEM) to attempt to intercept any wrought Ni anomalies found during manufacturing with the intent of turning the material into test bars. MTU

Aero Engines (MTU) found such an anomaly during an etch process of forged material of an IN-718 part, and they made this anomaly available for testing. The anomaly was later confirmed to be a dirty white spot.

A small test program was performed in an attempt to define a potential low cycle fatigue debit due to the presence of an anomaly. To determine the life debit, a specimen containing a surface-connected anomaly as well as six baseline specimens without any known anomalies were machined out of the same part and then tested in fatigue. The tests were performed in four-point bending at 750°F. P&W was chosen to perform this testing since they had an established relationship with MTU and were a subcontractor on the current PIRATE grant.

Unfortunately, the failure crack in the specimen with the anomaly initiated from a carbide, not the anomaly. All of the anomaly-free test specimens that were evaluated with fractography were also found to fail from a carbide. Therefore, it was not possible to determine a fatigue life debit for the dirty white spot specimen. Furthermore, the results from this test program call into question the ability to determine a fatigue life debit for surface connected wrought Ni anomalies at temperatures where carbides are active.

Additional details of the test program and the post-test analyses are provided in Appendix E.

3 Advanced methods for residual stress analysis

DARWIN enhancements completed on the previous PIRATE-1 grant provided significant new capabilities for predicting residual stress effects on fracture life and risk. Additional enhancements needed to increase model fidelity were also identified. Described here is a residual stress capability enhancement that was implemented on the current grant. Some additional enhancements are planned for a subsequent grant.

3.1 Incorporate local residual stress into bivariant SIF solutions

The effects of residual stresses on FCG rates are well known, and engineering methods to address these effects have been established (McClung, 2007). The key step is the superposition of static residual stress fields with cyclic (fatigue) service stress fields. Under the previous grant, tabular superposition methods for local univariant residual stress fields were implemented for all univariant SIF solutions in DARWIN. Further details are provided in Chapter 4 of the PIRATE Phase 1 Final Report (McClung, et al., [DOT/FAA/TC-17/15], 2018). This algorithm accommodates residual stress gradients that would arise from surface enhancement techniques such as peening or cold expansion of holes.

In this subtask, the algorithm and the associated GUI were extended to accommodate univariant residual stress effects on bivariant SIF solutions in DARWIN. The enhanced DARWIN residual stress profiles capability enables users to define a univariant residual stress field that is superimposed directly on 2D FE model geometries for use in fatigue crack growth life and fracture risk assessments (Figure 5). This feature enhancement is currently limited to the bivariant SIF models for surface and corner cracks in plates (SC31 and CC09, respectively).

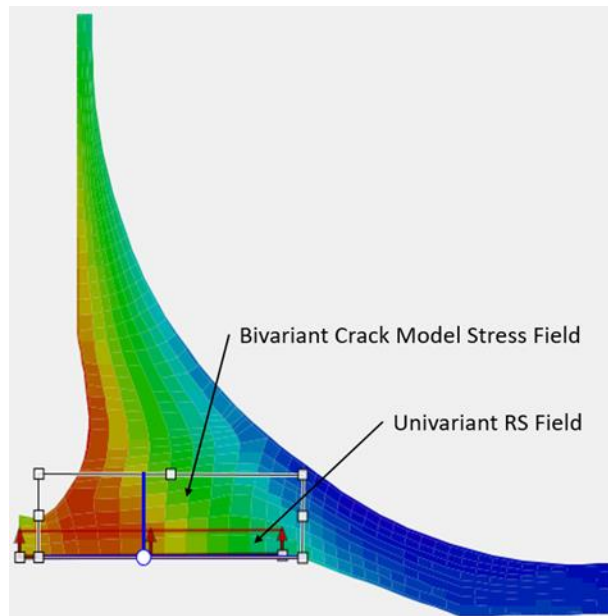


Figure 5. Univariant residual stress field superimposed on bivariant crack model in DARWIN GUI

4 Advanced probabilistic methods

DARWIN provides a robust probabilistic approach to assess the fracture risk of individual components containing rare inherent or induced anomalies. The computation time associated with fracture risk assessment typically scales with the number of elements in the finite element (FE) model. As users continue to use larger FE models for FAA AC assessments, enhancements are needed to improve the efficiency of probabilistic computations to maintain reasonable computation times for these assessments. Section 4.1 describes an enhancement completed on this grant that addresses computational efficiency associated with large FE models.

DARWIN also includes capabilities for assessment of continued airworthiness associated with AC 39-8 (Federal Aviation Administration, 2003). In the previous grant, DARWIN enhancements for continued airworthiness were focused on the influence of disk replacement

corrective actions on fleet risk. AC 39-8 also allows the use of inspection-related corrective actions to reduce fleet risk. Section 4.2 describes an enhancement that was implemented on the current grant to support the modeling of inspection-related corrective actions within DARWIN and the fleet assessment module.

4.1 Enhance Gaussian Process importance sampling

DARWIN includes a MC simulation capability to assess the fracture risk of components. The MC method is robust but computationally slow.

DARWIN also includes a probabilistic method called Gaussian Process (GP) importance sampling, which is also referred to as the GP method. This probabilistic method is similar to another DARWIN probabilistic method called Life Approximation function (LAF). Both probabilistic methods create surrogate models to estimate the relationship among input variables and fatigue crack growth lives. For probabilistic analysis, both methods apply MC simulation to their surrogate models to compute the fracture risk.

The major difference between these methods is the surrogate model. The LAF method employs a polynomial function as its surrogate model, whereas the GP method uses a GP response surface. The GP method developed on the previous grant was limited to three random variables relating fatigue crack growth life to initial crack size, stress scatter, and life scatter values. The LAF method in DARWIN is limited to four random variables: anomaly size, life scatter, inspection time, and NDE probability of detection.

DARWIN includes additional random input variables that were not previously supported by either the LAF or GP methods. The GP method was extended on this grant to include additional random variables associated with six degree of freedom (DOF) anomalies (three orthogonal dimension variables and three orthogonal orientation variables) and shop visit anomalies (shop visit time). A previously developed FCG life response surface was enhanced to support the additional variables. An additional response surface was implemented (as an optional feature) to model the relationship among formation life and its associated input random variables. This enables the GP method to provide treatment for all of the random input variables in DARWIN except for material processing-related random variables (which will be addressed on another project). Note that the GP method does not currently support random mission mixing.

The accuracy of the response surface method is dependent on how well the response surface fits the training data. The response surface models in DARWIN are based on responses that are obtained via execution of the DARWIN computational code at selected values of the input variables. The accuracy of the response surface is assessed via the “leave-one-out cross-

validation” approach. Response surface-model accuracy is communicated to the user in the GUI results section.

The GP method enhancement was implemented in DARWIN and was renamed “Monte Carlo w/Gaussian Process method (GPM)” (Figure 6). It provides computational efficiency that is comparable to the DARWIN Importance Sampling probabilistic method.

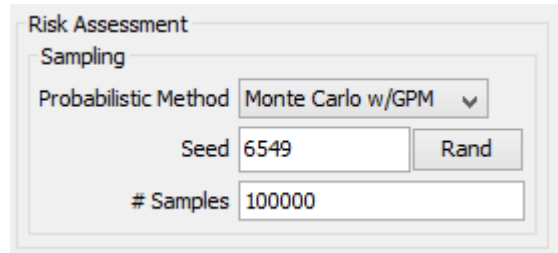


Figure 6. Selection of GPM probabilistic method in DARWIN GUI

4.2 Fleet risk module enhancements

The DARWIN Fleet Assessment module (FAM) assesses the risk of one or more fleets of aircraft based on disk risk results associated with individual DARWIN project files (*.dhf). The FAM is provided as a separate module that the user can access via the DARWIN tools menu. The initial version was released in DARWIN 7.1. It was subsequently enhanced to enable component replacement following a simulated inspection (replacement of the same component type in version 8.1, and replacement of a different type of component in version 8.2). In all previous versions, inspections could only be applied to individual DARWIN project files, and could not be applied across an entire fleet.

A new FAM enhancement was implemented on the current grant that enables the user to perform an inspection-based corrective action across an entire fleet of aircraft in accordance with AC 39-8 (Federal Aviation Administration, 2003). An overview of the inspection-based corrective actions enhancement is shown in Figure 7. The user defines an inspection-based corrective action by following five basic steps. In step 1, the user enables a new inspections feature in the FAM. In step 2, the user opens an inspection timetable definition menu (similar to the menu that is used to define inspections for individual DARWIN runs). In step 3, the user defines one or more inspection timetables. An inspection timetable is a set of inspection times characterized by a probability distribution. Inspection times are specified in terms of the times that fleets enter service (expressed in months). Several distributions (*e.g.*, normal, tabular, Weibull,

deterministic) are provided in the fleet assessment module for defining inspection timetables. In step 4, the user assigns an inspection timetable to one or more disks.

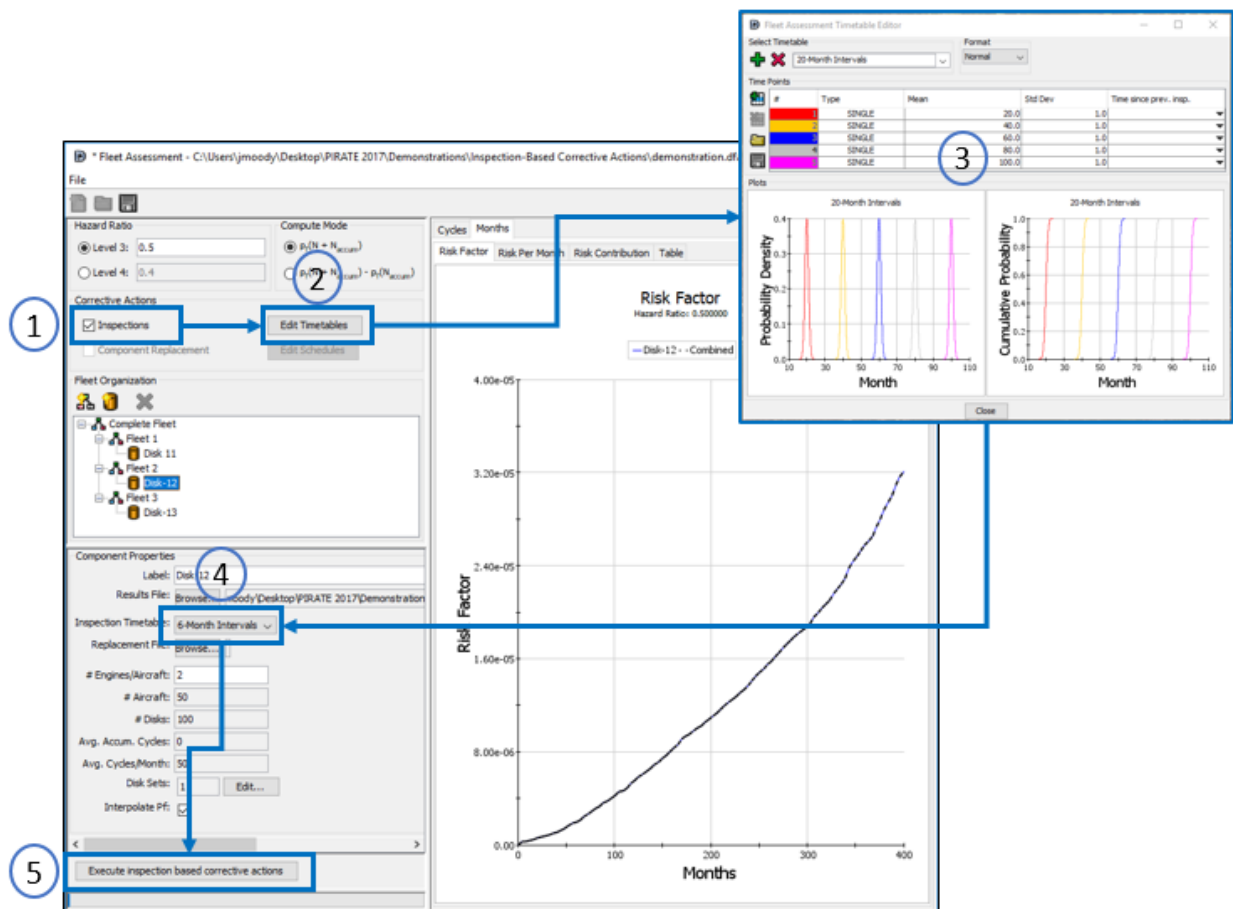


Figure 7. Overview of inspection-based corrective actions enhancement to DARWIN FAM

In the final step, the user executes the fleet risk analysis. During this process, the FAM transfers the month-based inspection timetable definitions to the cycle-based DARWIN project files for each disk associated with an inspection timetable. The month-based inspection times are converted to cycles and adjusted based on the disk set usage rate and number of accumulated cycles that are defined by the user. After all DARWIN project files have been updated with the fleet-wide inspection times, they are automatically executed to obtain the new disk risk curves via the DARWIN risk assessment code. Note that inspection timetables are only applicable to DARWIN projects that are configured to support the inspection-based corrective actions.

Upon completion of the DARWIN disk risk analyses, the fleet risk plots are automatically updated in the FAM to include the effects of inspection-based corrective actions. Example results for the FAM inspection-based corrective actions enhancement are shown in Figure 8. Note the different vertical scales in Figure 8(a) and Figure 8(b).

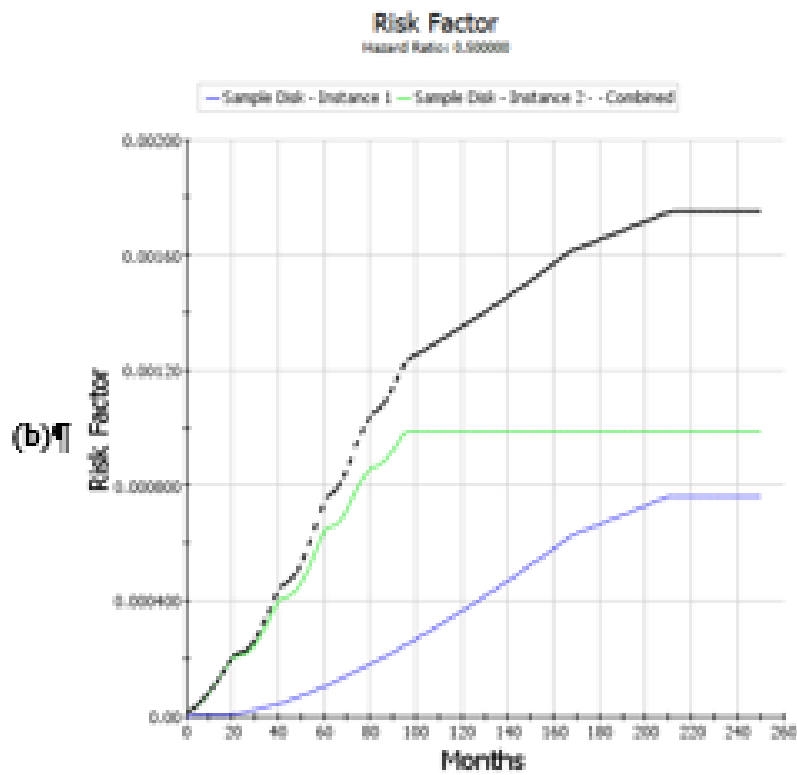
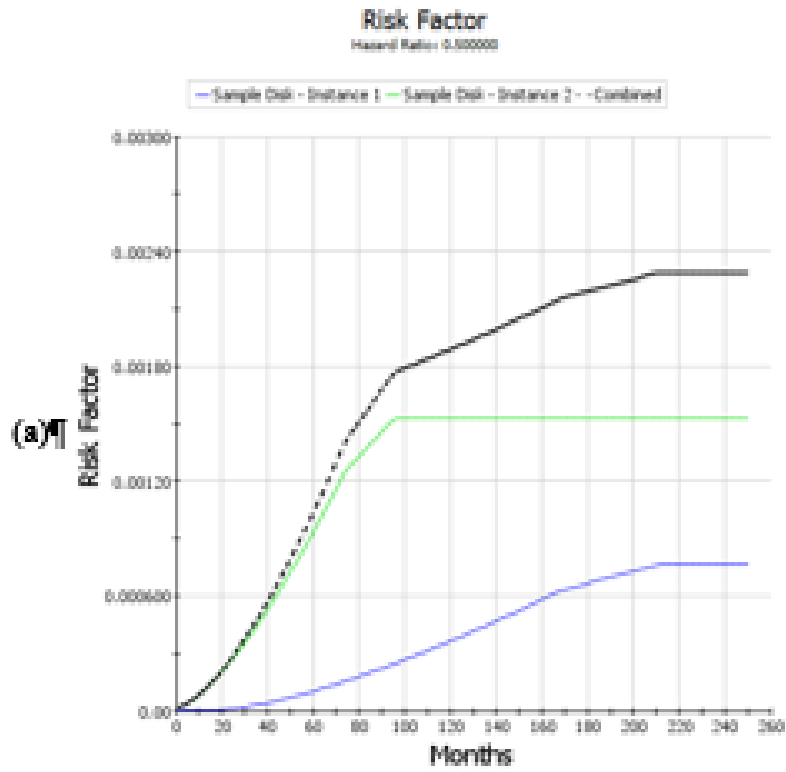


Figure 8. Example fleet risk results for DARWIN FAM inspection-based corrective actions enhancement: (a) without inspection; (b) with inspection

5 Further development of auto-modeling methods

The most significant enhancements in DARWIN during the previous grant were the development of new “auto-modeling” capabilities including automatic fracture model construction (so-called “Autoplate”), FCG life contours, and automatic model zoning for probabilistic analysis (“Autozoning”). These new features perform many of the model construction tasks much more quickly than a human user could do manually, and they eliminate much of the potential variability in DARWIN results from user to user. These enhancements have been eagerly embraced by industry. However, additional development was needed to meet needs for production use of DARWIN.

The Autoplate, life contour, and Autozoning methods implemented on previous grants, have all been based on the workhorse univariant SIF solutions for cracks in plain rectangular plates. However, DARWIN also includes several other advanced SIF solutions, including solutions incorporating fully bivariant stress gradients, which can provide improved accuracy for calculation of the crack driving force. Section 5.1 describes efforts completed on this grant to integrate bivariant SIF solutions into the auto-modeling schemes, thereby taking full advantage of the available fracture mechanics technology in the automatic calculation of life and risk.

One of the required steps in creating an engineering fracture model is to determine the size and orientation of a rectangular plate that approximates the crack growth plane in the component. The DARWIN Autoplate algorithm creates an optimum plate very quickly, often providing a superior result to a plate created manually by the user. Autoplate functionality is available for all 2D analysis modes (deterministic FCG life assessments, and both manually and automatically created zones for fracture risk assessments). However, for 3D models this capability was limited to automatic zoning associated with fracture risk assessments. Section 5.2 describes enhancements that were completed on this grant to enable automatic fracture model generation for 3D manual zoning.

In various auto-modeling modes, DARWIN computes life and risk contours that are displayed directly on the FE model. Apparent anomalies in these contours may require additional investigation, including evaluation of the size and orientation of individual fracture plates. DARWIN builds all of these plates during creation of life contours or automatic zones. However, in DARWIN versions developed on previous grants, the plates were not displayed in the GUI and the plate details were not available to the user in these automatic modes. Section 5.3

describes enhancements that were implemented on this grant that provide new display and output capabilities at user-selected nodes.

DARWIN users have high expectations regarding the speed and robustness of the computational engines for auto-modeling, as well as the functionality of the user interface. This is especially true as the auto-modeling capabilities are fully integrated into standard industry practice for production analysis, and as DARWIN is applied to production component models with increasing size and complexity. Continuous improvements are needed to ensure these objectives are achieved as additional features are implemented in the software. Section 5.4 describes several enhancements that were implemented in the computational engine, Autoplate algorithm, GUI, and FE model translator that improve the speed and robustness of DARWIN assessments.

5.1 Incorporate additional SIF solutions into auto-modeling

The focus of this subtask was on integrating bivariant SIF solutions into the DARWIN auto-modeling schemes by (1) extending the boundaries associated with bivariant fracture plates, and (2) enhancing the Shakedown algorithm to support bivariant fracture plates. These enhancements are described in Sections 5.1.1 and 5.1.2, respectively.

5.1.1 Enhanced bivariant plates

DARWIN versions that were developed on previous grants supported SIF solutions defined using bivariant plates (*i.e.*, plates with stress gradients in all directions on the crack plane). Those bivariant plates required stresses to be defined at every point in the plate, and so the geometry of the FE model had to enclose the plate completely. This restriction meant that several geometries could be accommodated by univariant plate solutions but not by bivariant plate solutions. Figure 9 shows four schematic geometries that could not be solved using these restricted definitions for bivariant plates: (a) tolerancing issues on the edge, (b) plates with far-field missing material, (c) plates with internal holes, and (d) plates with convex crack surfaces. Here red dots indicate grid points that do not have stress values, and white dots indicate the initial crack center.

DARWIN was enhanced on this grant to provide enhanced definitions for bivariant plates that provide treatment for the geometries shown in Figure 9(a), (b), and (c). This enables users to define and view bivariant plates for these geometries such as extension of plate boundaries beyond the FE model as shown in Figure 10. These enhanced definitions were implemented as an optional feature in DARWIN and are disabled by default. The issue of plates with convex crack surfaces (Figure 9[d]) will be addressed in a future grant.

When this option is enabled, the GUI performs a check to determine whether an enhanced definition is needed for each bivariate plate (this operation is invisible to the user and happens in the background). The check is accomplished by assessing the stress values at selected points within the plate (the GUI places points on a 100×100 grid within the plate). The enhanced definition is not needed if stress values are available at all points within the grid. However, if stress values are not available at one or more of the grid points, these points are marked by the GUI and then grouped into one of the four geometries shown in Figure 9. The GUI proceeds without any further checks for geometries with tolerance issues and far-field missing material (*i.e.*, Figure 9[a] and [b]). The GUI also prevents the construction of plates with convex crack surfaces (Figure 9[d]). This geometry type is not supported at this time, and requires further investigation. The GUI was also updated to display stresses in the zone plate visualization screen.

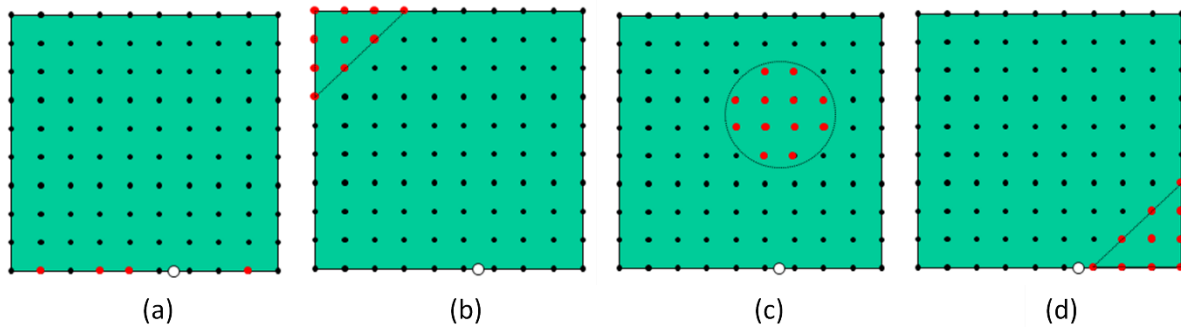


Figure 9. Problematic geometries for bivariate plates in finite element models:
(a) edge tolerancing; (b) far-field missing material; (c) internal holes, and (d) convex crack surface

Once the disabled nodes have been identified via the GUI, they are passed to the stress processing module for further analysis. If the user has enabled shakedown, the enhanced shakedown method for bivariate plates with missing material (described in the next section) is used to compute the relaxed stresses. The result is then passed to Flight_Life where it is treated as a complete rectangular bivariate plate with zero stresses at the disabled nodes.

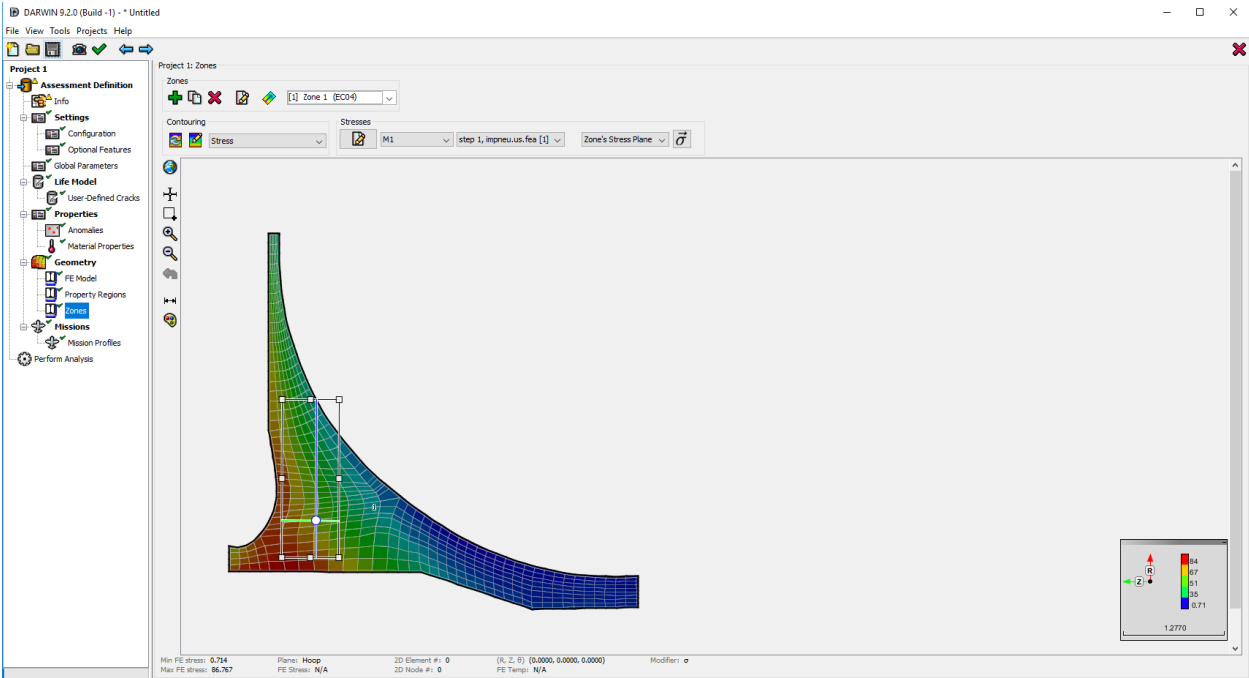


Figure 10. Bivariate plate extending beyond boundaries of FE model

5.1.2 Shakedown enhancement for bivariate plates

The DARWIN shakedown algorithm developed on previous grants used a load shedding approach to perform shakedown on rectangular bivariate fracture plates that was based on stratified areas in terms of iso-stress. This approach was enhanced on this grant to provide treatment for missing material in bivariate fracture plates (*i.e.*, plates containing “disabled” nodes as identified via the GUI). The problem with missing material is that the shakedown algorithm must accommodate the redistribution of stress from the region of local yielding over the remaining cross-section, but missing material is not capable of carrying load. The enhancement includes a new implementation for back-and-forth interpolation among user-specified stress points and the refined stress points required for shakedown, and revised force and moment formulations for active areas designated by active nodes (*i.e.*, nodes not designated “disabled”) that define a non-rectangular cross section.

For verification of this enhancement, twelve sets of FE results were generated based on three FE models and four types of remote loading. Each set contained three sub-sets of results from one elastic analysis and two elastic-plastic analyses corresponding to two elastic-plastic stress-strain constitutive curves displaying drastically different strain-hardening capacities. The three FE models used in the analysis are shown in Figure 11. These models represent one-half of a specimen subjected to remote loading along the longitudinal direction. The circular notch serves as a stress concentration. In Figure 11(a), a model is shown with some material missing at the

remote end. The same model with additional material removed at the remote end is shown in Figure 11(b). The model in Figure 11(c) has missing material at the stress concentration (*e.g.*, round hole). The elastic FE result along the non-rectangular cross section was used as input for the shakedown routine, and the computed elastic-plastic results were compared with elastic-plastic FE results. The computed results were consistent with the FE results. The approach appears to provide an efficient approximation for the elastic-plastic stress distribution resulting from shakedown.

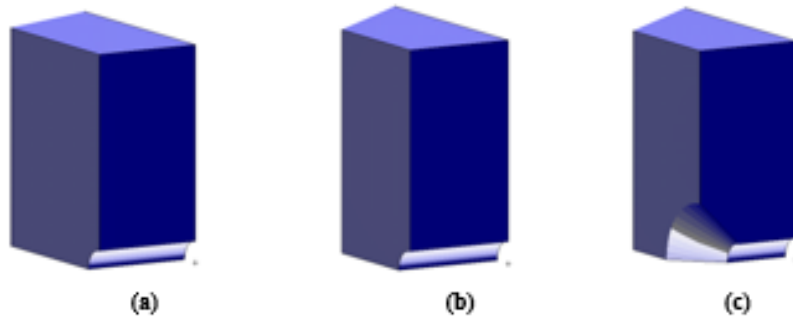


Figure 11. Models for verification of bivariant shakedown enhancement: (a) missing material at remote end; (b) additional missing material at remote end; (c) missing material at stress concentration

5.2 Add Autoplate functionality to 3D manual mode

The DARWIN Autoplate algorithm identifies the size and orientation of fracture mechanics models (*i.e.*, rectangular plates) based on the geometry, temperature, and stresses at a specified location in a FE model. All of the DARWIN autozoning algorithms (*i.e.*, exhaustive, optimal, GP pre-zone) use the Autoplate algorithm as part of the zone creation process. These autozoning algorithms are available for risk assessments using both 2D and 3D FE model geometries. Users can also invoke the Autoplate algorithm when manually creating zones via the DARWIN GUI, but this capability was previously limited to 2D FE models. For manual zone creation using 3D FE models, users were required to determine the size and orientation of fracture mechanics models using engineering judgment.

DARWIN was enhanced on this grant to enable users to create zones manually in 3D FE models using the Autoplate algorithm. One of the objectives of this effort was to develop a common interface for creating zones manually in both 2D and 3D FE model geometries. In DARWIN versions developed on previous grants, zones for 2D FE geometries were created in a single step in which the fracture model was placed directly on the FE model. For 3D FE geometries, a two-step process was used to create zones in which the user first created a slice plane, and then

subsequently placed a fracture model on the slice plane. The GUI was enhanced on this grant to create zones in 3D FE models in a single step. Now, when the user selects an initial crack location on the 3D FE model, the slice plane and fracture model are created simultaneously.

In DARWIN versions developed on previous grants, initial cracks could be placed at any location in 2D FE models, but for 3D FE models the initial crack locations were limited to nodes on the surface of FE models. The GUI was enhanced on this grant to enable users to specify the initial crack location anywhere on the surface of a 3D FE model (see Figure 12). This eliminated the need for a surface offset GUI button that was previously used to specify initial crack locations that were not located at 3D FE nodes (the GUI button was therefore removed).

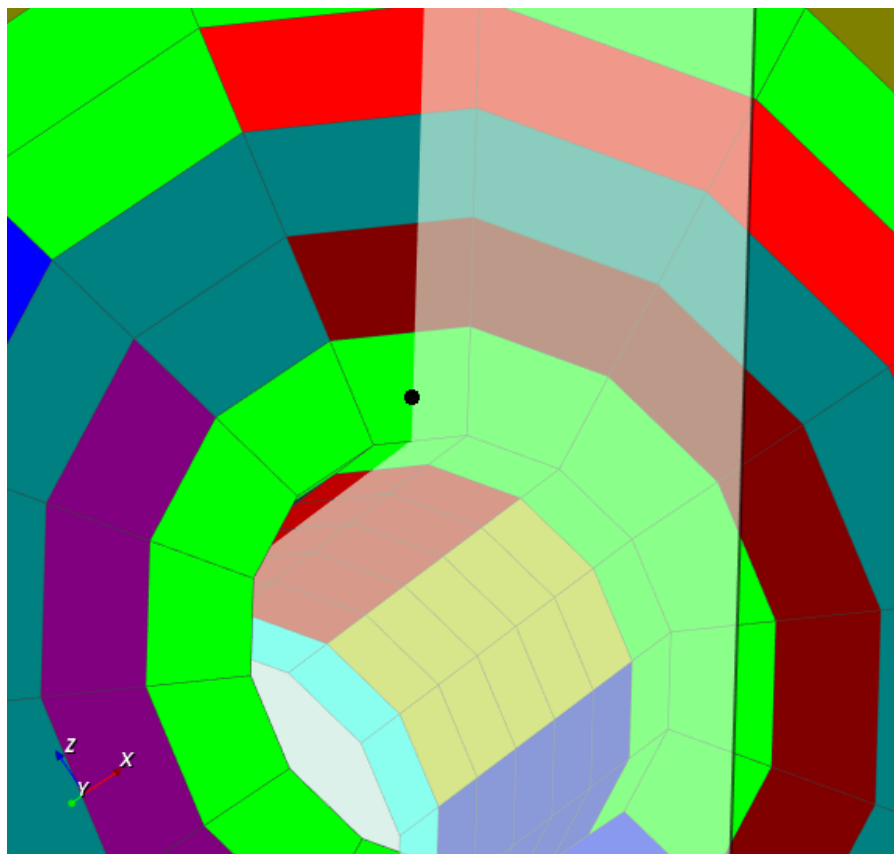


Figure 12. Initial crack on surface of 3D FE model at non-nodal location

These enhancements have resulted in a common interface for creating zones manually in both 2D and 3D FE model geometries. This will make the GUI easier to use and maintain compared to the separate interfaces for 2D and 3D manual zone creation in previous versions of DARWIN.

In DARWIN versions developed on previous grants, it was often difficult for users to determine whether a fracture model had been created by a user or via the Autoplate algorithm. This information was provided in a table only, and it was cumbersome for users to locate a specific fracture model in the table. The GUI fracture model display was enhanced on this grant as shown in Figure 13 to enable users to distinguish among models created by users and via Autoplate. Autoplate-defined plates are represented with a green border, and user-defined plates are represented with a white border.

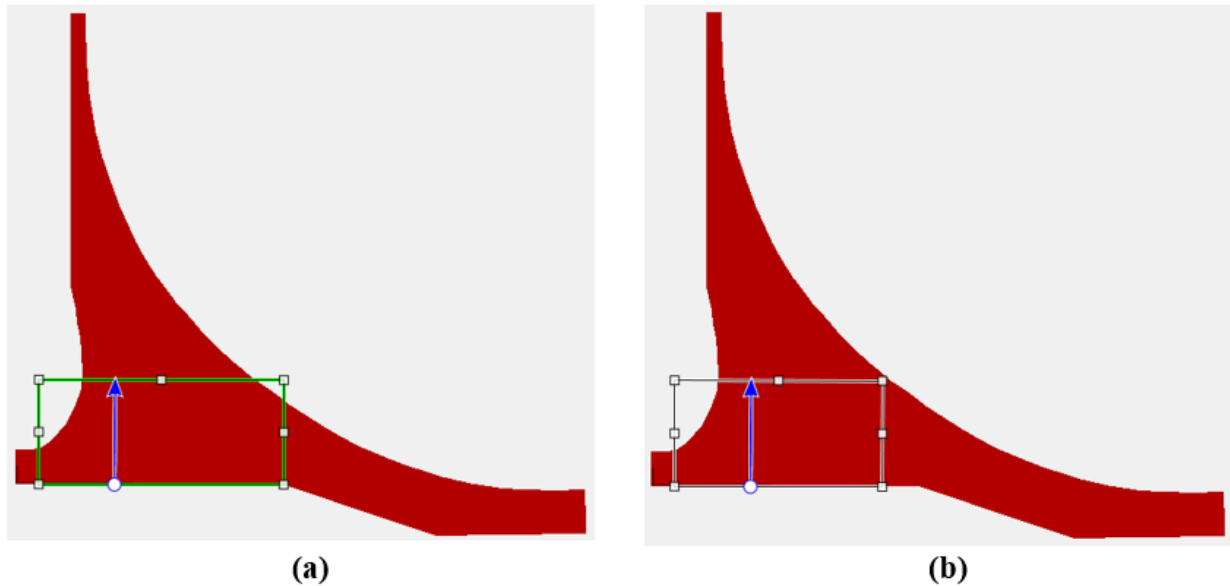


Figure 13. GUI fracture model display for
(a) Autoplate-defined plates with a green border; (b) user-defined plates with a white border

5.3 View and export fracture plates for life and risk contours

The life contours and autozoning features in DARWIN use the Autoplate algorithm to predict FCG life and fracture risk results at all of the nodes in an FE model. In DARWIN versions developed on previous grants, the fracture plates created by Autoplate were discarded after the analysis was completed and were not available for viewing by the user.

DARWIN was enhanced to enable users to view and export fracture plate information associated with life and risk contours. This optional output entitled “Export Intermediate Nodal Results” is activated in the GUI preferences menu, as highlighted in Figure 14. When this option is enabled, the DARWIN Computational Engine (DCE) records detailed information regarding the size, slice plane, stresses, and initial crack type associated with the fracture plates at each node in a FE model. The DCE outputs this information to a table in the DARWIN output (*.dhf) file. This

capability is available for life and risk assessment using the crack growth contours and optimal autozoning features, respectively.

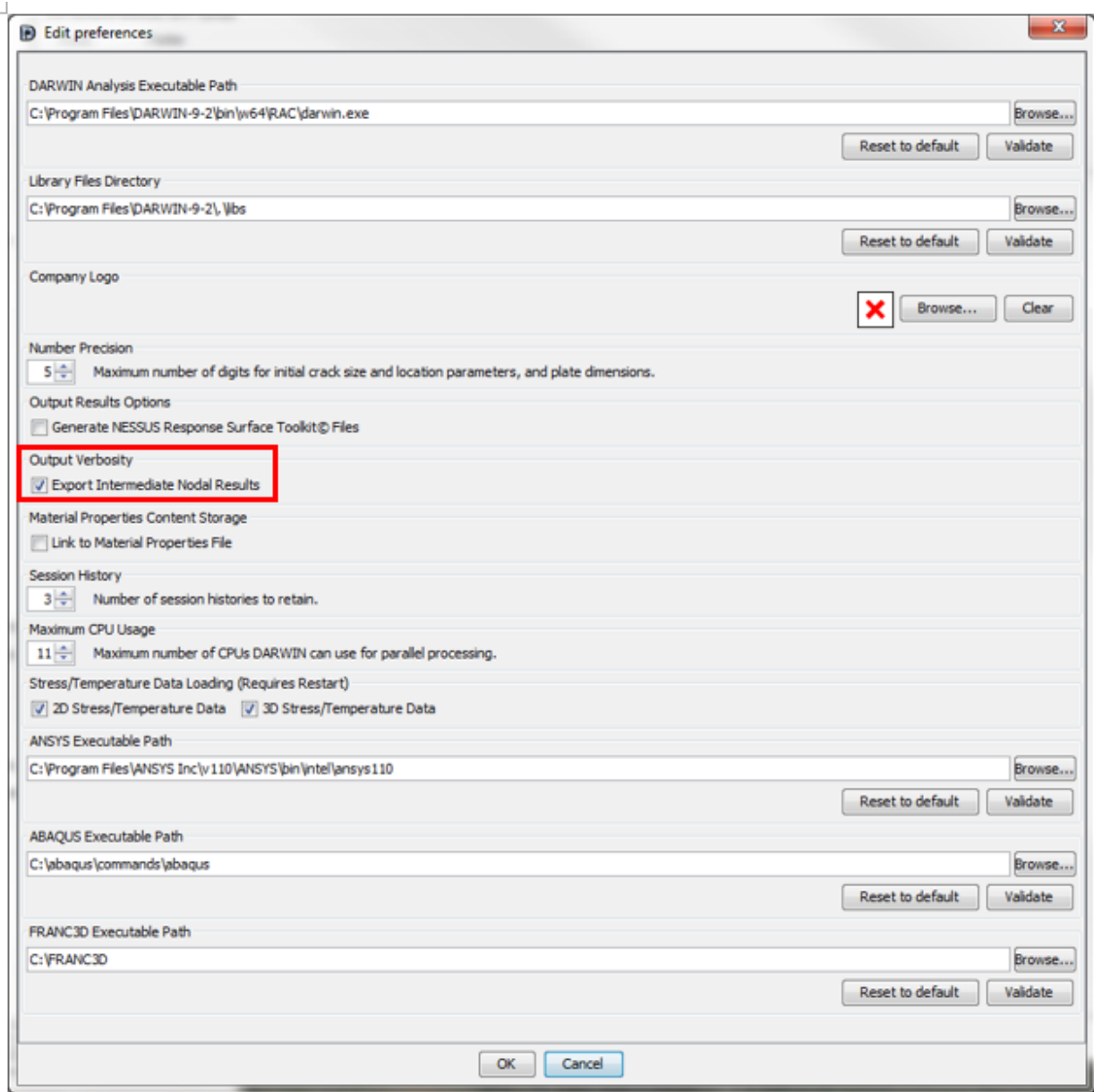


Figure 14. “Export Intermediate Nodal Results” selection in GUI preferences menu

In DARWIN versions developed on previous grants, the GUI provided the capability to view properties associated with zone fracture plates such as initial crack location, plate dimensions, and stress contours superimposed on the fracture plate. This visualization capability was extended on this grant for application to fracture plates associated with automatically-generated

life and risk contours. This enables users to click on a node, view the fracture plate, and view plate properties and associated stress contours as illustrated in Figure 15.

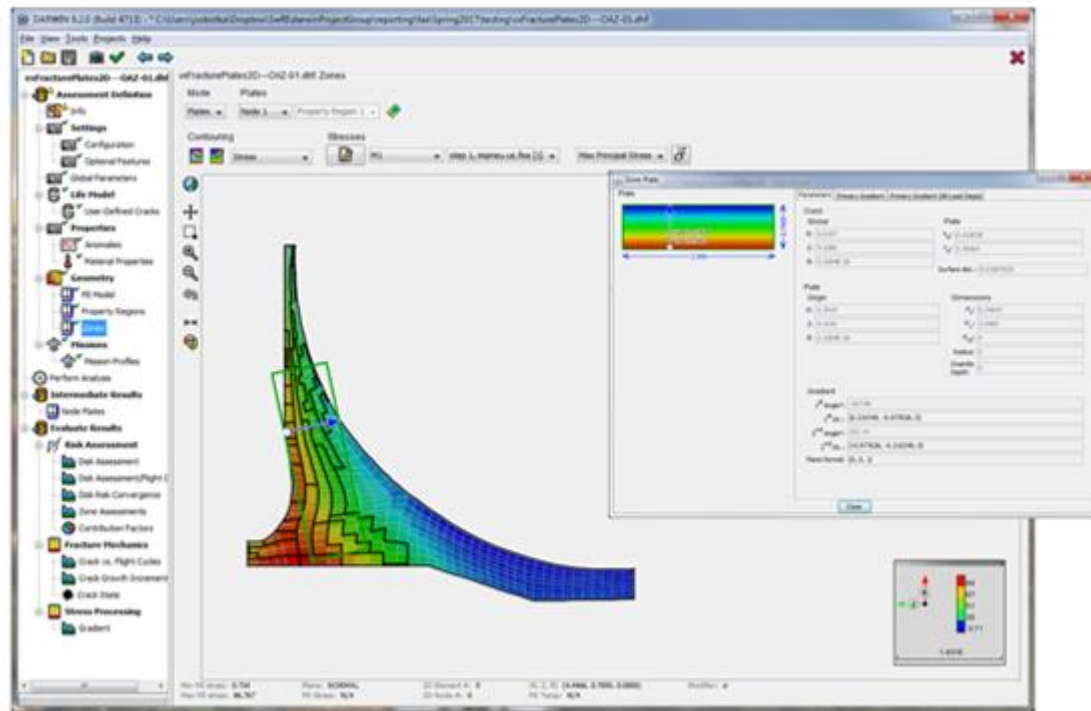


Figure 15. Example fracture plate associated with a single node in a 2D FE model

5.4 Maturation of auto-modeling capabilities for production use

A number of auto-modeling capabilities have been implemented in DARWIN over the past several years including Autoplate, exhaustive autozoning, optimal autozoning, and GP pre-zoning. These capabilities have significantly reduced the amount of human time and expertise required for component life prediction and risk assessment. However, additional maturation of auto-modeling capabilities is needed for DARWIN to support a wide range of very large, complex FE models used for production purposes by the aircraft engine industry, especially as improved computational capabilities encourage engineers to build larger and larger models.

As the auto-modeling capabilities in DARWIN are adopted and integrated into original equipment manufacturer (OEM) organizational processes, the robustness and speed of these new capabilities is being carefully considered, particularly for application to large FE models. Section 5.4.1 describes DARWIN enhancements that were implemented on this grant to reduce computation time for large FE models.

Accurate FE models are required for successful execution of the DARWIN Autoplate algorithm. However, FE models that are created by commercial FE software may sometimes contain incompatibilities that can cause Autoplate to fail. Section 5.4.2 describes an enhancement to the DARWIN FE2NEU algorithm to identify FE models containing incompatibilities that may affect the performance of the Autoplate algorithm.

Some of the FAA certification analysis modes require users to place initial cracks manually in 3D FE models. The 3D FE models associated with these analysis modes have become larger, and it has had an impact on the amount of human time that is required to complete certification assessments. Section 5.4.3 describes enhancements that have been implemented to reduce the time required to analyze user-defined cracks in large 3D FE models.

Use of larger 3D FE models in DARWIN assessments can also impact the time required for the GUI to respond to user commands and to import analysis results into the GUI. Section 5.4.4 describes an enhancement that has reduced GUI response times for large 3D FE models, and Section 5.4.5 describes an enhancement that reduces the time required to import analysis results associated with large 3D FE models.

The computation time of all DARWIN auto-modeling features is dependent on the speed of the Autoplate algorithm. Section 5.4.6 describes an enhancement to FE2NEU and Autoplate that reduces the computation time associated with Autoplate operations.

5.4.1 Improved support for large finite element models

DARWIN versions developed on previous grants did not provide adequate support for large FE models with large numbers of load steps. The time required to import and display large FE models in the GUI could be measured in double digit minutes or even hours. The time required to process these FE models in the DCE was extensive, and often terminated because the memory required to process the analysis exceeded available computer random access memory (RAM). The memory limitation was due to the use of a text-based file format for FE models. To resolve this problem, a binary file format called HSIESTA was introduced for storage and retrieval of FE results data. HSIESTA replaced an earlier file format (SIESTA) used by DARWIN to store the same information. HSIESTA stores information in a binary format that is more easily accessible to DARWIN.

This enhancement enables DARWIN to read, display, and utilize data directly from HSIESTA. This significantly reduces the time required to read and display the stresses and temperatures associated with large FE models. For example, consider a FE model with approximately 100,000 nodes and 1,000 load cases. Prior to the enhancement, the GUI required nearly ten minutes to

import and display the stresses and temperatures associated with a single load case. The time required to display the stresses and temperatures associated with another load case in the same model exceeded ten minutes and eventually timed out. Using the HSIESTA capability implemented on this grant, the same FE model was imported and displayed in approximately 10 seconds, or roughly 60 times faster than the previous DARWIN version that used SIESTA files. The GUI was also able to display the stresses and temperatures associated with other load cases in the file in roughly 8 seconds for each load case.

FE2NEU (DARWIN FE results file translator) was enhanced to translate FE models from commercial FE software (*e.g.*, ANSYS, ABAQUS) to the HSIESTA format. It was further enhanced to convert legacy SIESTA-formatted files to the HSIESTA format. This enables users to convert FE results from legacy files to the new HSIESTA format that was implemented in DARWIN.

The DCE was also enhanced to read and process data from HSIESTA. It was enhanced with new random access API functions that enable it to read data from specific regions of the HSIESTA file rather than importing the entire file into memory. Verification results have confirmed reduced memory usage for large FE models when the number of zones is much smaller than the number of elements/nodes.

5.4.2 FE2NEU finite element model triage algorithm

FE model sizes have increased dramatically in size over the past several years, and DARWIN users have reported problems working with larger FE models. This prompted an effort to evaluate the auto-modeling capabilities in DARWIN to identify and resolve code performance vulnerabilities. Each aircraft engine company within the Steering Committee provided FE models (protected by non-disclosure agreements) to SwRI for the purpose of evaluating the various auto-modeling capabilities within DARWIN. The FE models were representative of each organization's standard practices. Accordingly, the FE models exhibited a wide range of geometric features, element types, and FE mesh sizes. The FE models were a mixture of 2D and 3D models with mesh sizes ranging from 50,000 to 600,000 elements.

The following auto-modeling capabilities were considered in the evaluation:

- Life Contours
- Critical Initial Crack Size (CICS) Contours
- Optimal Autozoning for Inherent Anomalies

- Optional Autozoning w/Prezoning for Inherent Anomalies
- Optimal Autozoning for Surface Damage Anomalies

All five auto-modeling modes were considered for each of the seven models provided for thirty-five evaluations. The initial assessment focused on robustness, where robustness is defined as the ability of the DARWIN computational code to complete an analysis. Six of the seven FE models failed the robustness metric due to computational errors (often due to problems with the FE mesh) that caused the analyses to terminate prematurely.

To address this problem, a triage algorithm was developed and implemented in the DARWIN FE2NEU FE model translator. This algorithm assesses the compatibility of FE models that are intended for use in DARWIN. It performs a series of model quality checks (MQCs) during the conversion of an FE file from its native format to the DARWIN HSIESTA (*.fea) format.

FE2NEU now performs the following MQCs:

- All nodes must be connected to an element. Orphan nodes are prohibited.
- All nodes must have stresses and temperatures assigned to them for all load cases.
- All nodes must have unique locations. Coincident nodes are not supported.
- All elements must conform to the list of elements supported by the HSIESTA file format.
- All elements must have a positive volume. Negative volumes are prohibited.
- All element faces must have a positive area. Collapsed faces are prohibited.
- Models may only contain one component.
- Duration times for load cases must be consistent, i.e., all defined or none defined.

FE2NEU reports MQC results to the FE2NEU output console and stores the results in the HSIESTA-formatted *.fea file. Once the MQCs have been performed, FE2NEU inserts a digital signature into the *.fea file indicating that MQCs were performed. As shown in Figure 16, FE2NEU includes a new ‘Convert and Sign’ button that initiates the MQCs and stores the results and digital signature in the *.fea file. Further information regarding the FE Triage algorithm is provided in Appendix F.

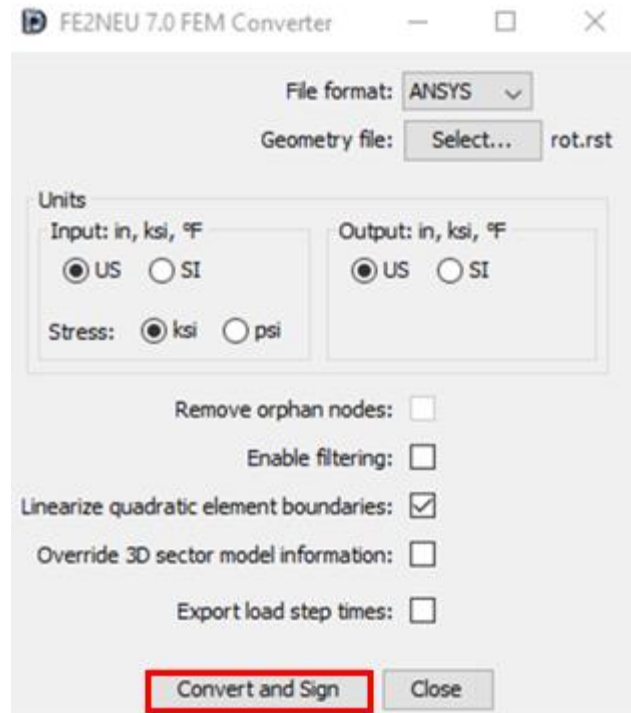


Figure 16. New FE2NEU ‘Convert and Sign’ button to execute MQCs and store results and digital signature in *.fea file

5.4.3 Speed enhancements for user-defined cracks

In DARWIN versions developed on previous grants, the crack growth plane was identified by the GUI prior to executing the Autoplate algorithm. This process involved the GUI loading all FE stress results for all load steps into memory. It required a significant amount of computer memory (potentially exceeding the available memory for large FE models) and could take several minutes to complete at a single location.

To resolve this problem, the Autoplate algorithm was enhanced to identify directly the crack growth plane for user-defined cracks. This enhancement enabled Autoplate to extract stresses at single elements and nodes (requiring significantly less memory) and compute the crack growth plane in a fraction of the time that was required by the GUI. The GUI was also enhanced to decrease the number of times that the display screen is refreshed to improve computational efficiency.

These enhancements have resulted in an 85-95% reduction in the computation time required to create user-defined cracks in large 2D and 3D FE models with large numbers of load steps. Actual speed improvement is dependent on FE model size and the number of load steps that are

applied. For example, the time required to place a crack and create a fracture mechanics plate at a single location in a large FE model (225,000 elements, 1000 load steps) was reduced from 250 seconds to 18 seconds. The GUI RAM associated with this model was reduced from 12.5 gigabyte (GB) to 1.9 GB.

5.4.4 GUI interaction with FE models speedup

In DARWIN versions developed on previous grants, the GUI executed a number of operations each time the user performed an action such as entering/importing data or clicking on a node in a FE model. For small FE models the response time was on the order of a few seconds, but for large 3D FE models the response time could be several minutes or more.

Several improvements were implemented in the GUI to reduce the response time when working with large 3D FE models. These improvements include application of contour data to the model all at once to avoid multiple redundant display events; refreshing only the contour that is currently displayed (rather than all contours); reloading data only when data changes have been confirmed; initializing data only for algorithms that are currently in use; and removal of redundant display algorithms. The speed enhancement has the most impact on geometry-related preprocessing operations such as assigning elements to a geometry, selecting a crack location, and viewing stress/temperature contours for specific load cases.

This speed enhancement provided approximately a 75% reduction in the GUI response time associated with large 3D FE models. This estimate is based on the response time required to perform GUI preprocessing tasks associated with a FCG life assessment at user-specified locations in a 1 million element 3D FE model (Windows 10, dual 2.3 GHz processors, 16 GB allocated RAM). Note that GUI response times will vary depending on the FE model size, number of project objectives, computer operating system, CPU power, and available RAM (among other factors).

5.4.5 DARWIN results file import speed enhancement

In DARWIN versions developed on previous grants, the entire results file had to be loaded into memory before any of the results could be displayed in the GUI. The GUI was enhanced to enable selected portions of the results file to be loaded into memory as needed to display specific results as they are selected by the user. This enhancement provided a 90-98% reduction in the time required for the GUI to open 2D and 3D results files with large numbers of zones (*i.e.*, 500 or more zones). It reduced the time required to open a results file and display component risk results (85-88% reduction), and also reduced the time required to open a results file and display risk contours (12-74% reduction) for 2D and 3D FE models with large numbers of zones.

5.4.6 Autoplate speed improvement enabled by FE2NEU enhancement

The computation time of all DARWIN auto-modeling features is dependent on the speed of the Autoplate algorithm. In DARWIN versions developed on previous grants, the Autoplate algorithm constructed a 2D FE model of the model geometry at the initial crack location in a 3D FE model. The resulting 2D FE model geometry and associated stress/temperature values were used for all Autoplate computations at the location. This process was repeated at each initial crack location and could be time-consuming for computing FCG life and fracture risk contours in large 3D FE models.

The FE2NEU finite element results file translator was enhanced to identify the finite elements that are located on the exterior surfaces of 3D FE models. This information is provided to the Autoplate algorithm during run time, and enables it to quickly identify the boundaries of the 3D geometry that are coincident with the crack growth plane at each initial crack location. This enables Autoplate to extract geometry and stress/temperature information directly from the 3D FE model. This new capability reduced the computation time for Autoplate and associated auto-modeling operations for large 3D FE models. The impact of this enhancement on auto-modeling speed will vary depending on FE model size and desired project objectives (*e.g.*, FCG life at user-specified locations, FCG life contours, fracture risk).

6 Improved user interfaces

The user interface for a sophisticated analysis tool plays a critical role in enhancing user efficiency, reducing the potential for human errors, and facilitating accurate interpretation of results. The advanced and novel DARWIN user interface has been a major factor in the rapid adoption of the tool by industry. This task focused on incorporating the latest developments in software engineering to support full integration of DARWIN into a variety of industrial production environments.

While AC 33.14-1 (Federal Aviation Administration, 2001), AC 33.70-2 (Federal Aviation Administration, Aug, 2009), and AC 33.70-3 (Federal Aviation Administration, 2023) prescribe probabilistic damage tolerance methods for specific anomaly threats, the more general AC 33.70-1 (Federal Aviation Administration, July, 2009) advises the use of deterministic damage tolerance calculations in some situations. DARWIN was originally developed to support the probabilistic approaches of AC 33.14-1 and AC 33.70-2, and the original DARWIN workflow involved the creation of a probabilistic “zone” before creating a fracture mechanics model. However, since DARWIN may also be used to perform deterministic fracture analysis for FAA purposes (and since many licensees use DARWIN for deterministic analysis), the deterministic analysis

framework has been streamlined in recent years. Section 6.1 describes an enhancement to the framework that enables the user to place an initial crack anywhere in a model and perform a deterministic life calculation without needing to create a zone.

Some DARWIN users routinely modify DARWIN input files manually using a text editor. Use of command line script programs can greatly reduce the amount of human time required to modify these files. Section 6.2 describes an enhancement to a DARWIN script program developed on a previous grant that enables the user to create and/or modify DARWIN input files without the use of the GUI.

DARWIN contains a number of optional features that are not needed or desired by all users. In addition, some companies may wish to provide default settings or values for their users that may differ from the defaults that are provided in DARWIN. Section 6.3 describes an enhancement implemented on this grant that enables users to choose different default settings for improved control (how our company always does it) or convenience (how I usually want to do it).

Over the past decade, DARWIN has been enhanced to enable risk assessment based on stress, temperature, and geometry information in 3D FE models. However, previous versions did not provide the capability for users to view contours inside 3D FE models. The GUI also provided limited options for definition of regions within 3D FE models. Section 6.4 describes advanced GUI visualization capabilities that were implemented on this grant to enable users to define and manipulate regions within 3D FE models.

6.1 Zoneless deterministic analysis

DARWIN was originally designed to assess the risk of fracture of components containing rare material and manufacturing anomalies as described in AC 33.14-1 (Federal Aviation Administration, 2001) and AC 33.70-2 (Federal Aviation Administration, Aug, 2009). The original DARWIN GUI workflow (*i.e.*, content and sequence of GUI menus and features) was intended to support the zone-based risk assessment methodology described in those ACs. However, many analysts also use DARWIN to assess deterministic FCG life, as described in AC 33.70-1 (Federal Aviation Administration, July, 2009).

DARWIN versions developed on previous grants enabled users to perform deterministic FCG analysis, but the risk assessment-based GUI workflow required additional input that was not required for deterministic analysis. For example, users had to define a zone for each initial crack location in a deterministic analysis, but much of the zone information was not used in the deterministic analysis.

This subtask focused on the enhancement of DARWIN to enable users to perform deterministic FCG life assessments without zones. A new GUI workflow was developed specifically for deterministic assessments in which a new “Life Assessment” project mode is defined in the first (configuration) GUI menu (Figure 17(a)). This enabled the GUI to display the analysis configuration settings that apply only to deterministic life assessment. The user no longer needs to specify the analysis mode nor the zone information for a deterministic analysis. The new configuration settings displays for the life assessment and risk assessment analysis methods are shown in Figure 17(a) and (b), respectively.

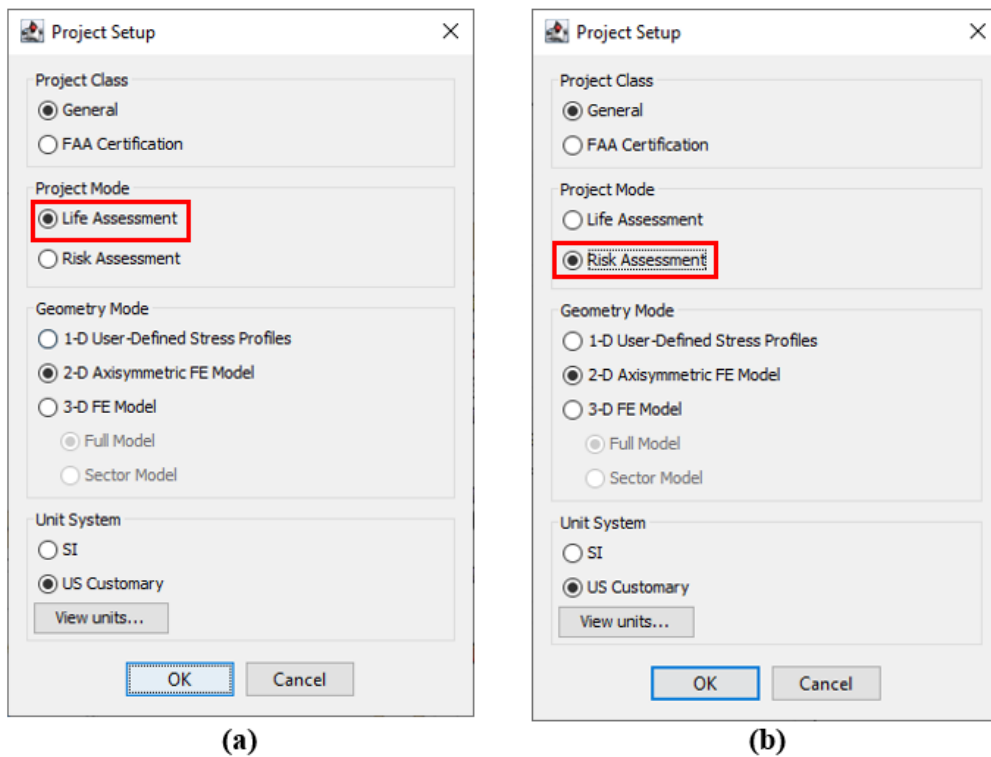


Figure 17. Enhanced DARWIN GUI configuration menus:
(a) life assessment, (b) risk assessment

The Optional Features menu (Figure 18) was enhanced for deterministic analysis to display only the information that is applicable to a deterministic life assessment. In DARWIN versions developed on previous grants, both deterministic and risk assessment, information was displayed in this section (risk-related information was displayed in gray for deterministic assessments).

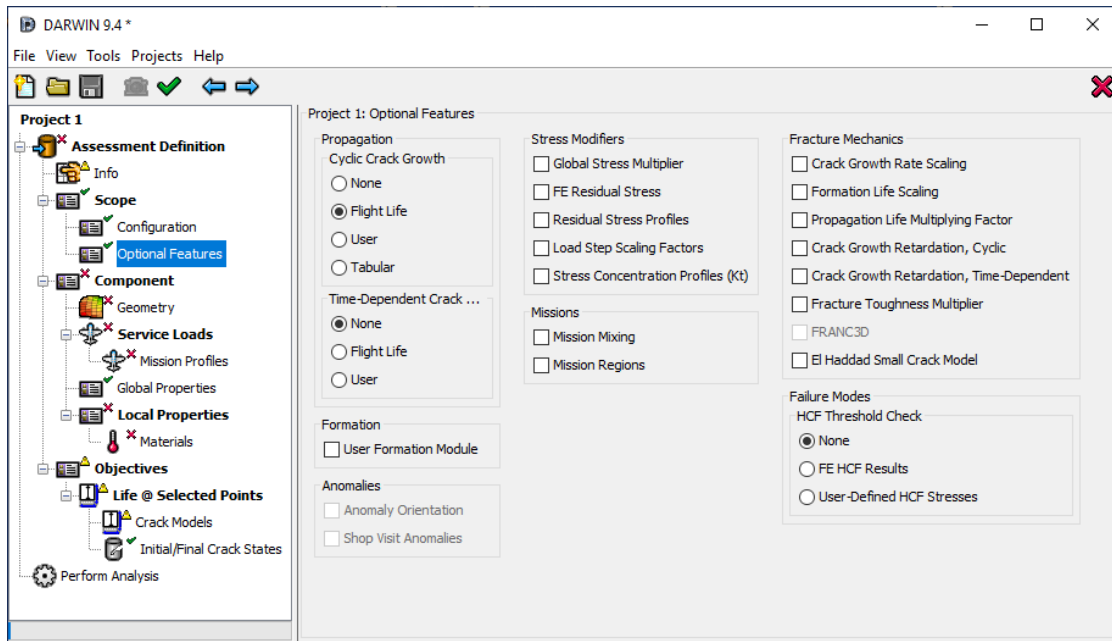


Figure 18. Enhanced DARWIN optional features menu for deterministic life assessment

The “Life Assessment” project mode enables users to perform individual FCG analyses at user-specified locations (Life @ Selected Points objective) or to construct a series of FCG life contours (Surface Life Contours, Volumetric Life Contours, or Volumetric CICS Contours objectives).

The Life @ Selected Points objective enables users to place initial cracks at multiple locations in a FE model and to perform a deterministic FCG life analysis at these locations. The user provides the crack location, crack type, crack growth plane, and fracture mechanics plate (via the Autoplate algorithm). A name can also be specified for each crack location. As shown in Figure 19, the display for the Life @ Selected Points objective is similar to a zone. Note that unlike zones, the Life @ Selected Points objective is defined by its location, and is not associated with a group of finite elements.

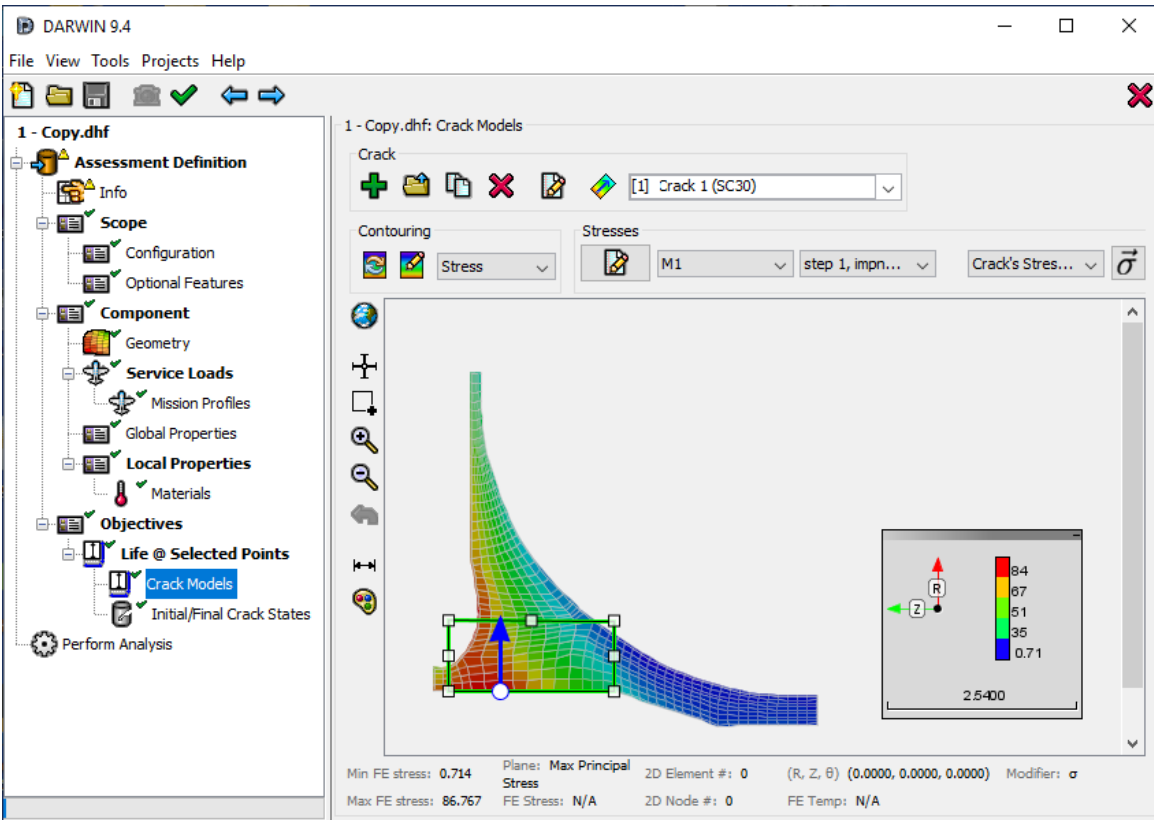


Figure 19. Enhanced GUI display for the Life @ Selected Points objective

The various contour objectives enable users to define one or more crack-growth contour models. This feature replaced the legacy life contours feature that was provided as a preprocessing tool in previous versions of DARWIN. The legacy life contours feature was executed by passing input data from the GUI to the DCE and contour information from the DCE to the GUI without the use of traditional input/output files. The new feature accomplishes this task using traditional input/output files, which is a more stable and extendable approach that has enabled the development of additional life contour features.

An enhanced Contour Models menu was introduced that enables users to define the parameters of crack-growth contour models (Figure 20). These parameters include name, location, initial crack state, and termination criterion. The location of each contour model is defined using contour regions. A contour region is a group of finite elements (similar to DARWIN “property regions”).

In DARWIN versions developed on previous grants, users had the ability to view propagation life contours only. This feature was enhanced to display contours for the formation and propagation portions of life, K_{max} , and final crack sizes in terms of depth (a), half-length (c), and area.

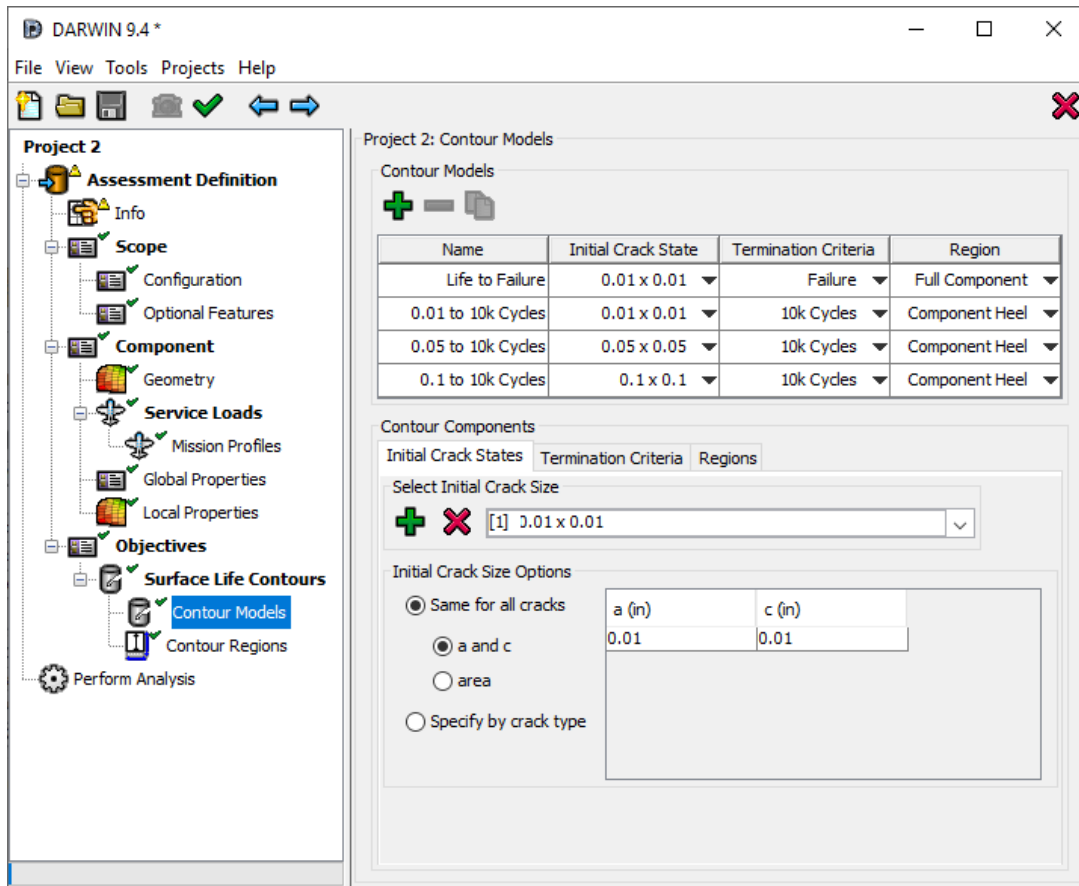


Figure 20. Enhanced DARWIN Contour Models menu

6.2 Scriptable input

The DARWIN software consists of two primary components: (1) GUI (Java-based user interface) intended for interaction with the user, and (2) DCE (Fortran-based computational code) and associated modules (such as Flight_Life) that perform the stress processing, life prediction, and risk assessment computations. The GUI's primary purpose is to prepare an input file for the Risk Assessment Code (RAC), and to display the results from the RAC. The DARWIN input file can be executed either via the GUI or in batch mode (independent of the GUI). Once the DCE input file has been created, it can be edited by the user as needed. In earlier versions of DARWIN, the DARWIN input file was formatted in American Standard Code for Information Interchange (ASCII) and could be modified using a standard text editor. In later versions of DARWIN, the file was stored in binary format that requires a special editor for review and editing of the file.

Some DARWIN users routinely modify DARWIN input files manually. To improve the efficiency of the process, these users have developed computer programs in command line scripting languages (also called “scripts”) that can automatically interrogate and edit DARWIN input files to change input values. The scripts can significantly reduce the amount of human time required to modify DARWIN input files. However, many of the scripts were developed for use with the previous ASCII format, and required updates to the binary format that is used in current versions of DARWIN. In addition, even if scripting were available, users would still be required to create the original input files via the GUI (requiring additional human time).

On a previous grant, SwRI developed a script program called the DARWIN Python Module (DPM) that enabled users to create and/or modify DARWIN input files without the use of the GUI. The script was originally developed to perform routine DARWIN software verification at SwRI, but could also be used to modify DARWIN input files for other purposes. That version of the DPM was provided to the Steering Committee for review, and then it was enhanced in response to Steering Committee comments.

The enhanced DPM was implemented as an independent module that is distributed with DARWIN. It included the following capabilities:

- Create new DARWIN project files
- Modify input data in existing DARWIN project files
- Query input and output data in DARWIN project files
- Execute DARWIN projects

An overview of the relationship among DARWIN and the DPM is shown in Figure 21. The DPM serves as an intermediary between user-provided Python scripts and the DARWIN project file (*.dhf) and executable program (darwin.exe). The user-provided Python script sends commands to the DPM, and DPM handles the complex tasks of querying, modifying, creating, and executing DARWIN projects.

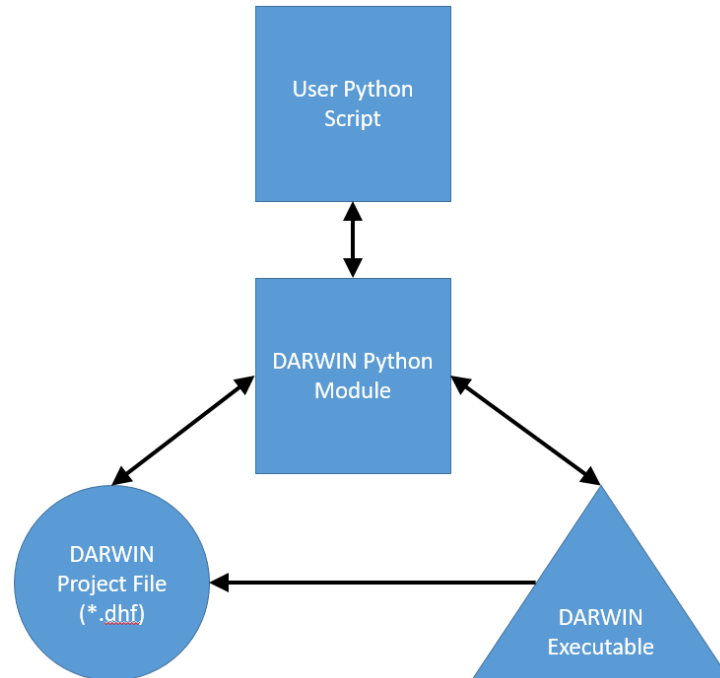


Figure 21. Relationship among DPM, user-provided Python scripts, and DARWIN project file and executable program

Project creation methods in the DPM are currently limited to the following analysis modes:

- 2D User-Defined Cracks
- 3D User-Defined Cracks
- 2D General Inherent Autozoning
- 3D General Inherent Autozoning

Support for additional analysis modes is planned for future grants. Further information regarding the DPM is provided in Appendix G.

Incorporating the DPM into a user-provided Python script consists of four fundamental steps:

1. Import the DARWIN Python module into a Python script

```
import darwin93
```

2. Initialize a DARWIN project object

```
projectObj = darwin93.Project()
```

The DARWIN project object is an in-memory representation of a new or existing DARWIN project file (*.dhf).

3. Import an existing DARWIN project file or create a new DARWIN project file

- Importing an existing DARWIN project file

```
projectObj.open_project({Path to existing DHF file})
```

- Creating a new DARWIN project file

```
projectObj.create_project({Path to new DHF file}, {Project Code})
```

4. Interact with the DARWIN project using the available methods

Example user-provided python scripts illustrating the four primary DPM capabilities (query, modify, create, and execute) are provided in Figure 22 through Figure 26, respectively.

```

import darwin93

projectObj = darwin93.Project()

projectObj.open_project({Path to existing DHF file})

resultsObj = projectObj.results
propLife = resultsObj.zone fractureResult('cycles', cycle="LAST")

# The results method creates a results class object that provides access to DARWIN project results
# The zone_fractureResult method retrieves the value(s) for the specified attribute and cycle.
# Results class objects contain several methods for various results types

serviceLife = projectObj.get_attribute('/darwin/input/serviceLife/@cycles')

# The get_attribute method retrieves the value of any attribute in the DHF provided that the DHF path is
known.

projectObj.close()

```

Figure 22. Example Python script utilizing DPM to query a DARWIN project

```

import darwin93

projectObj = darwin93.Project()

projectObj.open_project({Path to existing DHF file})

# The open_project method opens an existing DARWIN project file.

projectObj.title = 'Revised Project Title'

# The title method modifies the value assigned to the Title field located in the Info preprocessing menu

projectObj.set_attribute('/darwin/input/serviceLife/@cycles',10000)

# The set_attribute method modifies the value of any attribute in the DHF provided that the DHF path is
known.

projectObj.close()

```

Figure 23. Example Python script utilizing DPM to modify a DARWIN project

```

import darwin93
# The DARWIN Python module must be imported into a Python script in order to access the
# available methods

projectObj = darwin93.Project()
# The Project class creates an in-memory representation of a DARWIN project

projectObj.create_project({Path to new DHF file},1022)
# The create_project method creates a new DARWIN project file at the specified location. The
# project code indicates the type of project to create.
# Project Code 1022 creates a project with the following configuration:
#   Analysis Method: Life Assessment
#   Analysis Mode: General
#   Geometry Mode: 2D Axisymmetric FE Mode
#   Anomaly Type: 2D Anomaly
#   Deterministic Mode: User-Defined Cracks

projectObj.title = 'Example Project Title'
projectObj.description = 'This project was generated by DPM'
# The title and description methods assign values to the Title and Description fields located in
# the Info preprocessing menu

projectObj.unitSystem = 'US'
# The unitSystem method assigns a value to the Unit System field located in the
# Configuration preprocessing menu.
# Most Configuration menu fields are set by the project code.

projectObj.cyclicCrackGrowth = 'FLIGHT_LIFE'
# The cyclicCrackGrowth method assigns a value to the Cyclic Crack Growth field in the Optional
# Features preprocessing menu
# The cyclicCrackGrowth method represents a subset of the optional feature methods that
# are currently available in DPM

projectObj.geometry = {Path to FEA file}
# The geometry method imports an FEA file into a DARWIN project

missions = darwin93.Mission()
missions.add_all_fea_steps({Path to FEA file})
projectObj.missions = missions
# The Mission class creates a mission object that can be used to set up mission profile definitions
# The add_load_fea_steps method assigns all load steps in the specified FEA file to a mission
# The missions method imports the data in a mission object into a DARWIN project

```

Figure 24. Example Python script utilizing DPM to create a DARWIN project

```

projectObj.tmfMethod = 'TEMP MAX STRESS'
# The tmfMethod method assigns a value to the TME Crack Growth field located in the
# Global Properties preprocessing menu
# The tmfMethod method represents a subset of the global properties methods that
# are currently available in DPM

props = darwin93.Properties()
props.add_material('ALL',{Path to MAT file})
projectObj.properties = props

# The Properties class creates an object that can be used to define location-specific
# properties, e.g., materials and anomalies
# The add_material method assigns a specified material properties file to a group of elements
# The properties method imports the data in a properties object into a DARWIN project

cracks = darwin93.Cracks()
cracks.add_crack(title='Crack 1',location={node ID},size=[0.1,0.1])
projectObj.cracks = cracks

# The Cracks class creates an object that can be used to define crack models for user-defined
# crack analyses
# The add_crack method is used to define crack model parameters
# The cracks method imports the data in a cracks object into a DARWIN project

projectObj.close()

# The close method closes a project object and removes its data from memory

```

Figure 25. Example script utilizing DPM to create a DARWIN project (cont).

```

import darwin93

projectObj = darwin93.Project()

projectObj.open_project({Path to existing DHF file})

projectObj.execute(np=4)

# The execute method executes the DARWIN project

projectObj.close()

```

Figure 26. Example Python script utilizing DPM to execute a DARWIN project

6.3 Allow user or superuser to control default settings

DARWIN provides the capability for individual users to define the GUI environment by selecting options in the GUI preferences menu and enabling desired hidden features. The GUI preferences menu governs GUI pre-processing, execution, and post-processing behaviors. Hidden features govern the availability of organization-specific capabilities.

Each organization is likely to have a unique GUI environment, and control of that environment may be critical to ensure consistent usage of the DARWIN program among analysts. Some organizations do not wish to use all features, or may wish to make a reduced set of features available to some of their users. In addition, some organizations wish to provide default settings or numerical values for their users that may differ from the defaults that are provided in DARWIN.

New capabilities were developed on this grant that enable an organization to specify the DARWIN features that are available to their users and to specify default values for selected DARWIN inputs. These enhancements influence the DARWIN preference options and hidden features that are available each time the GUI is used. They also influence the GUI optional features, global parameters, and preferences menus. The enhancements consist of two new features: (1) file-based capability to customize the GUI environment, and (2) user-defined project rules defined via special template files. These features are described in Sections 6.3.1 and 6.3.2, respectively.

6.3.1 File-based capability to customize the GUI environment

The file-based capability to customize the GUI environment enables organizations to configure the GUI environment via an ASCII text-based file called a GUI Configuration File (GCF). The GCF is imported into DARWIN during installation. It imposes specific preference options and hidden features that are available each time the GUI is used. A common DARWIN GUI environment can be imposed throughout an organization by simply assigning the same GCF file to all DARWIN installations.

A GCF follows a simple key-value file format. Each environment-related field is associated with a unique key and an expected input type. The presence of field-specific keys is optional, however. For unspecified fields, the DARWIN GUI applies the default values. For specified fields, the field values are not modifiable. An example GCF is shown in Figure 27.

```
ENHANCED_BIVARIANT_PLATES=TRUE
LINK_MATERIAL_FILES=FALSE
MAX_CPUS=6
OUTPUT_INTERMEDIATE_RESULTS=TRUE
LIBRARY_DIRECTORY=../../darwin/libraries
```

Figure 27. Example GUI Configuration file

Two methods are provided for importing a GCF into a DARWIN installation. The first method involves placing the GCF in a dedicated subfolder in the DARWIN installation directory. Upon startup, the GUI checks the dedicated subfolder for a valid GCF and automatically applies the GCF rules if a file is located. The second method involves specifying the path to a valid GCF. The GCF path is defined in the GUI Preferences menu, as shown in Figure 28. This method is particularly useful if an organization intends to use a common GCF to control the GUI environment for DARWIN installations on multiple workstations.

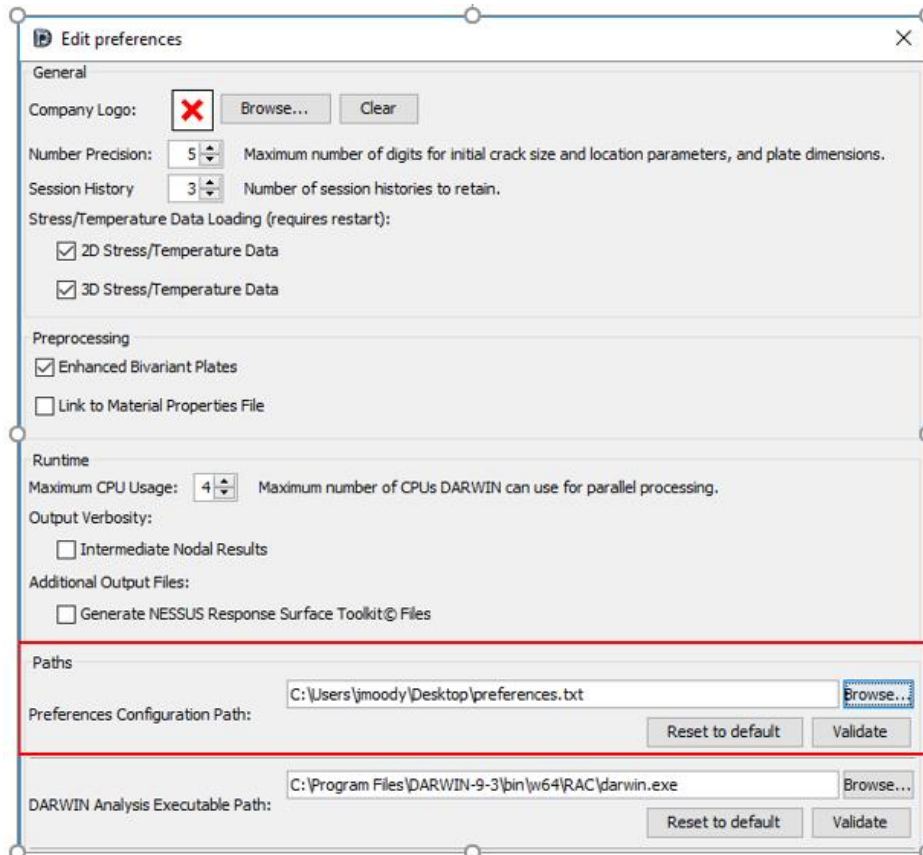


Figure 28. New preference menu field for optional specification of a GCF path

6.3.2 User-defined project rules defined via special template files

A new capability has been implemented in DARWIN for establishing organization-specific project rules. This capability allows organizations to establish custom rules for projects by creating ‘templates.’ A template is a special DARWIN project file that contains user-defined project rules regarding field restrictions and defaults. Templates can be used to initialize new projects (called template-based projects) that are forced to adhere to the rules defined in the template.

Templates can be used for a variety of purposes such as setting project defaults, preventing users from employing unauthorized features, and forcing projects to use particular field values. In addition, templates can be used to create analysis modes. An analysis mode is a targeted DARWIN project file that is used to analyze particular component types. Templates designed for analysis modes may have very restrictive rule sets.

DARWIN provides a dedicated GUI environment for the creation of templates. This mode (template mode) is available only to super-users (also known as template masters). Template mode differs from the standard DARWIN GUI environment in two ways. First, template mode only contains a subset of the preprocessing screens provided in the standard DARWIN GUI environment (*e.g.*, Info, Configuration, Optional Features, and Global Properties). Second, template mode contains additional fields called disablers that are used to disable or force field values depending upon the field type.

Within template mode, a template master creates a project in an identical fashion as would be done for creating any other DARWIN project. The template master then selects a value for each field and activates the value-specific disablers as necessary to disable or force field values (Figure 29).

For multiple option fields (*e.g.*, TMF Crack Growth), disablers prevent users from selecting the field value in template-based projects. For checkbox fields (*e.g.*, In-Service Inspections) and input fields (*e.g.*, number of samples) disablers prevent users from changing the default field value. When the template master saves the project, the GUI stores the template project file in the active template directory. Apart from allowing template masters to create templates, template mode also allows template masters to modify existing templates.

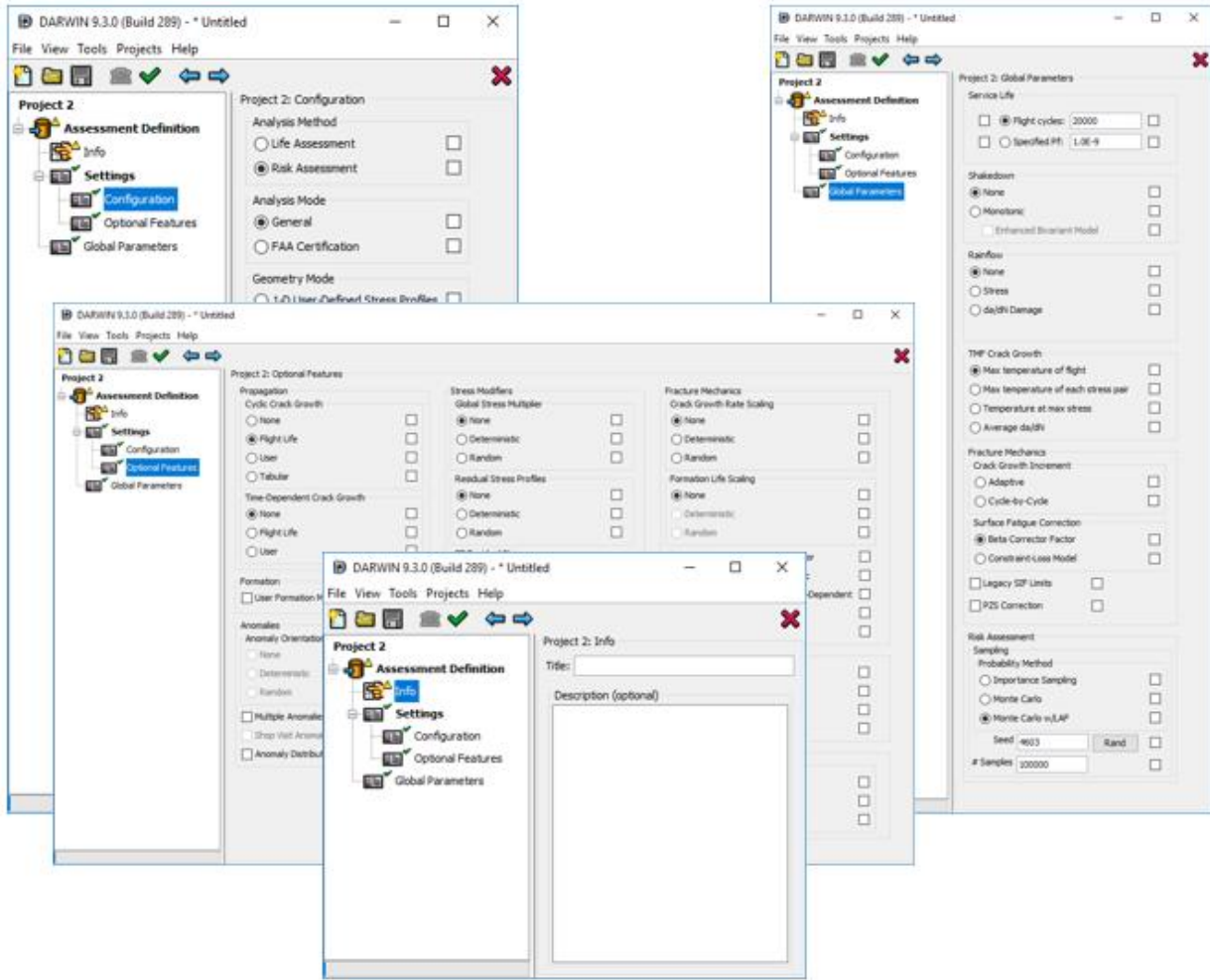


Figure 29. Overview of template mode, where super-users can set rules for fields

In the standard DARWIN GUI environment, (non-template mode) templates can be used to initialize DARWIN projects. When a new project is initialized in the DARWIN GUI and one or more template projects are available in the active template directory, the prompt shown in Figure 30 appears to enable the user to specify if the project will be based on a template file. An organization may elect to limit users to template-based projects only if desired.

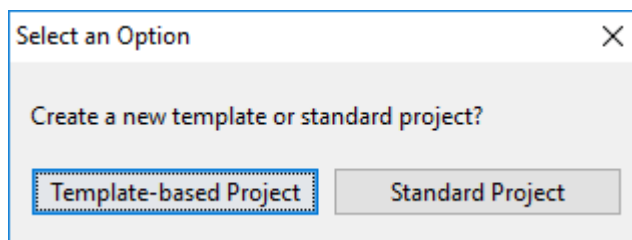


Figure 30. New project type prompt enabling users to specify use of template-based projects

The active template directory determines (a) where created templates are stored and (b) where to check for templates when a template-based project is created. By default, DARWIN stores and retrieves templates from a designated location in the DARWIN installation drive. However, organizations have the ability to store templates in custom locations. For example, an organization may wish to store templates on a shared drive that is accessible by all DARWIN-related workstations. This will make the templates available to all users within an organization. The template directory location can be specified in a dedicated field in the GUI Preferences menu, as shown in Figure 31.

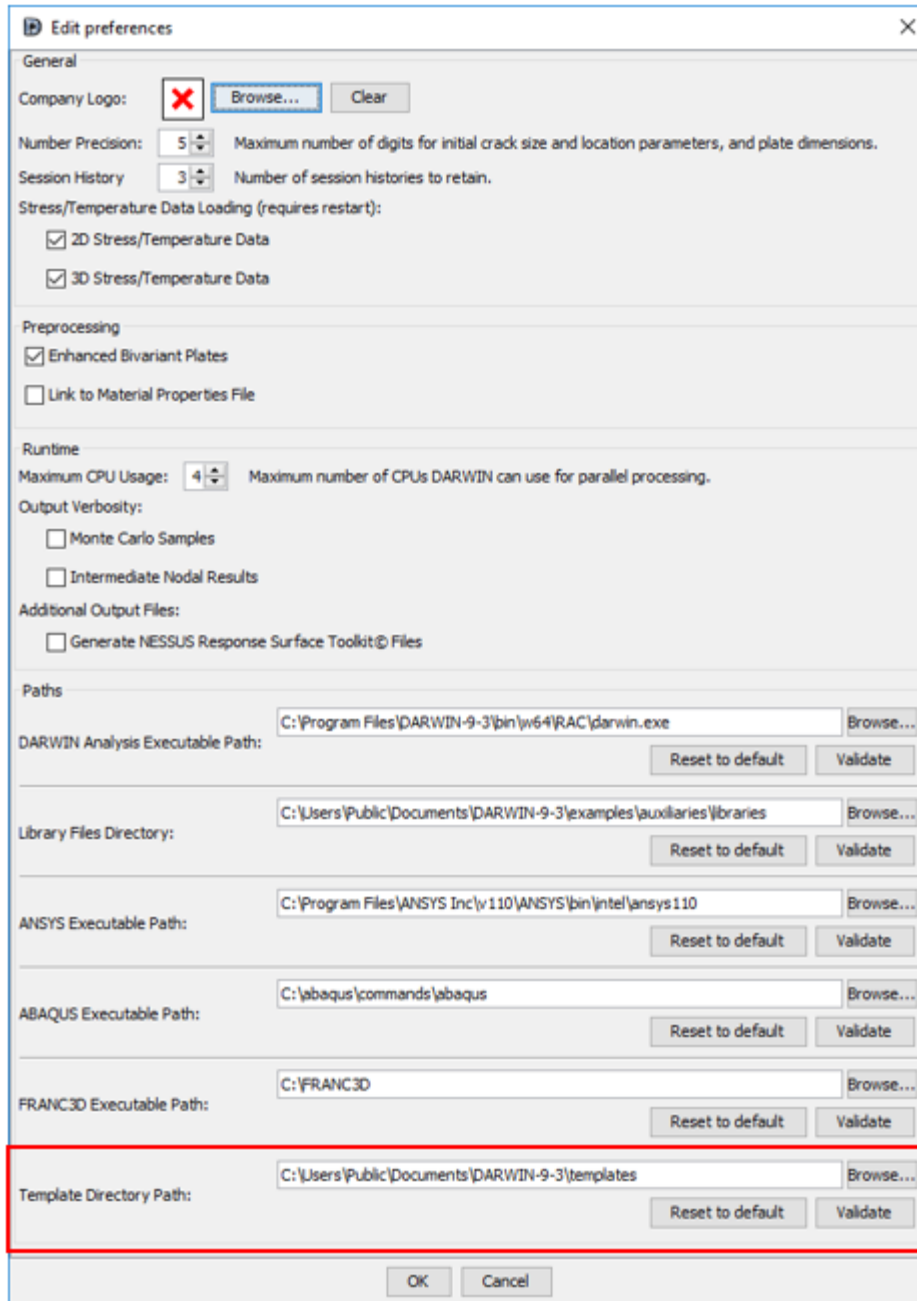


Figure 31. New GUI preferences menu field for the optional specification of a template directory path

In previous versions of DARWIN, hidden feature keys were used both to enable new features and to impose project rules. This led to confusion for both the user and SwRI user support, particularly when multiple hidden feature keys were enabled. Starting with DARWIN 9.3 Alpha,

hidden feature keys are used only to enable new features, and templates are used to impose project rules.

6.4 GUI visualization improvements

Nearly every planned new feature requires some form of GUI visualization. Improvements in the speed, accuracy, and robustness of DARWIN GUI visualization are required to enable the use of these new features in a production design environment. In previous versions of DARWIN, visualization of contours (*e.g.*, stress, life, risk contours) was limited to the exterior surfaces only. There was no capability for users to view contours inside 3D FE models. This additional capability was needed to enable users to define zones and view results for life and risk assessment of inherent anomalies in 3D FE models. The GUI previously provided only limited options for definition of regions (*i.e.*, groups of elements) within 3D FE models: selection of all elements, all surface elements, or all interior elements. Additional region selection capabilities were needed to support life and risk assessment of inherent anomalies in 3D FE models.

DARWIN was enhanced on this grant to provide advanced visualization capabilities that enable users to define and manipulate regions within 3D FE models. The enhanced GUI provides the following additional options for definition of regions in 3D models:

- Define region by list of elements. Enables users to import a list of element identifiers defined by external FE software (*e.g.*, Abaqus, ANSYS). The list of elements is imported into the GUI using the button and interface shown in Figure 32. In this example, the first ten thousand elements have been selected by the user via the pop-up menu.
- Define region by contour. Enables users to define regions by contour (*e.g.*, temperature in a group of elements). Users press the view contour button and then select from among the available contour colors. DARWIN automatically groups elements together that have similar contour values.
- Define region by contour range. Enables users to enter a contour range into the GUI. The GUI locates all elements that have the same contour range (*e.g.*, all stresses between 0 and 100 ksi). Figure 33 illustrates this capability by displaying the grouped elements above a minimum temperature.
- Define region by boxing elements. Enables users to select a group of elements that are within a bounding box. The user defines the box geometry on the screen via the mouse. DARWIN groups the elements within the box into a region, as shown in Figure 34.

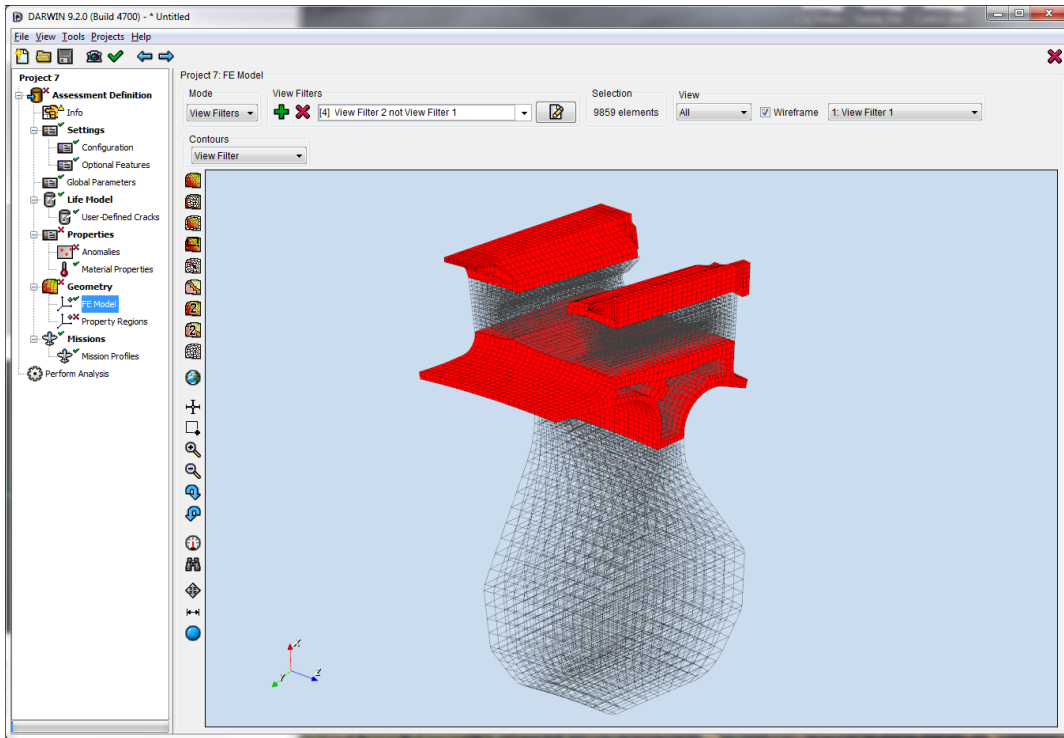


Figure 32. Example of region definition by element number capability

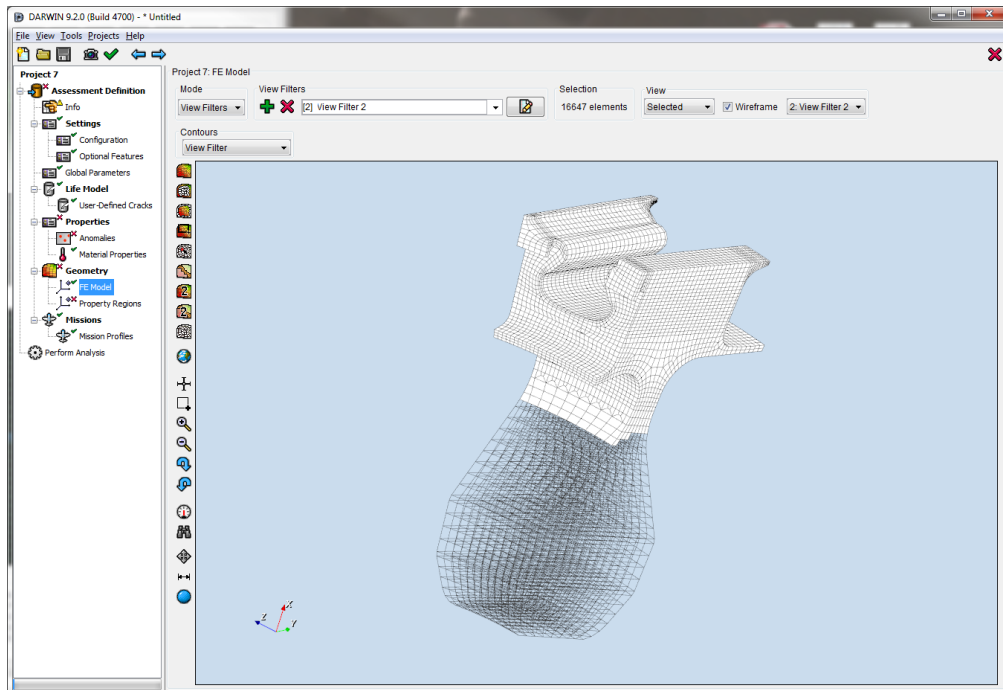


Figure 33. Example of region definition via selection of elements by contour range

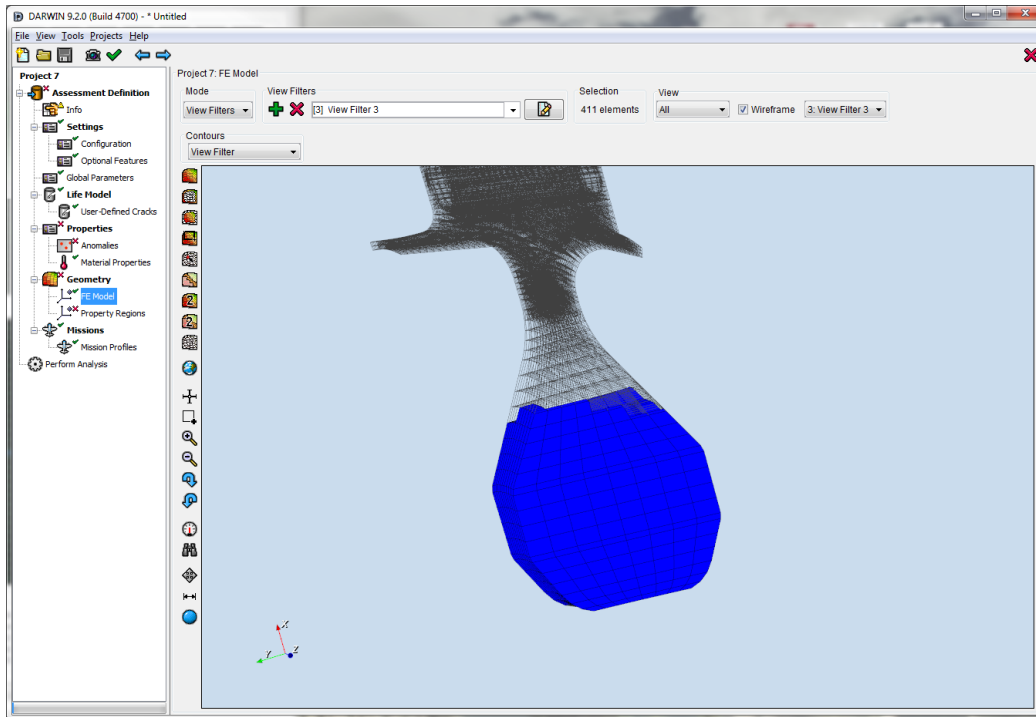


Figure 34. Example of region definition by selecting elements within a bounding box

The new options define property regions that enable users to specify properties (*e.g.*, material properties, anomalies, inspections) in the interior of a 3D FE model for life and risk assessment of inherent anomalies. The 3D regions can also be defined as view filters that enable users to visualize different parts of the geometry that previously could not be seen in DARWIN. View filters can be defined using any of the available 3D region selection tools and combined using the following Boolean operations:

- AND: Contains elements that are in both view filters and excludes elements that are only in one view filter.
- OR: Contains elements that are in both view filters.
- XOR: Contains elements that are in only one view filter and excludes elements that are in both view filters.
- NOT: Contains elements from the first view filter and excludes elements from the second view filter.

Figure 35 illustrates the effect of the Boolean operation NOT applied to the view filters created in Figure 32 and Figure 33. View filters can also be used to define property regions: first define the appropriate view filter, and then assign properties to all elements in a view filter.

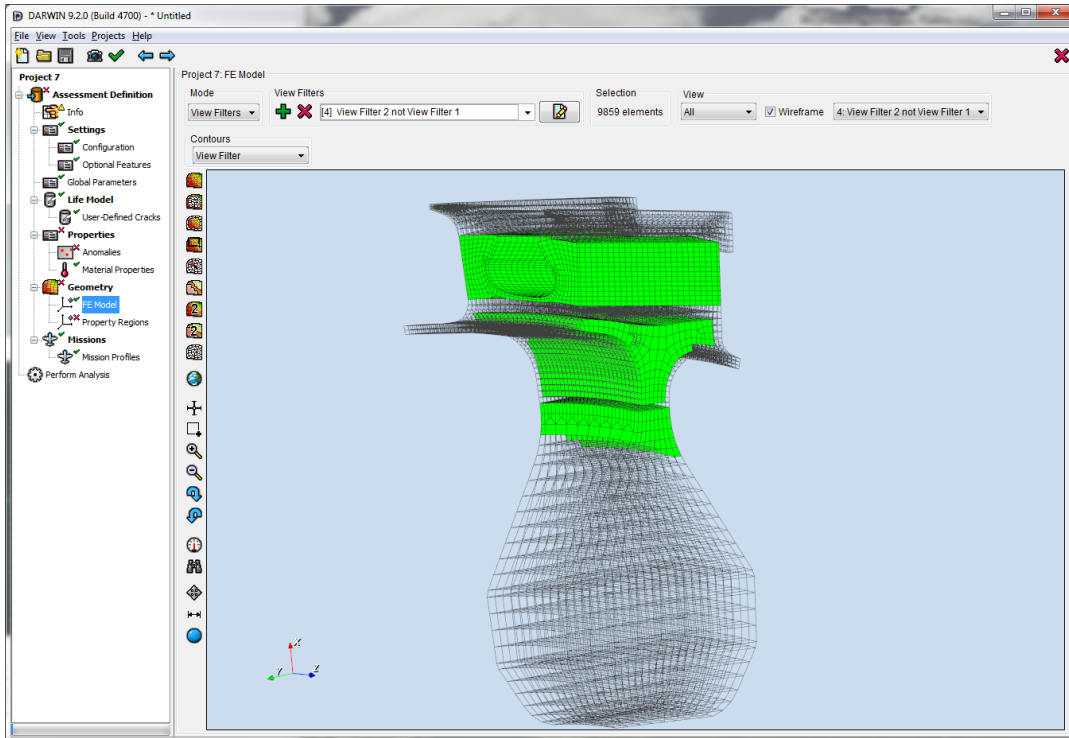


Figure 35. Illustration of DARWIN capability to create view filters.
 In this filter, elements shown in Figure 32 were removed from the elements shown in Figure 33

3D visualization features were also implemented in DARWIN:

- **Toggle Edges:** For very fine resolution models, the display of finite element edges may obscure fields hidden behind them such as stress and temperature contours. This feature enables users to either display or hide finite element edges, as shown in Figure 36.
- **Model Clipping:** Model clipping enables users to define a plane for clipping. Regions on one side of this plane are “clipped” from the component (*i.e.*, removed from the view) and a new interior surface appears that is defined by the clipping plane. Tools within the GUI enable users to define the location of the clip plane and its angle by moving a directional arrow. This capability is available for all 3D views. Figure 37 illustrates the interior of a 3D model by moving the clip plane through the model at a constant angle. Figure 38 presents the interior of a 3D model at different clipping angles.
- **Iso-Surfaces:** Iso-surfaces represent a technique where surfaces are defined based on field values. For example, an iso-surface might be defined by all stresses below some threshold value. This feature enables users to define an iso-surface defined on a 3D

geometry. These quantities may include stresses, temperatures, lives, and risk values. Users may define the value for the iso-surface using a slider that reports the current iso-surface value.

- Users may also determine if the iso-surface is defined above or below the defined value. Figure 39 shows iso-surfaces at various thresholds where the threshold provides and lower bound, and Figure 40 shows the corresponding iso-surfaces where the threshold provides an upper bound.

These visualization features are available in both pre-processing and post-processing analysis modes.

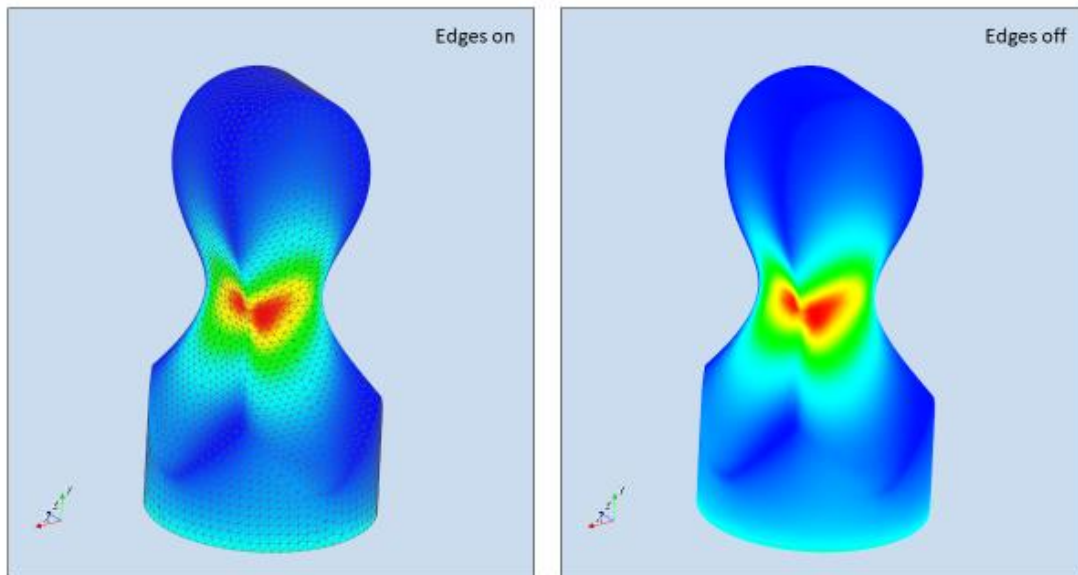


Figure 36. Illustration of Toggle Edges GUI 3D visualization feature

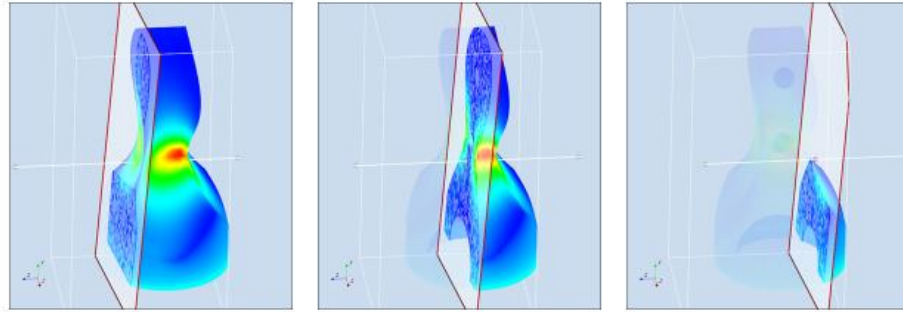


Figure 37. Illustration of Clipping GUI 3D visualization feature (at three different clip depths)

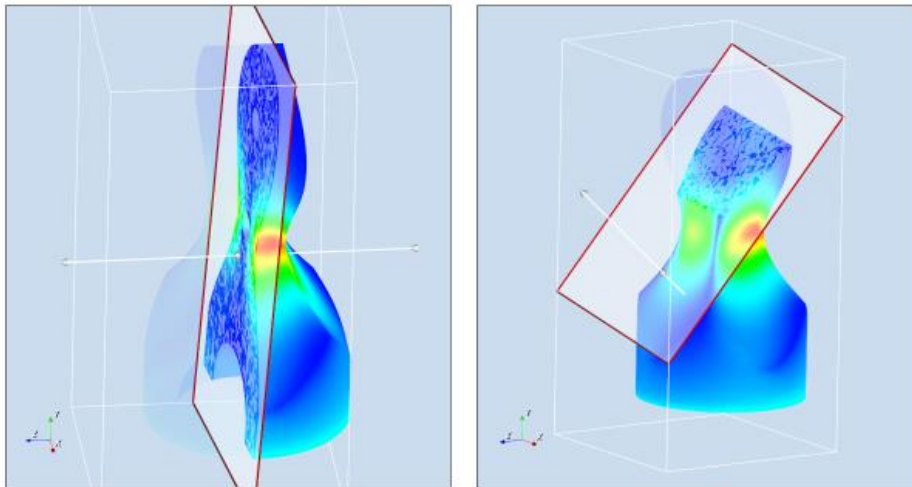


Figure 38. Illustration of Clipping feature at different clip angles.

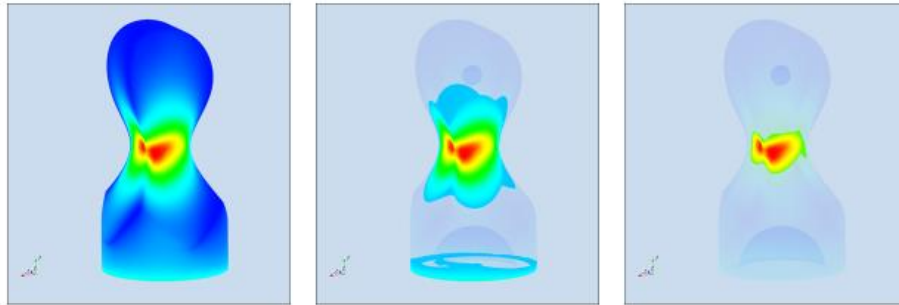


Figure 39. Illustration of Iso-Surfaces GUI 3D visualization feature (removing material above a selected threshold)

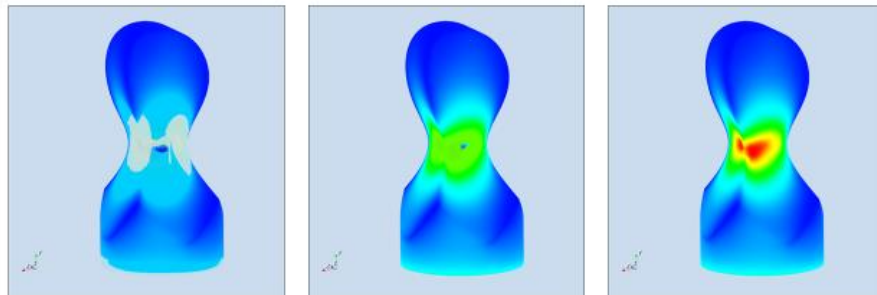


Figure 40. Illustration of iso-surfaces GUI 3D visualization feature (removing material below a selected threshold)

7 Direct DARWIN support for Advisory Circulars

As noted earlier, all of the activities in this grant and its predecessor grants were focused on supporting the development and implementation of various FAA ACs. More specifically, however, several new DARWIN features were developed previously to provide direct support for the specific requirements of AC 33.14-1 and AC 33.70-2 (Enright, et al., 2012). These features include exclusive analysis modes that automatically lock out any DARWIN capabilities

incompatible with the selected AC and FAA certification report forms tailored to each AC. This type of support needs to be maintained and extended as new ACs are developed or as old ACs are modified.

During PIRATE-2, the DARWIN team supported development of a new FAA AC (AC 33.70-5) on attachment slots. This work led to a new analysis mode in DARWIN for this specific purpose. The DARWIN implementation follows guidance provided by the RISC committee. The DARWIN team also supported two, revised FAA ACs for HA (AC 33.14-1 Change 1 and AC 33.70-3). This effort included adding new anomaly distributions to DARWIN that reflect the new ACs. Finally, we added new security features to the existing ACs in DARWIN that safeguard the fidelity of the FAA certification assessments against input file modifications.

7.1 New DARWIN analysis mode to support new AC on attachment slots

A new AC has been under development by the FAA to address damage tolerance analysis of attachment slots. The new AC had not yet been released at the end of the PIRATE-2 grant. The DARWIN team worked closely with RISC and the FAA during the development of the AC. DARWIN 9.4 includes a new capability for risk assessment of axial blade slots in accordance with the anticipated publication of AC 33.70-5. A new analysis mode for axial blade slots has been included as a separate project mode as shown in Figure 41. This mode enables users to define an axial blade slot region using one-dimensional (1D) stress profiles or 3D FE model geometries. Users can place cracks directly on blade slot edges and surfaces in 3D FE models. DARWIN computes the conditional fracture risk of the axial blade slot given that an anomaly of random initial size is present.

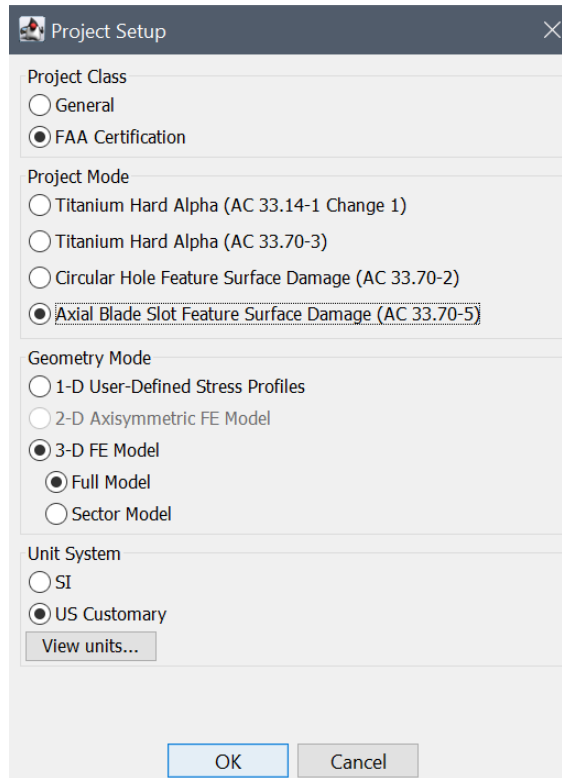


Figure 41. Selection of new axial blade slot analysis mode in DARWIN GUI

This implementation is based on the following assumptions, which are consistent with the AC:

- The crack is placed at the maximum principal stress location. By default, the DARWIN GUI places cracks at maximum principal stress locations, not minimum life or maximum risk locations. Users may alter the crack location if desired.
- Blade slot edges are “sharp” edges on the FE model as opposed to “rounded” surfaces. Rounded surfaces would require a new stress-intensity factor solution in DARWIN.
- Users can only define one axial blade slot on the FE geometry. DARWIN does not check for additional blade slots or for cyclic symmetry.
- Users are responsible for indicating how many actual blade slots are present in the component. The number of blade slots used by DARWIN for an assessment calculation is set using an expression provided by RISC that includes the raw number of blade slots and the manufacturing process. This number multiplies risk for a single blade slot to produce the overall risk value for the component.

- All anomalies are assumed to be present in the axial blade slot from the initial mission. Anomalies cannot form during the component's usage, and anomalies are not added to the component during shop visits.

DARWIN 9.4 enables users to select element edges or element faces in 3D FE models to create blade slot edge or surface regions, respectively. Cracks are placed at the maximum principal stress locations in these regions. Figure 42 shows a blade-slot surface region created in the GUI. DARWIN only enables one zone to be created in each region, *i.e.*, there is only one blade slot edge zone and (if needed) one blade slot surface zone. The DARWIN GUI enables users to define the surface region and edge region by three methods: clicking on each individual surface/edge, dragging a box around a region of surfaces/edges, or inputting a list of element numbers.

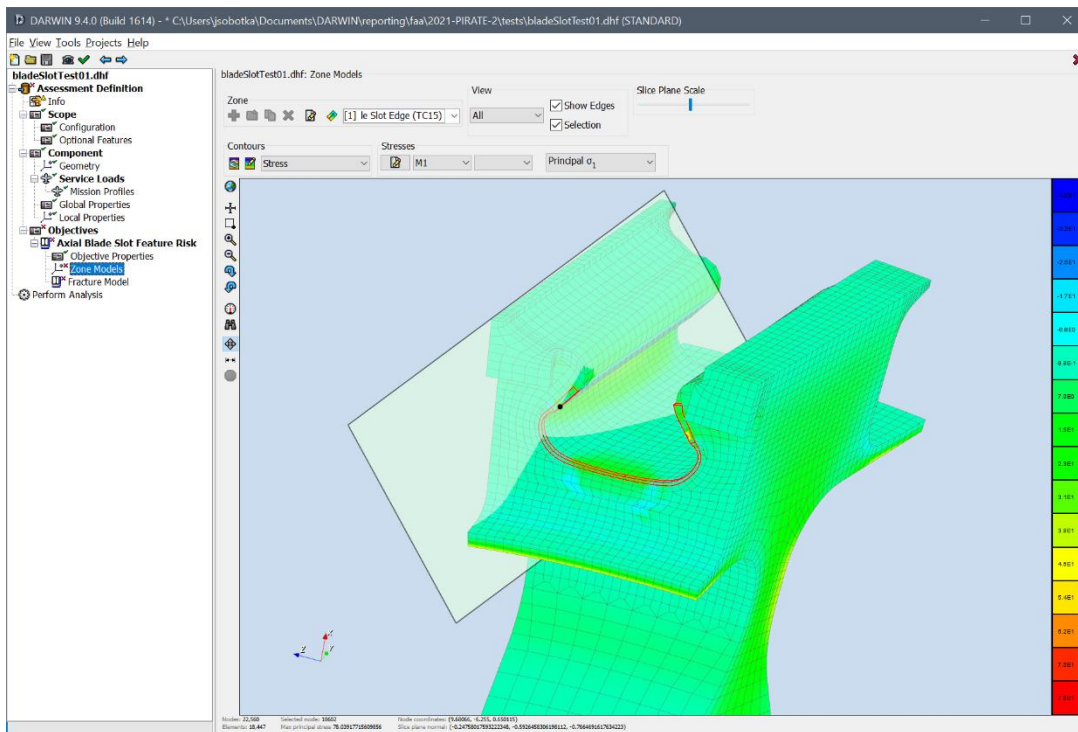


Figure 42. Defining a blade slot edge zone using the new axial blade slot capability

DARWIN 9.4 provides a new standard anomaly exceedance curve for blade slots. In contrast with other analysis modes, the anomaly exceedance curve is defined by feature (*i.e.*, the axial blade slot) rather than by area or volume. Consequently, the blade slot dimensions are not used in fracture risk computations. There is one exceedance curve for both surfaces and edges. It is available in United States (US) units and International System (SI) units. The exceedance curve is locked down. No other curve is available, and this curve cannot be modified by the user.

The axial blade-slot analysis mode is restricted to 1D and 3D geometry modes, and is limited to manual zoning. Many optional DARWIN features are disabled. By default, DARWIN enables the stress rainflow feature and sets the TMF crack growth algorithm to use the maximum temperature of the stress pair. Users may not change either option.

The Design Target Reliability (DTR) for axial blade slots has been set at 2 in 100,000, *i.e.*, 2.0e-5. By default, DARWIN sets the number of samples for a MC analysis at 100/DTR, *i.e.*, 5.0e6. Users may increase this number without penalty. Users may not reduce this number of samples.

DARWIN 9.4 features new manufacturing process credits that are available specifically for axial blade slots. These process credits are accessed via the properties tab of the zone editor as illustrated in Figure 43. When manufacturing credits are active, the zone fracture risk is divided by the sum of the selected manufacturing credits.

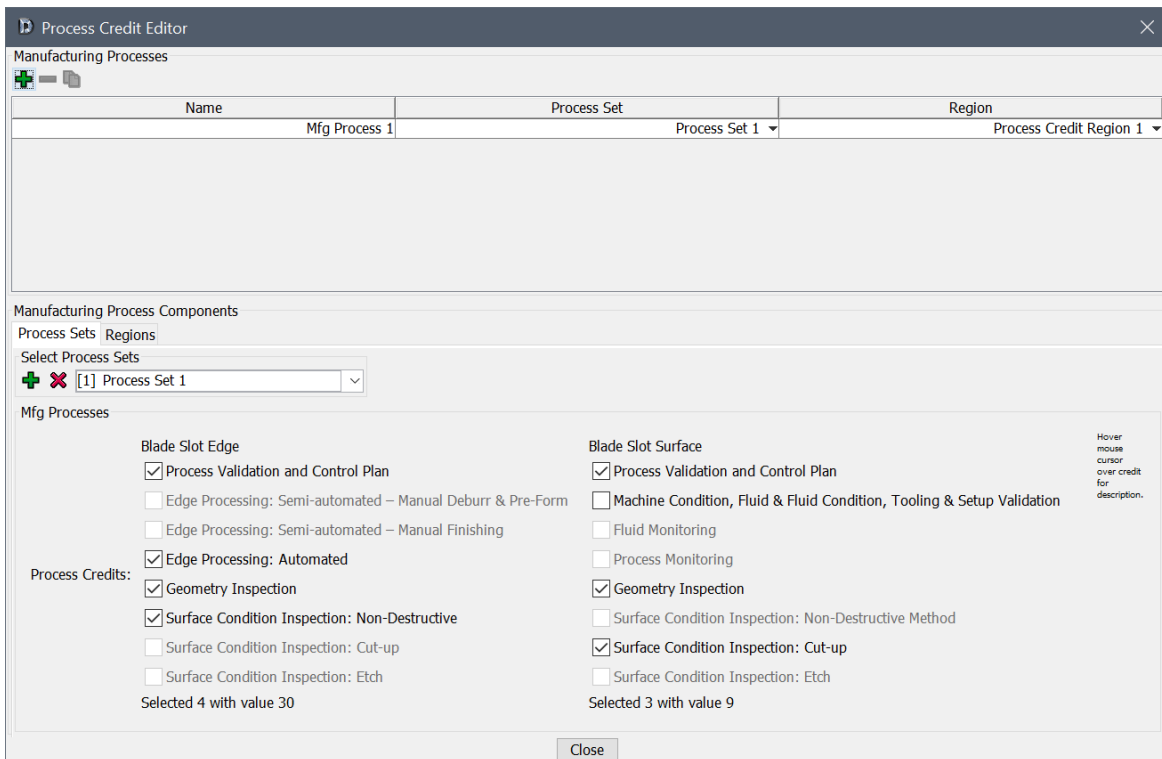


Figure 43. DARWIN GUI screen showing manufacturing process credits for axial blade slot

Blade-slot edge zones have the following manufacturing process credits:

- Process Validation and Control Plan (5×)
- Edge Processing: Semi-Automated – Manual Deburr & Pre-Form (5×)
- Edge Processing: Semi-Automated – Manual Finishing (8×)

- Edge Processing: Automated (15×)
- Geometry Inspection (5×)
- Surface Condition Inspection: Non-Destructive (5×)
- Surface Condition Inspection: Cut-Up (2×)
- Surface Condition Inspection: Etch (2×)

Blade-slot surface zones have the following manufacturing process credits:

- Process Validation and Control Plan (5×)
- Machine Condition, Fluid & Fluid Condition, Tooling & Setup Validation (5×)
- Fluid Monitoring (5×)
- Process Modeling (10×)
- Geometry Inspection (2×)
- Surface Condition Inspection: Non-Destructive (5×)
- Surface Condition Inspection: Cut-Up (2×)
- Surface Condition Inspection: Etch (2×)

For both types of manufacturing process credits, the DARWIN GUI prevents the pairing of processes that violate the forthcoming FAA AC 33.70-5 guidelines. For example, “process validation and control plan” is required to activate any of the other manufacturing credits.

The DCE calculates an overall fracture risk value for a component based on anomalies located at either the defined blade-slot edge zone or the blade slot surface zone.

This risk value represents the risk of the entire component, and is multiplied by the user-defined number of blade slots (with appropriate scaling defined by the forthcoming AC 33.70-5) and divided by the sum of any active manufacturing process credits.

The DARWIN GUI can generate a standard report for an axial blade-slot damage tolerance assessment. Figure 44 shows information from page 1 of this report. Figure 45 shows information from page 2 of this report. This report includes information on the engine, fracture probability, applied process credits, and outputs any warnings in the analysis.

FAA Mode - Axial Blade Slot Feature Surface Damage (AC33.70-5)

Component Description							
Engine: Component Name: Part Number: Materials: Ti64 props; Bilinear Paris FCG eqn., Closure stress ratio eqn. Service Bulletin Life: 20000							
Location 1 (Zone 1 - Blade Slot Edge)							
Fracture Probability w/ Process Credit: 0.000E0 Fracture Probability w/o Process Credit: 0.000E0 Number of Axial Blade Slots: 75 Anomaly Distribution Source: AC33.70-5					No image provided.		
Name	Inspection Time (flights)						POD
	ID	Type	Format	Mean	Std. Dev.	Link	
No Inspections.							
Manufacturing Processes (Blade Slot Edge)							
Manufacturing Processes							Credits
Process Validation and Control Plan							[X]
Edge Processing: Semi-automated – Manual Deburr & Pre-Form							[]
Edge Processing: Semi-automated – Manual Finishing							[]
Edge Processing: Automated							[X]
Geometry Inspection							[X]
Surface Condition Inspection: Non-Destructive							[X]
Surface Condition Inspection: Cut-up							[]
Surface Condition Inspection: Etch							[]
Warnings							
No warnings.							
				Diagram number: Prepared By:		Date: 2021-05-04 Approved By:	

Figure 44. Page 1 of the FAA report form generated via the DARWIN GUI for axial blade-slot damage tolerance assessment

FAA Mode - Axial Blade Slot Feature Surface Damage (AC33.70-5)

Component Description							
Engine: Component Name: Part Number: Materials: Ti64 props: Bilinear Paris FCG eqn., Closure stress ratio eqn. Service Bulletin Life: 20000							
Location 2 (Zone 2 - Blade Slot Surface)							
Fracture Probability w/ Process Credit: 0.000E0 Fracture Probability w/o Process Credit: 0.000E0 Number of Axial Blade Slots: 75 Anomaly Distribution Source: AC33.70-5					No image provided.		
Name	Inspection Time (flights)						POD
	ID	Type	Format	Mean	Std. Dev.	Link	
No Inspections.							
Manufacturing Processes (Blade Slot Surface)							
Manufacturing Processes				Credits			
Process Validation and Control Plan				[X]			
Machine Condition, Fluid & Fluid Condition, Tooling & Setup Validation				[]			
Fluid Monitoring				[]			
Process Monitoring				[]			
Geometry Inspection				[X]			
Surface Condition Inspection: Non-Destructive Method				[]			
Surface Condition Inspection: Cut-up				[X]			
Surface Condition Inspection: Etch				[]			
Warnings							
No warnings.							
				Diagram number:		Date: 2021-05-04	
				Prepared By:		Approved By:	

Figure 45. Page 2 of the FAA report form generated via the DARWIN GUI for axial blade-slot damage tolerance assessment.

This feature was originally implemented in DARWIN 9.2 using the initial specifications for the forthcoming AC 33.70-5 provided by RISC. This draft specification was subject to change but considered largely complete. This initial specification was implemented in DARWIN 9.2 as a hidden feature. It requires a keyword to access and is not available for general users as a result. However, RISC revised AC 33.70-5 after it was implemented into DARWIN 9.2 and released for user evaluation. Consequently, we implemented the revised version of AC 33.70-5 into the next

release of DARWIN (DARWIN 9.4) since modifying DARWIN 9.2 was not deemed reasonable at that time. In DARWIN 9.4, this feature is available to general users without a hidden feature keyword.

7.2 Modifications to existing DARWIN analysis modes to support AC updates

7.2.1 Hard alpha AC revisions

DARWIN was originally developed to assess the risk of titanium HA anomalies in engine components in accordance with AC 33.14-1 requirements. In 2017, the FAA issued a revision to AC 33.14-1 (called AC 33.14-1 Change 1) and AC 33.70-3 was issued in May 2023. DARWIN 9.4 was modified to support the requirements of both AC 33.14-1 Change 1 and the upcoming AC 33.70-3. DARWIN uses the same analytical methods to support AC 33.14-1 Change 1 and AC 33.70-3 that were used in the legacy implementation of AC 33.14-1. However, the anomaly distributions are different for AC 33.14-1 Change 1, and AC 33.70-3. The analysis mode for the legacy AC 33.14-1 was removed from DARWIN 9.4.

To support AC 33.14-1 Change 1, the following enhancements were implemented in DARWIN 9.4:

- Renamed the existing AC 33.14-1 certification mode for titanium HA anomalies to ‘Titanium Hard Alpha (AC 33.14-1 Change 1)’ to reflect the revision designation (see Figure 46)
- Added the revised AC 33.14-1 anomaly distributions (four) to the DARWIN certification library
- Removed the original AC 33.14-1 anomaly distributions from the DARWIN certification library; however, these distributions are still available for use in DARWIN
- Added GUI and RAC checks to ensure that the revised AC 33.14-1 anomaly distributions are applied
- Revised the HA certification report to provide a warning if anomaly distributions inconsistent with the revised AC 33.14-1 anomaly distributions are utilized in a titanium hard-alpha certification analysis

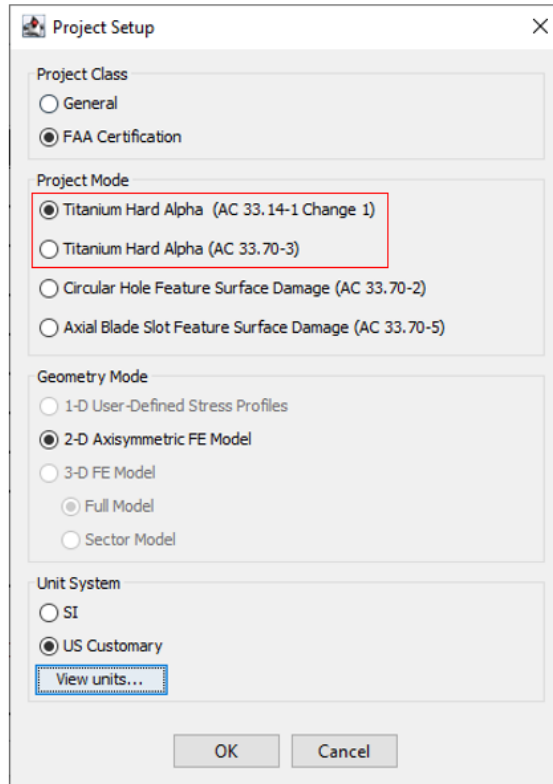


Figure 46. New titanium HA anomaly analysis modes in DARWIN 9.4

To support AC 33.70-3, DARWIN 9.4 includes the following enhancements:

- Introduced a new AC 33.70-3 certification mode for the analysis of titanium HA anomalies (see Figure 46)
- Added the AC 33.70-3 anomaly distributions (six) to the DARWIN certification library
- Added GUI and RAC checks to ensure that the AC 33.70-3 anomaly distributions are applied
- Added an AC 33.70-3 HA certification report. This report will provide a warning if utilized anomaly distributions are inconsistent with the AC 33.70-3 anomaly distributions

7.2.2 Security features for anomaly distribution and POD data

DARWIN contains anomaly size distribution and probability of detection (POD) curve data files that are used in FAA certification assessments. These files are located in a designated AC certification directory in DARWIN. The files cannot be edited within DARWIN, but they may be edited outside of DARWIN. In previous versions of DARWIN, the data files contained in the

DARWIN AC certification directory could potentially be modified by users (accidentally or deliberately) and then applied to FAA certification assessments without someone (*e.g.*, the user, a supervisor, or the FAA) knowing that the correct standard file was not used.

DARWIN has now been enhanced to prevent users from modifying AC certification directory files and attempting to apply them as the correct standard files for FAA certification assessments. A special keyword (also known as a hash signature) has been added to all anomaly size distribution and POD curve data files (*i.e.*, correct standard files) in the DARWIN AC certification directory. The hash signature is generated based on the entire data contained in the file and a hidden keyword only known to the SwRI development team. Hash signatures are a standard method to assure the contents of a document have not been changed. The hash signature contains a long string of letters and numbers. Changing any aspect of the file will invalidate the hash signature. Figure 47 shows the hash signature of a signed anomaly distribution file.

```
SIGNATURE 60b36af8b1427559a0c0c61765938477622aa66bf32fb61cde61ba3f1a596d3a
TITLE
Example Anomaly Distribution for 2D Anomalies (Weight Reference-Based)
DESCRIPTION
Example anomaly distribution for 2D anomalies provided in terms of anomaly area
MODEL 1DOF
UNITS US
NEEDS_PRODUCTION_INSPECTION NO
DIMENSION_REDUCTION NONE
DOF AREA
DIST_TYPE EXCEEDANCE 93
GENERATION_SPACE LOG_LIN
REFERENCE WEIGHT
ASPECT_RATIO 1.0
DENSITY 0.160999998
! area in sq. mils and exceedance in #/million lbs.
AREA EXCEEDANCE
3.5236 60.299
3.9435 55.762
4.4135 51.542
4.9395 47.616
```

Figure 47. Signed anomaly distribution (*.dist) file with hash signature highlighted

The hash signature is based upon a cryptographic algorithm referred to as SHA-256. SHA-256 developed by the National Security Agency (NSA) for cryptographically securing sensitive data. It converts a set of data to produce a unique, virtually non-duplicable 256-bit alphanumeric code, *i.e.*, a hash signature. The hash signature can then be used to encrypt data for a variety of

purposes such as cryptography, checksum generation, and compression. In DARWIN, it is used to ensure the data validity of correct standard files.

When the hash signature is present and the file is unmodified, DARWIN recognizes the file as a correct standard file for FAA certification assessment. If the hash signature is present but the file and/or keyword has been modified by the user, DARWIN will issue an error and will prevent the file from being imported into the GUI. If the hash signature is not present, DARWIN will recognize the file as a user-provided file and will issue a warning to the FAA certification report indicating that a user-provided file was used in the analysis.

DARWIN also now includes a new feature called the File Signing Tool for embedding hash signatures into data files. The capability to create hash signatures for anomaly distribution and POD curve files contained in the DARWIN AC certification directory is limited to the SwRI software development team. Access to this capability is controlled via a hidden feature keyword. However, the tool can be used to embed hash signatures in other files as well, and it will be useful to protect of other files and features in the future.

8 DARWIN testing and evaluation

This task was focused on formal testing and evaluation of the DARWIN software. A description of the contents of the DARWIN software versions released during the grant is provided in Section 8.1. The new versions were evaluated by the primary software developer (SwRI) and submitted to the aircraft engine companies represented on the Steering Committee for review via incremental Alpha and Beta software releases as described in Section 8.2. These companies evaluated the functionality and stability of DARWIN while also comparing DARWIN results against their own company codes, fleet experience, and test data as described in Section 8.3. Once these evaluations had been completed and all issues and bugs had been satisfactorily resolved, the software was released for use by licensed DARWIN users.

8.1 DARWIN code releases

DARWIN development was performed throughout the grant with major software releases occurring roughly once a year. For each major new version, two or more incremental (Alpha) versions were submitted to the Steering Committee for review periods lasting at least three months. Each of these incremental releases typically contained only a small number of new features, facilitating a focused review. The official “final” Alpha release contained all new features, and a longer review period was generally provided at that time. During these review periods, the Steering Committee provided feedback regarding the accuracy and usability of the

software, including the identification of bugs, and this feedback was addressed by SwRI. After the Alpha review period was completed and reported issues were resolved, a Beta version was released to RISC for review. During the Beta review period, RISC and the Steering Committee provided additional feedback that was also addressed by SwRI. Following these reviews, a final Production version was released to licensed users.

A summary of the features associated with the major software releases is provided in this section. Further details about many of these features are provided in previous chapters of this report. Note that some of the new features in each version were funded by sources other than the FAA, such as licensees or Small Business Innovative Research (SBIR) projects funded by other U.S. Government agencies. Some further information about those other projects is provided later in this report. For completeness, all features (both FAA-funded and non-FAA-funded) are included in the lists that follow. For clarity, the non-FAA features are denoted in italics.

8.1.1 DARWIN 9.0

An initial DARWIN 9.0 Alpha version was completed and released under a previous FAA grant. Under the current grant, this version was extensively verified and enhanced to address bugs identified by SwRI and the Steering Committee. The Beta version was released to RISC for review on December 18, 2015. The Production version of DARWIN 9.0 was released to licensed users on May 13, 2016. DARWIN 9.0 included the following new features:

- Optimal Gaussian Process Pre-zoning
- 3D Sector Models
- SIF Solution for Angled Corner Cracks
- *Formation Life Scaling*
- *Anomaly Distribution Tracking*
- *Micromechanical Crack Initiation*
- Enhancements for Large Finite Element Models

8.1.2 DARWIN 9.1

The DARWIN 9.1 Alpha final version was released to the Steering Committee for review on September 30, 2016. Following an extensive review period, the Beta version was released to RISC for review on March 31, 2017. The Production version was released to licensed users on August 25, 2017. DARWIN 9.1 included the following new features:

- Zoneless Deterministic Analysis
- Autoplate for 3D Finite Element Models
- Improved Support for Large Finite Element Models
- Enhanced Monte Carlo with Gaussian Process Response Surface
- *Critical Initial Crack Size Contours*

8.1.3 DARWIN 9.2

The DARWIN 9.2 Alpha final version was released to the Steering Committee for review on September 30, 2017. After an extensive review period, the Beta version was submitted to RISC for review on May 31, 2018. The Production version of DARWIN 9.2 was released to licensed users on June 4, 2019. This version included the following capabilities:

- FAA Certification Mode for Axial Blade Slots (with hidden feature keyword)
- Fleet Risk Module Enhancement
- Bivariant Plate Enhancement
- 3D GUI Visualization Enhancements
- Life/Risk Contour Fracture Plates Visualization
- GUI File Access Speed Enhancement
- *2D/3D Surface Autozoning*
- *Dhondt Fatigue Crack Growth Model*
- *El Haddad Small Crack Model*
- *Location-Specific POD Curves*
- *Restart Using Intermediate Fracture Plates*
- *Autoplate Speed/Robustness Improvements*
- *GUI Node Selection Speed Improvement*
- *Hot Corrosion Enhancements*
- *Shakedown Enhancement for 1D Geometry Mode*
- *Mission Scaling Enhancements*

- *Crack Size Termination Criterion Enhancement*
- *3D Anomalies Enhancements*
- *Production Inspections on Non-Hoop Planes*
- *Direct Import of ANSYS and ABAQUS Load Step Times*
- *New Treatment of Material Properties Interpolation*

8.1.4 DARWIN 9.3

The DARWIN 9.3 Alpha final version was released to the Steering Committee for review on September 28, 2018. DARWIN 9.3 Alpha was later merged into the DARWIN 9.4 Alpha version (see below), so there were no Beta or Production releases associated with this version. DARWIN 9.3 Alpha included the following capabilities:

- 3D GUI Visualization Enhancements
- Constraint-Loss Surface Fatigue Crack Correction Model
- Revised Limits for Stress Intensity Factor Solutions
- Updated Titanium Hard Alpha Anomaly Distributions
- Python-Based Scripting Tool
- Setting GUI Preferences via an External File
- User-Defined Project Rules
- *Autoplate Node-Skipping Enhancement*
- *Automodeling Speed Enhancements*
- *User-Defined Cracks Enhancement*

8.1.5 DARWIN 9.4

DARWIN 9.4 Alpha was first released to the Steering Committee for review on August 31, 2019. Due to some delays in the review of DARWIN 9.3, which caused a substantial overlap with the development and review of DARWIN 9.4, it was determined that it would be more cost effective to combine DARWIN 9.3 and 9.4 into a single version labeled DARWIN 9.4. The combined version DARWIN 9.4 Alpha 2 was released to the Steering Committee for review on September 30, 2020. The Steering Committee reported a number of bugs that were subsequently

fixed by SwRI. At the end of the period of performance of this grant, SwRI was in the process of preparing an updated DARWIN 9.4 Alpha for Steering Committee Review. The Beta version will be submitted to RISC for review upon completion of Steering Committee review. This continuing work on DARWIN 9.4 is being supported by a subsequent grant.

The combined DARWIN 9.4 version included the following capabilities:

New features and enhancements for FAA certification assessments:

- Axial Blade Slots (Update)
- Updated Titanium HA Anomaly Distributions
- Security Features for Anomaly Distribution and POD Data

New general features:

- 3D GUI Visualization Enhancements
- SIF Solution for Semi-Elliptical Surface Crack on Hollow Cylinder
- Constraint-Loss Surface Fatigue Crack Correction Model
- FE2NEU Finite Element Model Triage Algorithm
- Python-Based Scripting Tool
- *Objectives-Based Project Definition*

Speed and robustness improvements:

- Speed Enhancements for User-Defined Cracks
- DARWIN Results File Import Speed Enhancements
- *Autoplate Node-Skipping Enhancement*
- *Automodeling Speed Enhancements*

General enhancements:

- Updated Limits for SIF Solutions
- User-Defined Project Rules
- Setting GUI Preferences via an External File
- *User-Defined Cracks Enhancement*

8.1.6 DARWIN 10.0

DARWIN 10.0 Alpha was released to the Steering Committee for review on September 30, 2020. The Beta version will be submitted to RISC for review upon completion of Steering Committee review. This version included the following capabilities:

New general features:

- Residual Stress Profiles in 2D FE Models Extended to Bivariant Crack Types

Speed and robustness improvements:

- GUI Speed Enhancement for Large 3D FE Models
- Autoplate Speed Enhancement for Large 3D FE Models

8.2 DARWIN internal verification testing

Quality controls must be implemented during the software development process to ensure the reliability of the resulting engineering software. Although it is impractical to test all of the possible combinations of input variables that may influence the results, a substantial number of test problems should be developed to ensure that the software provides the intended results. In addition, support must be provided to solve problems reported by the user community.

Internal (SwRI) verification of DARWIN consisted of the creation and execution of verification test problems to identify bugs and subsequent software implementation to resolve them. Several internal procedures were used to reduce the effort associated with this process and to identify bugs as quickly as possible after code is developed. Examples of these procedures include modular code development in which verification is performed on individual modules prior to integrating them into the main source code, incremental code releases in which the software is periodically provided to the Steering Committee for review prior to a major release, and automated verification in which verification testing is automatically performed whenever a code developer uploads completed source code into the DARWIN source code repository. A summary of these procedures is provided in Sections 8.2.1, 8.2.2, and 8.2.3, respectively. These practices substantially reduced the number of bugs in the major code releases and reduced the human time associated with the software maintenance effort.

8.2.1 Modular code development and verification

The DARWIN verification procedure provides verification at the module level. Module-based verification focused the verification effort on new code, in which new or modified modules were

verified prior to integration with the rest of the source code. This approach helped to maintain the overall stability of DARWIN.

8.2.2 Incremental code releases

Major DARWIN releases typically include a number of features requiring several months of Steering Committee review and several months of bug fixes. Whenever possible, features were submitted to the Steering Committee for review in smaller incremental releases to shorten the review period. This enabled the Steering Committee and SwRI to focus on a smaller number of features at a time. It also enabled a more thorough examination of each individual feature. This improved the quality of the code development process because the code developers received more immediate feedback on recently developed features.

8.2.3 Automated verification procedure

The DARWIN automated software verification procedure provides continuous verification of the DARWIN Fortran code throughout the software development process. The verification procedure begins when a new bug is discovered during testing (dynamic analysis, regression, internal, or generative) or is reported by an OEM. When a revision code is submitted to address the bug, an internal algorithm automatically compiles the revised source code to generate a new software build, and performs regression testing of the new build. During this stage, a suite of pre-built DARWIN projects is executed, and selected output values are compared to reference results. If results are not within established tolerance values, the source of the difference is identified and either the reference results are updated or a new bug is logged. If results are within tolerances, then the revised code is automatically prepared for release on the DARWIN website. For bugs that are reported by OEMs or users, the reporter is notified when a new build is available. The automated verification procedure reduces the human time required for verification, helping to identify bugs as they are introduced during the software development period.

8.3 Steering Committee evaluation

Independent evaluation of DARWIN is necessary to ensure accuracy and user confidence. Feedback from engine company users is invaluable to identify problems and potential improvements during the development period. DARWIN was evaluated by each of the four PIRATE Steering Committee companies throughout the project. Each company participated in substantial code review efforts to verify the numerical accuracy of the DARWIN software. The OEMs provided continuous guidance regarding the content and design of new features, and

provided evaluation of DARWIN use in a production environment. A summary of Steering Committee numerical verification, design guidance, and evaluation for production activities is provided in Sections 8.3.1, 8.3.2, and 8.3.3, respectively.

8.3.1 Design guidance for new features

The Steering Committee was instrumental in the development of new features. Prior to the implementation of each feature, the Steering Committee was consulted regarding design content and placement of new features within the user interface. This resulted in fewer changes to the design and user interface during the evaluation period.

8.3.2 Numerical verification

Numerical verification consisted of a series of studies performed by the OEMs focused on comparison of DARWIN predictions to experimental data, field experience, and OEM in-house computational results. These studies included an extensive set of test cases that were exercised by multiple users within each of the four OEM companies. The studies were performed using DARWIN versions 9.0 through 10.0 on PC computer platforms. OEM evaluation of DARWIN Alpha and Beta versions identified a number of bugs that were fixed prior to production release of the code, and helped to improve user confidence in the quantitative results.

8.3.3 Evaluation for production use

The PIRATE Steering Committee performed a series of evaluations to assess the practical use of DARWIN in a design environment. Over the course of the PIRATE program, the OEMs provided general feedback regarding their experiences with the DARWIN code. The response was generally very positive. Feedback from DARWIN licensees has also been positive.

9 Technology transfer

9.1 Progress reports and review meetings

Regular communication with the FAA, the project Steering Committee, and the aircraft engine industry facilitated effective oversight of the research project as well as timely transfer of important new results. Written reports included brief monthly progress reports and substantially longer interim progress reports. One-day program review meetings with the FAA were usually held about once per year, with specific schedules directed by the FAA. The project Steering Committee conducted a one-day or two-day working meeting in conjunction with each program review meeting. A short status report on program activities was presented at many RISC

meetings (held three times per year). At least once per year, the SwRI Program Manager and one of the SwRI co-Principal Investigators attended the RISC meeting in person and made the project presentation. This facilitated additional interaction with the FAA personnel present at the RISC meeting. The Steering Committee often held a working meeting in conjunction with this particular RISC meeting. At other RISC meetings, the SwRI Program Manager sometimes gave a project presentation via a telephone link. In addition, the project Steering Committee conducted periodic telephone meetings, typically one or two times per month. In-person RISC, Steering Committee, and FAA review meetings were suspended during the last year of the project due to the coronavirus pandemic, and virtual meetings were conducted instead.

9.2 Conference presentations and journal articles

Significant results from this research program were disseminated to a much broader audience in the gas turbine engine community and the international technical community in disciplines such as fracture mechanics through presentations at conferences and symposia or publications in archival technical journals. A number of additional publications and presentations during the term of this grant were based on DARWIN-related research funded primarily by non-FAA sources. However, all of this additional research was based on the solid foundation of FAA funding to develop advanced technology and software for probabilistic integrity and risk assessment of turbine engine components, whether through this grant or through its predecessor grants. A total of 20 published papers (most of them presented at international conferences) and 21 additional presentations without manuscripts occurred during the term of the current grant. A complete listing of these presentations and publications is provided in Appendix H.

9.3 DARWIN commercial licensing

At the request of industry and the FAA, an infrastructure was developed previously to support the formal use of DARWIN by engine companies for official FAA and company purposes. The DARWIN software was first offered for commercial licensing in 2000. The licensing activity has grown slowly and steadily since that date. DARWIN license fees collected by SwRI are used exclusively to enhance the DARWIN code and to provide user support for the benefit of engine manufacturers, other licensees, and the FAA. No FAA funds from the current project were used to support the licensing activity.

At the end of this grant, twenty-two commercial DARWIN licenses were active, including thirteen manufacturers of gas turbine engines for aircraft applications. Other licensees included manufacturers of gas turbine engines for land-based power generation, consulting firms, and a manufacturer of aerospace structures.

9.4 DARWIN training

A major DARWIN training workshop was conducted on March 20-22, 2018, at the SwRI facility in San Antonio, Texas. The first day of the workshop was an overview of DARWIN background, capabilities, and development plans, including an extensive demonstration of the software. The second and third days of the workshop comprised hands-on training in which each attendee learned how to perform deterministic and probabilistic analysis using a developmental version of DARWIN 9.2. Candid photographs from one of the training sessions are shown in Figure 48, Figure 49, and Figure 50. Special attention was given throughout the workshop to recent DARWIN enhancements. Because the FAA provided financial support for preparing and presenting the workshop through this grant, there was no registration fee for attendees.

Seventy-two persons attended the workshop in person (not including SwRI instructors and participants). A group photograph is shown in Figure 51. In addition, more than sixty persons participated in the first day of the workshop through WebEx links. Onsite participants represented about thirty-seven different organizations from ten different countries.



Figure 48. Candid photograph of participants in DARWIN workshop



Figure 49. Candid photograph of instructor and participants in DARWIN workshop



Figure 50. Candid photograph of instructors and participants in DARWIN workshop



Figure 51. Group photograph of instructors and participants in DARWIN workshop

The following organizations attended the workshop in person onsite:

- Aircraft Engine Manufacturers
 - Aviadvigatel
 - GE Aviation
 - Honda
 - Honeywell
 - IHI Corporation
 - ITP
 - Kawasaki Heavy Industries
 - Mitsubishi Heavy Industries Aero Engines
 - MTU Aero Engines
 - Pratt & Whitney
 - Rolls-Royce Corporation

- Rolls-Royce Deutschland
- Safran Aircraft Engines
- US Government Agencies
 - FAA
 - NASA Glenn Research Center
 - NASA Johnson Space Center
 - NASA Kennedy Space Center
 - NASA Langley Research Center
 - NASA Marshall Space Flight Center
 - Air Force Research Laboratory
 - USAF – Tinker AFB
 - NAVAIR
 - US Army Research Laboratory
 - US Army – Redstone Arsenal
 - National Institute of Standards and Technology
- Others
 - Aerojet Rocketdyne
 - Airbus
 - Arconic Fastening Systems
 - Arconic Titanium and Engineered Products
 - Bell Helicopter Textron
 - Boeing
 - European Space Agency
 - Florida Turbine Technologies
 - Lockheed Martin Aeronautics

- Northrop Grumman
- Siemens Energy
- Sikorsky

The following organizations participated remotely in the workshop on the first day via WebEx:

- Aircraft Engine Manufacturers
 - GE Aviation
 - Honeywell
 - MTU
 - Pratt & Whitney
 - P&W Canada
 - Safran Helicopter Engines
- US Government Agencies
 - Air Force Research Laboratory
 - Air Force Life Cycle Management Center
 - FAA
 - NASA Glenn Research Center
 - NASA Langley Research Center
- Others
 - European Aviation Safety Agency
 - European Space Agency
 - Florida Turbine Technologies
 - National Research Council – Canada
 - Safran Additive Manufacturing
 - Safran Landing Systems

- Siemens Energy
- Sikorsky

The curriculum from the March 2018 workshop (and from previous FAA-sponsored workshops) was adapted to present training workshops to several DARWIN commercial licensees at their company sites. However, all of the costs of preparing and presenting the training to licensees, including all travel costs, were paid by the licensing companies. During the term of this grant, SwRI staff presented the training workshop three times for licensee companies in Japan, India, and the United States. Approximately one hundred fifteen people participated in this licensee training.

One additional DARWIN training workshop (again two days in length) was presented for the Naval Air Systems Command (NAVAIR) at Patuxent River, Maryland, in August 2018. Sixteen persons from NAVAIR participated in the training. All expenses for the training and related travel were supported by NAVAIR.

9.5 Technology transfer to other U.S. government agencies

DARWIN is available royalty-free to all U.S. government agencies. To date, DARWIN has been distributed to NASA and to several branches of the Department of Defense including the Army, Air Force, and Navy. During the current grant, DARWIN was distributed to NASA Glenn Research Center (Cleveland, OH); NASA Johnson Space Center (Houston, TX); NASA Marshall Space Flight Center (Huntsville, AL); U.S. Naval Air Systems Command (Patuxent River, MD); U.S. Naval Surface Warfare Center (Carderock Division) (West Bethesda, MD); National Institute of Standards and Technology (Gaithersburg, Maryland); U.S. Air Force Research Laboratory (AFRL) (Dayton, OH); and U.S. Air Force Life Cycle Management Center (AFLCMC) (Dayton, OH).

9.6 DARWIN spin-off projects

One of the clearest indications of technology transfer to other government agencies, as well as commercial licensees, is the growing number of independent research projects funded by these other organizations for additional development and implementation of new DARWIN technology that is specifically relevant to their own applications. While most of these independent projects have been modest in size, they have each contributed to the growing capabilities of DARWIN. In most cases, the technology resulting from the project has been implemented in the commercial production version of DARWIN and/or published, and therefore is available to all DARWIN users.

The following sub-sections provide short descriptions of some of the spin-off projects.

9.6.1 Minimum low cycle fatigue life

AFRL has been conducting research for many years on improved methods for predicting low cycle fatigue (LCF) life in turbine engine rotors (Larsen, et al., 2013). They have developed a new method for predicting the minimum LCF life based on a probabilistic fracture mechanics analysis in which the crack formation life is assumed zero and the initial crack size is based on a statistical description of microstructural anomalies such as inclusions or pores. This paradigm is entirely consistent with DARWIN methods for calculating fracture risk. Recognizing this, AFRL has been using DARWIN as an internal research tool to support their work (Golden, et al., 2019). This motivated AFRL to fund SwRI to modify DARWIN so that the AFRL minimum LCF life model could be more easily used in their desired form and could be made more widely available.

Minimum (min) LCF lives are computed in DARWIN using an algorithm (Life for specified Pf) that was developed on a previous FAA grant. DARWIN was enhanced under AFRL funding to provide two new analysis modes for assessment of minimum LCF lives: (1) min LCF life screening mode, and (2) min LCF life feature mode. In the screening mode, DARWIN computes and displays minimum LCF life contours on component FE models using approximate (but fast-running) methods. This mode enables the user to identify the regions of the component with the most potential for further analysis. The feature mode computes accurate minimum LCF life values at the feature locations identified in the screening mode. The DARWIN GUI was enhanced to support these new analysis modes, and restructured via a new “objectives” framework that enables users to select multiple specific objectives for DARWIN analysis.

DARWIN was also enhanced under AFRL funding to provide treatment for small crack effects associated with early crack growth from microstructural anomalies. This new algorithm consisted of a new bilinear Paris model used by AFRL for their min LCF life calculations in which the two linear regions of the model are based on FCG rates associated with small and large cracks. New random variables were introduced for the Paris slope and intercept coefficients to address the inherent scatter in FCG rates for both small and large cracks.

9.6.2 Hot corrosion

Anticipated increases in turbine inlet temperatures will increase the likelihood of Type II corrosion damage, which is typically characterized by localized corrosion pitting caused by melting of sulfur-containing salts. These Type II hot corrosion pits have been shown to decrease the fatigue resistance of superalloys due to initiation of fatigue cracks at hot corrosion pits.

However, the rigorous analytical models and tools needed by turbine engine designers to predict Type II corrosion effects are not currently available.

Elder Research, Inc. (ERI) and SwRI were previously awarded Small Business Technology Transfer (STTR) Phase I and II projects by NASA Glenn Research Center (GRC) to develop physics-based modeling tools for predicting the initiation of hot corrosion and addressing pit and fatigue crack formation in Ni-based alloys subjected to corrosive environments. In the Phase I project, a probabilistic framework for linking pit initiation and growth, pit transition to crack, and combined cycle- and time-dependent crack growth in the DARWIN platform was developed. In the Phase II project, modeling tools for treating the evolution and coalescence of hot corrosion pits and microcracks as a function of time and temperature were developed, including visualization tools for monitoring the progression of hot corrosion damage in DARWIN (Chan, Enright, Moody, Thomas, & Goodrum, 2020; Chan, Enright, Moody, Thomas, & Goodrum, 2020; Chan, Enright, Moody, & Fitch, 2016).

ERI, SwRI and Rolls-Royce were subsequently awarded a STTR Sequential Phase II project by NASA GRC to validate the DARWIN hot corrosion capability against field data, develop a set of physics-based coating life modeling tools for treating concurrent fatigue, oxidation, and hot corrosion mechanisms; and implement coating life modeling tools in DARWIN. The DARWIN hot corrosion capability was enhanced to include new composite active state criteria, domain and time-based plots of active state in DARWIN, and the ability for users to define or import environmental and material parameters directly via the GUI. A new set of physics-based equations for modeling the fatigue and oxidation life of ductile and ceramic coatings was implemented in DARWIN and successfully validated against coated Ni-based superalloy literature data for both aeroengine and ground-based gas turbine platforms. The new DARWIN hot corrosion capability successfully predicted the occurrence of hot corrosion for a Rolls-Royce engine that had experienced hot corrosion in the field. Further evaluation is planned by Rolls-Royce in the future using the new DARWIN capability developed on this project. This technology will significantly improve the current ability to simulate and avoid corrosion fatigue failure of engine disks or metallic structural components due to prolonged exposure to extreme environments at elevated temperatures.

9.6.3 Additive manufacturing

Additive manufacturing (AM) is a novel fabrication process with the potential to create unique parts (beyond the capabilities of conventional manufacturing methods) relatively quickly and inexpensively. Propelled by this promise, AM applications are expected to increase rapidly for aerospace applications in the near future. Although early applications of AM have been for non-

structural components, the use of metallic AM for safety-critical structural parts is following quickly.

However, the emergence of AM for these critical parts is also bringing significant structural integrity challenges. For example, the AM process can, when not properly designed and controlled, create anomalies such as gas porosity or incomplete fusion. These anomalies can potentially occur anywhere in the volume of the AM component. If they occur in a region of significant cyclic stress, the anomalies can nucleate cracks that, in turn, can grow to cause fracture of the component.

A zone-based PDT methodology has been proposed as an appropriate framework for the assessment and certification of AM parts (Gorelik, 2017). These are the methods already implemented in DARWIN. However, additional research is needed to evaluate the suitability of DARWIN for AM applications, to identify gaps in DARWIN capabilities and to address those gaps with new features, and to address input data challenges.

DARWIN has attracted considerable interest at several government agencies and by several licensees for potential applications to AM parts. This interest has led to several funded projects and several enhancements to DARWIN, as described in the following sub-sections.

9.6.3.1 DARPA AM project

SwRI participated in an AM project that was led by Honeywell and funded by the Defense Advanced Research Projects Agency (DARPA) through their Open Manufacturing Program. This project was focused on simulating and validating the Direct to Metal Laser Sintering (DMLS) AM process for production of aerospace hardware. In the third and final phase of the project, SwRI implemented several enhancements in DARWIN to support probabilistic damage tolerance assessment of AM parts: Autoplate node-skipping capability, automodeling speed improvements, and new crack initiation models for AM features. Each is described in the following paragraphs.

The Autoplate node-skipping capability enables DARWIN to identify nodes that result in fatal computational errors during the execution of Autoplate and the various automodeling algorithms. This new capability calls the DARWIN computational code from a wrapper program that continues to run even when the DARWIN code has terminated. Using existing restart capabilities built into the DARWIN automodeling methods, the wrapper program iteratively restarts an analysis each time a termination-inducing error occurs. During the restart of the analysis, DARWIN flags the failed node, skips it, and resumes the analysis beyond the failed node. The process continues until all automodeling data have been obtained, providing a robust platform for

assessment of large 3D FE models that would typically be used in AM damage tolerance assessments.

Automodeling speed improvements that significantly improve computation speed for 3D FE models were implemented in the Autoplate and OpenMP parallel processing algorithms. Previous versions of Autoplate included an algorithm that located geometry boundaries on 2D slice planes of 3D FE models. The algorithm was restructured to locate the boundary in 30% of the time required by the previous algorithm. The OpenMP parallel processing capability includes an algorithm that manages the generation and storage of seed values associated with MC simulation. The algorithm was restructured to manage seeds in 75% of the time required by the previous algorithm.

These speed improvements have resulted in a 50-70% reduction in the total computation time required to generate life and CICS contours for 3D FE models, and a 50% reduction in the computation time associated with risk assessment of 3D FE models (when parallel processing is used). Actual speed improvement is dependent on FE model size and the number of CPUs applied in parallel processing.

The new crack initiation models for AM features are recently-developed physics-based fatigue life models that treat crack nucleation at pores, inclusions, and surface irregularities in parts fabricated via AM techniques (Sobotka, Enright, & McClung, 2019; Sobotka & McClung, 2020). The models were selected considering crack formation mechanisms and microstructural features associated with additively manufactured nickel materials as well as the size and distribution of pores and inclusions. The influence of surface condition on fatigue life was addressed by considering the stress concentration factors associated with topological features such as surface steps and patterns on machined surfaces or as-fabricated surfaces. The resulting fatigue life models were calibrated using available fatigue data and then implemented in DARWIN.

9.6.3.2 NASA AM projects

NASA Marshall Space Flight Center (MSFC) funded two small projects related to DARWIN applications for AM during the period of performance of the PIRATE-2 grant.

One of the most significant input variables to the PDT analysis is the anomaly distribution, often characterized as an exceedance curve that describes both the size and frequency of the anomalies. However, the development of an accurate statistical description of the anomaly distribution for a specific application is a nontrivial task requiring data that may not be readily

available. In this situation, alternative methods for estimating or inferring anomaly populations are needed.

One NASA-MSFC project focused on the estimation of AM anomaly distributions. An analysis framework was developed to elucidate the influence of anomaly size, location, and rate on fracture risk from both a probabilistic and traditional deterministic damage tolerance perspectives. Three different cases were considered in this study: extensive, limited, and no anomaly data. Step-by-step instructions were provided for the creation of anomaly distributions, and examples were provided to illustrate the process for each case. Several different approaches were identified for characterizing anomaly occurrence rates when no anomaly data are available. Suggestions were also provided regarding treatment of anomaly populations associated with off-nominal build conditions.

A second NASA-MSFC project focused on enhancements to DARWIN to support potential AM applications, including analysis robustness for large 3D FE models and speed improvements for CICS calculations.

Several methods were identified to reduce the amount of computer memory required for FCG life and risk assessments. One method, an enhancement to the DARWIN zone tree algorithm, was implemented and demonstrated for several FE models of various sizes. The enhancement reduced computer memory usage by as much as 83% for the FE models considered in this project. Several approaches were identified to reduce the computation time associated with CICS calculations. An approach utilizing user-provided initial guess values was implemented under this project. CICS response surface, identified in this project, was implemented independently via funding from DARWIN licensees, and then evaluated in this project. The combined enhancements reduced computation time by as much as 99% for the FE models considered in this project.

9.6.3.3 FAA AM project

The FAA funded a study project on the potential application of DARWIN to AM parts that was still underway at the completion of the PIRATE-2 grant. This effort has three major tasks. In one task, probabilistic damage tolerance methods are being critically compared with other promising candidate methods for assessing the structural integrity of higher-criticality AM parts, including both deterministic and probabilistic methods focused on crack initiation or crack growth. Potential strengths and weaknesses of each method are being identified and assessed. In a second task, the feasibility of using DARWIN for AM applications is being evaluated. Significant gaps between current DARWIN capabilities and needed capabilities for AM applications are being identified, strategies for addressing the gaps are being outlined, and implementation plans are

being developed. The goal is to address those gaps with actual DARWIN software enhancements in future work. In the third task, DARWIN is being used to analyze a finite model provided by an industrial partner of an actual airframe part being considered by AM. The goal of that exercise is to demonstrate feasibility and identify additional gaps.

9.6.4 Licensee-funded enhancements

Several additional projects were conducted for individual commercial licensees. Some of the new features developed under those projects were made available only to the funding licensee as password-protected hidden features. These projects, proprietary in nature, are not mentioned here. However, other new features developed under these projects were made available to other DARWIN licensees (with the advance approval of the funding licensee). For example, the following new features were implemented under funding from P&W: (1) 2D/3D surface autozoning, (2) Dhondt fatigue crack growth model, (3) El Haddad small crack model, (4) Shakedown enhancement for 1D geometry mode, (5) Mission scaling enhancements, and (6) Crack size termination criterion enhancement. Short descriptions of each are provided below. Additional information is available in the DARWIN user Manual.

1. 2D/3D surface autozoning: In previous versions of DARWIN, autozoning was not supported for risk assessment of surface damage anomalies (manual zoning was the only option for this anomaly type). On this project, the optimal autozoning framework that was previously developed for risk assessment of inherent (volume-based) anomalies was extended to support surface damage anomalies. This enabled users to assign properties (*e.g.*, anomaly distributions, materials, inspections) to finite element surfaces, and identifies the optimal placement of these surfaces into surface zones. Similar to the autozoning capability for inherent anomalies, this new feature provides life and risk contours as well as zone risk convergence values.
2. Dhondt fatigue crack growth model: A new cyclic fatigue crack growth equation was implemented in DARWIN that includes dependency of threshold on stress ratio. The model, labeled “Dhondt,” is a modified version of the DARWIN Walker crack growth model.
3. El Haddad small crack model: In previous versions of DARWIN, treatment of small cracks was limited to the NASGRO fatigue crack growth model. The NASGRO model uses a small crack correction parameter to account for small crack effects on the driving force of fatigue crack growth analyses. A new El Haddad small crack correction parameter was introduced in DARWIN to account for small crack effects by increasing

the effective crack driving force at very small crack sizes. It can be applied to all DARWIN fatigue crack growth models (except the NASGRO model, which already provides treatment for small cracks).

4. Shakedown enhancement for 1D geometry mode: DARWIN was enhanced to provide treatment for both plane stress and plane strain conditions when using shakedown in the 1D geometry mode. When plane stress is selected, stress values that are orthogonal to the user-defined input stress profiles are set to near-zero values. When plane strain is selected, the stress in one orthogonal direction is set to a near-zero value, and the stress value in the other orthogonal direction is set to the user-defined stress profile values multiplied by a constant (Poisson's ratio).
5. Mission scaling enhancements: DARWIN was enhanced to provide independent scaling options for stress and temperature at each load step. For example, stress values can be multiplied by a user-specified value, and temperature values can be replaced by a user-specified value within the same load step. This enhancement includes the capability for users to add or subtract user-specified values from the stress and temperature values that are extracted from finite element models.
6. Crack size termination criterion enhancement. DARWIN enables users to specify fatigue crack growth termination criterion in terms of failure (*i.e.*, stress intensity factor exceeds fracture toughness), user-specified life, or user-specified length or area. The crack size termination option was enhanced to enable the user to specify separate termination lengths for different crack dimensions (such as a and c). The crack growth termination message was also enhanced to report which crack dimension (*e.g.*, a or c) has reached the termination length.

10 Summary

The Federal Aviation Administration (FAA) is working with the aircraft engine industry to develop an enhanced life management process, based on probabilistic damage tolerance principles, to address the threat of material or manufacturing anomalies in high-energy rotating components. The multi-year "Probabilistic Integrity and Risk Assessment of Turbine Engines, Phase 2" (PIRATE-2) research grant supported this effort by developing enhanced predictive tool capability and supplementary material/anomaly behavior characterization and modeling. Grant activity included development of methods to treat surface anomalies at attachment slots for all rotor materials; enhancement of methods to treat inherent material anomalies in all rotor materials; new capabilities for fleet risk assessment and continued airworthiness; and first steps

to expand the scope of Design Assessment of Reliability With INspection (DARWIN[®]) to address life-limited engine parts other than rotors. Southwest Research Institute[®] (SwRI[®]) led the effort; industry partners GE Aviation, Honeywell, Pratt & Whitney, and Rolls-Royce Corporation served as major subcontractors and Steering Committee; and Elder Research played a key subcontracting role. Major PIRATE-2 accomplishments included the following:

- New DARWIN[®] versions 9.0, 9.1, 9.2, 9.3, 9.4, and 10.0 were released to the FAA and industry. Each new version was evaluated thoroughly by the development team, the project steering committee, and Rotor Integrity Steering Committee (RISC) before being released for production use.
- Twenty-two commercial DARWIN licenses were active at the end of this grant, including thirteen manufacturers of gas turbine engines for aircraft applications. Many of these commercial software licenses are at the corporate level and represent a combined total of hundreds of individual DARWIN users. Licensing revenue was used to fund additional enhancements of DARWIN as well as user support, including training workshops for licensees. DARWIN is available royalty-free to all U.S. government agencies. During this grant, DARWIN was distributed to eight government facilities at the United States (U.S.) Air Force, National Aeronautics and Space Administration (NASA), the U.S. Navy, and the National Institute of Standards and Technology (NIST).
- A comprehensive three-day DARWIN training workshop was conducted with FAA funding in March 2018. Seventy-two persons attended the workshop in person, and more than sixty additional persons participated in the first day of the workshop through WebEx. Onsite participants represented thirty-seven organizations from ten different countries.
- Four two-day DARWIN training workshops funded by participants were presented in the U.S. and two foreign countries for licensee companies or the Naval Air Systems Command (NAVAIR). About one hundred people participated in those four workshops.
- Growing interest in DARWIN among other U.S. government agencies led to a number of DARWIN spin-off projects funded by the Air Force Research Laboratory (AFRL), NASA, Defense Advanced Research Projects Agency (DARPA), and individual DARWIN licensee companies. These projects typically result in significant new capabilities in the production DARWIN software delivered to all users. Several of these spin-off projects, including a separate project funded by the FAA, specifically addressed the potential use of DARWIN for additively manufactured metallic components.

- A new analysis mode was implemented in DARWIN to perform risk assessment of axial blade slots in accordance with the methods to be included in a forthcoming FAA Advisory Circular (AC) 33.70-5. This mode enables users to define an axial blade slot region using 1D stress profiles or 3D finite element (FE) model geometries. The implementation includes all appropriate manufacturing process credits and a standard reporting form.
- DARWIN was originally developed to assess the risk of titanium hard alpha (HA) anomalies in engine components in accordance with AC 33.14-1. The FAA issued a revision called AC 33.14-1 Change 1 in 2017 and new AC 33.70-3 in May 2023. DARWIN was modified to support the requirements of both AC 33.14-1 Change 1 and AC 33.70-3. The same analytical methods are used in all three cases. However, new anomaly distributions were implemented to support AC 33.14-1 Change 1 and AC 33.70-3.
- DARWIN was enhanced to prevent users from deliberately or accidentally modifying standard anomaly size distribution and probability of detection (POD) curve data files and attempting to apply them as the correct standard files for FAA certification assessments. A special keyword (also known as a hash signature) was added to all the standard files in the DARWIN AC certification directory. The hash signature is generated based on the entire data contained in the file and a hidden keyword only known to the SwRI development team. Changing any aspect of the file will invalidate the hash signature. If the hash signature is present but the file and/or keyword has been modified by the user, DARWIN will issue an error and will prevent the file from being imported into the graphic user interface (GUI). If the hash signature is not present, DARWIN will recognize the file as a user-provided file and will issue a warning to the FAA certification report indicating that a user-provided file was used in the analysis.
- A new bivariant weight function stress intensity factor (SIF) solution for an external circumferential elliptical surface crack in a hollow cylinder was developed, implemented in DARWIN, and verified. The solution includes a novel crack front parameterization that enforces normality for the surface tip interaction with the cylinder surface while maintaining a part-elliptical shape that can evolve naturally. This new solution allows DARWIN to address surface cracks in shafts and casings more accurately.
- DARWIN SIF geometry limits and crack transition algorithms were comprehensively reviewed and revised for internal consistency, as well as consistency with the same SIF

solutions in the widely used NASGRO[®] fracture mechanics software (also developed at SwRI). The changes eliminated some unnecessary over-conservatism in a few situations.

- An alternative surface correction factor method was implemented as an option in DARWIN to account for the observed effect of the free surface on the growth of a part-through crack near the surface. This so-called constraint loss model, which has historically been employed by some engine manufacturers, gives similar but not identical results to the default surface correction factor model already in DARWIN.
- The accuracy of ten SIF solutions in DARWIN was verified by comparing DARWIN SIF results against high-fidelity SIF solutions from 3D FE analyses. The verification matrix efficiently interrogated a wide range of crack sizes, crack shapes, and cracked body dimensions as well as applied stress gradients. The solutions covered almost all analyses performed in DARWIN by most users. The DARWIN SIF results for more than 90% of the specific configurations considered were found to be within 5% of the FE solutions, most even closer, and the few cases with larger errors were generally conservative and/or inconsequential. One solution with somewhat larger (mostly conservative) errors was revised to improve its accuracy.
- A benchmarking study was conducted to perform validation of DARWIN SIF solutions and their use for fatigue crack growth (FCG) life predictions using Ti-6Al-4V. Baseline FCG tests were performed with simple through crack tension geometries to develop high quality FCG properties. The FCG response of other benchmark experiments for different geometries and loading modes was compared with predictions using the baseline properties. The predictions were accurate (within material scatter) or modestly conservative under all conditions considered.
- A very limited exploratory study was conducted to investigate the interaction of thermo-mechanical fatigue (TMF) and shot-peening residual stress (RS) effects on crack growth. A few experiments were conducted using Inconel 718, and the results were compared with predictions using different TMF crack growth models. The study indicated that, for a single set of test conditions considered, the “average da/dN ” TMF method predicted experimental results reasonably well and was more accurate than some alternative models.
- A small test program was performed in an attempt to define a potential low-cycle fatigue debit due to the presence of a naturally-occurring anomaly in Inconel 718. A specimen containing a surface-connected dirty white spot as well as six baseline specimens without

any known anomalies were machined out of the same part and tested in four-point bending fatigue at 750°F. Unfortunately, the failure crack in the specimen with the anomaly initiated from a carbide, not the anomaly. All of the anomaly-free test specimens evaluated with fractography were also found to fail from a carbide. Therefore, it was not possible to determine a fatigue life debit for the anomaly specimen. The results from this test program call into question the ability to determine a fatigue life debit experimentally for surface-connected wrought Ni anomalies at temperatures where carbides are active.

- DARWIN was enhanced to allow local univariant RS profiles to be applied to bivariant SIF solutions for surface and corner cracks in plates. The RS profiles are superimposed on 2D FE model geometries for use in FCG life and fracture risk calculations.
- The Gaussian Process Importance Sampling probabilistic method was extended to include additional random variables associated with six degree of freedom 3D anomalies and shop visit anomalies. An additional response surface was implemented (as an optional feature) to model the relationship among formation life and its associated input random variables.
- The DARWIN Fleet Assessment Module was enhanced to enable users to perform an inspection-based corrective action across an entire fleet of aircraft in accordance with AC 39-8.
- Fracture modeling capabilities in DARWIN were expanded to permit enhanced plate definitions for bivariant SIF solutions. Previously, stresses had to be defined at every point inside the bivariant fracture plate, which required the plate to be completely contained inside the component model, and could lead to over-conservatism. Bivariant plates are now allowed to extend outside the component model on the three edges remote from the crack location, extend outside the component model along the front edge of the plate when missing material is due to tolerancing issues, and extend across the component model when internal cavities are encountered. The bivariant shakedown algorithm was also enhanced to accommodate these different types of missing material.
- DARWIN Autoplate functionality previously available for 2D and 3D autozoning and for 2D manual model creation was extended to 3D manual fracture models, using a common interface for both 2D and 3D models. Also, initial cracks can now be placed at any location on the surface of a 3D model, not only at nodes.
- DARWIN was enhanced to enable users to view and export fracture plates associated with automatically-generated life and risk contours.

- A new HDF5 binary file format (HSIESTA) was introduced for storage and retrieval of FE geometries and results data. This reduces the time required for DARWIN to read and display the stresses and temperatures associated with large FE models, and allows larger models to be used with significantly reduced memory usage. The FE2NEU results file translator was enhanced to translate models from commercial FE software and legacy DARWIN SIESTA files to the HSIESTA format.
- A triage algorithm was developed and implemented in FE2NEU to assess the compatibility of FE models intended for use in DARWIN. This algorithm performs a series of model quality checks during the conversion of an FE file from its native format to the HSIESTA format. The algorithm screens and reports issues in the FE file that could prevent DARWIN from reading and using the FE model.
- Several different improvements were implemented in the GUI and in FE2NEU to reduce the response time when loading, displaying, and operating on large 3D models. The Autoplate algorithm was enhanced to identify directly the crack growth plane for user-defined cracks, rather than requiring the plane to be identified by the GUI. This provided a significant reduction in the computation time to create user-defined cracks in large 2D and 3D models with large numbers of load steps.
- The original framework of DARWIN was focused on supporting zone-based probabilistic fracture risk calculations (*e.g.*, AC 33.14-1 (Federal Aviation Administration, Aug, 2009) and AC 33.70-2 (Federal Aviation Administration, Aug, 2009)), but AC 33.70-1 (Federal Aviation Administration, July, 2009) also advises the use of deterministic -damage tolerance calculations in some situations. DARWIN was enhanced to provide a streamlined method for users to set up a deterministic fracture life calculation directly.
- With previous versions of DARWIN, some users routinely modified DARWIN input files manually using a text editor, which requires significantly less human time than using the GUI for large numbers of runs. More recent versions of DARWIN use a binary file form, which cannot be modified using regular text editors. In response, the DARWIN Python Module (DPM), based on a script program developed on a previous grant, was developed to enable users to create and/or modify DARWIN input files without the use of the GUI.
- DARWIN contains a number of optional features that are not needed or desired by all users. In addition, some companies may wish to provide default settings or values for their users that may differ from the defaults that are provided in DARWIN. DARWIN

was enhanced to enable an individual organization to specify the DARWIN features that are available to their users and to specify default values for selected DARWIN inputs.

- DARWIN was enhanced to provide advanced visualization capabilities that enable users to define and manipulate regions within 3D FE models. Regions can be defined by a list of elements, by contours, by contour range, or by boxing elements. The 3D regions can also be defined as view filters that enable users to visualize different parts of the geometry that previously could not be seen in DARWIN. View filters can be combined using Boolean operations such as AND, OR, XOR, and NOT. New visualization features such as edge toggling, model clipping, and iso-surfaces were also implemented.
- Significant results from this research program and related spin-off projects were disseminated to a much broader audience in the gas turbine engine community or the international technical community through conference presentations or publications in archival technical journals. A total of 20 published papers (most of them presented at international conferences) and 21 additional presentations without manuscript occurred during the term of the current grant.

11 References

- ASME. (2019). *Guide for Verification and Validation in Computational Solid Mechanics*,. New York, NY: ASME International.
- Boyce, B. L., & Ritchie, R. (2001). Effect of Load Ratio and Maximum Stress Intensity on the Fatigue Threshold in Ti-6Al-4V. *Engineering Fracture Mechanics*, 68, 129-147.
- Chan, K. S. (2001). Constitutive relations for inelastic deformation and damage accumulation in hard alpha titanium. *ASME Transactions, Journal of Engineering Materials and Technology*, 123, 281-286. doi:<https://doi.org/10.1115/1.1373653>
- Chan, K. S., Burns, J. T., Enright, M. P., Moody, J. P., & Goodrum, W. (2020). Validation of hot corrosion and fatigue models in HOTPITS. *Journal of Engineering Materials and Technology*, 142, 031001. doi: <https://doi.org/10.1115/1.4045710>
- Chan, K. S., Enright, M. P., Moody, J. P., & Fitch, S. K. (2016). Physics-based modeling tools for predicting type II hot corrosion in Ni-based superalloys. *Superalloys 2016: Proceedings of the 13th International Symposium on Superalloys*. Seven Springs, PA. doi: <https://doi.org/10.1002/9781119075646.ch98>
- Chan, K. S., Enright, M. P., Moody, J. P., Thomas, C., & Goodrum, W. (2020). HOTPITS: The DARWIN approach to assessing risk of hot corrosion induced fracture in gas turbine components. *Engineering Fracture Mechanics*, 228, 106889. doi:<https://doi.org/10.1016/j.engfracmech.2020.106889>
- Chan, K. S., Perocchi, L., & Leverant, G. R. (2000). Constitutive properties of hard alpha titanium. *Metallurgical and Materials Transactions A*, 31A, 3029-3040. doi:<https://doi.org/10.1007/s11661-000-0082-6>
- Enright, M. P., & Millwater, H. R. (2002). Optimal sampling techniques for zone-based probabilistic fatigue life prediction. *Proc. 43rd Structures, Structural Dynamics, and Materials Conference, AIAA Paper 2002-1383*. Denver, Colorado: AIAA. doi:<https://doi.org/10.2514/6.2002-1383>
- Enright, M. P., Lee, Y.-D., McClung, R. C., Huysse, L., Leverant, G. R., Millerwater, H. R., & Fitch, S. K. (2003). Probabilistic surface damage tolerance assessment of aircraft turbine rotors. *Proc. 48th ASME International Gas Turbine & Aeroengine Technical Congress, Paper GT-2003-38731*. Atlanta, Georgia: ASME.

- Enright, M. P., Liang, W., Moody, J. P., & Fitch, S. K. (2010). Development of risk contours for assessment of aircraft engine components. *Proc. 12th AIAA Non-Deterministic Approaches Conference, AIAA-2010-2846*. Orlando, FL: AIAA.
doi:<https://doi.org/10.2514/6.2010-2846>
- Enright, M. P., McClung, R. C., Liang, W., Lee, Y.-D., Moody, J. P., & Fitch, S. K. (2012). A tool for probabilistic damage tolerance of hole features in turbine engine rotors. *Proceedings of the ASME Turbo Expo 2012: Turbine Technical Conference and Exposition. Volume 7: Structures and Dynamics, Parts A and B*. Copenhagen, Denmark.
doi:<https://doi.org/10.1115/GT2012-69968>
- Enright, M. P., Moody, J. P., & Sobotka, J. C. (2016). Optimal automated risk assessment of 3D gas turbine engine components. *Proceedings of ASME Turbo Expo 2016, Paper GT2016-58091*. Seoul, South Korea. doi:<https://doi.org/10.1115/GT2016-58091>
- Enright, M., Millwater, H. R., & Huyse, L. (2006). Adaptive optimal sampling methodology for reliability prediction of series systems. *AIAA Journal*, *44*(3), 523-528.
doi:<https://doi.org/10.2514/1.11290>
- Federal Aviation Administration. (2001). *Damage tolerance for high energy turbine engine rotors*. Advisory Circular 33.14-1. Retrieved from https://www.faa.gov/regulations_policies/advisory_circulars/index.cfm/go/document.information/documentID/22920
- Federal Aviation Administration. (2003). *Continued airworthiness assessments of powerplant and auxiliary power unit installations of transport category airplanes*. Advisory Circular 39-8. Retrieved from https://www.faa.gov/documentLibrary/media/Advisory_Circular/AC_39-8.pdf
- Federal Aviation Administration. (2023). *Damage tolerance for material anomalies in titanium life-limited turbine engine rotors*. Advisory Circular 33.70-3. Retrieved from https://www.faa.gov/documentLibrary/media/Advisory_Circular/AC_33.70-3.pdf
- Federal Aviation Administration. (Aug, 2009). *Damage tolerance of hole features in high-energy turbine engine rotors*. Advisory Circular 33.70-2, Table 1: Template styles.
doi:https://www.faa.gov/documentLibrary/media/Advisory_Circular/AC_33_70-2.pdf
- Federal Aviation Administration. (July, 2009). *Guidance material for aircraft engine life-limited parts requirements*. Advisory Circular 33.70-1. Retrieved from https://www.faa.gov/documentLibrary/media/Advisory_Circular/AC_33_70-1.pdf

- Fitch, S. K., McClung, R. C., Enright, M. P., Lee, Y.-D., Huyse, L., & Fitch, S. K. (2004). Efficient fracture design for complex turbine engine components. *Proc. 49th ASME International Gas Turbine & Aeroengine Technical Congress, Paper GT-2004-53323*. Vienna, Austria: ASME.
- Golden, P. J., Whitney-Rawls, A., Jha, S. K., Porter, W. J., Buchanan, III, D., Prasad, K., . . . John, R. (2019). Probabilistic prediction of minimum fatigue life behavior in alpha + beta titanium alloys. *Fatigue and Fracture of Engineering Materials and Structures*, 42(3), 674-685. doi:10.1111/ffe.12942
- Gorelik, M. (2017). Additive manufacturing in the context of structural integrity. *International Journal of Fatigue*, 94(2), 168-177. doi:<https://doi.org/10.1016/j.ijfatigue.2016.07.005>
- Huyse, L., & Enright, M. P. (2003). Efficient statistical analysis of failure risk in engine rotor disks using importance sampling techniques. *Proc. 44th Structures, Structural Dynamics, and Materials Conference, Paper 2003-1838*. Norfolk, Virginia. doi:<https://doi.org/10.2514/6.2003-1838>
- Larsen, J. M., Jha, S. K., Szczepanski, C. J., Caton, M. J., John, R., Rosenberger, A. H., . . . Jira, J. R. (2013). Reducing uncertainty in fatigue life limits of turbine engine alloys. *International Journal of Fatigue*, 57, 103-112.
- Laz, P. J., Chan, K. S., McClung, R. C., & Leverant, G. R. (2003). Effects of CTE-induced residual stresses around hard alpha particles on fatigue crack growth in Ti-6Al-4V. *Fatigue and Fracture of Engineering Materials and Structures*, 26(12), 1145-1157. doi: <https://doi.org/10.1046/j.1460-2695.2003.00714.x>
- Lee, Y.-D., McClung, R. C., & Chell, G. G. (2008). An efficient stress intensity factor solution scheme for corner cracks at holes under bivariate stressing. *Fatigue and Fracture of Engineering Materials and Structures*, 31(11), 1004-1016. doi:<https://doi.org/10.1111/j.1460-2695.2008.01292.x>
- Leverant, G. R., McClung, R. C., Wu, Y.-T., Millwater, H. R., Riha, D. S., Enright, M. P., . . . Srivatsa, S. (2000). *Turbine rotor material design, [DOT/FAA/AR-00/64], Grant No. 95 G 041*. Department of Transportation, Federal Aviation Administration.
- McClung, R. C. (2007, March). A literature survey on the stability and significance of residual stresses during fatigue. *Fatigue and Fracture of Engineering Materials and Structures*, 30(3), 173-205. doi:<https://doi.org/10.1111/j.1460-2695.2007.01102.x>

- McClung, R. C., Enright, M. P., Lee, Y.-D., Liang, W., Moody, J. P., Fitch, S. K., . . . Peralta, A. D. (2018). *Probabilistic design for rotor integrity [DOT/FAA/TC-18/6], Grant No. 2005-G-005, SwRI Project 18.11481*. Final Report, Federal Aviation Administration. Retrieved from <https://www.tc.faa.gov/its/worldpac/techrpt/tc18-6.pdf>
- McClung, R. C., Enright, M. P., Lee, Y.-D., Moody, J. P., Sobotka, J. C., Bhamidipati, V., . . . Peralta, A. D. (2018). *Probabilistic integrity and risk assessment of turbine engines, [DOT/FAA/TC-17/15], Grant No. 11-G-009, SwRI Project 18.16853*. Final Report, Federal Aviation Administration.
- McClung, R. C., Lawless, B. H., Gorelik, M., Date, C., Gill, Y., & Piasik, R. S. (1999). Fatigue crack growth of titanium rotor alloys in vacuum and air. In R. E. Boyer, *Fatigue Behavior of Titanium Alloys* (pp. 211-218). The Minerals, Metals, and Materials Society.
- McClung, R. C., Lee, Y.-D., Enright, M. P., & Liang, W. (2014). New methods for automated fatigue crack growth and reliability analysis. *ASME Journal of Engineering for Gas Turbines and Power, Paper 062101, 136*(6). Also published as Paper GT2012-69121, Proceedings of ASME Turbo Expo 2012, Copenhagen, Denmark). doi:<https://doi.org/10.1115/1.4026140>
- McClung, R. C., Lee, Y.-D., Liang, W., Enright, M. P., & Fitch, S. K. (2010). Automated fatigue crack growth analysis of components. *Proceedings, 10th International Fatigue Congress (Fatigue 2010)*. Prague, Czech Republic. See also *Procedia Engineering*, Vol. 2, Issue 1, 2010, pp. 629-637. doi:<https://doi.org/10.1016/j.proeng.2010.03.068>
- McClung, R. C., Leverant, G. R., Enright, M. P., Huyse, L., Lee, Y.-D., Waldhart, C. J., . . . Srivatsa, S. K. (2008). *Turbine rotor material design—Phase II, [DOT/FAA/AR-07/13], Grant No. 99-G-016*. Department of Transportation, Federal Aviation Administration.
- McKeighan, P. C., Perocchi, L. C., Nicholls, A. E., & McClung, R. C. (1999). Characterizing the cracking behavior of hard alpha defects in rotor grade Ti-6-4 alloy. *Fatigue Behavior of Titanium Alloys*, 349-356.
- Millwater, H. R., Wu, J., Riha, D. S., Enright, M. P., Leverant, G. R., McClung, R. C., . . . Meyer, J. (2000). A probabilistically-based damage tolerance analysis computer program for hard alpha anomalies in titanium rotors. Paper 2000-GT-0421. *Proceedings of the ASME Turbo Expo 2000: Power for Land, Sea, and Air. Volume 4: Manufacturing Materials and Metallurgy; Ceramics; Structures and Dynamics; Controls, Diagnostics and Instrumentation*. Munich, Germany. doi:<https://doi.org/10.1115/2000-GT-0421>

- Moody, J. P., Enright, M. P., & Liang, W. (2013). An optimal automated zone allocation approach for risk assessment of gas turbine engine components. *Proceedings of the ASME Turbo Expo 2013: Turbine Technical Conference and Exposition. Volume 7A: Structures and Dynamics*. San Antonio, TX: ASME. doi:<https://doi.org/10.1115/GT2013-95129>
- Moody, J., Millwater, H., & Enright, M. (2007). Automatic risk assessment methodology for gas turbine engines employing adaptive mesh refinement techniques. *Proceedings of the ASME Turbo Expo 2007: Power for Land, Sea, and Air. Volume 5: Turbo Expo 2007*. Montreal, Canada: ASME. doi:<https://doi.org/10.1115/GT2007-27576>
- Newman, J. C., & Raju, I. S. (1984). Prediction of Fatigue Crack-Growth Patterns and Lives in Three-Dimensional Cracked Bodies. *Advances in Fracture Research (Fracture 84), Sixth International Conference on Fracture, Vol. 3*, pp. 1597-1608.
- Newman, J. J., & Raju, I. S. (1984). Prediction of fatigue crack-growth patterns and lives in three-dimensional cracked bodies. *Advances in Fracture Research (Fracture 84), Sixth International Conference on Fracture. Vol. 3*, pp. 1597-1608. NASA Langley Research Center. doi:<https://ntrs.nasa.gov/api/citations/19840014911/downloads/19840014911.pdf>
- Sheldon, J. W., Bain, K. R., & Donald, J. K. (1999). Investigation of the Effects of Shed-Rate, Initial K_{max}, and Geometric Constraint on ΔK_{th} in Ti-6Al-4V at Room Temperature. *International Journal of Fatigue, 21*, 733-741.
- Simpson, T. W., Lin, K. J., & Chen, W. (2001). Sampling strategies for computer experiments: Design and analysis. *International Journal of Reliability and Applications, 2*, 209-240.
- Sobotka, J. C., & McClung, R. C. (2020). Characterization of stress fields near pores and application to fatigue lives. In N. Shamsaei, S. Daniewicz, N. Hrabe, S. Beretta, J. Waller, M. Seifi, & N. D. Shamsaei (Ed.), *Structural Integrity of Additive Manufactured Parts, ASTM STP 1620*. (pp. 367-380). ASTM. doi:10.1520/STP162020180141
- Sobotka, J., Enright, M., & McClung, R. (2019). Application of critical distances to fatigue at pores. *Fatigue and Fracture of Engineering Materials and Structures, 42*(8), 1646-1661. doi:<https://doi.org/10.1111/ffe.13004>
- Van Stone, R. H., Gilbert, M. S., Gooden, O. C., & Laflen, J. H. (1988). Advances in fracture research (fracture 84), Sixth international conference on fracture. In T. Cruse (Ed.), *Fracture Mechanics: Nineteenth Symposium, ASTM STP 969* (pp. 637-656). ASTM.

Wu, Y., Enright, M. P., & Millwater, H. R. (2002). Probabilistic methods for design assessment of reliability with inspection. *AIAA Journal*, 40(5), 937-946.

Wu, Y.-T., Enright, M. P., & Millwater, H. R. (2000). Efficient and accurate methods for probabilistic analysis of titanium rotors. *Proc. 8th ASCE Joint Specialty Conference on Probabilistic Mechanics and Structural Reliability*, Paper PMC2000-221. Notre Dame, Indiana.

A Development and verification of a new Stress Intensity Factor solution for an external circumferential elliptical surface crack in a hollow cylinder

List of Figures

Figure A- 1. Geometric parameterization of SC34.....	A-3
Figure A- 2. Displacement of ellipse center from exterior surface of hollow cylinder to ensure crack tip perimeter intersects exterior cylinder surface perpendicularly	A-5
Figure A- 3. Comparison of crack front definitions using new SC34 parameterization and corresponding plate parameterization	A-7
Figure A- 4. Solution space regions.....	A-10
Figure A- 5. Finite element geometric features for surface crack in hollow shaft and cylinder ..	A-12
Figure A- 6. Maximum principal stress along crack front defined by new parameterization ..	A-14
Figure A- 7. Geometry correction factor over crack front for eight different loading conditions	A-15
Figure A- 8. Coordinate system deployed in WF formulation for SC34.....	A-16
Figure A- 9. Variations of stress functions used for verification.....	A-24
Figure A- 10. Formal verification results for initial implementation of SC34	A-29
Figure A- 11. Formal verification results for second implementation of SC34 with enhanced reference solution matrix	A-31
Figure A- 12. Formal verification results for final implementation of SC34 with enhanced reference solution matrix and support for small cracks	A-34

List of Tables

Table A-1. Adjustments to some parameters for PWF integration in Solution Region V.....	A-22
Table A- 2. Comparison of FE and WF results for SC34.....	A-25
Table A- 3. Relative error (%) statistics for initial implementation of SC34	A-28
Table A- 4. Relative error (%) statistics for second implementation of SC34 with enhanced reference solution matrix	A-32
Table A- 5. Relative error (%) statistics for final implementation of SC34 with enhanced reference solution matrix and support for small cracks	A-33

A.1 Introduction

Previous development of DARWIN[®] and its associated fracture mechanics capabilities focused exclusively on rotors, which are generally the most safety-critical components in an aircraft engine. However, FAA Advisory Circular 33.70-1 (FAA, 2009) addresses all engine life-limited parts, noting that their failure is likely to result in a hazardous engine effect, and directs that applicants should meet specific integrity requirements by executing a series of life management activities that include damage tolerance analysis. In this particular effort, a new engineering stress intensity factor (SIF) solution was developed, verified, and implemented in DARWIN to address a surface crack in a hollow cylinder. This is one-step in a planned expansion of DARWIN capabilities to address new classes of life-limited engine parts such as shafts and casings.

The new SIF solution for an external circumferential elliptical surface crack in a hollow cylinder is denoted SC34. Figure A- 1 shows the parametric idealization for this new SIF solution, based on four measurable dimensions. Here, D represents the diameter; t is the thickness; a is the crack depth; and c is the crack half-length along the surface of the cylinder. The new solution has geometric limits defined by $4 \leq D/t \leq 256$, $0 < a/t \leq 0.9$, and a wide range of a/c -ratios that depend on other parameters. The new crack case is a weight function solution that employs bivariant stress gradients, though it is limited to stress gradients that are symmetric about X -axis in DARWIN to avoid some computational issues during fatigue crack growth. It is analogous to other bivariant weight function solutions in DARWIN, such as SC31 or CC09.

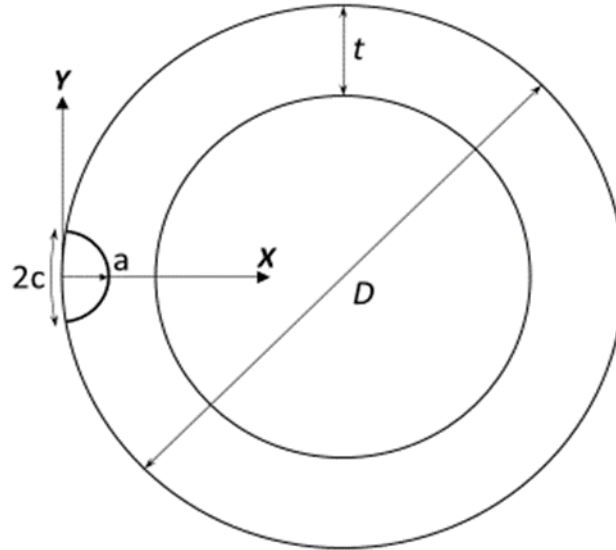


Figure A- 1. Geometric parameterization of SC34

A.2 Definition of crack tip perimeter

DARWIN versions developed on previous grants supported cracks in hollow cylinders (such as a shaft or casing) by idealizing the geometry as a surface crack in a plate. This idealization neglects crack-front constraint provided by the cylinder geometry; that is, the uncracked portion of the cylinder ahead of the crack that reduces crack-front opening. Furthermore, this approach may lead to potentially large discrepancies between the idealized geometry and real geometry if the crack is large relative to the curvature of the cylinder.

To alleviate these issues, Southwest Research Institute® (SwRI) developed a new parameterization for a crack front defined in circular shafts and casings. Previous parameterizations locate an elliptical crack front that is centered on the surface of the circular shaft/casing, or they locate a circular crack front normal to the circular shaft/casing. The first parameterization scheme leads to numerical difficulties in the finite element analysis (FEA) since crack fronts may intersect the geometry at shallow oblique angles that may be non-physical. The second parameterization scheme overly confines the crack front to a possibly non-physical shape and only supports crack advance along one degree of freedom. This restriction would prohibit bivariate weight-function (WF) solutions, thereby ruling out (for example) consideration of surface residual stresses in conjunction with axial or bending stresses.

The definition of crack tip perimeter for SC34 follows a novel approach. This approach enforces normality for the surface tip intersection with the cylinder surface. While the crack tip perimeter is defined in accordance with the description for an ellipse, the center of this ellipse is not required to be on the exterior surface of the hollow cylinder. Its location can be shifted outwards

or inwards such that the crack tip front at the surface is perpendicular to the exterior circumferential surface of the cylinder. Imposing this requirement uniquely defines a crack front description for a surface crack characterized by a measurable crack depth a_m and measurable surface crack length $2c_m$. Note that in these detailed development sections, *measured* dimensions will be referred to by the subscript 'm' (e.g., a_m refers to the measured depth dimension).

In this derivation, we require that the ellipse intercept the exterior surface of the cylinder at a normal angle (see Figure A- 2). This requirement sufficiently constrains the location of the ellipse/cylinder system to determine three geometric locations that uniquely define the semi-major axis a_E , the semi-minor axis c_E , and the offset δR of the ellipse relative to the cylindrical surface. The derivation makes use of the following geometric descriptions for the exterior cylindrical surface and the ellipse in connection to the center of the hollow cylinder (designated as the origin of the coordinate system):

- any point along the ellipse: $(x_E, y_E) = (a_E \cdot \cos \phi - (R_M + \delta R), c_E \cdot \sin \phi)$
- any point along the exterior surface of the cylinder: $(x_M, y_M) = (R_M \cdot \cos \theta, R_M \cdot \sin \theta)$
- tangent vector at any point along the ellipse: $\langle nx_E, ny_E \rangle = \langle -a_E \cdot \sin \phi, c_E \cdot \cos \phi \rangle$
- tangent vector at any point along the cylinder: $\langle nx_M, ny_M \rangle = \langle -R_M \cdot \sin \theta, R_M \cdot \cos \theta \rangle$

Three equations are derived in accordance with the original restriction:

1. $x_E = x_M$,
2. $y_E = y_M$, and
3. $\langle nx_E, ny_E \rangle \cdot \langle nx_M, ny_M \rangle = 0$.

In the above, R_M denotes the outer radius of the hollow cylinder, and both angles θ and ϕ are in reference to the axis connecting the center of the ellipse to the center of the cylinder.

To facilitate the derivation, three normalized parameters are used; respectively, they are $\alpha = a_E/R_M$, $\kappa = c_E/R_M$, and $\rho = \delta R/R_M$.

To simplify further the expression for the solutions, two extra parameters mentioned mostly in the next sections are introduced and they are:

$$p = \sin^2 \widetilde{c}_m \tag{A-1}$$

$$q = \widetilde{a}_m \tag{A-2}$$

Both relate to the specified crack dimensions through their normalized forms. The definition of normalized crack depth \widetilde{a}_m and surface crack length $2\widetilde{c}_m$ is given by $\widetilde{a}_m = (a_E - \delta R)/R_M$ and $\widetilde{c}_m = \pi - \theta$.

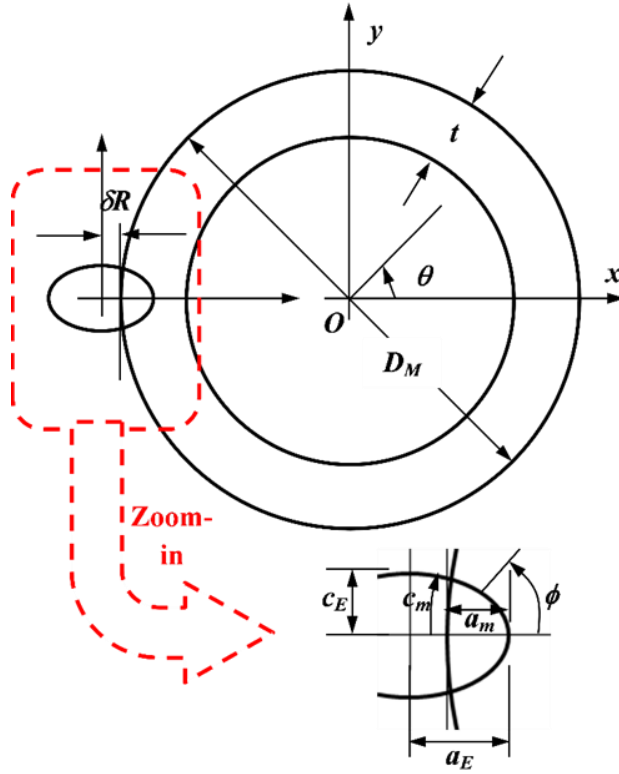


Figure A- 2. Displacement of ellipse center from exterior surface of hollow cylinder to ensure crack tip perimeter intersects exterior cylinder surface perpendicularly

The solutions for a_E , c_E , and δR can be analytically determined and are in terms of a parameter ξ_m . They are given by:

$$\kappa = \sqrt{\frac{p \cdot \xi_m}{1 - p}} \quad \text{A-3}$$

$$\alpha = \sqrt{\xi_m \cdot (\xi_m - 1 + \kappa^2)} \quad \text{A-4}$$

$$\rho = -1 + \sqrt{\xi_m + \alpha^2} \quad \text{A-5}$$

with:

$$\xi_m = \frac{1 - q}{\frac{2}{\sqrt{1 - p}} - \frac{1}{1 - q}} \quad \text{A-6}$$

The angle $\phi = \phi_o$ at interception is given by $\phi_o = \arccos[\alpha/(1 + \rho)] = \arccos[a_E/(R_M + \delta R)]$. Note the numerical sign of δR designates the relative location of the ellipse to the cylinder. A negative sign means the center of the ellipse is inside the cylinder, and a positive sign means the center of the ellipse is outside of the cylinder.

This parameterization has been derived analytically using symbolic mathematical software and verified using Python scripting capabilities. For small cracks relative to the shaft diameter, the parameterization recovers the surface crack in a plate geometry. This new parameterization reduces numerical difficulties, supports crack advance along two degrees of freedom, and features two measurable crack front dimensions (i.e., the crack depth (a_M) and crack length (c_M) along the surface). This parameterization supports cracks oriented normal to the axial direction of the shaft/casing.

Figure A- 3 illustrates the crack-front definition provided by SC34 relative to a corresponding definition for a surface crack in a plate (e.g., SC31). Here, both definitions set the same dimensions for the crack depth and crack length. The thickness values are identical as well. In Figure A- 3, the non-dimensional ratio $D_m/t = 8$ yields a thick shaft. However, the following considerations apply to thinner casing geometries with $D_m/t \gg 8$.

Images in Figure A- 3 indicate that the two parameterizations produce aligned crack fronts for small cracks. For these small cracks, the crack fronts share nearly identical crack curvature and the difference in the c-tip location is minimal. Results indicate nearly identical SIF solutions from finite element (FE) results using the SC34 solution and the SC31 solution for this small-crack geometry.

For larger cracks, the two parameterizations produce divergent crack fronts with different curvatures and different locations for the c-tip. The plate parameterization produces a semi-elliptical crack front, while the SC34 parameterization produces a nearly straight crack front. The plate parameterization produces a c-tip location far removed from the actual intersection of the crack front with the free surface, and this c-tip location intersects the free surface at an oblique angle. The plate parameterization also features a c-tip location with more constraint from the additional material along its length and its distance from the a-tip. This plate definition may result in a less conservative solution than the parameterization proposed in this work. SIFs using

the SC34 parameterization disagree with SIFs computed using SC31 for many geometries with thick shafts and large cracks as a result.

Crack fronts defined by identical dimensions

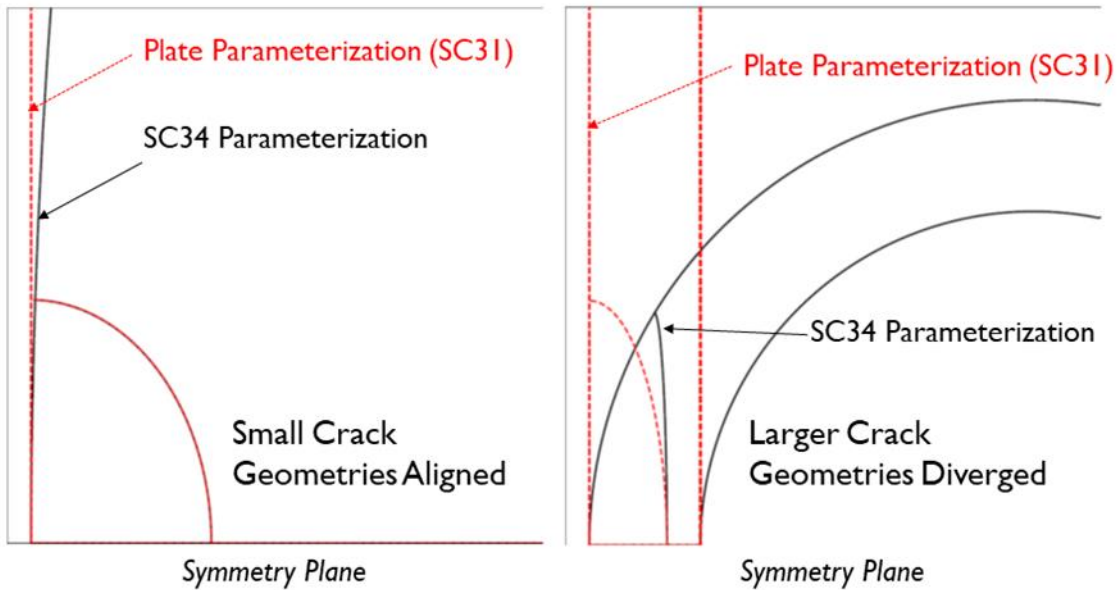


Figure A- 3. Comparison of crack front definitions using new SC34 parameterization and corresponding plate parameterization

A.3 Regions in solution space

Separate regions can be identified in the solution space in relation to the specified parameters p and q . The separate regions are based on three factors:

1. the pre-defined solution limits,
2. the relative offset δR between the center of the ellipse and the surface of the cylinder, and
3. the shape parameter of the ellipse a_E/c_E .

In the following, the three governing factors are described.

Solutions limits

The limits of the reference solutions used to facilitate the weight function (WF) development constitute the solution limits. The matrix of reference solutions is in terms of three normalized parameters: a_m/t , D_M/t , and $(c_m - c_{min})/(c_{max} - c_{min})$, where $D_M = 2R_M$ denotes the outer diameter of the hollow cylinder and t is the wall thickness.

Here $2c_{min}$ and $2c_{max}$ denote the minimum and maximum allowable surface crack lengths that are in connection to the specified crack depth. Their definitions are given by:

$$c_{min} = 0.5a_m \quad \text{A-7}$$

$$c_{max} = \frac{D_M}{2} \cos^{-1} \left(1 - \frac{2a_m}{D_M} \right) \quad \text{A-8}$$

The discrete values used to populate the elements inside the matrix are given by:

$$\begin{aligned} \frac{a_m}{t} &= 0.1, 0.3, 0.5, 0.7, 0.9 & \text{A-9} \\ \frac{c_m - c_{min}}{c_{max} - c_{min}} &= 0, 0.1, 0.3, 0.5, 0.7, 0.9 \\ \frac{D_M}{t} &= 4, 8, 16, 32, 64, 128, 256 \end{aligned}$$

The combination leads to $5 \times 6 \times 7 = 210$ geometric models in total. For each D_M/t ratio, there can be 30 different a_m/c_m ratios.

Relative offset δR

The loci denoting $\delta R = 0$ were derived from Equations A-3, A-4, and A-5. The solution is to segregate the scenarios with $\delta R > 0$ from those with $\delta R < 0$ relating to the specified crack depth and surface length. The derivation starts by equating Equation A-5 to zero, which leads to $\alpha^2 = 1 - \xi_m$. Substituting the new expression for α in the equation into Equation A-4 determines the relationship between p and q that fulfills the $\delta R = 0$ requirement. The equation is given by:

$$p_{\delta R} = 2q_{\delta R}^2 - q_{\delta R}^4 \quad \text{A-10}$$

where the subscript δR denotes the values of p and q resulting in $\delta R = 0$.

Shape parameter of the ellipse

The formulation for the point weight function (PWF) varies in accordance with the shape parameter of the ellipse. It thus requires identifying the loci to differentiate the scenario with $a_E/c_E < 1$ from its counterpart $a_E/c_E > 1$. The derivation starts by assuming $a_E = c_E = R$ from the beginning. This assumption leads to $\xi_m = 1$, and the relationship fulfilling this requirement between the specified p and q is given by:

$$p_{cir} = 1 - \left[\frac{2}{(1 - q_{cir}) + \frac{1}{1 - q_{cir}}} \right]^2 \quad \text{A-11}$$

where the subscript *cir* denotes the values of p and q resulting in $a_E/c_E = 1$.

Summarizing the above limits and loci identifies the segregated regions as depicted in Figure A- 4.

Note the solution space regions where the characterization is based on three factors:

1. the pre-defined solution limits p_{max} and p_{min} ,
2. the relative offset δR , and
3. the shape parameter a_E/c_E .

In the figure, symbols represent the geometric dimensions utilized by discrete reference solutions, and different symbol sets signify different a_m/t ratios. Only the data points with $D_M/t = 4$ are presented to reduce point clutter. The solution limits are denoted by dashed lines where the loci with the maximum and the minimum $p = \sin^2 \widetilde{c}_m$ values are color-coded by blue and red. The loci defined by Equations A-10 and A-11 are depicted in solid lines. Using Figure A- 4 helps to identify the applicable regions and facilitates the development of PWFs. For example, scenarios where $\delta R < 0$ and $a_E \geq c_E$ would never occur, and thus no development was invoked.

The development of the WF methodology deploys various forms of the PWF and integration limits in accordance with regions identified in Figure A- 4. In general, five solution regions are designated as follows. Their respective WF formulations are presented in the next sections.

- Solution region I: $\delta R > 0$ and $a_E > c_E$
- Solution region II: $\delta R > 0$ and $a_E = c_E$
- Solution region III: $\delta R > 0$ and $a_E < c_E$
- Solution region IV: $\delta R = 0$ and $a_E < c_E$
- Solution region V: $\delta R < 0$ and $a_E < c_E$

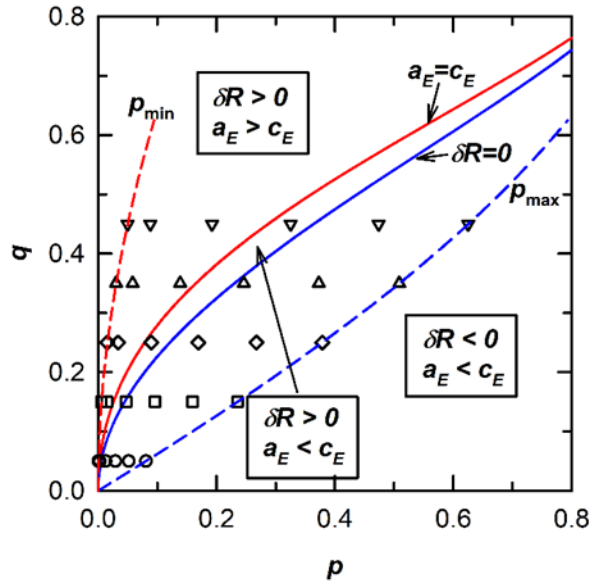


Figure A- 4. Solution space regions

A.4 Finite element analyses

From each of the 210 geometries defined in Equation A-9, the weight function solution requires three stress-intensity factor values at the a-tip and at the c-tip. These solutions represent different tractions applied to the crack faces (i.e., a uniform traction, a linearly varying traction along the X-axis, and a linearly varying traction along the Y-axis). Additional tractions were prescribed to the crack face to support verification efforts. Tractions remain normal to the crack plane and may vary in magnitude at any point on the cross-section.

All FE analyses have a 3D geometry with a semi-elliptical crack front. The semi-elliptical crack front is modeled as a linearized ellipse surrounded by rings of elements arranged in concentric circles. This geometric arrangement forms the crack tube (highlighted in Figure A- 5) that is necessary for SIF calculations in Abaqus. The crack tube represents the major difficulty associated with building the FE model. It requires significant time and effort to form an appropriate geometry. For example, geometric deviations on the order of 10^{-3} times the crack length can lead to invalid SIF values. The crack tube has 20-node hexahedron elements with full integration. On the crack front, the mid-side node has been shifted to the quarter point to accommodate the stress singularity.

There are two transition regions to connect the crack front with the far-field region 3D shell region. The first transition region features 10-node tetrahedral elements to mesh the non-standard topology of the region around the crack tube. Figure A- 5 labels this region the *TET transition*.

The element size decreases towards the crack tube region to capture increasing stress gradients. For very deep/long cracks, the transition region may completely fill the remaining cross-section. This region completely encloses the crack tube.

The *HEX transition* region (as labeled in Figure A- 5) relates to hexahedron elements and represents the second transition region. It encloses the TET transition. This region has a more regular geometry that permits meshing with brick elements. These elements have eight nodes (linear displacements) and feature full integration. The meshing scheme places at least four elements through the thickness in this region.

The far-field region links the transition region to the far ends of the shaft/cylinder. Figure A- 5 labels this region as the *3D Shell Region* to indicate the element category: 3D continuum shell elements that support only a single element through the thickness. In Abaqus, continuum shell elements look like normal continuum elements with displacement degrees of freedom. These elements have kinematic and constitutive behavior similar to shell elements. Consequently, only one shell element is required through the thickness to capture the limited stress gradients in this region. Preliminary studies with regular continuum elements (multiple elements per thickness) and continuum shell elements reveal negligible differences in stress-intensity factor values using either formulation. However, the continuum shell elements require fewer computational resources.

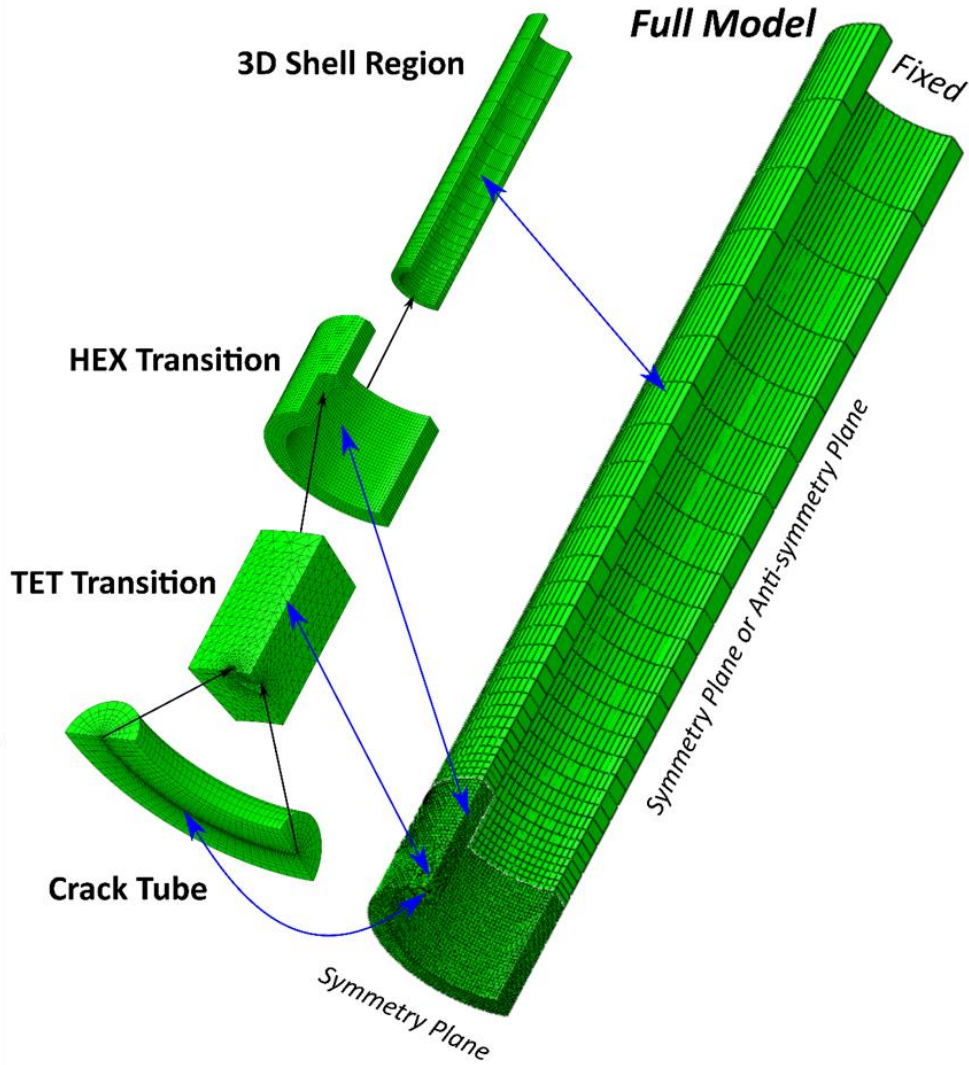


Figure A- 5. Finite element geometric features for surface crack in hollow shaft and cylinder

All analyses assume an isotropic linear-elastic material model (Hooke's law) with uniform material properties throughout the geometry. The value of Poisson's ratio ($\nu = 0.3$) is consistent with values found in most isotropic metals. The models use the linear kinematic formulation, small strain (i.e., deformations are assumed to have a negligible effect on the geometry).

All cracked models here are symmetric or anti-symmetric in the geometry, loading, and material about the crack plane. Consequently, only a quarter of the geometry needs to be modeled in these analyses, and exploiting this symmetry reduces computational costs. Zero displacements normal to the uncracked ligament preserve symmetry (i.e., they are symmetric boundary conditions). Displacements at arbitrarily selected points prevent rigid body motion.

Across the $Y = 0$ plane, the loading may be symmetric or anti-symmetric, and these analyses enforce appropriate boundary conditions. Symmetric loading requires crack plane tractions to be invariant with respect to Y or vary with some sum of even powers of Y . Anti-symmetric loading requires that crack plane tractions vary with respect to some sum of odd powers of Y . Anti-symmetric loading leads to crack-face closure that produces to negative stress-intensity factor values in the current framework. While this is non-physical, it leads to a theoretically appropriate solution used to calibrate the weight function solutions.

Abaqus computes SIF solutions using the domain integral technique. The domain integral technique transforms the line integral of the J -integral to a volume integral that facilitates numerical calculations. Abaqus computes the J -integral values along the crack front and then converts them to the corresponding SIF values. Here, $K_I \neq 0$ whereas $K_{II} = K_{III} = 0$ for all geometries and loadings. Boundary effects introduce numerical issues into the domain integral computations near free surfaces. These studies locate characteristic SIF values for crack tips at some distance from free surfaces.

We exploited the Python scripting capability in Abaqus computer-aided engineering (CAE) to generate FE solutions. The Python scripting interface enables user-created scripts to define the geometric configuration, apply loads, adopt material response, set meshing parameters, and create domain integral definitions. Python scripting also supports data processing and transfer (e.g., to/from Excel spreadsheets). Python features libraries that reduce the scripting process. There are several advantages to the scripting interfaces besides the obvious efficiencies (e.g., consistent model definitions and more rigorous modeling techniques).

Results from the FE analysis need to be verified before they are released into the verification matrix. A two-tiered approach was adopted. First, select cases were examined for general solution quality that includes balanced reaction forces, smooth displacement and stress gradients, and SIF convergence with mesh refinement. We ensured consistent solution quality by incorporating the relevant parameters into the scripts/solution matrix. Second, all cases were checked to ensure that SIF values converged over domains and that SIF values are smooth over the crack front. If a solution failed to satisfy these second quality checks, then it was rerun at a higher mesh refinement or the SIF was smoothed to eliminate oscillations across the crack front.

Figure A- 6 illustrates results from the FE analyses. This figure shows contours of the maximum principal stress near the crack front. In this figure, stresses peak in the crack front region. For this geometry, the SIF is higher at the a-tip than at the c-tip, as reflected by the larger stress bands in this image. Stresses die-off behind the crack front and approach the inner surface of the shaft.

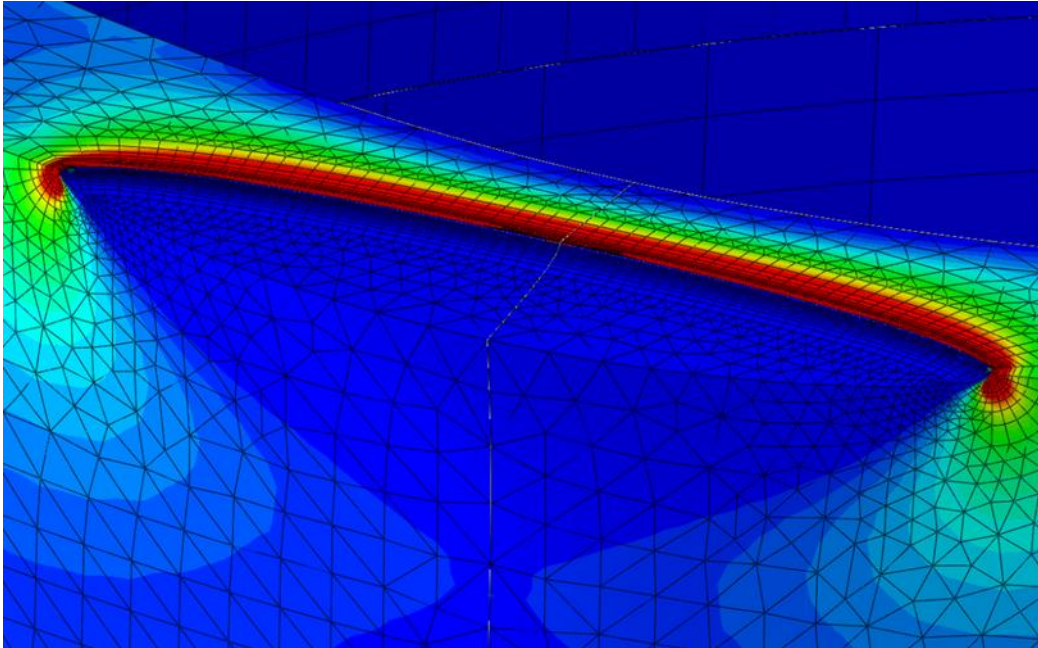


Figure A- 6. Maximum principal stress along crack front defined by new parameterization

Figure A- 7 shows a representative plot of normalized stress-intensity factors over the crack front. These results are from a symmetric loading history with eight unique tractions over the crack front. Black lines indicate the raw data, red lines show an interpolation of this data, and the red dots indicate discrete values passed to the weight function calibration. The discrete values were evaluated at the 2% and 98% locations of the non-dimensional parameter ϕ that characterizes the location along the crack front. For reference, the a -tip is located at $\phi = 0$, and the c -tip is located at $\phi = \pm\phi_{Max}$. Here, ϕ_{Max} represents the location where the crack front intersects the free surface. Only the first two pseudo-times in this series inform the weight function calibration; the remaining stresses are available for verification of the weight function. Agreement between the raw data and interpolated values suggest limited numerical instabilities.

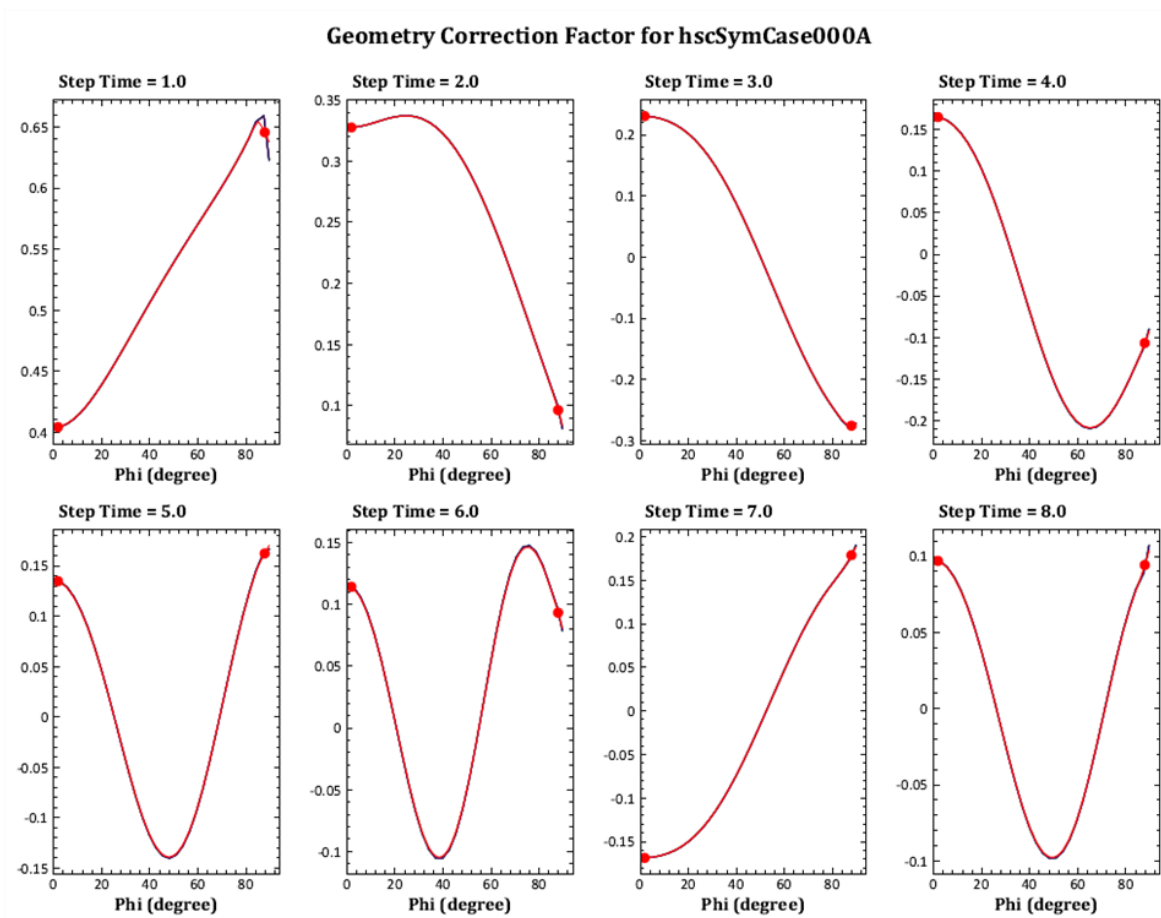


Figure A- 7. Geometry correction factor over crack front for eight different loading conditions

A.5 Weight function formulation

In contrast to the previous coordinate system depicted in Figure A- 2, the derivation of the weight function formulation uses a different coordinate system (see Figure A- 8). It is directly linked with the ellipse (or the circle if $a_E = c_E = R$) whose semi-major axis with the vertex c_E is along the x -axis, semi-minor axis with the vertex a_E along the y -axis, and center is the origin. Additionally, in order to align with the previous development for bivariate models, the notation conversion from a_E to a and from c_E to b is deployed.

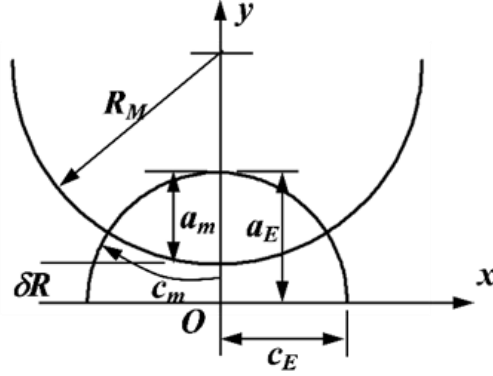


Figure A- 8. Coordinate system deployed in WF formulation for SC34

The PWF and its correction terms are postulated in the following equation:

$$W_{QQ'} = \frac{\sqrt{\mathfrak{R}^2 - r^2}}{\pi \ell_{QQ'}^2 \sqrt{\pi \mathfrak{R}}} \left\{ 1 + \Pi_1 \sqrt{1 - \left(\frac{r}{\mathfrak{R}}\right)^2} + \Pi_2 \left(1 - \frac{y'}{y}\right)^{2.2} + \Pi_3 \left[1 - \frac{x}{\text{sign}(Q', x) \cdot x'}\right]^{1.5} \right\} \quad \text{A-12}$$

The stress intensity factor can be determined by integrating the product of the PWF and the bivariate crack opening stress over the crack surface area as given by:

$$K_{Q'} = \int W_{QQ'} \cdot \sigma(x, y) dA \quad \text{A-13}$$

where Q' denotes the crack tip location of interest along the crack tip perimeter, $Q(x, y)$ the integration point on crack surface, x' and y' are the chordal lengths, and \mathfrak{R} and r are elliptical distances in reference to the same elliptical angle as Q . The coefficients Π_1 , Π_2 and Π_3 are determined by reference solutions. The details of the above parameters depend on the crack shape and are provided in the following sections. Note the two crack tip locations of interest along the perimeter are designated by a -tip and c -tip. Their elliptical angles with the current coordinate system are denoted by η_c . The a -tip corresponds to the deepest crack tip location with its elliptical angle $\eta_c = 90^\circ$. The c -tip in the formulation is hardcoded to be 3° inside the surface. So, its angular value depends on the location where the exterior cylindrical surface intersects the ellipse (or the circle) as designated previously by the angle ϕ_o . Using the current coordinate system, this angle is given by $\eta_c = (90^\circ - \phi_o) + \Delta\eta = \eta_o + \Delta\eta$ where $\Delta\eta = 3^\circ$.

Solution Region I: $\delta R > 0$ and $a > b$

The parametric form of the ellipse is in terms of its focus $c = \sqrt{a^2 - b^2}$, elliptical radius ξ and elliptical angle η , and can be described by:

$$x = c \cdot \sinh \xi \cdot \cos \eta, \quad y = c \cdot \cosh \xi \cdot \sin \eta \quad \text{A-14}$$

The elliptical perimeter is governed by $\xi_o = 0.5 \cdot \ln[(1 + \alpha_e)/(1 - \alpha_e)]$, with $\alpha_e = b/a$ and defined by $x = c \cdot \sinh \xi_o \cdot \cos \eta$ and $y = c \cdot \cosh \xi_o \cdot \sin \eta$. The parameters used in Equation A-12 for the PWF are listed as follows:

$$\begin{aligned} Q &= (c \cdot \sinh \xi \cdot \cos \eta, c \cdot \cosh \xi \cdot \sin \eta) & \text{A-15} \\ Q' &= (c \cdot \sinh \xi_o \cdot \cos \eta_c, c \cdot \cosh \xi_o \cdot \sin \eta_c) \\ Q_R &= (c \cdot \sinh \xi_o \cdot \cos \eta, c \cdot \cosh \xi_o \cdot \sin \eta) \\ Q^* &= (0, c \cdot \sin \eta) \\ \mathfrak{R} &= \ell_{QRQ^*} = c\sqrt{\mathcal{A}} \\ r &= \ell_{QQ^*} = c\sqrt{\mathcal{B}} \\ \ell_{QQ'} &= c\sqrt{\mathcal{P}} \\ y' &= \frac{c}{\alpha_e} \sqrt{\sinh^2 \xi_o - \sinh^2 \xi \cdot \cos^2 \eta} \\ x' &= c \cdot \alpha_e \sqrt{\cosh^2 \xi_o - \cosh^2 \xi \cdot \sin^2 \eta} \end{aligned}$$

The integral in Equation A-13 becomes:

$$K_{Q'} = \sqrt{c} \int \int \frac{\sigma(\xi, \eta) \sqrt{\mathcal{A} - \mathcal{B}}}{\pi \sqrt{\pi \sqrt{\mathcal{A}} \cdot P}} \left[1 + \Pi_1 \sqrt{1 - \frac{\mathcal{B}}{\mathcal{A}}} + \Pi_2(\dots)^{2.2} + \Pi_3(\dots)^{1.5} \right] \cdot (\cos^2 \eta + \sinh^2 \xi) d\eta d\xi \quad \text{A-16}$$

The integration limits vary and are dictated by the following two parameters:

$$\xi_{lower} = \cosh^{-1} \frac{R_M + \delta R + R_M \sin \vartheta}{c \cdot \sin \eta} \quad \text{A-17}$$

$$\eta_m = \sin^{-1} \frac{\delta R}{c} \quad \text{A-18}$$

The elliptical angle in Equation A-18 is always larger than η_0 that denotes the angle at intersection. The value of $\sin \vartheta$ is related to geometric parameters and the elliptical angle of point Q. It is given by:

$$\sin \vartheta = \frac{-\cos^2 \eta \cdot (R_M + \delta R) - \sqrt{\sin^2 \eta \cdot [-\cos^2 \eta \cdot (R_M + \delta R)^2 + c^2 \cos^2 \eta + R_M^2]}}{R_M} \quad \text{A-19}$$

The integration in Equation A-16 is then carried out as follows:

1. $\eta_0 < \eta_c < \eta_m$

$$K_{Q'} = \sqrt{c} \left\{ \left[\int_{\eta_0}^{\eta_c} \int_{\xi_{lower}}^{\xi_o} (\dots) d\xi d\eta + \int_{\eta_c}^{\eta_m} \int_{\xi_{lower}}^{\xi_o} (\dots) d\xi d\eta \right] + \left[\int_{\pi-\eta_m}^{\pi-\eta_c} \int_{\xi_{lower}}^{\xi_o} (\dots) d\xi d\eta + \int_{\pi-\eta_c}^{\pi-\eta_0} \int_{\xi_{lower}}^{\xi_o} (\dots) d\xi d\eta \right] + \int_{\eta_m}^{\pi-\eta_m} \int_0^{\xi_o} (\dots) d\xi d\eta \right\} \quad \text{A-20}$$

2. $\eta_0 < \eta_m < \eta_c$

$$K_{Q'} = \sqrt{c} \left\{ \int_{\eta_0}^{\eta_m} \int_{\xi_{lower}}^{\xi_o} (\dots) d\xi d\eta + \int_{\pi-\eta_m}^{\pi-\eta_0} \int_{\xi_{lower}}^{\xi_o} (\dots) d\xi d\eta + \left[\int_{\eta_m}^{\eta_c} \int_0^{\xi_o} (\dots) d\xi d\eta + \int_{\eta_c}^{\pi-\eta_m} \int_0^{\xi_o} (\dots) d\xi d\eta \right] \right\} \quad \text{A-21}$$

Solution Region II: $\delta R > 0$ and $a = b = R$

The parametric form for a circle is in terms of the radius R , the radial normalized parameter ξ , and the tangential angle η . The governing equation is given by:

$$x = r \cos \eta = \xi R \cos \eta, \quad y = r \sin \eta = \xi R \sin \eta \quad \text{A-22}$$

The parameters used in Equation. A-12 for the PWF are listed as follows:

$$\begin{aligned}
Q &= (\xi R \cos \eta, \xi R \sin \eta) & \text{A-23} \\
Q' &= (R \cos \eta_c, R \sin \eta_c) \\
Q_R &= (R \cos \eta, R \sin \eta) \\
Q^* &= (0,0) \\
\mathfrak{R} &= \ell_{Q_R Q^*} = R \\
r &= \ell_{Q Q^*} = \xi R \\
\ell_{Q Q'} &= R\sqrt{\mathcal{A}} \\
y' &= R\sqrt{1 - \xi^2 \cos^2 \eta} \\
x' &= R\sqrt{1 - \xi^2 \sin^2 \eta}
\end{aligned}$$

The integral in Equation A-13 becomes:

$$K_{Q'} = \sqrt{R} \int \int \frac{\sigma(\xi, \eta) \sqrt{1 - \xi^2}}{\pi \sqrt{\pi} \cdot \mathcal{A}} \left[1 + \Pi_1 \sqrt{1 - \xi^2} + \Pi_2(\dots)^{2.2} + \Pi_3(\dots)^{1.5} \right] \cdot \xi d\eta d\xi \quad \text{A-24}$$

The integration limits are governed by the following parameter:

$$\xi_{lower} = \cosh^{-1} \frac{R_M + \delta R + R_M \sin \vartheta}{R \cdot \sin \eta} \quad \text{A-25}$$

and the integration described in Equation A-24 is carried out by:

$$K_{Q'} = \sqrt{R} \left[\int_{\eta_o}^{\eta_c} \int_{\xi_{lower}}^1 (\dots) d\xi d\eta + \int_{\eta_c}^{\pi - \eta_o} \int_{\xi_{lower}}^1 (\dots) d\xi d\eta \right] \quad \text{A-26}$$

with the value of $\sin \vartheta$ given by:

$$\sin \vartheta = \frac{-\cos^2 \eta \cdot (R_M + \delta R) - \sqrt{-\sin^2 \eta \cdot [\cos^2 \eta \cdot (R_M + \delta R)^2 - R_M^2]}}{R_M} \quad \text{A-27}$$

Solution Region III: $\delta R > 0$ and $a < b$

The parametric form of the ellipse is in terms of its focus $c = \sqrt{b^2 - a^2}$, elliptical radius ξ and elliptical angle η , and can be described by:

$$x = c \cdot \cosh \xi \cdot \cos \eta, \quad y = c \cdot \sinh \xi \cdot \sin \eta \quad \text{A-28}$$

The elliptical perimeter is governed by $\xi_o = 0.5 \cdot \ln[(1 + \alpha_e)/(1 - \alpha_e)]$, with $\alpha_e = a/b$ and defined by $x = c \cdot \cosh \xi_o \cdot \cos \eta$ and $y = c \cdot \sinh \xi_o \cdot \sin \eta$. The parameters used in the PWF are listed in the following:

$$\begin{aligned}
Q &= (c \cdot \cosh \xi \cdot \cos \eta, c \cdot \sinh \xi \cdot \sin \eta) & \text{A-29} \\
Q' &= (c \cdot \cosh \xi_o \cdot \cos \eta_c, c \cdot \sinh \xi_o \cdot \sin \eta_c) \\
Q_R &= (c \cdot \cosh \xi_o \cdot \cos \eta, c \cdot \sinh \xi_o \cdot \sin \eta) \\
Q^* &= (c \cdot \cos \eta, 0) \\
\mathfrak{R} &= \ell_{Q_R Q^*} = c\sqrt{\mathcal{A}} \\
r &= \ell_{Q Q^*} = c\sqrt{\mathcal{B}} \\
\ell_{Q Q'} &= c\sqrt{\mathcal{P}} \\
y' &= \alpha_e \cdot c\sqrt{\cosh^2 \xi_o - \cosh^2 \xi \cdot \cos^2 \eta} \\
x' &= \frac{c}{\alpha_e} \sqrt{\sinh^2 \xi_o - \sinh^2 \xi \cdot \sin^2 \eta}
\end{aligned}$$

The integral in Equation A-13 becomes:

$$\begin{aligned}
K_{Q'} &= \sqrt{c} \int \int \frac{\sigma(\xi, \eta) \sqrt{\mathcal{A} - \mathcal{B}}}{\pi \sqrt{\pi \sqrt{\mathcal{A}} \cdot P}} \left[1 + \Pi_1 \sqrt{1 - \frac{\mathcal{B}}{\mathcal{A}}} + \Pi_2(\dots)^{2.2} + \Pi_3(\dots)^{1.5} \right] & \text{A-30} \\
&\cdot (\sin^2 \eta + \sinh^2 \xi) d\eta d\xi
\end{aligned}$$

The integration limits vary and are dictated by the following parameter:

$$\xi_{lower} = \sinh^{-1} \frac{R_M + \delta R + R_M \sin \vartheta}{c \cdot \sin \eta} \quad \text{A-31}$$

The value of $\sin \vartheta$ is related to geometric parameters and given by:

$$\sin \vartheta = \frac{-\cos^2 \eta \cdot (R_M + \delta R) - \sqrt{-\sin^2 \eta \cdot [\cos^2 \eta \cdot (R_M + \delta R)^2 + c^2 \cos^2 \eta - R_M^2]}}{R_M} \quad \text{A-32}$$

The integration in Equation A-30 can then be carried out as follows:

$$K_{Q'} = \sqrt{c} \left[\int_{\eta_o}^{\eta_c} \int_{\xi_{lower}}^{\xi_o} (\dots) d\xi d\eta + \int_{\eta_c}^{\pi - \eta_o} \int_{\xi_{lower}}^{\xi_o} (\dots) d\xi d\eta \right] \quad \text{A-33}$$

Solution Region IV: $\delta R = 0$ and $a < b$

The same parametric form for the ellipse in Solution Region III is deployed. The only changes are the usage of the degenerated forms of Equations A-31 and A-32 as a result of $\delta R = 0$. They are given by:

$$\xi_{lower} = \sinh^{-1} \frac{R_M + R_M \sin \vartheta}{c \cdot \sin \eta} \quad A-34$$

$$\sin \vartheta = \frac{-\cos^2 \eta \cdot R_M - \sqrt{-\sin^2 \eta \cdot [\cos^2 \eta \cdot R_M^2 + c^2 \cos^2 \eta - R_M^2]}}{R_M} \quad A-35$$

Carrying out the integration described in Equation A-33 determines the stress intensity factors at a - and c -tips.

Solution Region V: $\delta R < 0$ and $a < b$

The same parametric form for the ellipse in Solution Region III is deployed. Because it is possible that the cylinder can embody nearly the whole ellipse, the determination of integration limits becomes more involved. In the following, listed are parameters that the integration uses for the limits, where $d = |\delta R|$.

$$\sin \vartheta = \frac{\cos^2 \eta \cdot (d - R_M) - \sqrt{-\sin^2 \eta \cdot [\cos^2 \eta \cdot (R_M - d)^2 + c^2 \cos^2 \eta - R_M^2]}}{R_M} \quad A-36$$

$$\xi_{\delta} = \sinh^{-1} \frac{a \cdot \sin \eta_o}{c \cdot \sin \eta}$$

$$\vartheta_s = \sin^{-1} \frac{d - R_M}{R_M}$$

$$\eta_s = \cos^{-1} \frac{R_M \cos \vartheta_s}{c}$$

$$\xi_{lower} = \sinh^{-1} \frac{R_M - d + R_M \sin \vartheta}{c \cdot \sin \eta} = \xi_{upper}$$

In the above definition, η_s is always larger than η_o . The integration in Equation A-13 is then carried out as follows:

$$K_{Q'} = \sqrt{c} \left\{ \begin{array}{l} \left[\int_{\eta_o}^{\eta_c} \int_{\xi_\delta}^{\xi_o} (\dots) d\xi d\eta + \int_{\eta_c}^{\pi-\eta_o} \int_{\xi_\delta}^{\xi_o} (\dots) d\xi d\eta \right] + \\ \left[\int_{\eta_o}^{\eta_s} \int_{\xi_{lower}}^{\xi_\delta} (\dots) d\xi d\eta + \int_{\eta_s}^{\pi-\eta_s} \int_0^{\xi_\delta} (\dots) d\xi d\eta + \int_{\pi-\eta_s}^{\pi-\eta_o} \int_{\xi_{lower}}^{\xi_\delta} (\dots) d\xi d\eta \right] \\ \int_{-\pi+\eta_s}^{-\eta_s} \int_0^{\xi_{upper}} (\dots) d\xi d\eta \end{array} \right\} \quad \text{A-37}$$

The last integral in the above equation for SIFs requires some attentions for the scenario where the cylinder nearly embodies the whole ellipse and the value of ξ can become larger than the elliptical radius ξ_o (i.e., outside the ellipse). The revisions affect the fourth term with the coefficient Π_3 that invokes the determination of chordal length x' as well as the lengths with \mathfrak{R} (or ℓ_{QRQ^*}) and $\ell_{QQ'}$ appearing in the integrand of Equation A-12. The adjustments are applied only when $\xi_{upper} > \xi_o$ to ensure not to overflow the PWF during integration. The adjustments are listed in Table A-1.

Table A-1. Adjustments to some parameters for PWF integration in Solution Region V

Affected parameter or term	Related parameter	Adjustment
\mathcal{A}	\mathfrak{R} or ℓ_{QRQ^*}	$\cosh \xi_o$ replaced by $\cosh \xi_{upper}$
P	$\ell_{QQ'}$	$\cosh \xi_o$ replaced by $0.25 \cdot (\cosh \xi_{upper} - \cosh \xi_o) + \cosh \xi_o$ $\sinh \xi_o$ replaced by $0.25 \cdot (\sinh \xi_{upper} - \sinh \xi_o) + \sinh \xi_o$
Π_3 term		ξ replaced by $(\xi \cdot \xi_o / \xi_{upper})$

A.6 Verification

Some information on the verification efforts provided is also reported in Appendix B. We provide the full information on the verification efforts here because these efforts lead to modifications of the SC34 solution that improved its accuracy.

Initial verification

The reference stresses used to develop the reference solutions are in terms of three simple stress gradients. In connection to the coordinate system depicted in Figure A- 8, the gradients are given by:

$$\begin{aligned}\sigma_1(x, y) &= 1 & \text{A-38} \\ \sigma_2(x, y) &= \frac{y - \delta R}{a_m} \\ \sigma_3(x, y) &= \frac{x}{R_M \sin \vartheta_o}, \text{ where } \vartheta_o = \frac{c_m}{R_M}\end{aligned}$$

The last two gradients are selected to be linear to facilitate the development. Both result in zero stress values at the crack origin (not the center of the ellipse) and unit stress values at the vertexes. The anti-symmetric feature of the third reference stress σ_3 with respect to the y -axis is to facilitate the development of *true* bivariate formulation instead of *symmetric* bivariate formulation. For consistency, the verification confirms that using the reference stresses would retreat back to the reference solutions.

For further verification, more FE analyses were performed. The computation invoked applying more aggressive stress gradients over the crack surface. The functions describing the stress gradients are in terms of the following two normalized parameters relating to the specified crack depth and surface crack length.

$$\tilde{x} = \frac{x}{R_M \sin(\sin \vartheta_o)}, \text{ and } \tilde{y} = \frac{y - \delta R}{a_m} \quad \text{A-39}$$

In total, there are eight gradients and their definitions are given as follows:

$$\begin{aligned}\sigma_4(x, y) &= 1.5 \cdot \tilde{y}^2 - 0.5 & \text{A-40} \\ \sigma_5(x, y) &= 2.5 \cdot \tilde{y}^3 - 1.5 \cdot \tilde{y} \\ \sigma_6(x, y) &= 4.375 \cdot \tilde{y}^4 - 3.75 \cdot \tilde{y}^2 + 0.375 \\ \sigma_7(x, y) &= 7.875 \cdot \tilde{y}^5 - 8.75 \cdot \tilde{y}^3 + 1.875 \cdot \tilde{y} \\ \sigma_8(x, y) &= 1.5 \cdot \tilde{x}^2 - 0.5 \\ \sigma_9(x, y) &= 4.375 \cdot \tilde{x}^4 - 3.75 \cdot \tilde{x}^2 + 0.375 \\ \sigma_{10}(x, y) &= 2.5 \cdot \tilde{x}^3 - 1.5 \cdot \tilde{x} \\ \sigma_{11}(x, y) &= 7.875 \cdot \tilde{x}^5 - 8.75 \cdot \tilde{x}^3 + 1.875 \cdot \tilde{x}\end{aligned}$$

The variations from σ_4 to σ_7 are essentially identical to those from σ_8 to σ_{11} (except the switch between σ_9 and σ_{10}) in relation to normalized parameters. Figure A- 9 is provided to depict the variation for σ_4 to σ_7 or σ_8 , σ_{10} , σ_9 , and σ_{11} , respectively. The label of the abscissa denotes the normalized parameters as $x_{norm} = \tilde{x}$ and $y_{norm} = \tilde{y}$.

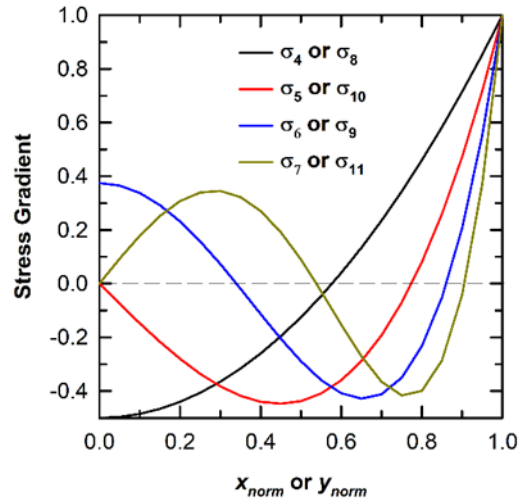
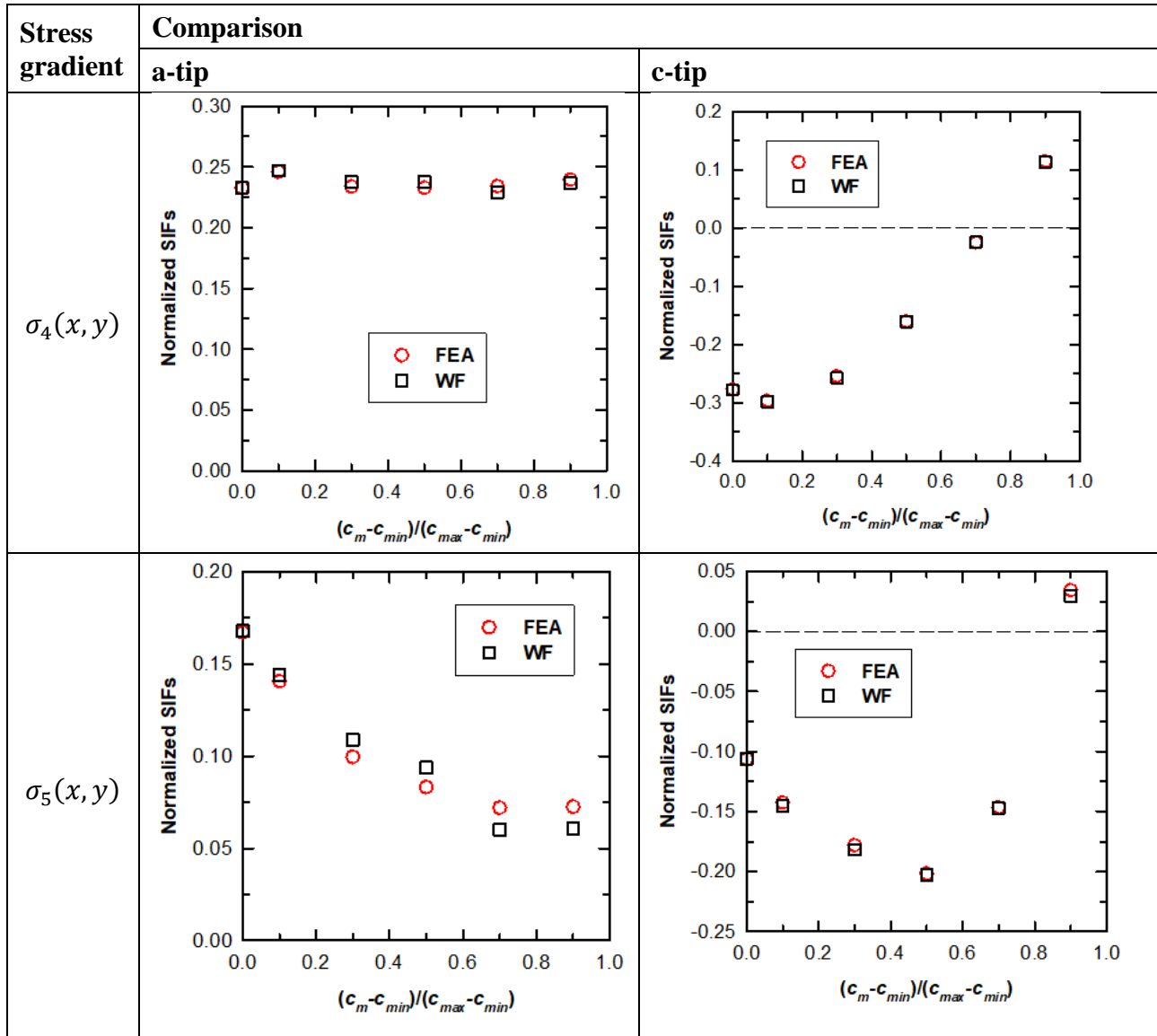
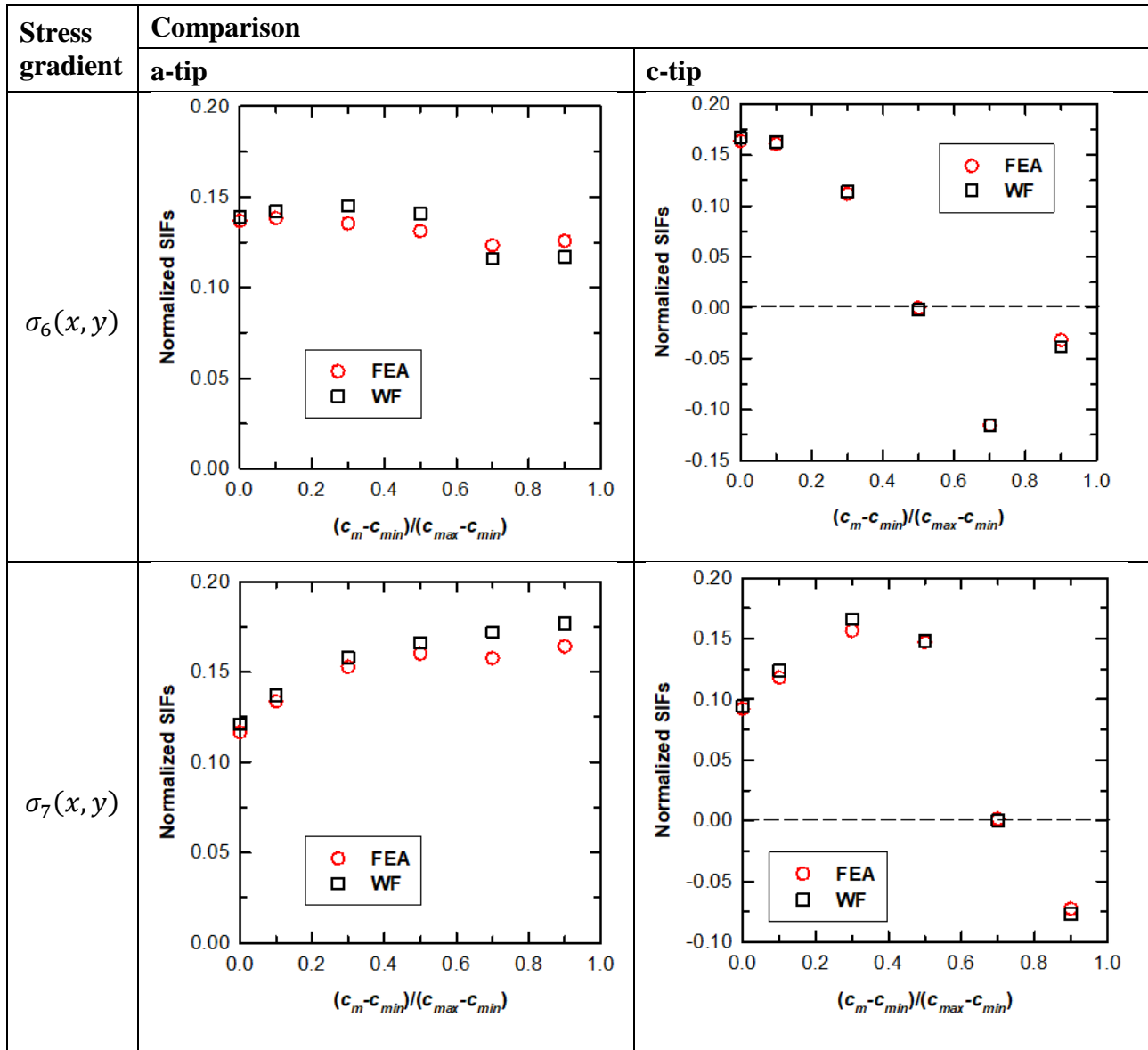


Figure A- 9. Variations of stress functions used for verification

Table A- 2 presents the comparison of the FE results against the results from WF formulation for SC34. The normalization factor for the ordinate is $\sqrt{\pi a_m}$. The specific geometric dimensions are $D_M/t = 4$ and $a_m/t = 0.1$. Only the results from σ_4 to σ_7 (gradients along the crack depth direction) are displayed. The comparison shows the WF approach captures most of the salient features in SIF variations and its results are in very good agreement with those using FE.

Table A- 2. Comparison of FE and WF results for SC34





Formal verification

Formal verification follows the procedure developed during earlier efforts to quantify uncertainty in SIF solutions (*i.e.*, for elliptical and part-elliptical cracks in rectangular cross-sections). The verification process involves semi-randomly sampling geometries from the solution space using the Latin Hypercube Sampling (LHS) methodology to create a space-filling design of experiment. In this work, we selected 500 geometries from the geometric parameters as follows:

$$0.05 \leq \frac{a_m}{t} \leq 0.9 \quad \text{A-41}$$

$$0.25 \leq \frac{a_m}{c_m} \leq 2 \quad \text{A-42}$$

$$4 \leq \frac{D}{t} \leq 256 \quad \text{A-43}$$

These geometries span the range of cracks, crack shapes, and shafts/casings relevant to practical engineering assessments. These geometries do not include very elongated crack shapes ($a_m/c_m < 0.25$). While such elongated cracks may be initially present, these crack shapes are not stable, and the crack rapidly advances into the more stable shapes investigated here.

During the LHS process, we sample a_m/c_m in \log_2 space. This log scaling ensures that LHS roughly provides the same number of points between $0.25 \leq a_m/c_m \leq 0.5$, $0.5 \leq a_m/c_m \leq 1$, and $1 \leq a_m/c_m \leq 2$. Linear scaling on a_m/c_m would sample about 33% more points in $1 \leq a_m/c_m \leq 2$ vs. $0.25 \leq a_m/c_m \leq 1$. Lower ratios of a_m/c_m develop more frequently in preliminary fatigue crack growth analyses using SC34, and the linear sampling is less desirable as a result. Similar reasoning led us to sample D/t over \log_4 space to capture thicker shafts in the analysis rather than focus on very thin casings.

This work selected two loadings relevant for shafts/casings. The loading S_0 represents a uniform tension load applied normal to the cross-sectional area. The loading S_1 represents a linear-bending load with decreasing stresses in the direction of crack advance.

SC34 was also integrated into version 9.2 of NASGRO[®]. This implementation of SC34 is identical to the implementation in DARWIN. Consequently, verification was performed using NASGRO rather than DARWIN since it requires considerably less effort to generate large numbers of SIF results with NASGRO than with DARWIN. However, results using DARWIN would be identical to those obtained from NASGRO.

Formal verification was accelerated by the Python scripting capability developed to build FEAs that define the reference solution matrix. Here, we initiated the scripting process with new inputs from the LHS process and the relevant applied stresses. This process built new FEA input files, extracted results, and processed output SIF values.

This investigation defines relative error (%) as:

$$4 \leq \frac{D}{t} \leq 256 \quad \text{A-44}$$

Here, F is the geometry correction factor computed either by DARWIN (F_{DARWIN}) or by the FEA (F_{FEA}). The geometry correction factor provides a normalized value for the SIF as follows:

$$F = \frac{K_I}{S \times \sqrt{\pi a_m}} \quad \text{A-45}$$

Here, S represents the normalized stress magnitude (S_0 or S_1). The SIF value can be from either the a_m -tip or the c_m -tip. Consequently, this work examines four geometry corrections factors:

- F_0^a – geometry correction factor at a_m -tip for S_0 loading;
- F_1^a – geometry correction factor at a_m -tip for S_1 loading;
- F_0^c – geometry correction factor at c_m -tip for S_0 loading; and
- F_1^c – geometry correction factor at c_m -tip for S_1 loading.

Figure A- 10 shows the formal verification results for the initial implementation of SC34. This figure shows relative error as function of geometry (a_m/t , a_m/c_m , and D/t), as a function of F , and as probability distribution functions (PDF) or cumulative distribution functions (CDF) that visualize overall error. Each subfigure shows relative error for the four geometry correction factors of interest. Table A- 3 provides statistics of the relative error in Figure A- 10(f).

Table A- 3. Relative error (%) statistics for initial implementation of SC34

SIF	min	1%	5%	10%	25%	50%	75%	90%	95%	99%	max
F_0^a	-22.09	-15.91	-7.46	-3.94	-0.71	-0.14	0.37	0.78	1.09	1.63	2.66
F_1^a	-22.08	-15.89	-7.44	-3.89	-0.68	-0.07	0.45	0.87	1.13	1.83	2.87
F_0^c	-14.15	-12.14	-9.19	-6.11	-2.27	-0.89	0.06	1.52	2.94	6.83	16.56
F_1^c	-14.14	-12.13	-9.15	-6.04	-2.17	-0.65	0.21	1.72	3.11	6.89	16.69

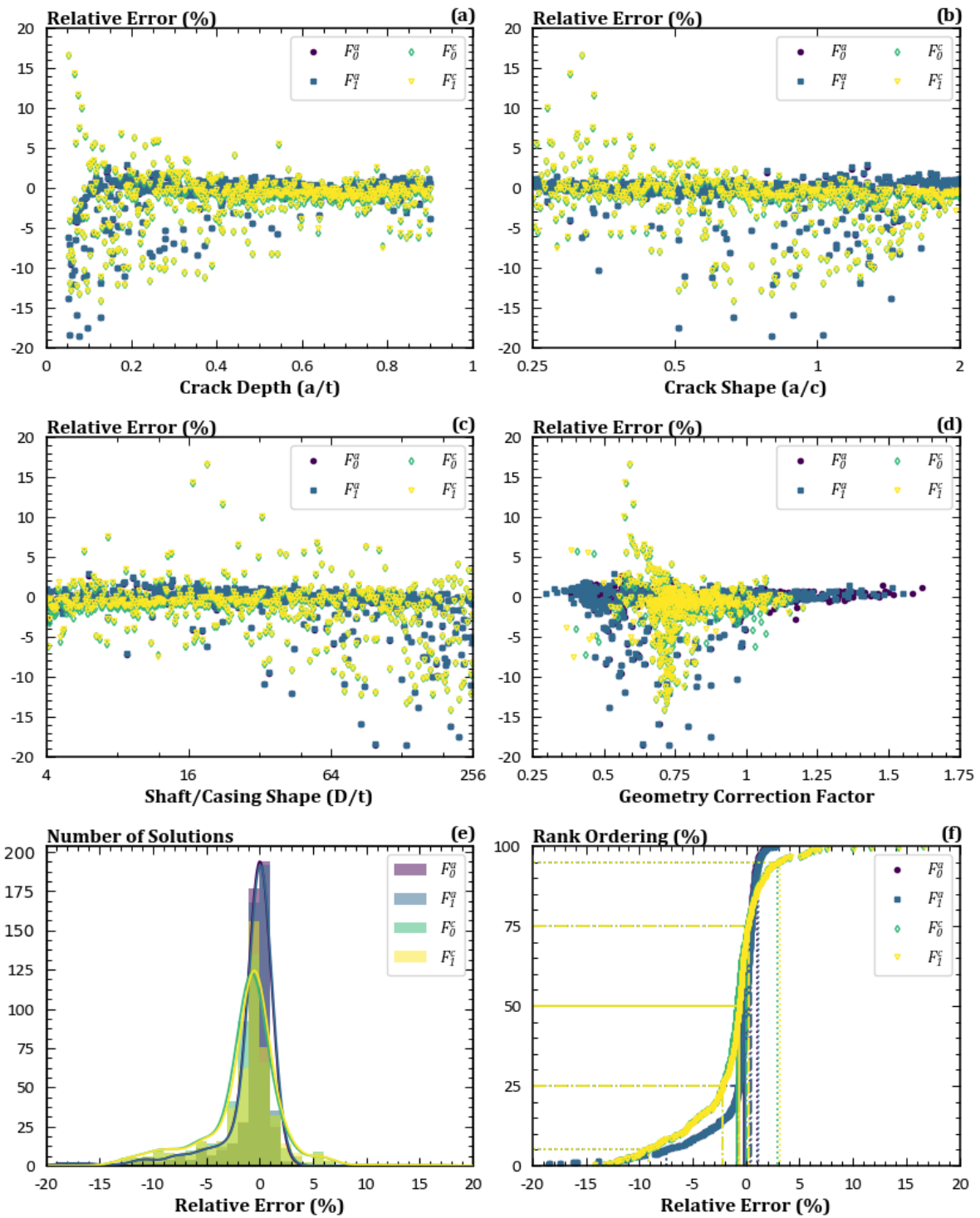


Figure A- 10. Formal verification results for initial implementation of SC34

These results indicate the following:

- SIFs had more error variability than desired in a SIF WF solution. SIFs at the a_m -tip had large non-conservative errors. SIFs at the c_m -tip featured larger error variability. Median error values were less than 1%, though they tended to be non-conservative.
- These errors were not isolated to small F -values that would have suggested potential precision issues. Instead, error magnitudes tended to decrease as $F \rightarrow 0$.
- Errors showed dependence on the geometry. Errors showed a strong dependence on a_m/c_m and a_m/t . Errors were less dependent on D/t .
- Loading effects on errors were negligible. For large D/t ratios, differences between geometry correction factors became increasingly small due to limited variation on crack plane stress from uniform tension and remote bending.

After reviewing this information, we discovered that these errors reflected the sparsity of the reference solution matrix. Consequently, we enhanced the solution matrix as follows:

$$\frac{a_m}{t} = 0.1, 0.3, 0.5, 0.7, 0.9 \quad \text{A-46}$$

$$\frac{c_m - c_{min}}{c_{max} - c_{min}} = 0, 0.04, 0.1, 0.3, 0.5, 0.7, 0.9$$

$$\frac{D_M}{t} = 4, 8, 16, 32, 64, 128, 256$$

The value of $(c_m - c_{min})/(c_{max} - c_{min}) = 0.04$ represents a new geometry added to the solution matrix to improve the accuracy of SC34. This new value required an additional 35 FEAs to determine the relevant SIFs. These SIF values were then added to the WF formulation, integrated into NASGRO, and released for testing.

Figure A- 11 shows the formal verification results for the second implementation of SC34 with an enhanced reference solution matrix. This figure shows the same relative error plots provided in Figure A- 10. Table A- 4 provides statistics of the relative error in Figure A- 11(f).

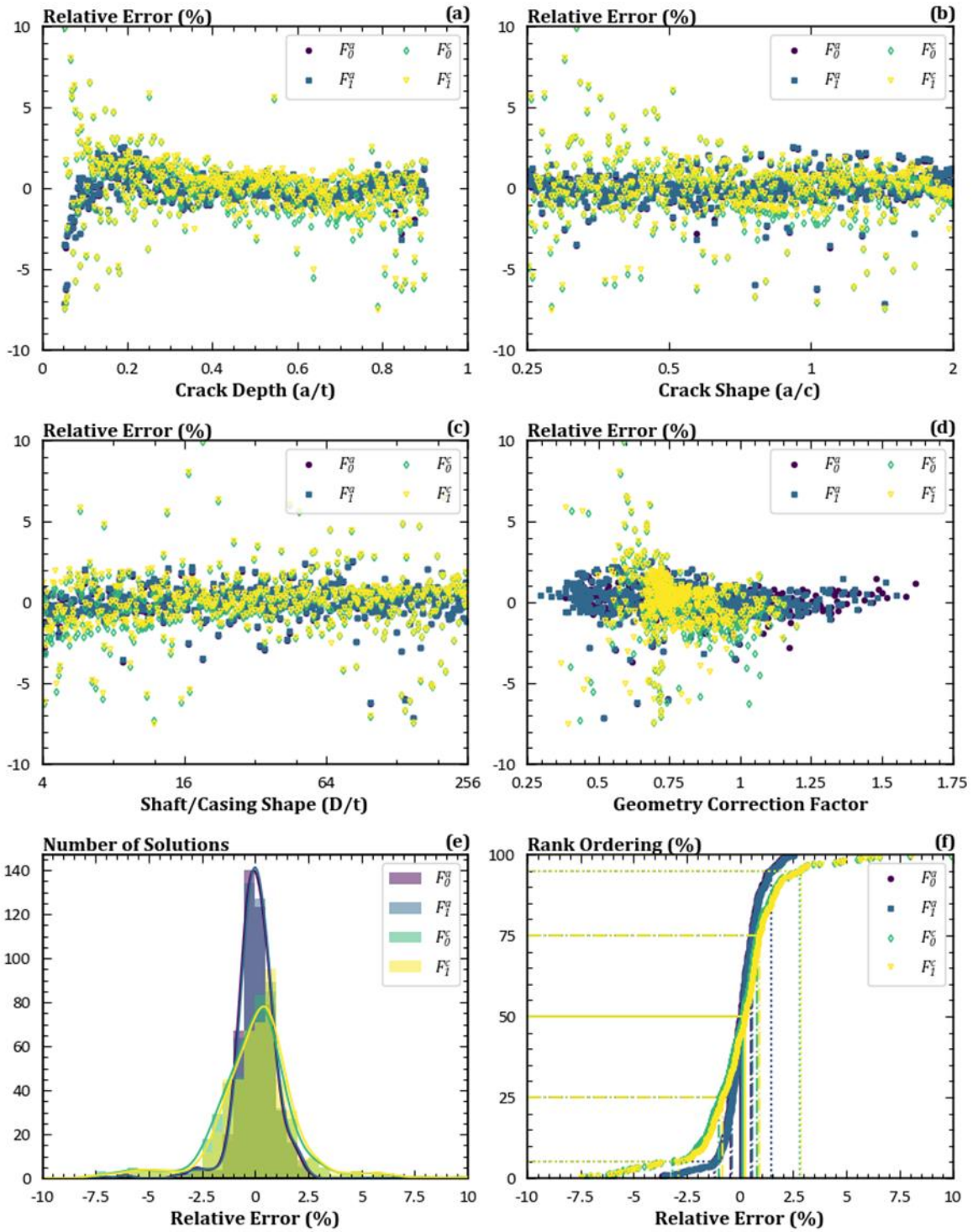


Figure A- 11. Formal verification results for second implementation of SC34 with enhanced reference solution matrix

Table A- 4. Relative error (%) statistics for second implementation of SC34 with enhanced reference solution matrix

SIF	min	1%	5%	10%	25%	50%	75%	90%	95%	99%	max
F_0^a	-7.14	-3.01	-1.24	-0.84	-0.45	0.04	0.53	1.01	1.45	2.06	2.53
F_1^a	-7.12	-3.15	-1.17	-0.82	-0.37	0.09	0.57	1.11	1.48	2.11	2.55
F_0^c	-7.43	-6.21	-3.17	-1.99	-0.97	0.13	0.79	1.66	2.82	6.03	10.58
F_1^c	-7.51	-6.12	-2.88	-1.65	-0.81	0.25	0.91	1.78	2.84	6.12	10.59

These results indicate the following:

- Adding the additional point to the solution improved the accuracy of the solution. For example, the error bounds in Figure A- 11 are -10% to +10%. In Figure A- 10, these error bounds were 20% to +20%. Furthermore, the new set of reference solutions eliminated the non-conservative bias of solutions at the a_m -tip. Solutions at c_m -tip continued to show more variability than solutions at the a_m -tip, but it was more limited using the enhanced reference matrix solution.
- The variability of error with a_m/c_m was reduced by the enhanced reference solution matrix. It was no longer the major source of solution error in SC34.
- While errors are limited, there was a trend towards increasing error magnitudes as $a_m/t \rightarrow 0$. This trend leads to non-conservative errors at the a_m -tip and large error magnitudes at the c_m -tip.

Increasing errors as $a_m/t \rightarrow 0$ suggest potentially large life prediction errors for small cracks. Small cracks often represent the majority of fatigue crack growth lives. Furthermore, non-conservative errors at the a_m -tip for small a_m values may lead to threshold effects that would halt predicted crack growth rates while real crack growth continued.

Consequently, SC34 was modified again to support crack growth for small cracks. SC34 features an additional reference solution if $a_m/t < 0.1$. This solution is derived from the SC31 SIF solution with a fixed value of $2c/W$. However, this solution was recast in terms of the same parameters that define the SC34 reference solution. SC34 for $a_m/t > 0.1$ is unchanged from the previous implementation. After adding this capability, it was integrated into SC34 in NASGRO, and the updated version of NASGRO was employed to re-calculate the SIFs for SC34.

Figure A-12 shows the formal verification results for the final implementation of SC34 with an enhanced reference solution matrix and support for small cracks. This figure shows the same

relative error plots provided in Figure A- 10. Table A- 5 provides statistics of the relative error in Figure A- 12(f).

Table A- 5. Relative error (%) statistics for final implementation of SC34 with enhanced reference solution matrix and support for small cracks

SIF	min	1%	5%	10%	25%	50%	75%	90%	95%	99%	max
F_0^a	-2.78	-1.32	-0.93	-0.71	-0.38	0.10	0.60	1.24	1.92	2.53	3.21
F_1^a	-3.14	-1.29	-0.92	-0.67	-0.31	0.17	0.66	1.31	2.05	2.57	3.22
F_0^c	-7.27	-5.79	-2.61	-1.97	-1.06	0.07	0.70	1.48	2.01	4.43	6.57
F_1^c	-7.51	-5.61	-2.47	-1.69	-0.90	0.17	0.84	1.64	2.14	4.47	6.58

These results represent the final error metrics for SC34. The extrapolation procedure eliminated the increasing error trends as $a_m/t \rightarrow 0$ shown in Figure A- 11. The small crack support also reduced errors at both the a_m -tip and the c_m -tip. These results indicate that errors never exceed 3.2% at the a_m -tip. At the c_m -tip, errors never exceed 7.5%. Most SC34 solutions are much closer to the FEA results than suggested by the minimum and maximum values shown here. For the a_m -tip, more than 90% of the solutions are between -0.93% and 2.05% of the FEA value. For the c_m -tip, more than 90% of the solutions are between -2.6% and 2.14% of the FEA value. The median values indicate a slight conservatism in the overall solution.

The final implementation of SC34 was integrated into the production version of DARWIN 9.3/9.4. Earlier implementations of SC34 of DARWIN were only included in alpha and beta codes not intended for production use.

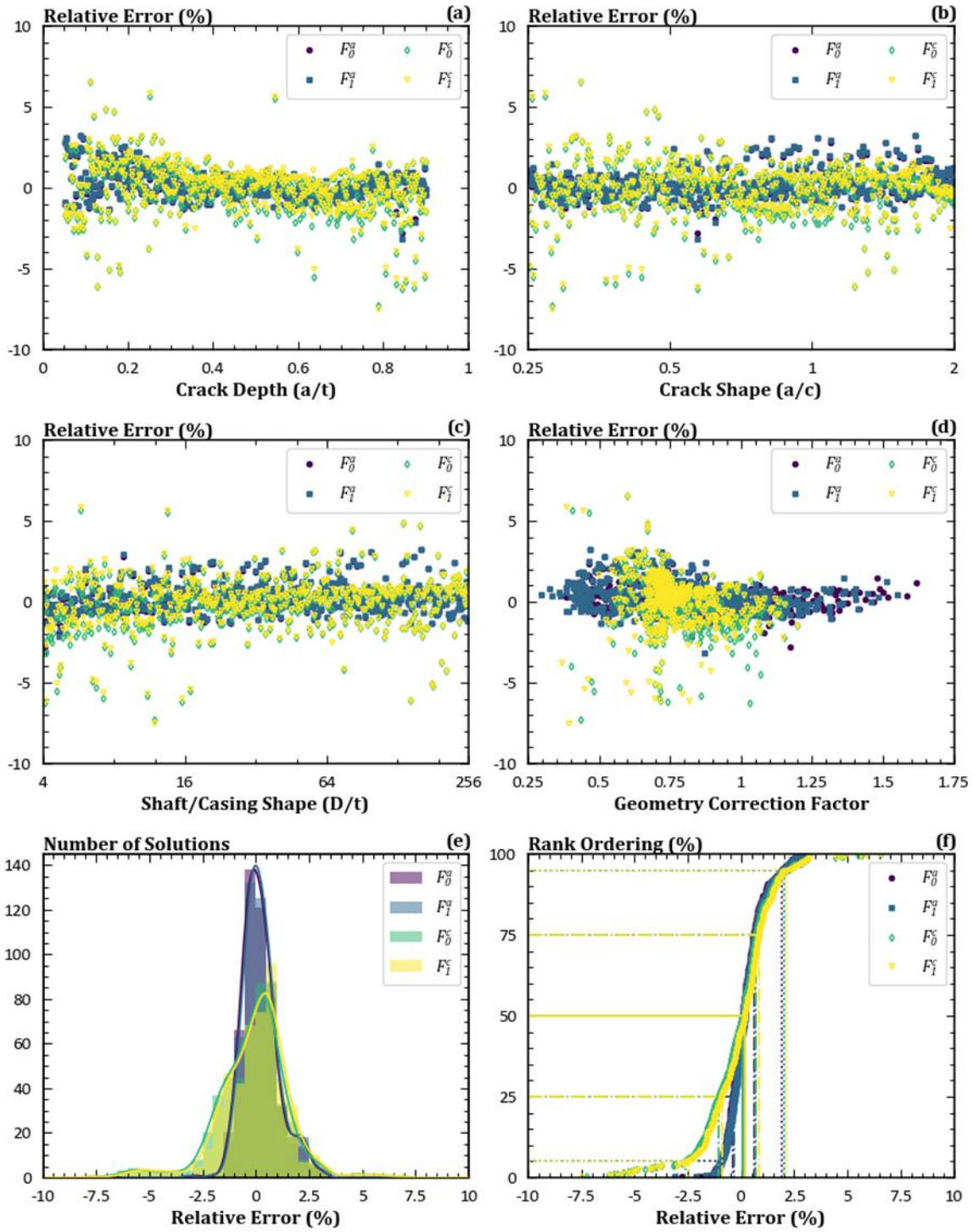


Figure A- 12. Formal verification results for final implementation of SC34 with enhanced reference solution matrix and support for small cracks

References

Federal Aviation Administration. (July, 2009). *Guidance material for aircraft engine life-limited parts requirements*. Advisory Circular 33.70-1. Retrieved from https://www.faa.gov/documentLibrary/media/Advisory_Circular/AC_33_70-1.pdf

B SIF solution verification

List of Figures

Figure B- 1. Illustration of the corner crack mesh and crack tube for the FEAs	B-10
Figure B- 2. Credibility of FEA SIF solutions using exact analytical solution by Irwin	B-13
Figure B- 3. Comparison of independent Abaqus SIF solutions to Newman-Raju solutions ..	B-16
Figure B- 4. Core DARWIN SIF solution geometries for corner, surface, and embedded cracksB-	17
Figure B- 5. Verification approach comparing weight function SIFs against FEA SIFs	B-18
Figure B- 6. Finite element geometric features in a corner crack solution.....	B-20
Figure B- 7. CC11 geometry correction factors vs. Abaqus.....	B-23
Figure B- 8. Histogram of CC11 SIFs vs. Abaqus SIFs	B-24
Figure B- 9. Rank ordering of CC11 SIFs vs. Abaqus SIFs	B-24
Figure B- 10. CC09 geometry correction factors vs. Abaqus.....	B-26
Figure B- 11. Histogram of CC09 SIFs vs. Abaqus SIFs	B-27
Figure B- 12. Rank ordering of CC09 SIFs vs. Abaqus SIFs	B-27
Figure B- 13. SC30 (a-tip) geometry correction factors vs. Abaqus	B-29
Figure B- 14. SC30 (c-tip) geometry correction factors vs. Abaqus	B-30
Figure B- 15. SC30 (c1-tip) geometry correction factors vs. Abaqus	B-30
Figure B- 16. Histogram of SC30 SIFs vs. Abaqus SIFs.....	B-31
Figure B- 17. Rank ordering of SC30 SIFs vs. Abaqus SIFs	B-31
Figure B- 18. SC31 (a-tip) geometry correction factors vs. Abaqus	B-34
Figure B- 19. SC31 (c-tip) geometry correction factors vs. Abaqus	B-34
Figure B- 20. SC31 (c1-tip) geometry correction factors vs. Abaqus	B-35
Figure B- 21. Histogram of SC31 SIFs vs. Abaqus SIFs.....	B-35
Figure B- 22. Rank ordering of SC31 SIFs vs. Abaqus SIFs	B-36
Figure B- 23. EC05 (a-tip) geometry correction factors vs. Abaqus	B-38
Figure B- 24. EC05 (a1-tip) geometry correction factors vs. Abaqus	B-38
Figure B- 25. EC05 (c-tip) geometry correction factors vs. Abaqus	B-39
Figure B- 26. EC05 geometry correction factors vs. Abaqus (cont)	B-39
Figure B- 27. Histogram of EC05 SIFs vs. Abaqus SIFs	B-40
Figure B- 28. Rank ordering of EC05 SIFs vs. Abaqus SIFs	B-40
Figure B- 29. EC04 (a-tip) geometry correction factors vs. Abaqus	B-43
Figure B- 30. EC04 (a1-tip) geometry correction factors vs. Abaqus	B-43

Figure B- 31. EC04 (c-tip) geometry correction factors vs. Abaqus	B-44
Figure B- 32. EC04 (c1-tip) geometry correction factors vs. Abaqus	B-44
Figure B- 33. Histogram of EC04 SIFs vs. Abaqus SIFs	B-45
Figure B- 34. Rank ordering of EC04 SIFs vs. Abaqus SIFs.	B-45
Figure B- 35. Geometry of a quarter-elliptical corner crack at a hole offset in a plate	B-47
Figure B- 36. Geometries selected for this verification study by the LHS method.....	B-48
Figure B- 37. Relative error metrics for CC08 geometry correction factors	B-51
Figure B- 38. Relative error metrics for CC10 geometry correction factors	B-53
Figure B- 39. Relative error metrics for CC26 geometry correction factors	B-55
Figure B- 40. Geometric correction factors at the a -tip for CC10 as a function of crack length .	B-56
Figure B- 41. Geometric correction factors at the c -tip for CC10 as a function of crack length .	B-57
Figure B- 42. Geometry of CC12 - a corner crack spanning a chamfer in a plate	B-58
Figure B- 43. Mises stress in the crack region for three crack plane loadings	B-59
Figure B- 44. Relative error plots of CC12 under S_0 loading at the a -tip (left) and c -tip (right)	B-60
Figure B- 45. Relative error plots of CC12 under $S\xi$ loading at the a -tip (left) and c -tip (right).	B-60
Figure B- 46. Relative error plots of CC12 under $S\eta$ loading at the a -tip (left) and c -tip (right)	B-61
Figure B- 47. Geometric parameterization of SC34	B-62
Figure B- 48. Formal verification results for SC34	B-64

List of Tables

Table B- 1. Geometric parameters for the Newman-Raju solution verification sampling by LHS	B-14
Table B- 2. Minimum and maximum dimensions of the crack tip solution CC11 and the FEA models	B-21
Table B- 3. Traction gradients applied to corner cracks in verification study.....	B-22
Table B- 4. Minimum and maximum dimensions of the crack tip solution CC09 and the FEA models	B-25
Table B- 5. Traction gradients applied to corner cracks in verification study.....	B-25
Table B- 6. Minimum and maximum dimensions of the crack tip solution SC30 and the FEA models	B-28

Table B- 7. Traction gradients applied to surface cracks in verification study	B-28
Table B- 8. Minimum and maximum dimensions of the crack tip solution SC31 and the FEA models	B-32
Table B- 9. Traction gradients applied to surface cracks in verification study	B-32
Table B- 10. Minimum and maximum dimensions of the crack tip solution EC05 and FEA models	B-37
Table B- 11. Traction gradients applied to surface cracks in verification study	B-37
Table B- 12. Minimum and maximum dimensions of the crack tip solution EC04 and the FEA models	B-41
Table B- 13. Traction gradients applied to surface cracks in verification study	B-41
Table B- 14. Stresses applied during FEA of corner crack at a hole by step time	B-50
Table B- 15. Relative error (%) statistics for the final implementation of SC34 with an enhanced reference solution matrix and support for small cracks	B-65

B.1 Introduction

This document summarizes efforts during the PIRATE-2 grant to verify the accuracy of stress intensity factor (SIF) solutions used in DARWIN for fatigue crack growth (FCG) life predictions. In the aerospace industry, the reliability of engines and airframes is often maintained by damage tolerance approaches that in turn depend on SIF solutions (McClung, Lee, Cardinal, & Guo, 2013). Under the conditions of linear-elastic fracture mechanics, the SIF solution relates the geometry, crack front, and applied far-field loading to the driving force for FCG (e.g., by the Paris equation) and final fracture (e.g., when the SIF value exceeds the material toughness). Small errors in the SIF solutions may lead to more significant errors in FCG life predictions, since the crack growth rate is usually proportional to the SIF value raised to some power. For example, many metallic alloys have a Paris exponent on the order of three to four, and sustained errors in the SIF solutions on the order of 10% may lead to incorrect life predictions on the order of 30%-50%.

Unfortunately, most relevant crack geometries are not tractable with analytical methods, i.e., solving the relevant partial differential equations in their strong form with a finite number of terms. Classical handbooks (Tada, Paris, & Irwin, 1973) concentrate on through-thickness cracks in 2D geometries, and they provide few exact SIF solutions for 3D cracks, despite the dominance of these configurations in practical engineering applications. The few analytical solutions for 3D cracks typically address cracks in infinite bodies that lack interactions with nearby free surfaces.

Instead, most researchers have developed 3D SIF solutions using numerical methods (e.g., finite element analysis – FEA) to determine near-front stresses, strains, and displacements. These near-front stresses, strains, and displacements then drive various numerical techniques (Nikishkov & Atluri, 1987; Shivakumar, Tan, & Newman, 1988; Barsoum, 1976) that compute SIF values along the crack front, although most FCG life calculation methods employ only two to four specific locations around the crack front. This approach provides SIF values for one specific geometry and loading, and many such numerical analyses are required to build a potentially large SIF database with a range of geometric parameters and applied loading conditions (Fawaz & Andersson, 2004; Fawaz, 1999; Fawaz, 1998).

For example, the SIF database for a corner crack at a hole by Fawaz and Anderson (2004) includes 226,875 SIF solutions at various geometries and loadings. SIF solutions that are incorporated into FCG software (e.g., DARWIN[®] or NASGRO[®]) often include interpolation routines to map results at geometries with known solutions to other geometries.

While direct interpolation of the SIF database remains a popular option, certain geometries support the development of weight function (WF) SIF solutions Rice (1972). WFs are integral kernel functions (a type of Green's function) that take as input stresses from the uncracked geometry over the crack front area to produce a SIF value. WFs enable the SIF to be computed for a wide variety of loading conditions since they only require stresses from the corresponding uncracked geometry. Many DARWIN WF solutions have been derived using semi-analytical approaches (Shen & Glinka, 1991; Glinka & Shen, 1991; Lee, McClung, & Chell, 2008). The SIF database informs parameters that define the WF in the semi-analytical approach. In the current implementation, the numerical SIF solution interpolates these parameters over the defined geometric space.

Several methods have been proposed to verify SIF solutions defined by WFs. In one common approach (John, Kaldon, Johnson, & Coker, 1995; Wang & Lambert, 1997). WFs are first calibrated at a series of discrete geometries from SIF values driven by stresses defined by low-order polynomials. Then, the WFs are compared against SIF values driven by stresses defined by higher-order polynomials. Often, this approach employs the same meshes for calibration and verification. A different approach (Ferahi & Meguid, 1998) involves employing legacy solutions of high fidelity as benchmark results. Wu (2019) proposed a point-by-point comparison of WF solutions for the special case of a SIF under a pair of point loads. However, this approach does not support 3D geometries since this approach requires Green's functions for cracks in finite bodies, which are not available.

In this work, we develop new methodologies to verify existing WF SIF solutions in popular FCG software packages, DARWIN and NASGRO. Due to the constraints of 3D SIF solutions, this methodology necessarily features code-to-code comparisons between WF SIF solutions and independent FEA SIF solutions. Code-to-code comparisons introduce additional uncertainty, and we acknowledge this uncertainty by developing distributions of error characterized by a credibility measure. These distributions have been developed by semi-randomly sampling from the solution space of the WF SIF solutions and then determining the ratio of the WF SIF solution to the FEA SIF solution at the appropriate tips. Each comparison provides one point in the distribution. By accumulating many points, we build up a semi-discrete distribution that characterizes error for the WF solution space. In the remainder of this appendix, we describe the verification framework, detail FEAs produced by an automated scripting framework, verify these FEAs against analytical and legacy solutions, apply this verification framework to existing WF SIF solutions employed by the aerospace industry, and then summarize our results.

B.2 Verification framework

Overview of design of experiment

The WF methodology supports two fundamentally different types of degrees of freedom: variation of the geometry and variation of the applied stresses. Both types of degrees of freedom have an infinite number of potential solutions that must be reduced to a limited number.

For a geometry characterized by N independent geometric dimensions, the Buckingham Pi theorem indicates that only $N - 1$ non-geometric ratios are needed to describe the geometry and the normalized linear-elastic response. For example, if a geometry can be described by the crack length (a) and the plate thickness (t), then the ratio of these dimensions (a/t) sets the geometry correction factor defined as:

$$F_I = \frac{K_I}{\sigma\sqrt{\pi a}} \quad (\text{B-1})$$

K_I represents the mode I SIF, σ is some measure of the applied stress, and a indicates a crack dimension. Non-dimensional parameters that drive F_I -values are assumed to be continuous over some range and thus impossible to verify for all possible real numbers in the solution range.

Consequently, we select a series of discrete points within the solution space. Traditional experiment design (e.g., a fractional factorial design) approaches become rapidly intractable due to the exponential increase of the solution size as the number of variables increase. Instead, we adopt a modified Latin Hypercube Sampling (LHS) technique to design the experiment (McKay, Beckman, & Conover, 1979; Simpson, Lin, & Chen, 2001). LHS is a statistical method to generate a design space. It iteratively positions points to cover as much space as possible while ensuring that each sample lies on a separate hyperplane. The number of LHS points can be tailored to the computational budget of the verification program. Finally, LHS supports an iterative process to reduce the correlation of geometric parameters.

The current scheme allows LHS to operate over uniform intervals of the geometric ratios. However, this scheme can lead to geometries with inappropriate dimensions that are not relevant for practical FCG calculations. For example, WF solutions presented here idealize the cross-section as a rectangular “plate” defined by a width and thickness dimension. This issue can be treated in one of two ways. First, sampled geometries can be excluded from the verification matrix if the dependent geometries exceed some threshold. For example in plate geometries, the width-to-thickness (or vice-versa) ratio can exceed values of ten since this ratio is a derived ratio from the set of sampled geometric ratios. These plates are excessively skinny and do not provide

a reasonable geometry for our expected use case. Consequently, they can be removed from the solution space. Alternatively, limits for dependent geometry can be embedded within an independent variable using a third variable that is distinct from the combined variables. This approach requires some degree of effort as the required non-dimensional variables may not be readily apparent. However, it leads to a more uniform sampling of the geometries.

Stress gradients input to the WF provide the second major solution parameter. We characterize stress gradients as functions of one dimension (for univariant WFs) or two dimensions (for bivariant WFs). Again, there are an infinite number of these functions, similar to the geometry. However, most engineering structures have stress gradients that can be readily decomposed into a few low-level polynomial functions. Consequently, the stresses input to the WFs and applied to the FEAs involve polynomials of the fourth order or less, as will be shown in the following results.

Credibility measure

Verification requires some quantifiable measure of the goodness of the solution (Oberkampf, Trucano, & Hirsch, 2004; Oberkampf & Roy, 2010) that we will denote as the credibility measure. For the same nominal geometry and loading, we can define our credibility measure (C) as the ratio of the predicted geometry correction factor from the WF (F_I^{WF}) to the actual geometry correction factor from the FEA (F_I^{FEA}), *i.e.*:

$$C = \frac{F_I^{WF}}{F_I^{FEA}} \quad (B-2)$$

The credibility measure C in Equation (B-2) is a non-dimensional quantity that approaches unity as the actual solution approaches the predicted solution. Conservative values of the actual solutions lead to C -values greater than one, while non-conservative solutions lead to C -values less than one. This credibility measure provides a local measure at discrete locations along the crack front, in this case the crack tips defined for the WF's. Implicitly, C assumes that F_I^{WF} and F_I^{FEA} have the same precision and may have problems as $F_I^{FEA} \rightarrow 0$. Alternatively, the credibility measure can be defined as a percent error. Here, a solution matches the FEA result at a percent error of one. The credibility measure C in Equation (B-2) can be mapped onto a percent error measure by subtracting one from its value and converting to a percentage.

It is important to recognize the drawbacks of the code-to-code comparison performed here and how these drawbacks limit credibility. Specifically, we never calculate the analytical SIF solution from mechanics first principles, although that would be ideal. Instead, the FEAs produce

an estimate for the geometry correction factor with some built-in error while the WFs have their own built-in error. Let F_I^{ACT} represent the actual solution of the geometry correction factor that could be computed analytically, and let us define the following expressions for various errors between the test code (F_I^{WF}), the benchmark code (F_I^{FEA}), and the actual solution:

$$\delta_{TB} = |F_I^{WF} - F_I^{FEA}| \quad (B-3)$$

$$\delta_{BA} = |F_I^{FEA} - F_I^{ACT}| \quad (B-4)$$

$$\delta_{TA} = |F_I^{WF} - F_I^{ACT}| \quad (B-5)$$

where Equation (B-3) provides the error computed by the code-to-code comparison; Equation (B-4) indicates the error indicated by select comparison studies of the benchmark code to actual solutions; and Equation (B-5) indicates the desired error that indicates how good the test code is relative to the exact solution. The errors in Equations (B-3)-(B-4) may be used to provide a bound for error in Equation (B-5) using the triangle inequalities, *i.e.*,

$$||\delta_{TB}| - |\delta_{BA}|| \leq |\delta_{TA}| \leq |\delta_{TB}| + |\delta_{BA}| \quad (B-6)$$

Equation (B-6) states that the range of error for δ_{TA} is controlled by the error from δ_{TB} and δ_{BA} . The errors are linked. Driving down one error (e.g., δ_{TB}) will drive down the maximum error bound of δ_{TA} , but it will increase the minimum error bound of δ_{TA} if δ_{BA} does not decrease simultaneously. The following sections provide some metrics for the range of errors in the benchmark solutions and in the test code solutions, δ_{TB} .

Discussion

The remainder of this work focuses on one particular error metric: the rank ordering of the credibility measure C . For one crack-tip (e.g., the a -tip), we determine C for every geometry and loading combination from the FEA and the particular WF, e.g., CC11. These C -values are then sorted into ascending order and normalized by the number of these solutions plus one. The resulting rank ordering plot then forms a cumulative-distribution function (CDF) that indicates the credibility of the solution. The subsequent figures illustrate the median value and extreme (5% / 95%) values of C for each solution. These figures provide a data-rich measure of the credibility of the solutions. However, several other types of figures created by the authors are generally not shown in this work.

Histogram plots of the credibility measure show the number of discrete solutions that are within some credibility measure. They provide a discrete probability distribution function (PDF) that is the derivative of the CDF.

Scatter plots of the predicted solution vs. the actual solution in real space qualitatively demonstrate the credibility of the solutions. Poor solutions have many-to-most points far from the one-to-one line that indicates an exact solution, while good solutions have many-to-most points on or near this one-to-one line. These figures can be made more quantitative by plotting the straight reference lines that show bias. For example, the conservative 25% bias line shows the set of all predicted solutions that are 25% higher than the actual solutions. This line may be plotted as $P = 1.25 \times A$, where P and A provide the predicted and actual values respectively. These lines should be plotted to ensure symmetric bias about the one-to-one line, *i.e.*, the non-conservative bias line is $P = 0.8 \times A$ in a plot with equal length axes; it is not $P = 0.75 \times A$. These bias lines form wedges, and all solutions within these wedges are within the same level of bias.

Scatter plots of the predicted solution vs. the actual solution in some mapped bias space eliminate two drawbacks of the simple scatter plot described above: It is difficult to distinguish quantitatively small numbers that bunch together near zero, and it is difficult to distinguish the variation of many points within some bias wedge if the wedge is small. These issues can be alleviated by interpreting the actual value and predicted value as a single complex number: $Z = A + Pi$, with $i \equiv \sqrt{-1}$. For some bias level, let θ equal the angle from the horizontal axis to the lower bias line, and let $\Delta\theta$ equal the angle from the lower bias line to the (symmetric) upper bias line. (Consequently, $2\theta + \Delta\theta = \pi/2$.) Now we apply a conformal mapping to first rotate the wedge clockwise by an angle of θ , *i.e.*,

$$\bar{Z}_1(Z) = Z \times \exp(-i\theta) \quad (\text{B-7})$$

Then we expand the wedge from $\Delta\theta$ to $\pi/2$ and normalize the wedge so that points with a pre-mapping magnitude of $|Z|$ retain this same magnitude in the new mapped space, *i.e.*,

$$\bar{Z}(\bar{Z}_1(Z)) = \bar{Z}_1^{\frac{\pi}{2\Delta\theta}} \times |\bar{Z}_1|^{1-\frac{\pi}{2\Delta\theta}} \quad (\text{B-8})$$

Consequently, straight lines in Z remain straight lines in \bar{Z} .

This mapping has several benefits: it eliminates regions of the original scatter plot without relevant data by setting an appropriate bias level; it focuses the plot over a single region of the solution space; and it supports quantitative estimates using logarithmic scatter plots by expanding internal bias wedges. Logarithmic scatter plots in mapped space are particularly

useful for our applications. Small cracks dominate fatigue lives, and these cracks have geometric correction factors with small magnitudes that cannot be readily visualized using a linear scale. In a logarithmic scale, bias lines become straight lines with a 1:1 slope and an offset determined by the basis level.

B.3 Finite element analysis

Overview

In this work, all SIF solutions have a 3D geometry with an elliptical (or part-elliptical) crack front that reflects crack shapes often encountered in practice. The elliptical crack front has been modeled as a linearized ellipse surrounding by rings of elements arranged in concentric circles, as shown in Figure B- 1. This geometric arrangement forms the crack tube that is necessary for SIF calculations in Abaqus. The crack tube represents the major computational cost associated with the FEA model. It requires significant time and effort to form an appropriate geometry. For example, geometric deviations on the order of 10^{-3} times the crack length can lead to invalid SIF values. The crack tube contains 20-node hexahedron elements with full integration. On the crack front, the mid-side node has been shifted to the quarter point to accommodate the stress singularity.

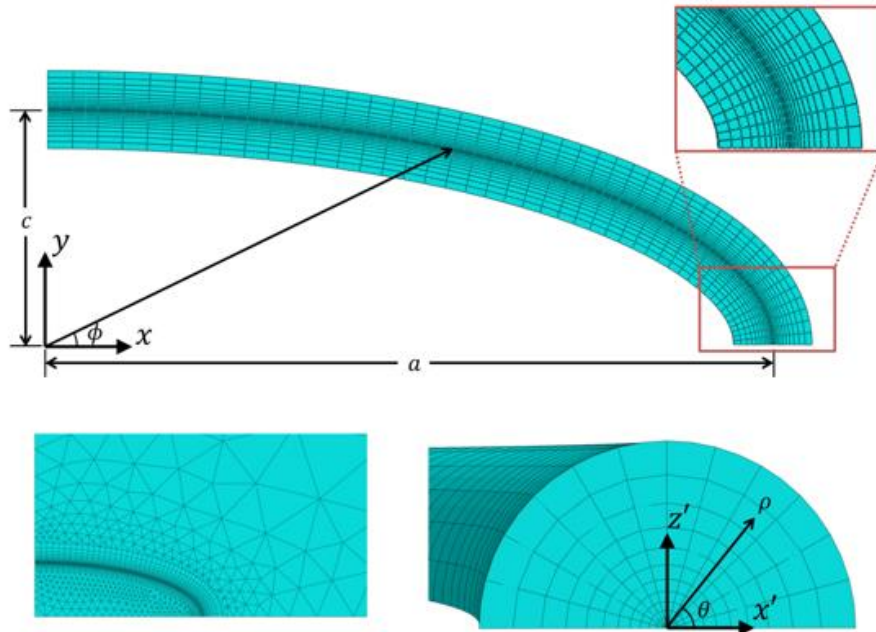


Figure B- 1. Illustration of the corner crack mesh and crack tube for the FEAs

A transition region connects the crack front to the far-field region. The transition region features 10-node tetrahedral elements to mesh the non-standard topology of the region around the crack tube. The element size decreases towards the crack tube region to capture increasing stress gradients. For very deep/long cracks, the transition region may completely fill the cross-section.

A far-field region contains the transition region. In Figure B- 1, the far-field region has elements ahead of the a -tip and c -tip to fill out the cross section for smaller cracks. The far-field region always features a rectangular section of elements elongated normal to the crack plane. Here, it is shown elongated in the horizontal direction. These elements fill the space and allow the stresses to accommodate zero stresses at the far-field boundaries. The far-field region features 8-node hex elements.

The models use the linear kinematic formulation (small strain); *i.e.*, deformations are assumed to have a negligible effect on the geometry. All analyses assume an isotropic linear-elastic material model (Hooke's law) with uniform material properties throughout the geometry. The value of Poisson's ratio ($\nu = 0.3$) is consistent with values found in most isotropic metals. Computational studies (Nakamura & Parks, 1988) indicate that 3D SIFs vary with Poisson's ratio, though there is limited sensitivity near $\nu = 0.3$.

All cracked models in this verification are symmetric in the geometry, loading, and material above and below the crack plane. Consequently, only half of the geometry needs to be modeled in these analyses, and exploiting this symmetry reduces computational costs. Zero displacements normal to the uncracked ligament preserve symmetry, *i.e.*, they are symmetric boundary conditions. Displacements at arbitrarily selected points prevent rigid body motion.

Loads remain normal to the crack plane and may vary in magnitude at any point on the cross-section. Loads may be applied to top/bottom surfaces or to the crack face. Nonlinear tractions applied to the top/bottom surfaces are redistributed to equivalent stresses only composed of uniform and linear stress distributions as suggested by St. Venant's principle. We achieve SIF solutions from nonlinear tractions by applying them to the crack face.

Abaqus computes SIF solutions using the domain integral technique. The domain integral technique transforms the line integral of the J-integral to a volume integral that facilitates numerical calculations. Abaqus computes the J-integral values along the crack front and then converts them to the corresponding SIF values. Due to the loading, geometry, and material, $K_I \neq 0$ whereas $K_{II} = K_{III} = 0$ for all cases. This physical constraint is checked during the analyses. Boundary effects introduce numerical issues into the domain integral computations near free

surfaces (Pook, 1994). These studies locate characteristic SIF values for crack tips at some distance from free surfaces.

We exploited the Python scripting capability in Abaqus CAE to generate FEA solutions. The Python scripting interface enables user-created scripts to define the geometric configuration, apply loads, adopt material response, set meshing parameters, and create domain integral definitions. Python scripting also supports data processing and transfer, e.g., to/from Excel spreadsheets. Python also features libraries that reduce the new code that needs to be written to process the results. There are several advantages to the scripting interfaces besides the obvious efficiencies, e.g., consistent model definitions and more rigorous modeling techniques.

Results from the FEA need to be verified before they are released into the verification matrix. A two-tiered approach was adopted. First, select cases were examined for general solution quality that includes balanced reaction forces, smooth displacement and stress gradients, and SIF convergence with mesh refinement. We ensure consistent solution quality by incorporating the relevant parameters into the scripts/solution matrix. Second, all cases were checked to ensure that SIF values converged over domains and that K-values are smooth over the crack front. If a solution failed to satisfy these second quality checks, then it was re-run at a higher mesh refinement or the SIF was smoothed to eliminate oscillations across the crack front. A few poor combinations of the geometry and loads resulted in repeated inferior solutions despite repeated attempts. These results were not placed into the verification matrix of FEA SIF solutions.

The range of geometries examined here is limited by the FEA method. The crack must have a finite size that supports a precise definition of the crack front geometry using finite precision numbers. The crack must not break through the geometry at a free surface except at the crack tips; otherwise, a crack front cannot be defined that results in extractable SIFs. Finally, the crack front must not be too elongated. Otherwise, computational costs may make the analysis ensemble intractable.

Exact solution

Irwin (1962) provides one of the few exact solutions of SIFs for a 3D elliptical crack. The 3D crack has finite dimensions a and c such that $a \geq c$, and it is centered in an infinite body loaded by a remote, uniform traction (σ) normal to the crack face. Irwin's solution provides the SIF along the crack front as:

$$K_I = \frac{\sigma\sqrt{\pi c}}{E(k)} \left(\sin^2 \phi + \frac{c^2}{a^2} \cos^2 \phi \right)^{1/4} \quad (\text{B-9})$$

$$E(k) = \int_0^{\pi/2} \sqrt{1 - k^2 \sin^2 \psi} \, d\psi \quad (\text{B-10})$$

where $k = 1 - c^2/a^2$ and ϕ indicates the location along the crack front, with $\phi = 0$ at the a -tip and $\phi = \pi/2$ at the c -tip for example. Equation (B-9) indicates that K_I decreases at the a -tip and increases at the c -tip as a/c increases. This result suggests that the errors at the a -tip are less important to fatigue life calculations than errors at the c -tip for large a/c . For this case, the c -tip grows faster than the a -tip and thus controls life (a/c will change as the crack grows, gradually approaching $a/c = 1$ in this case).

Figure B- 2 shows the credibility measure of the Abaqus FEA solutions as a function of the crack shape (a/c) from circular cracks ($a/c = 1$) to elongated cracks ($a/c = 10$) (Irwin, 1962). These solutions utilize a constant discretization level with 60 elements along the crack front. Increasing the number of elements reduces error but increases computational costs. The Abaqus solutions approximate the infinite body of the exact solution by placing the crack inside of a box with dimensions equal to 100 times the crack front.

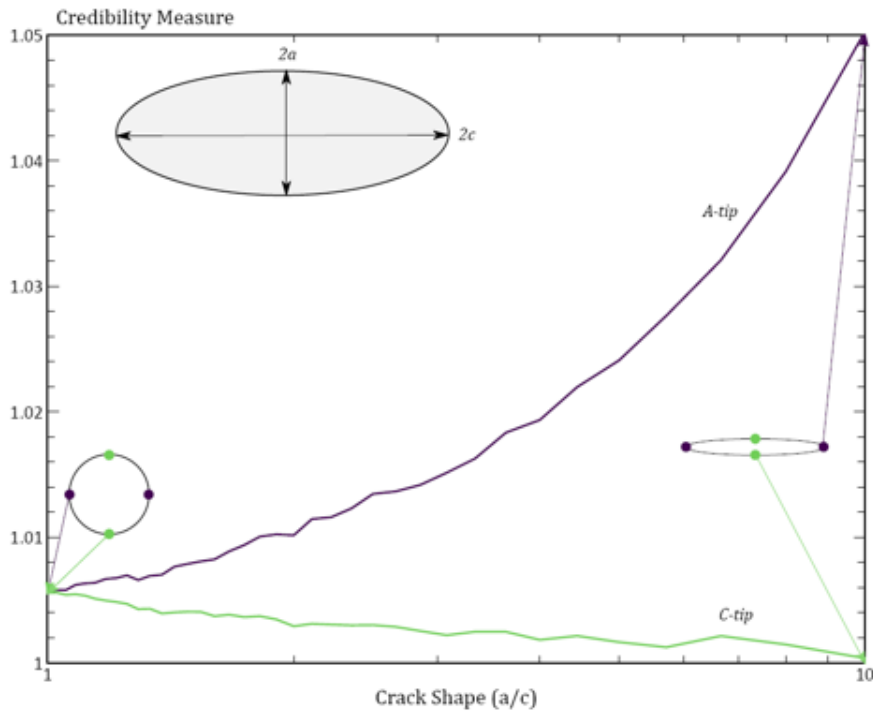


Figure B- 2. Credibility of FEA SIF solutions using exact analytical solution by Irwin

As shown in Figure B- 2, error in the Abaqus result increases/decreases at the a -tip/ c -tip as the crack elongates (a/c increases). For circular cracks, the SIF at the a -tip and c -tip have the same error in their solutions due to symmetry for this (and only this) geometry. For more elongated crack tips, error increases at the pointed a -tip, as it requires significant discretization for its geometry. The error in the c -tip decreases in contrast as its smooth, almost flat shape is increasingly well modeled by a piecewise linear description of the ellipse. Errors remain less than 1% for practical crack shapes ($0.5 \leq a/c \leq 2$) that mostly drive FCG processes.

Legacy solutions

Newman and Raju (1981) provide closed-form solutions (referred to as Newman-Raju solutions for the remainder of this document) for the tips of a surface crack centered in a plate under tension and bending loading. Newman and Raju document the FEAs that provide SIF values used to fit their empirical solution curves. In terms of a surface crack solution, this solution limits the dimensions as follows: $a/t \leq 0.1$, $a/c \leq 1.0$, $2B/W = 1$, and $2c/W \leq 0.5$. These solutions have a high degree of credibility in the aerospace industry; they have been used in many, many fracture critical applications since their initial publication. However, these solutions are based on old FEAs with only a few thousand degrees of freedom and have unknown levels of discretization errors as a result of this simplification.

Table B- 1 shows the geometric solution limits for the Newman-Raju (referred to as NR81) and the range of parameters sampled by the LHS process. Three parameters completely describe the geometry: a/c , a/t , and $2c/W$. These parameters prevent both small cracks and large cracks that are not computationally tractable. These parameters were further constrained by only retaining samples of a/c , a/t , and $2c/W$ that lead to reasonable plate sizes for this application ($0.05 \leq W/t \leq 50$). More than half of the sampled 500 geometries fail to meet this criterion and only 213 geometries were selected for analysis.

Table B- 1. Geometric parameters for the Newman-Raju solution verification sampling by LHS

SIF	a/c		a/t		$2c/W$		W/t	
	Min	Max	Min	Max	Min	Max	Min	Max
NR81	0	1	0	1.00	0	0.5	N/A	N/A
FEA	0.125	1	0.01	0.90	0.01	0.5	0.05	50

These Newman-Raju solutions support uniform stress field and in-plane bending moments about the W -axis. To match these stresses, the FEAs set a constant stress and a linearly varying stress both over the remote ends and over the crack faces. As expected, stresses applied to the remote

ends and stresses applied to crack faces lead to equivalent SIFs along the crack front. This result suggests that there is sufficient mesh refinement over the crack faces.

The semi-elliptical crack front has two degrees of freedom given by its depth (a) and its length (c). Consequently, FCG calculations only require SIFs at these two locations along the crack front, and it is at these two locations where the Newman-Raju solutions provide SIFs. Consequently, we limit our comparisons to SIFs at these two locations.

For each tip, Figure B- 3 shows several scatter plots of the predicted geometry correction factors from the Newman-Raju solutions to the actual geometry correction factors from the FEAs. These results include geometry correction factors from the uniform stress fields and the linear stress fields. Most of the Newman-Raju solutions are within 5% of the new FEA results, and all solutions are within 25% of the FEA results. Solutions at the c -tip agree slightly better than solutions at the a -tip. The conformal mapping (applied to (a) and (c)) expands the scatter plot over the 25% wedge of solutions and allows the quality of the fit to be more easily distinguished. In particular, the lognormal plot indicates that the solutions become more accurate as the geometry correction factor increases in magnitude, possibly due to computational precision increasing with the SIF magnitude.

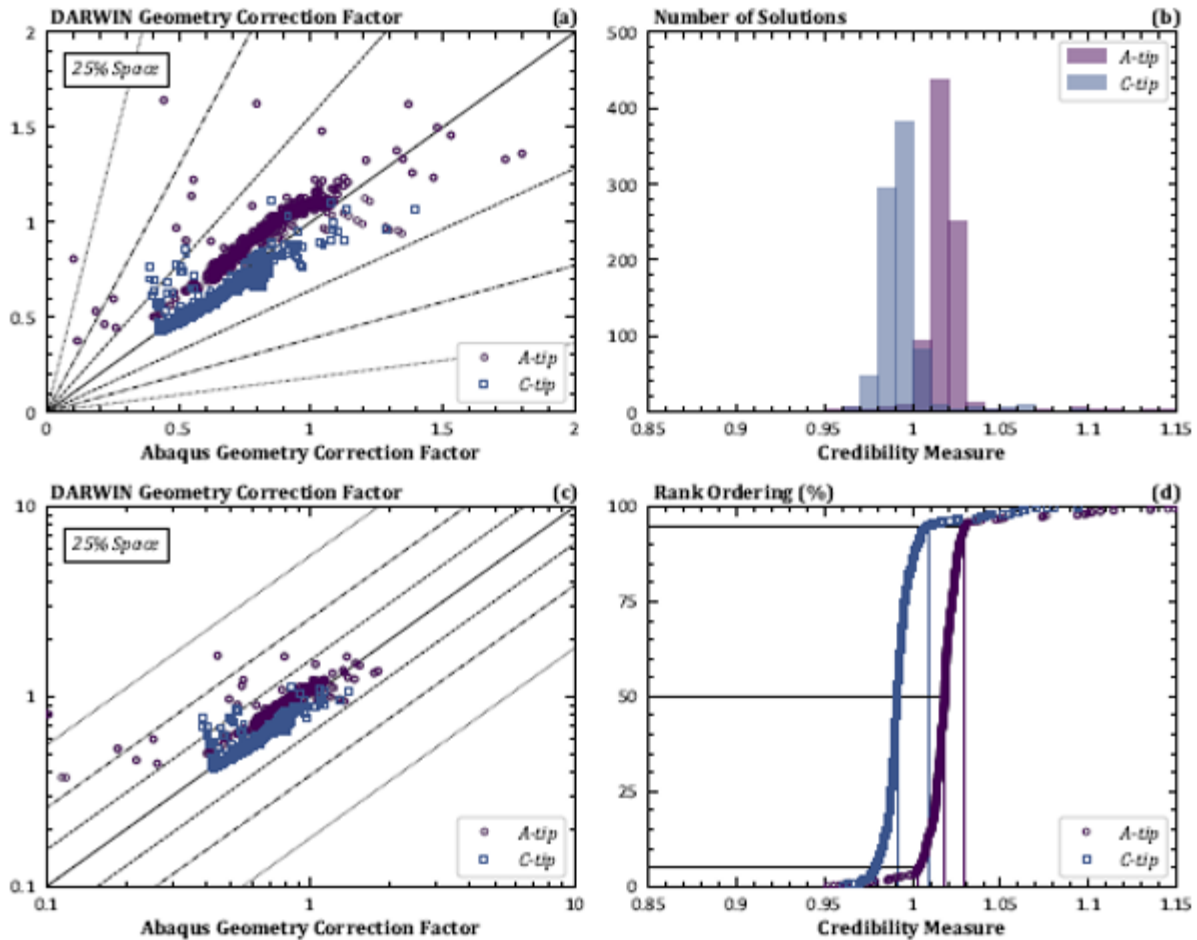


Figure B- 3. Comparison of independent Abaqus SIF solutions to Newman-Raju solutions

Figure B- 3(d) provides the rank ordering of the credibility measure; *i.e.*, a CDF of the quality of the solutions that is the derivative of the PDF in Figure B- 3(b). That is, Figure B- 3(d) provides the percentage of solutions at or below the credibility measure. Figure B- 3(d) shows a shift in the credibility measure from the *a*-tip to the *c*-tip, with the Newman-Raju solutions being in better agreement at the *c*-tip than *a*-tip as suggested by the scatter plots. More than 90% of the solutions have $\pm 5\%$ error. Descriptive statistics of these CDFs indicate that the median *a*-tip credibility is +1.8% vs. -0.9% for the *c*-tip. Both solutions have relatively little scatter as indicated by the low standard deviations, though the *a*-tip solutions show more scatter than the *c*-tip solutions as illustrated in Figure B- 3. For both the *a*-tip and *c*-tip solutions, excessive error ($\pm 5\%$) in the Newman-Raju solutions tends to be conservative, *i.e.*, the error will lead to shorter fatigue lives than would be predicted by the FEA solutions.

B.4 Verification for core DARWIN solutions

Overview

The initial verification effort focused on the core DARWIN solutions for cracks in rectangular prismatic bodies shown in Figure B- 4. These core DARWIN solutions are the SIF solutions used most often for life and risk assessments. In Figure B- 4, these cracks are grouped by row as either WFs for univariant stresses (meaning stresses only vary in the primary direction) or WFs for bivariant stresses (meaning stress vary in the primary and secondary directions). These cracks are grouped by column based on their geometry: corner cracks (CCxx), surface cracks (SCxx), and embedded cracks (ECxx).

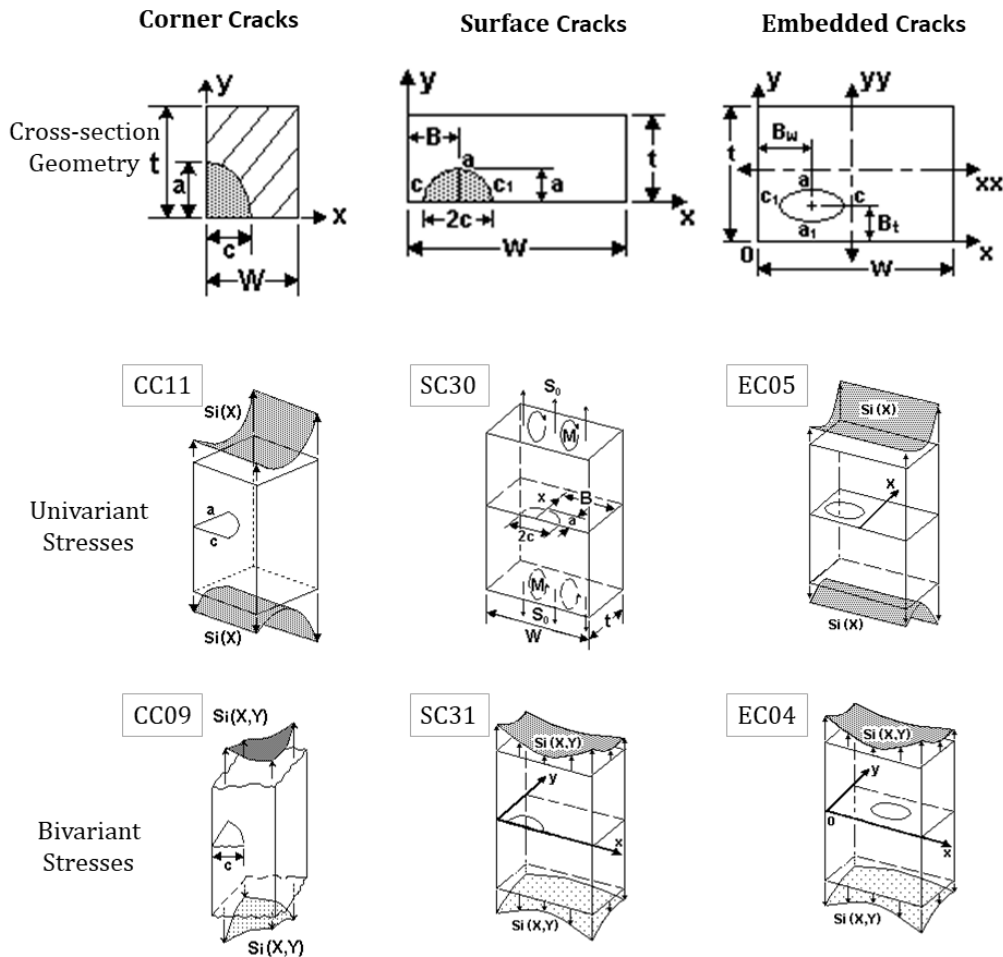


Figure B- 4. Core DARWIN SIF solution geometries for corner, surface, and embedded cracks

Univariant WFs are employed by Autoplate as the default solutions. Consequently, the first row of solutions (CC11, SC30, and EC05) represent the most common SIF solutions used in DARWIN. Bivariant WFs are employed by users in manual analysis modes to support geometries with a strong stress variation in the secondary direction. The bivariant solutions require larger computational costs and (until recent developments) required that the plate completely enclose the geometry. The univariant solutions are more computationally efficient and can have regions of the plate not enclosed by the geometry. These considerations make univariant SIF solutions a more attractive option in many cases. Furthermore, these univariant solutions are reasonably accurate for geometries without very strong stress gradients in the secondary direction.

Approach

Figure B- 5 illustrates the verification approach adopted in this section. During verification, we generate two sets of SIFs using DARWIN weight functions (e.g., CC11) and independent FEAs. An FEA is considered independent in this sense if it does not contribute to the solution matrix of the weight function. The verification study spans multiple geometries (e.g., ratios of *a/c*) and stress variations (e.g., linear across the thickness).

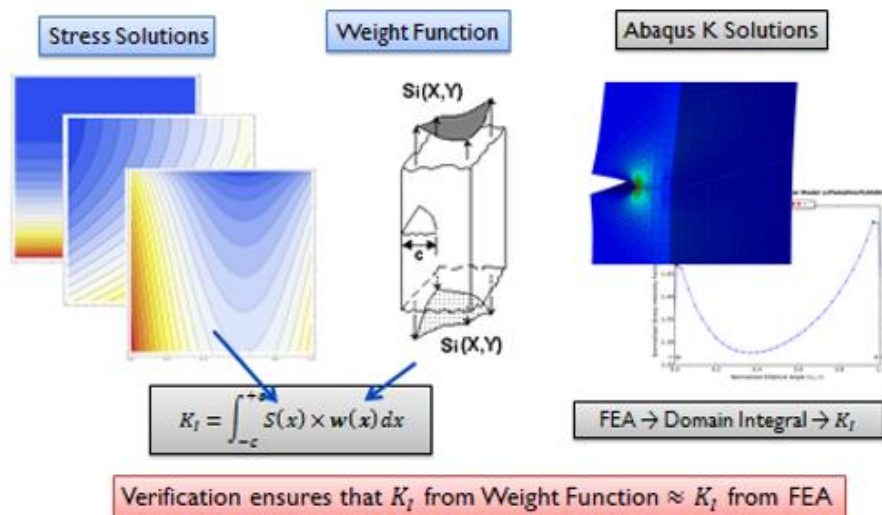


Figure B- 5. Verification approach comparing weight function SIFs against FEA SIFs

Verification ensures that the SIF from DARWIN approximately equals the corresponding SIF from the FEA. In general, the two numbers do not coincide exactly. The DARWIN SIF features error from the solution matrix values, interpolation procedure, and numerical integration of the weight function. The FEA solutions have error from the geometric discretization, the domain

integral technique, the application of stresses, and other sources. Consequently, the verification can only be approximate.

In this verification study, the DARWIN SIF solutions have been approximated using the corresponding SIF solutions in NASGRO 8.1. The two codes share identical core SIF routines. In other words, they are exactly the same solution. However, SIF solutions are much easier to access directly in NASGRO than in DARWIN because they do not require plates be set up on an uncracked finite element. Finally, NASGRO outputs SIF solutions directly using the NASSIF module whereas DARWIN does not export SIF solution results conveniently.

One small difference between the DARWIN and NASGRO solutions is that the DARWIN solutions force all stress gradients to a discretization that is not available in NASGRO. For example, all bivariate stress solutions in DARWIN extract stress values onto a 100×100 grid. DARWIN integrates the stress solution by the weight function over the 10,000 points on this grid to compute SIF values. NASGRO only supports a direct integration over a 20×20 grid. Higher density grids are interpolated using an optimal point spacing routine that smooths stresses. In univariate solutions, DARWIN discretizes stresses as a 100-point line, and NASGRO downgrades this solution to 20 points that are optimally spaced.

As a result of NASGRO's downgrade, there is a computational cost associated with higher density grids, but there is little additional benefit to the solution quality unless the stress gradients are very steep. In this study, we employ the optimal point spacing routine in the NASGRO calculations with a 21-point line or 21×21 point grid for surface cracks and corner cracks. The embedded crack solutions feature steeper stress gradients that require higher refinement. Consequently, we adopt an 81-point line or a 81×81 point grid for embedded crack solutions.

SIFs from FEAs are more involved. Figure B- 6 provides the major geometric regions of the FEA solutions. The crack front/tube is surrounded by a transition region that links to a far-field region. In these models, mesh ties connect these three regions by enforcing equivalent displacements at the boundaries. Mesh ties enable displacements to be transferred from one region to another without an exact conforming mesh that is difficult to create for the 3D crack geometry.

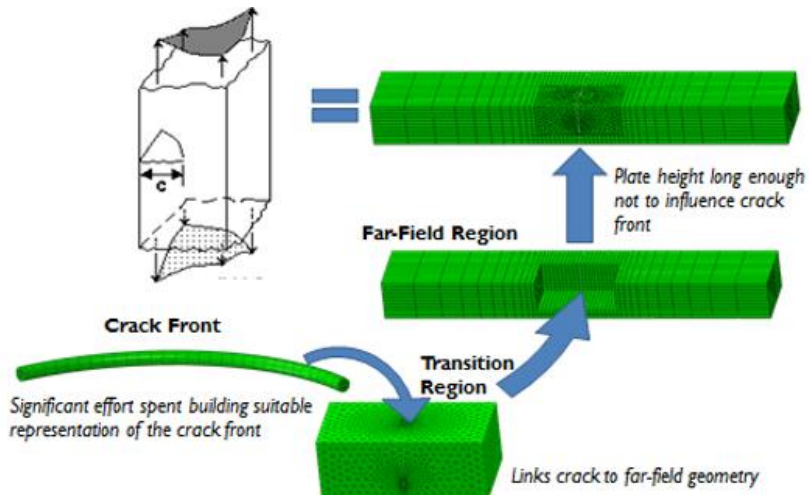


Figure B- 6. Finite element geometric features in a corner crack solution

We modified LHS to remove geometries with inappropriate plate dimensions – where the width-to-thickness (or vice-versa) ratio exceeds value of 10. That is, we removed plate definitions that were excessively skinny.

Some of these solutions employ a filtering scheme to eliminate non-physical SIF values from consideration. There are two filtering methods adopted in this section.

- The first method removes SIFs from the database based on crack shape, size, and distance to the surface. The cracks removed using this scheme represent non-physical cracks with limited practical value, e.g., cracks with large aspect ratios (a/c) that are extremely deep and near the free surface. These geometries are unlikely to develop in any realistic FCG scenario.
- The second method removes SIFs at tips with values that are much lower than the SIF value at the maximum tip. Tips with lower SIFs have fewer contributions to crack growth, and the crack shapes that induce these SIFs are unstable. Again, these geometries are unlikely to develop in realistic FCG scenario.

These unrealistic geometries arise due to the extremely large solution space supported by the various DARWIN SIF solutions. For example, CC11 supports a/c ratios up to 40. Any sampling methodology (including LHS) within this solution space leads to combinations of parameters that are not practical yet allowed by the geometric limits of the solution.

The two methodologies adopted here attempt to isolate these impractical geometries and unimportant SIF solutions. These filtered solutions often lead to larger errors that do not reflect the actual quality of the solutions. These larger errors reflect round-off errors due to poor numerical discretization of the FE geometry caused by constraints on the computing resources

and the internal framework of Abaqus (e.g., the use of single point numbers to store nodal locations). These errors likely reflect larger values of δ_{BA} in Equation (B-6), not large values of δ_{TA} .

In later sections, we adopt a third methodology that simply removes very small values of the geometry correction factors from consideration. These small values reflect near-zero values of SIFs (except under very large loadings) that may not exceed the FCG threshold value. This third methodology is probably the cleanest way to filter impractical SIFs from the error distributions. It was only adopted after the conclusion of this work for different SIF geometries.

B.5 Univariant corner crack model (CC11)

Figure B- 4 shows a representation of the univariant corner crack-in-plate solution that is incorporated into DARWIN and NASGRO. This geometry represents a semi-elliptical corner crack in a plate that has major dimensions for the width, thickness, and crack tip lengths. In CC11, stress varies along the X-direction that is aligned with the a -tip dimension, but it does not vary with the normal direction. That is, CC11 represents a univariant stress gradient.

Table B- 2 indicates the minimum and maximum dimensions of the crack tip solution CC11 as well dimensions for the FEA. LHS was applied to the geometric ratios for crack shape (a/c), crack depth (a/t), and crack length (c/W). We excluded geometries that were outside of the acceptable ratios of W/t as shown in Table B- 2. There are 172 total geometries in the SIF solutions matrix.

Table B- 2. Minimum and maximum dimensions of the crack tip solution CC11 and the FEA models

SIF	a/c		a/t		c/W		W/t	
	Min	Max	Min	Max	Min	Max	Min	Max
CC11	0.025	40	0	0.95	0	0.95	N/A	N/A
FEA	0.125	8	0.01	0.95	0.01	0.9	0.1	10

Table B- 3 presents traction gradients applied to CC11 in the verification study. The traction gradients are limited to univariant functions normalized by the plate thickness. They are applied to the top/bottom surface and to the crack face. Every traction listed in Table B- 3 was applied to every geometry in the solution matrix. The total number of solutions for the CC11 verification study is 860.

Table B- 3. Traction gradients applied to corner cracks in verification study

Application	Equation
Top/Bottom	Uniform
Top/Bottom	$1 - X/t$
Crack Face	Uniform
Crack Face	$1 - X/t$
Crack face	$(1 - X/t)^2$

Figure B- 7 shows predicted geometry correction factors from DARWIN against Abaqus geometry correction factors. The geometry correction factor provides a convenient normalization of SIF values. It removes the effect of the load magnitude and crack length. Results in Figure B- 7 indicate the level of agreement between weight function solutions (vertical axis) and FEA solutions (horizontal axis). Points on the one-to-one line have perfect agreement. Visually, Figure B- 7 indicates that the CC11 solutions are within $\pm 10\%$ of the FEA solution. CC11 is slightly more accurate at the *a*-tip than at the *c*-tip, but the difference is not large.

However, this visual inspection does not adequately characterize the agreement between CC11 and the FEA solution.

Figure B- 8 provides a histogram of CC11 SIFs vs. FEA SIFs. Here, SIFs from CC11 have been normalized by Abaqus SIF to provide a ratio that measures the accuracy of the CC11 solution. When this ratio equals unity, the solutions exactly agree. As shown in Figure B- 8, CC11 results are slightly higher than the FEA results – on average by about one percent. Ninety percent of the CC11 solutions have a ratio between 0.983 and 1.049 for the *a*-tip and between 0.977 and 1.054 for the *c*-tip.

Figure B- 9 provides the rank ordering of the CC11 SIF ratio to the Abaqus SIF ratio. It also indicates the median value and extreme values for the SIF solutions. Figure B- 9 provides another illustration of the accuracy of CC11 relative to the FEA solution. It may also be interpreted as a cumulative probability distribution – that is for any given disagreement level, it estimates the number of solutions at or below that level.

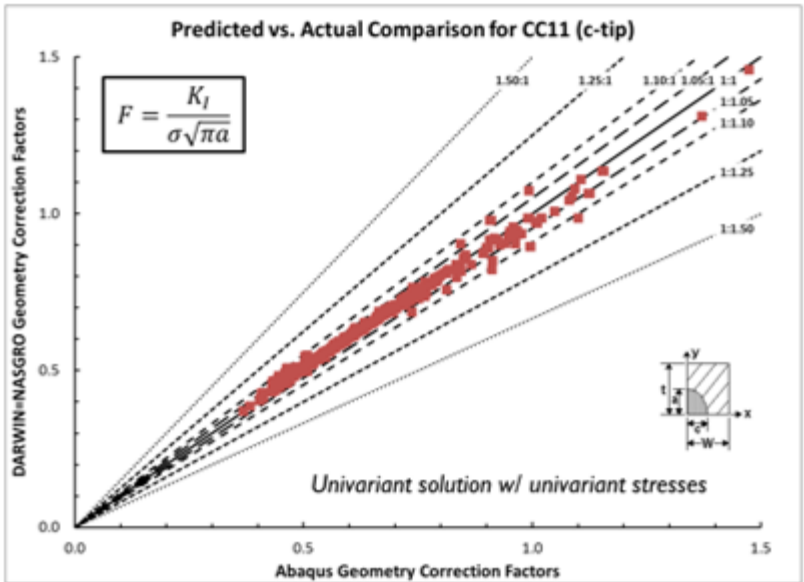
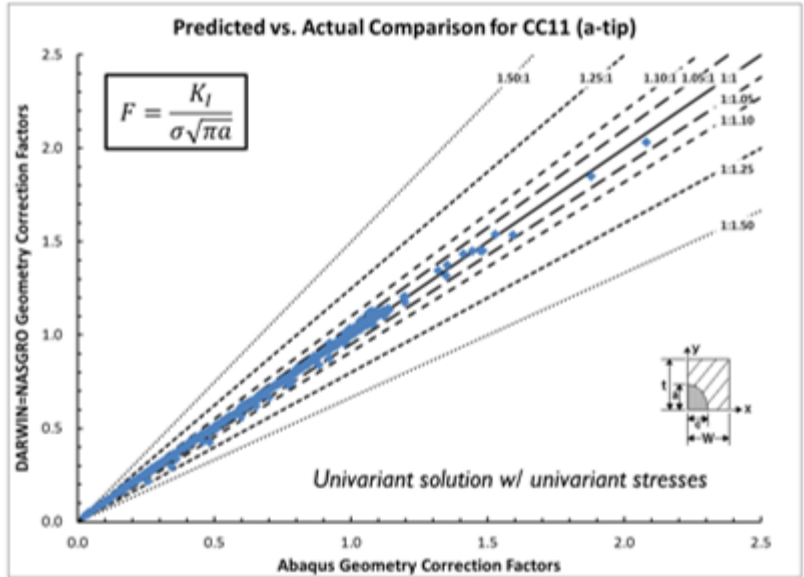


Figure B- 7. CC11 geometry correction factors vs. Abaqus

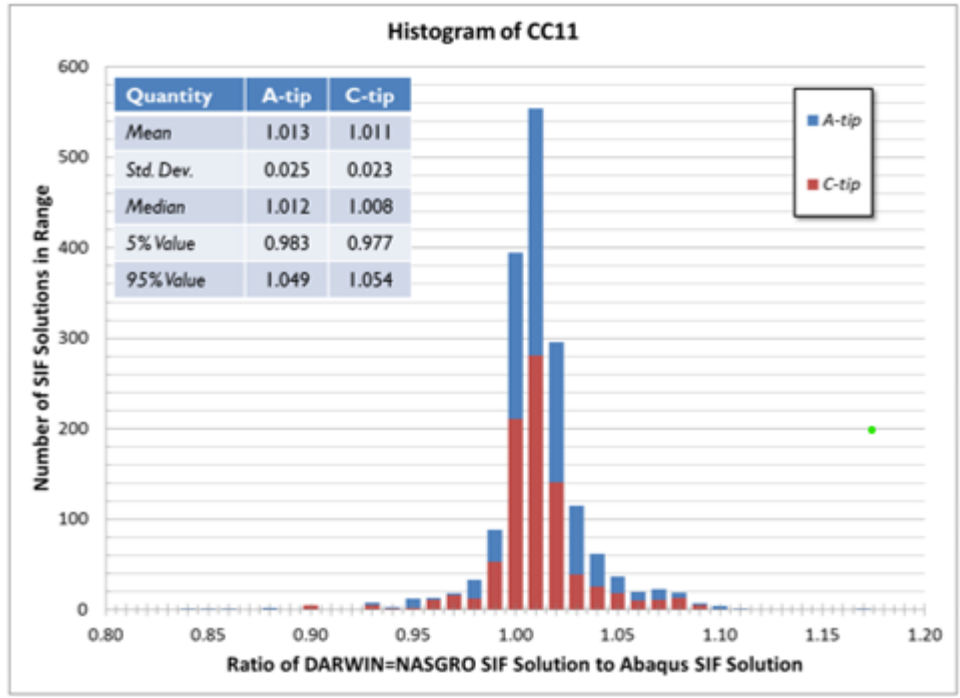


Figure B- 8. Histogram of CC11 SIFs vs. Abaqus SIFs

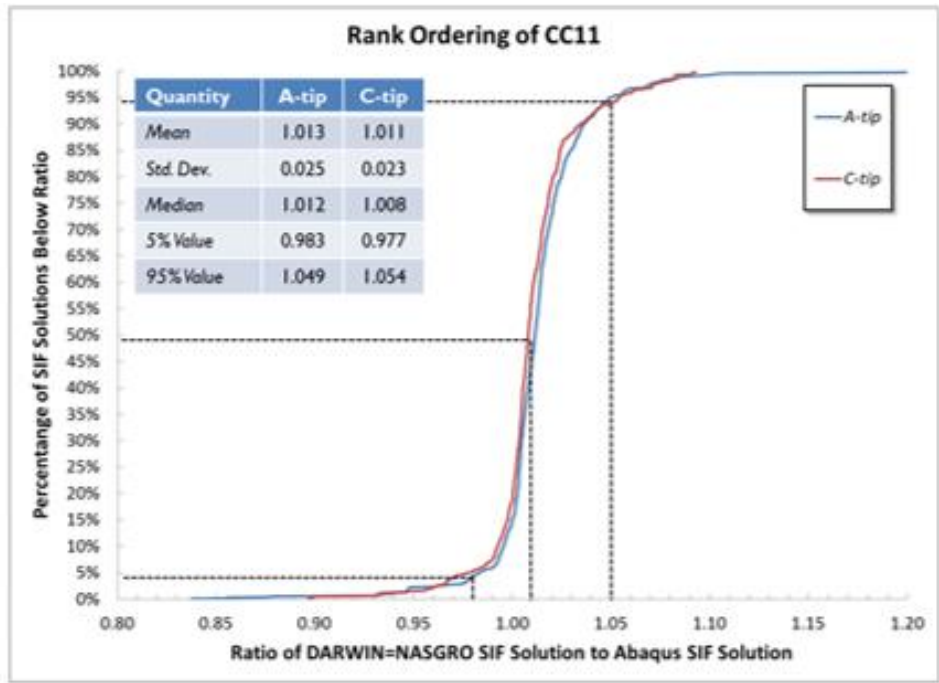


Figure B- 9. Rank ordering of CC11 SIFs vs. Abaqus SIFs

B.6 Bivariant corner crack model (CC09)

Figure B- 4 shows a representation of the bivariant corner crack-in-plate solution that is incorporated into DARWIN and NASGRO: CC09. This geometry represents a semi-elliptical corner crack in a plate that has major dimensions for the width, thickness, and crack tip lengths. In CC09, stress varies along the X-direction that is aligned with the c-tip dimension and with the Y-direction that is aligned with the a-tip dimension. That is, CC09 represents a bivariant stress gradient.

Table B- 4 indicates the minimum and maximum dimensions of the crack tip solution CC09 as well dimensions for the FEA. LHS was applied to the geometric ratios for crack shape (a/c), crack depth (a/t), and crack length (c/W). We excluded geometries that were outside of the acceptable ratios of W/t as shown in Table B- 4. There are 172 total geometries in this SIF solutions matrix. Table B- 5 presents traction gradients applied to CC09 in the verification study. Every traction listed in Table B- 5 was applied to every geometry in the solution matrix. The total number of solutions for the CC09 verification study is 1732.

Table B- 4. Minimum and maximum dimensions of the crack tip solution CC09 and the FEA models

SIF	a/c		a/t		c/W		W/t	
	Min	Max	Min	Max	Min	Max	Min	Max
CC09	0.025	40	0	0.95	0	0.95	N/A	N/A
FEA	0.125	8	0.01	0.95	0.01	0.9	0.1	10

Table B- 5. Traction gradients applied to corner cracks in verification study

Application	Equation
Top/Bottom	Uniform
Top/Bottom	$1 - Y/t$
Top/Bottom	$1 - X/W$
Top/Bottom	$1 - Y/t - X/W$
Crack Face	Uniform
Crack Face	$1 - Y/t$
Crack Face	$1 - X/W$
Crack Face	$1 - Y/t - X/W$
Crack Face	$(1 - Y/t)^2$

Application	Equation
Crack Face	$(1 - X/W)^2$
Crack Face	$(1 - Y/t - X/W)^2$

Figure B- 10 shows predicted geometry correction factors from DARWIN against Abaqus geometry correction factors. Figure B- 11 provides a histogram of the ratios of CC09 SIFs vs. FEA SIFs. Figure B- 12 provides the rank ordering of the CC09 SIF ratio to the Abaqus SIF ratio. Ninety percent of the CC09 solutions have a ratio between 0.982 and 1.049 for the *a*-tip and between 0.977 and 1.054 for the *c*-tip.

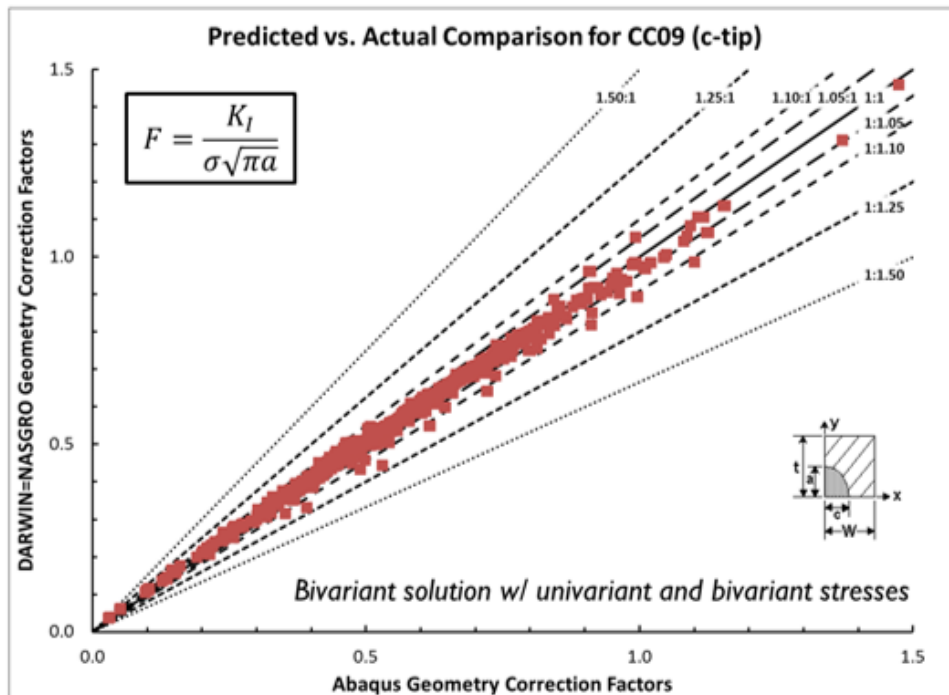


Figure B- 10. CC09 geometry correction factors vs. Abaqus

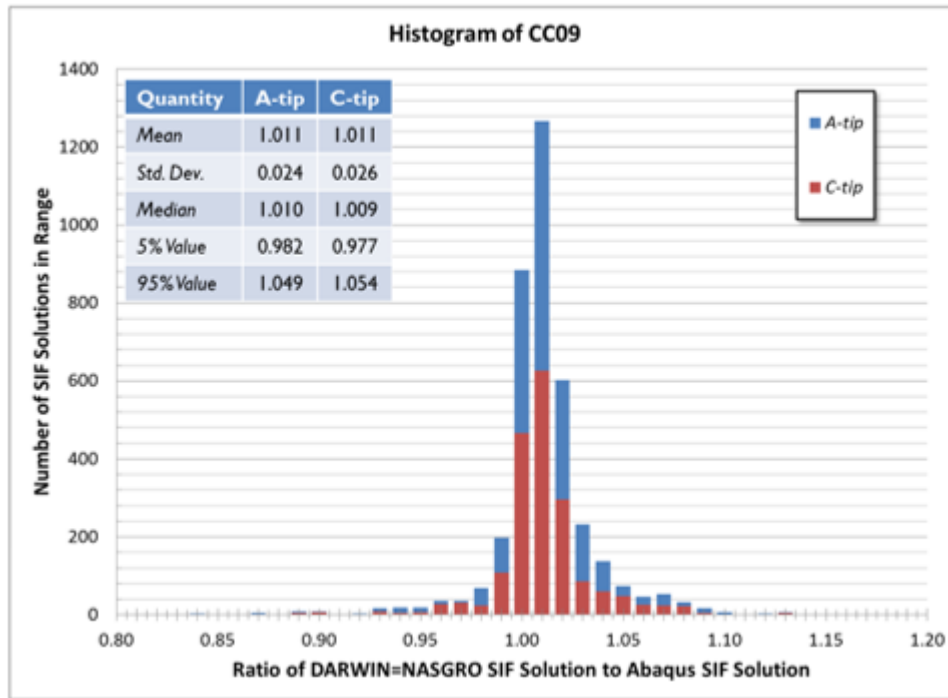


Figure B- 11. Histogram of CC09 SIFs vs. Abaqus SIFs

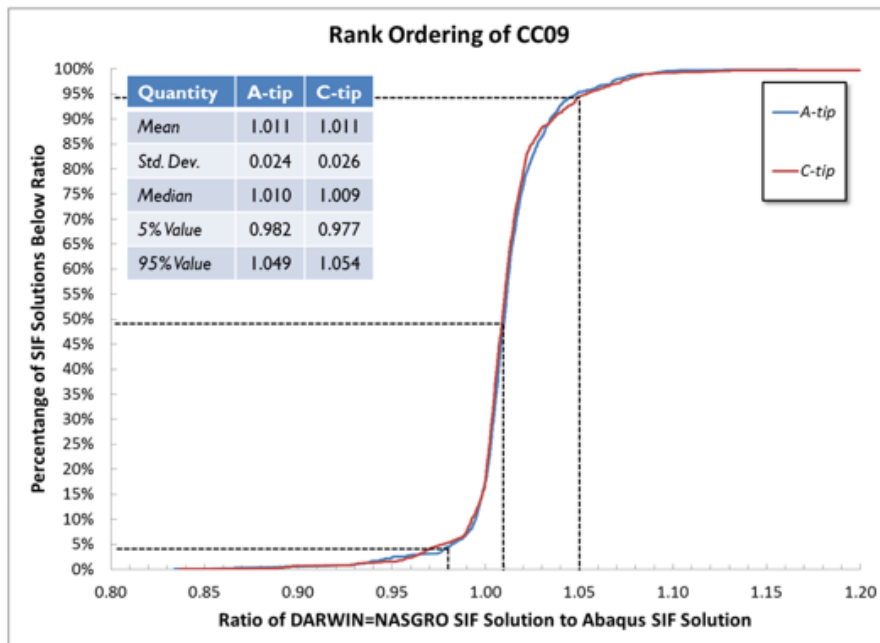


Figure B- 12. Rank ordering of CC09 SIFs vs. Abaqus SIFs

B.7 Univariant surface crack model (SC30)

Figure B- 4 shows a representation of the univariant surface crack-in-plate solution that is incorporated into DARWIN and NASGRO: SC30. This geometry represents a semi-elliptical surface crack in a plate that has major dimensions for the width, thickness, crack offset, and crack tip lengths. In SC30, stress varies along the X-direction that is aligned with the a -tip. That is, SC30 can represent univariant stress gradients in this direction.

Table B- 6 indicates the minimum and maximum dimensions of the crack tip solution SC30 as well dimensions for the FEA. LHS was applied to the geometric ratios for crack shape (a/c), crack depth (a/t), and crack length (c/W and $c/(W - B)$). We excluded geometries that were outside of the acceptable ratios of $2B/W$ and W/t as shown in Table B- 6. We also excluded certain geometries that showed a non-physical crack shape: highly elongated cracks ($a/c > 3$) that are either very deep ($a/t > 0.7$) or very long ($c/B > 0.7$). The maximum value of c/B was excluded as well since it is not a stable crack configuration. There are 242 total geometries in the SIF solutions matrix because of these exclusions.

Table B- 7 presents traction gradients applied to SC30 in the verification study. Certain tractions applied to certain geometries lead to inconsistent FEA SIF results – that is, SIF values along the crack front showed severe oscillation. These SIF solutions were removed from comparison plots. The total number of solutions for the SC30 verification study is 1914.

Table B- 6. Minimum and maximum dimensions of the crack tip solution SC30 and the FEA models

SIF	a/c		a/t		c/B		$c/(W - B)$		$2B/W$		W/t	
	Min	Max	Min	Max	Min	Max	Min	Max	Min	Max	Min	Max
SC30	0.125	8	0	0.95	0	1.0	0.0	1.0	0.1	1.9	N/A	N/A
FEA	0.125	8	0.01	0.95	0.01	0.9	0.01	0.9	0.1	1.9	0.1	10

Table B- 7. Traction gradients applied to surface cracks in verification study

Application	Equation
Top/Bottom	Uniform
Top/Bottom	$1 - X/t$
Crack Face	Uniform
Crack Face	$1 - X/t$
Crack Face	$(1 - X/t)^2$

Application	Equation
Crack Face	$(1 - X/t)^3$
Crack Face	$(1 - X/t)^{1/2}$
Crack Face	$(1 - X/t)^{1/3}$

Figure B- 13 through Figure B- 15 show predicted geometry correction factors from DARWIN against Abaqus geometry correction factors. Figure B- 16 provides a histogram of ratios for SC30 SIFs vs. FEA SIFs. Figure B- 17 provides the rank ordering of the SC30 SIF ratio to the Abaqus SIF ratio. It also indicates the median value and extreme values for the SIF solutions. SC30 results are slightly higher than the FEA results – on average by about one percent at the c-tips and by about four percent at the a-tip. The a-tip discrepancy is most prevalent for very small geometric correction factors and may represent a numerical artifact of the solution. At the a-tip, 90% of the SC30 solutions are between 0.9% and 9.6% of the FEA solutions. At the c-tip, 90% of the SC30 solutions are between -1.4% and 5.8% of the FEA solutions. At the c1-tip, 90% of the SC30 solutions are between -2.0% and 4.0% of the FEA solutions. The slight bias of the SC30 solution suggests a conservative result for FCG calculations.

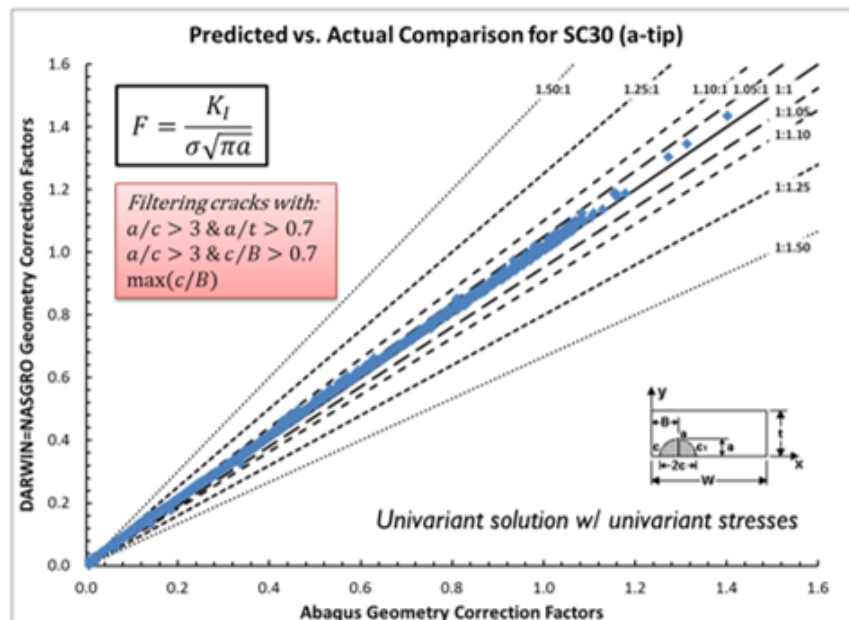


Figure B- 13. SC30 (a-tip) geometry correction factors vs. Abaqus

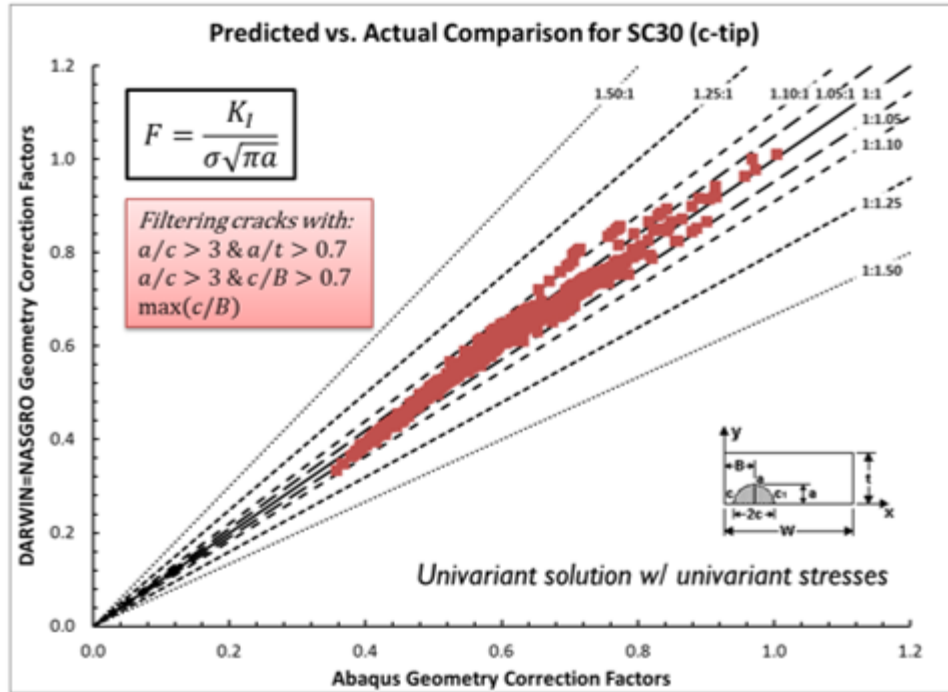


Figure B- 14. SC30 (c-tip) geometry correction factors vs. Abaqus

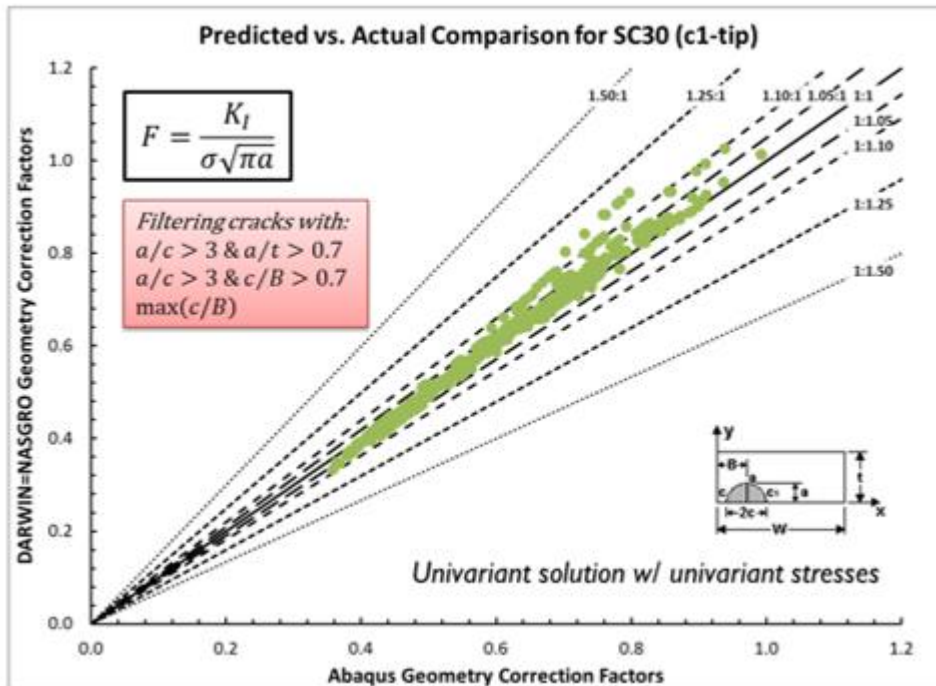


Figure B- 15. SC30 (c1-tip) geometry correction factors vs. Abaqus

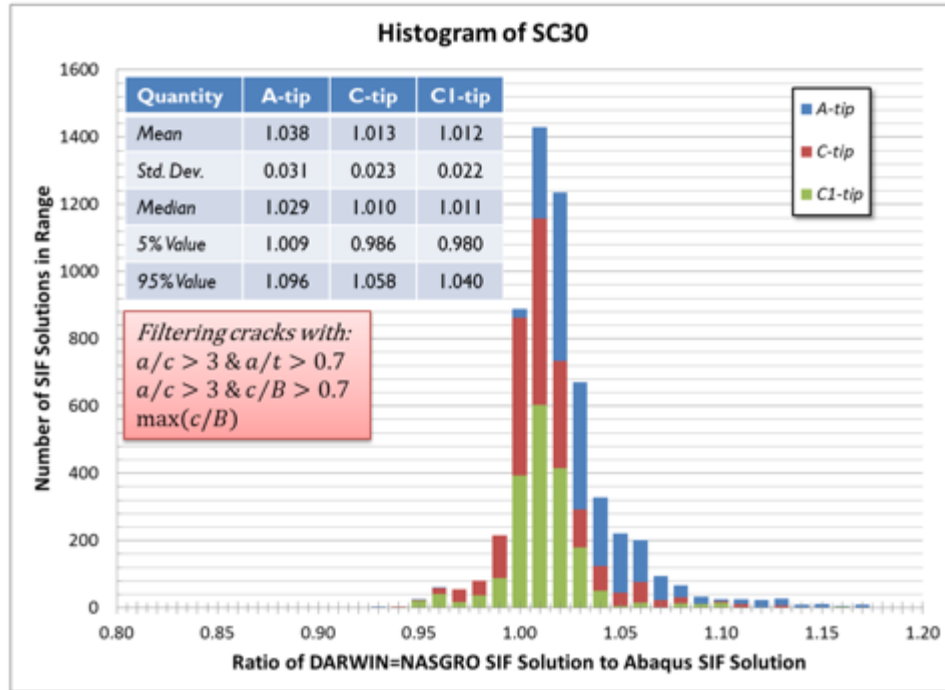


Figure B- 16. Histogram of SC30 SIFs vs. Abaqus SIFs

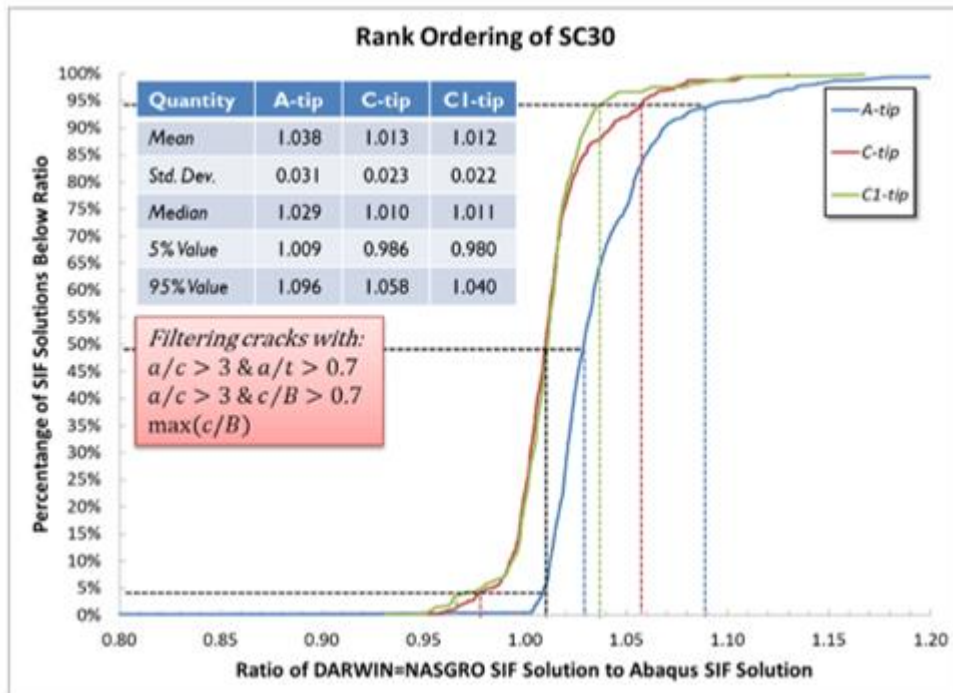


Figure B- 17. Rank ordering of SC30 SIFs vs. Abaqus SIFs

B.8 Bivariant surface crack model (SC31)

Figure B- 4 shows a representation of the bivariant surface crack-in-plate solution that is incorporated into DARWIN and NASGRO: SC31. This geometry represents a semi-elliptical surface crack in a plate that has major dimensions for the width, thickness, crack offset, and crack tip lengths. In SC31, stress varies along the X-direction, aligned with the c-tip, and varies along the Y-direction aligned with the a-tip. That is, SC31 can represent bivariant stress gradients.

Table B- 8 indicates the minimum and maximum dimensions of the crack tip solution SC31 as well dimensions for the FEA. LHS was applied to the geometric ratios for crack shape (a/c), crack depth (a/t), and crack length (c/W and $c/(W - B)$). We excluded geometries that were outside of the acceptable ratios of $2B/W$ and W/t as shown in Table B- 8. We also excluded certain geometries that showed a non-physical crack shape: highly elongated cracks ($a/c > 3$) that are either very deep ($a/t > 0.7$) or very long ($c/B > 0.7$). The maximum value of c/B was excluded as well since it is not a stable crack configuration. There are 242 total geometries in the SIF solutions matrix because of these exclusions.

Table B- 9 presents traction gradients applied to SC31 in the verification study. Certain tractions applied to certain geometries lead to inconsistent SIF results – that is, SIF values along the crack front showed severe oscillation. These SIF solutions were removed from comparison plots. The total number of solutions for the SC31 verification study is 5216.

Table B- 8. Minimum and maximum dimensions of the crack tip solution SC31 and the FEA models

SIF	a/c		a/t		c/B		$c/(W - B)$		$2B/W$		W/t	
	Min	Max	Min	Max	Min	Max	Min	Max	Min	Max	Min	Max
SC30	0.125	8	0	0.95	0	0.9	0.0	0.9	0.1	1.9	N/A	N/A
FEA	0.125	8	0.01	0.95	0.01	0.9	0.01	0.9	0.1	1.9	0.1	10

Table B- 9. Traction gradients applied to surface cracks in verification study

Application	Equation
Top/Bottom	Uniform
Top/Bottom	$1 - Y/t$
Top/Bottom	$1 - X/W$
Crack Face	Uniform
Crack Face	$1 - Y/t$

Application	Equation
Crack Face	$1 - X/W$
Crack Face	X/W
Crack Face	$1 - 1/2 \times (Y/t + X/W)$
Crack Face	$(1 - Y/t)^2$
Crack Face	$(1 - X/W)^2$
Crack Face	$1 - 1/2 \times (1 - X/W + Y/t)^2$
Crack Face	$(1 - Y/t)^3$
Crack Face	$(1 - Y/t)^{1/2}$
Crack Face	$(1 - Y/t)^{1/3}$
Crack Face	$1/2 \times ((1 - Y/t)^2 + X/W)$
Crack Face	$1/2 \times ((1 - 2X/W)^2 + 1 - Y/t)$
Crack Face	$1/2 \times ((1 - 2X/W)^2 + (1 - Y/t)^2)$
Crack Face	$1/3 \times ((1 - 2X/W)^2 + (1 - Y/t)^2 + X/W)$
Crack Face	$1/3 \times ((1 - 2X/W)^2 + (1 - Y/t)^{1/2} + (1 - X/W))$
Crack Face	$2/5 \times ((1 - 2X/W)^2 + (1 - Y/t)^3 + 1/2 \times X/W)$
Crack Face	$2/5 \times (1/2 \times (1 - 2X/W)^2 + (1 - Y/t) + X/W)$
Crack Face	$1/2 \times (1/2 \times (1 - 2X/W)^2 + (1 - Y/t)^{1/3} + 1/2 \times X/W)$

Figure B- 18 through Figure B- 20 show predicted geometry correction factors from DARWIN against Abaqus geometry correction factors. Figure B- 21 provides a histogram of ratios of SC31 SIFs vs. FEA SIFs. Figure B- 22 provides the rank ordering of the SC31 SIF ratio to the Abaqus SIF ratio. SC31 results are slightly higher than the FEA results – on average by about one percent at the *c*-tips and by about four percent at the *a*-tip. The *a*-tip discrepancy is most prevalent for small geometric correction factors where *c*-tip factors are much higher. That is, *a*-tip discrepancies represent non-equilibrium crack fronts growing into equilibrium shapes. The discrepancies may not greatly affect the overall solution results as a result. At the *a*-tip, 90% of the SC31 solutions are between 0.6% and 9.8% of the FEA solutions. At the *c*-tip, 90% of the SC31 solutions are between -2.6% and 5.5% of the FEA solutions. At the *c*1-tip, 90% of the SC31 solutions are between -3.5% and 2.5% of the FEA solutions. The slight bias of the SC31 solution suggests a conservative result for FCG calculations.

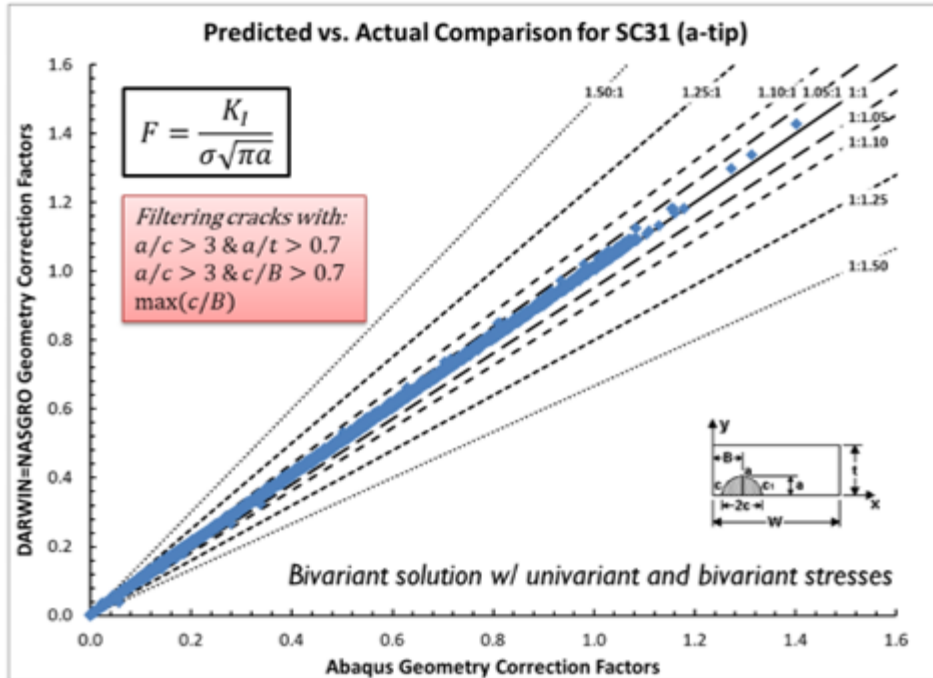


Figure B- 18. SC31 (a-tip) geometry correction factors vs. Abaqus

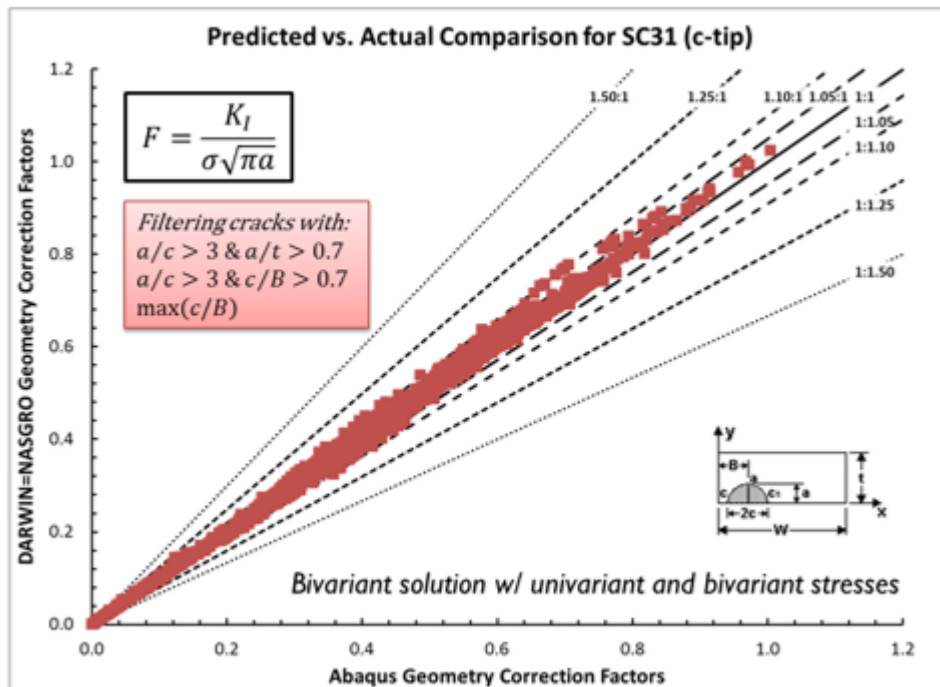


Figure B- 19. SC31 (c-tip) geometry correction factors vs. Abaqus

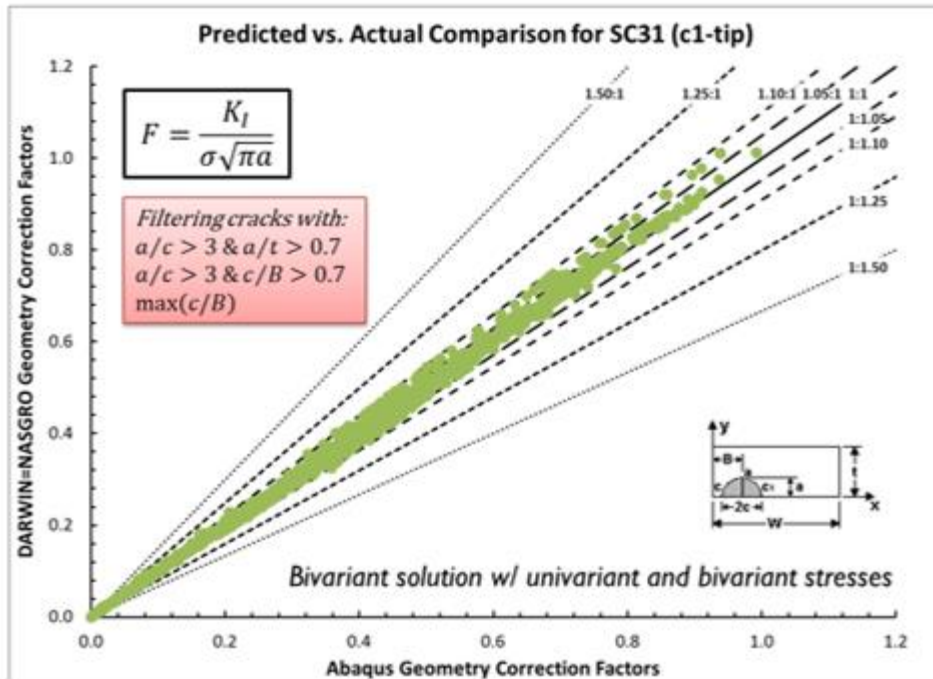


Figure B- 20. SC31 (c1-tip) geometry correction factors vs. Abaqus

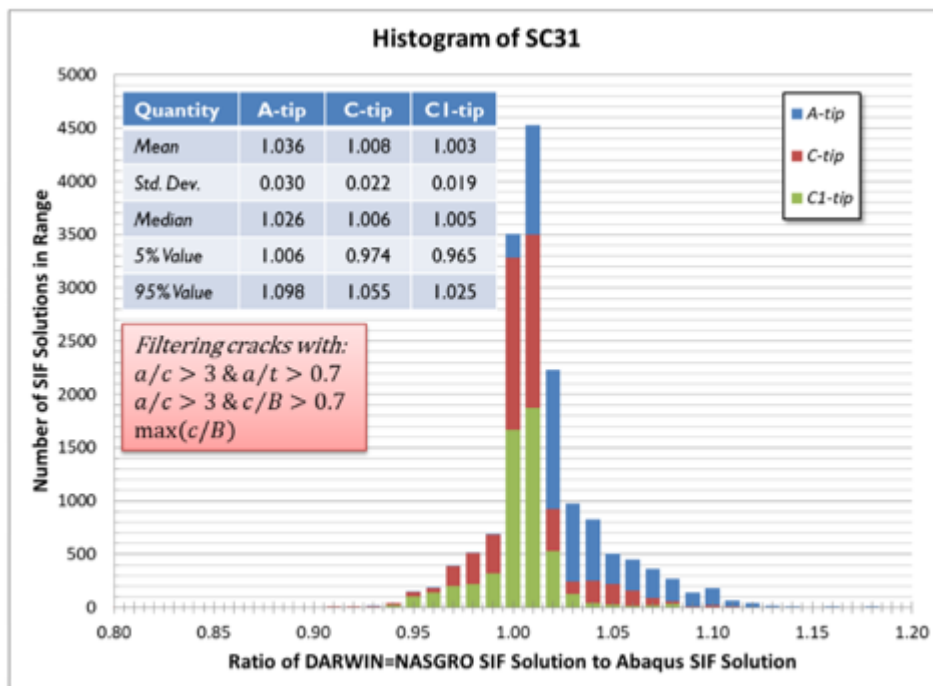


Figure B- 21. Histogram of SC31 SIFs vs. Abaqus SIFs

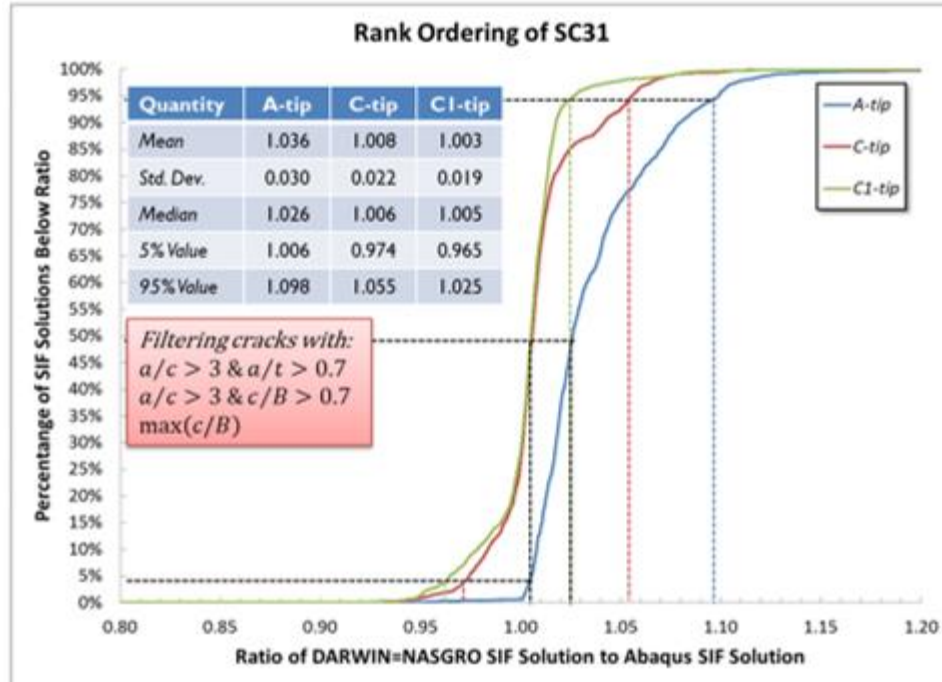


Figure B- 22. Rank ordering of SC31 SIFs vs. Abaqus SIFs

B.9 Univariant embedded crack model (EC05)

Figure B- 4 shows a representation of the univariant embedded crack-in-plate solution that is incorporated into DARWIN and NASGRO: EC05. This geometry represents an elliptical embedded crack in a plate that has major dimensions for the width, thickness, crack offset, and crack tip lengths. In EC05, stress varies along the X-direction that is aligned with the a -tip. That is, EC05 can only represent univariant stress gradients.

Table B- 10 indicates the minimum and maximum dimensions of the crack tip solution EC05 as well dimensions for the FEA. LHS was applied to the geometric ratios for crack shape (a/c), crack depth (a/t and $a/(t - B_t)$), and crack length (c/W and $c/(W - B)$). Note that many of these geometries are unstable, e.g., very elongated crack geometries will grow to more circular crack shapes. We excluded geometries that were outside of the acceptable ratios of W/t as shown in Table B- 10. There are 205 total geometries in the SIF solutions matrix.

Table B- 10. Minimum and maximum dimensions of the crack tip solution EC05 and FEA models

SIF	a/c		a/B_t		$a/(t - B_t)$		c/B_w		$c/(W - B_w)$		W/t	
	Min	Max	Min	Max	Min	Max	Min	Max	Min	Max	Min	Max
EC05	0.01	10	0	0.99	0	0.99	0	0.99	0	0.99	N/A	N/A
FEA	0.1	10	0.01	0.9	0.01	0.9	0.01	0.9	0.1	0.9	0.1	10

Table B- 11 presents traction gradients applied to EC05 in the verification study. The traction gradients include univariant functions. The total number of solutions for the EC05 verification study is 1025.

Table B- 11. Traction gradients applied to surface cracks in verification study

Application	Equation
Crack Face	Uniform
Crack Face	$1 - X/t$
Crack Face	$1 + (1 - X/t)^2$
Crack Face	$2 - (1 - 2X/t)^2$
Crack Face	$1 - (1 - 2X/t)^4$

The crack growth rates differ from tip-to-tip for the same loading, e.g., the position of one tip may be effectively stationary relative to another tip that grows at a much higher rate. Here, the stationary crack tip may be located in a low stress region or far from a boundary. The stationary tip may also represent a non-physical crack tip, e.g., the a -tip when $a/c \gg 1$. We label stationary tips as tips that grow at 10% the rate of the maximum growth tip. (Here, the crack growth rate is approximated as a Paris equation with exponential coefficient of 3.) These stationary tips are removed from the following results.

Figure B- 23 through B- 26 show predicted geometry correction factors from DARWIN against Abaqus geometry correction factors. Figure B- 27 provides a histogram of ratios of EC05 SIFs vs. FEA SIFs. Figure B- 28 provides the rank ordering of the EC05 SIF ratio to the Abaqus SIF ratio. EC05 results are slightly higher than the FEA results – on average by about one percent. At the a -tip, 90% of the EC05 solutions are between -0.1% and 4.4% of the FEA solutions. At the $a1$ -tip, 90% of the EC05 solutions are between -0.2% and 5.7% of the FEA solutions. At the c -tip, 90% of the EC05 solutions are between -0.9% and 4.7% of the FEA solutions. At the $c1$ -tip, 90% of the EC05 solutions are between -1.1% and 5.1% of the FEA solutions.

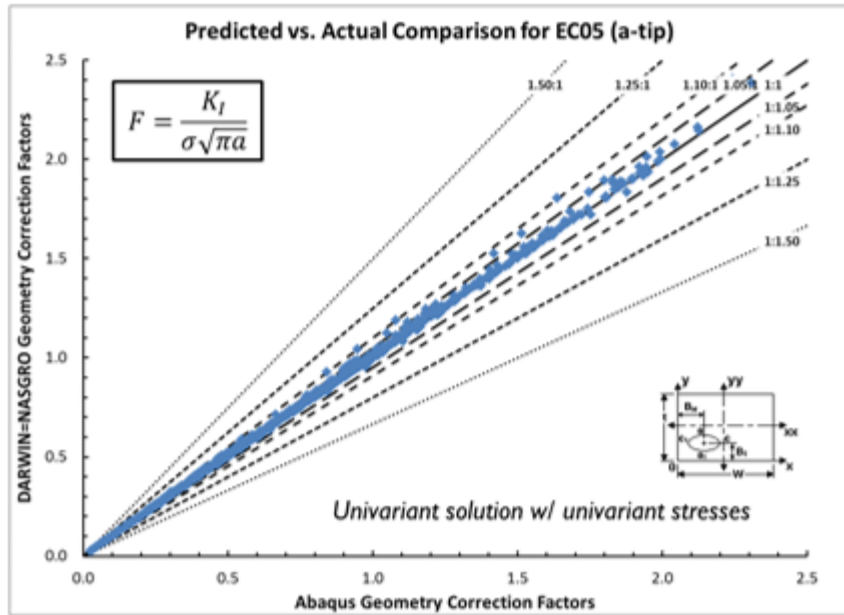


Figure B- 23. EC05 (a-tip) geometry correction factors vs. Abaqus

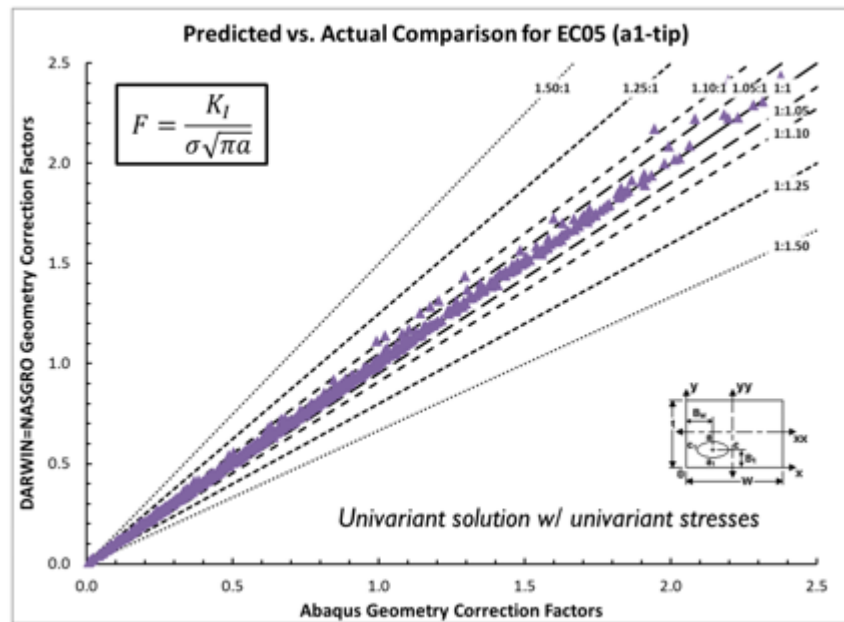


Figure B- 24. EC05 (a1-tip) geometry correction factors vs. Abaqus

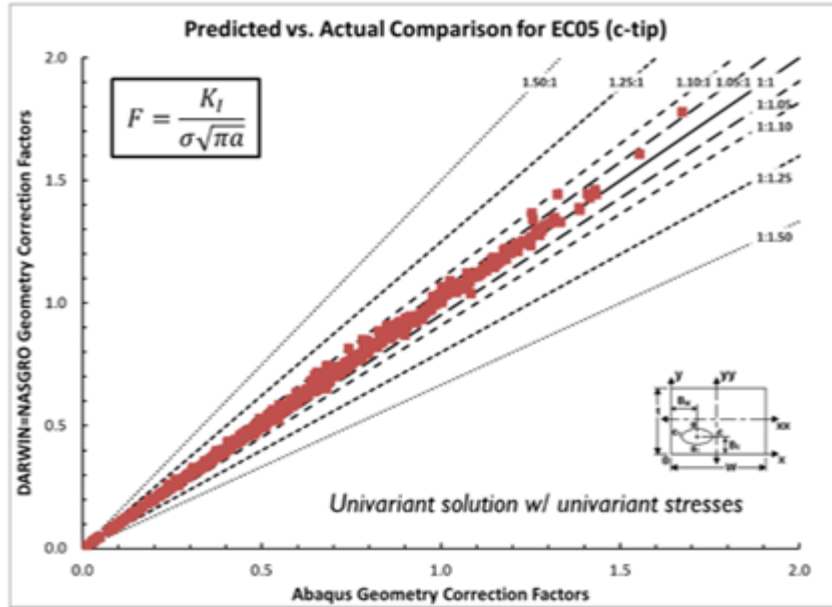


Figure B- 25. EC05 (c-tip) geometry correction factors vs. Abaqus

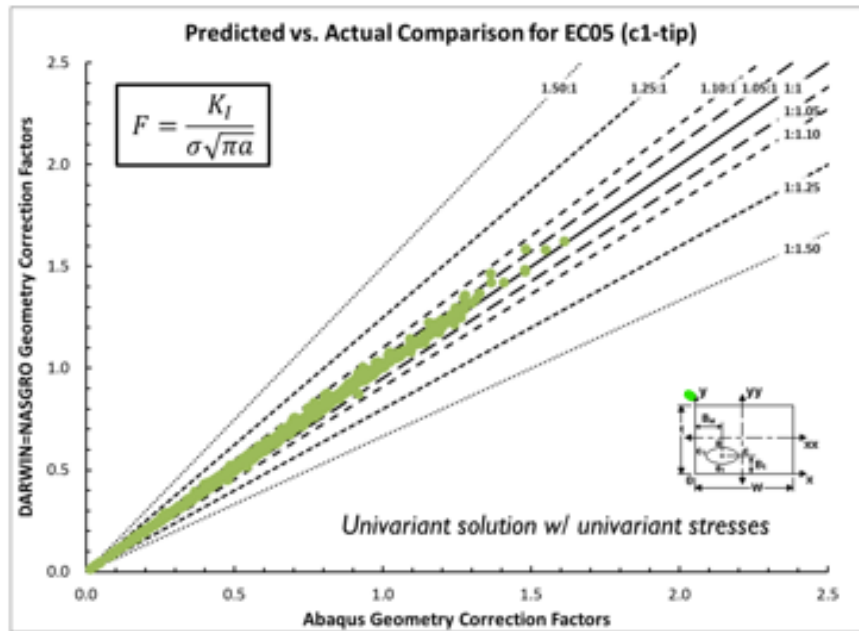


Figure B- 26. EC05 geometry correction factors vs. Abaqus (cont)

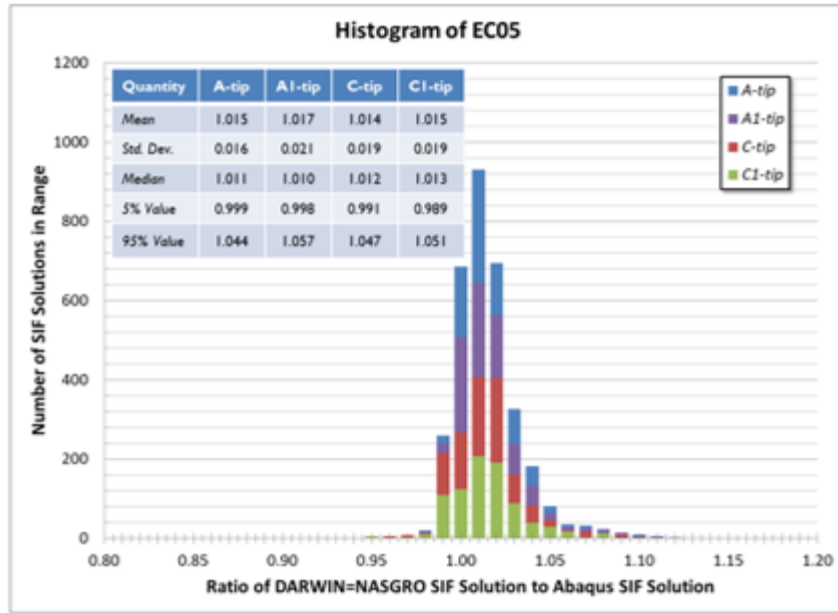


Figure B- 27. Histogram of EC05 SIFs vs. Abaqus SIFs



Figure B- 28. Rank ordering of EC05 SIFs vs. Abaqus SIFs

B.10 Bivariant embedded crack model (EC04)

Figure B- 4 shows a representation of the bivariant embedded crack-in-plate solution that is incorporated into DARWIN and NASGRO: EC04. This geometry represents an elliptical embedded crack in a plate that has major dimensions for the width, thickness, crack offset, and crack tip lengths. In EC04, stress varies along the X-direction, aligned with the a -tip, and varies along the Y-direction, aligned with the c -tip. That is, EC04 can represent bivariant stress gradients.

Table B- 12 indicates the minimum and maximum dimensions of the crack tip solution EC04 as well dimensions for the FEA. LHS was applied to the geometric ratios for crack shape (a/c), crack depth (a/t and $a/(t - B_t)$), and crack length (c/W and $c/(W - B_w)$). Note that many of these geometries are unstable, e.g., very elongated crack geometries will grow to more circular crack shapes. We excluded geometries that were outside of the acceptable ratios of W/t as shown in Table B- 12. There are 205 total geometries in the SIF solutions matrix. Table B- 13 presents traction gradients applied to EC04 in the verification study. The total number of solutions for the EC04 verification study is 2460.

Table B- 12. Minimum and maximum dimensions of the crack tip solution EC04 and the FEA models

SIF	a/c		a/B_t		$a/(t - B_t)$		c/B_w		$c/(W - B_w)$		W/t	
	Min	Max	Min	Max	Min	Max	Min	Max	Min	Max	Min	Max
EC04	0.01	10	0	0.99	0	0.99	0	0.99	0	0.99	N/A	N/A
FEA	0.1	10	0.01	0.9	0.01	0.9	0.01	0.9	0.1	0.9	0.1	10

Table B- 13. Traction gradients applied to surface cracks in verification study

Application	Equation
Crack Face	Uniform
Crack Face	$1 - Y/t$
Crack Face	$1 + X/W$
Crack Face	$1 - 1/2 \times (Y/t + X/W)$
Crack Face	$1 + (1 - Y/t)^2$
Crack Face	$2 - 1/2 \times (1 - X/W + Y/t)^2$
Crack Face	$1 + 1/2 \times (X/W + (1 - Y/t)^2)$
Crack Face	$3 - (1 - 2X/W)^2 - (1 - 2Y/t)^2$
Crack Face	$3 - (1 - 2X/W)^4 - (1 - 2Y/t)^4$

Application	Equation
Crack Face	$2 - (1 - 2Y/t)^2$
Crack Face	$3 - (1 - 2X/W)^4 - (1 - 2Y/t)^2$
Crack Face	$1 - (1 - 2Y/t)^4$

The crack growth rates differ from tip-to-tip for the same loading, e.g., the position of one tip may be effectively stationary relative to another tip that grows at a much higher rate. Here, the stationary crack tip may be located in a low stress region or far from a boundary. The stationary tip may also represent a non-physical crack tip, e.g., the *a*-tip when $a/c \gg 1$. We label stationary tips as tips that grow at 10% the rate of the maximum growth tip. (Here, the crack growth rate is approximated as a Paris equation with exponential coefficient of 3.) These stationary tips are removed from the following results.

Figure B- 29 through B- 32 show predicted geometry correction factors from DARWIN against Abaqus geometry correction factors. Figure B- 33 provides a histogram of ratios of EC04 SIFs vs. FEA SIFs. Figure B- 34 provides the rank ordering of the EC04 SIF ratio to the Abaqus SIF ratio. EC04 results are slightly higher than the FEA results – on average by about one percent. At the *a*-tip, 90% of the EC04 solutions are between -1.0% and 4.3% of the FEA solutions. At the *a*1-tip, 90% of the EC04 solutions are between -1.1% and 5.3% of the FEA solutions. At the *c*-tip, 90% of the EC04 solutions are between -1.9% and 3.9% of the FEA solutions. At the *c*1-tip, 90% of the EC04 solutions are between -2.0% and 4.7% of the FEA solutions.

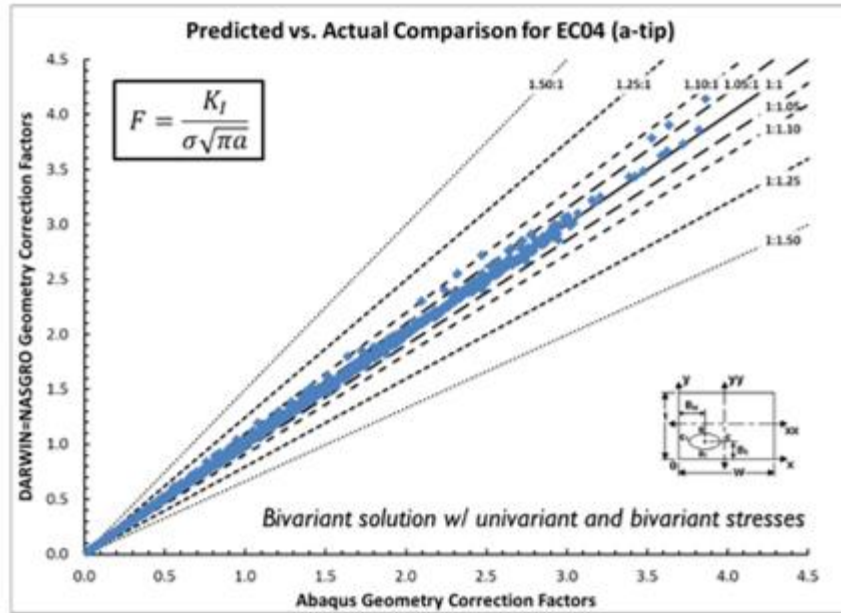


Figure B- 29. EC04 (a-tip) geometry correction factors vs. Abaqus

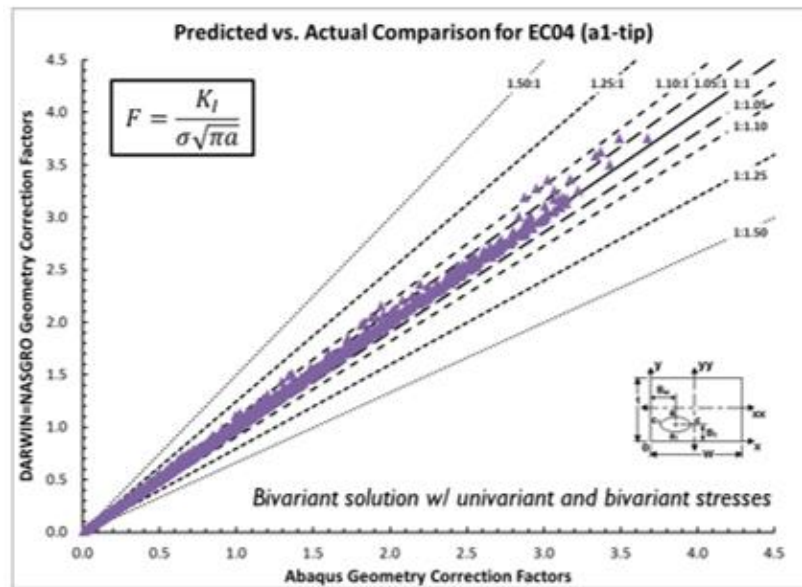


Figure B- 30. EC04 (a1-tip) geometry correction factors vs. Abaqus

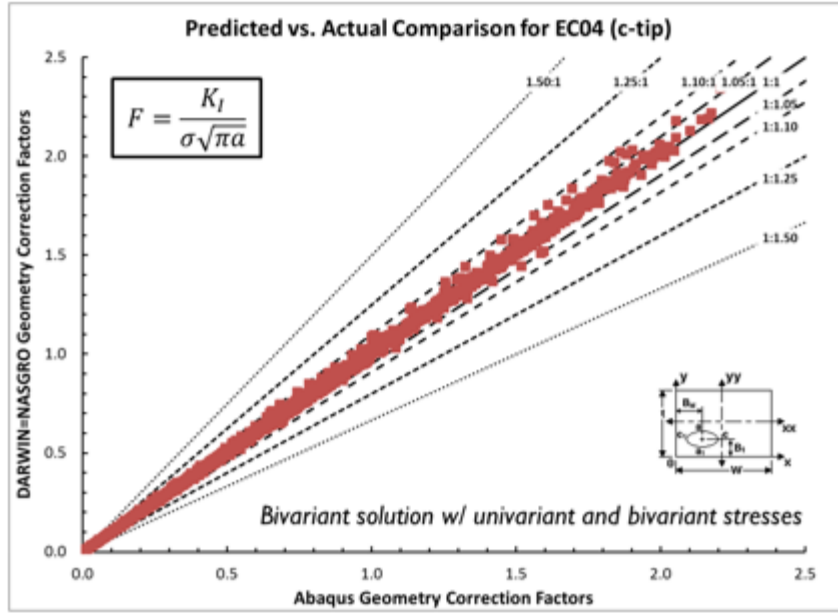


Figure B- 31. EC04 (c-tip) geometry correction factors vs. Abaqus

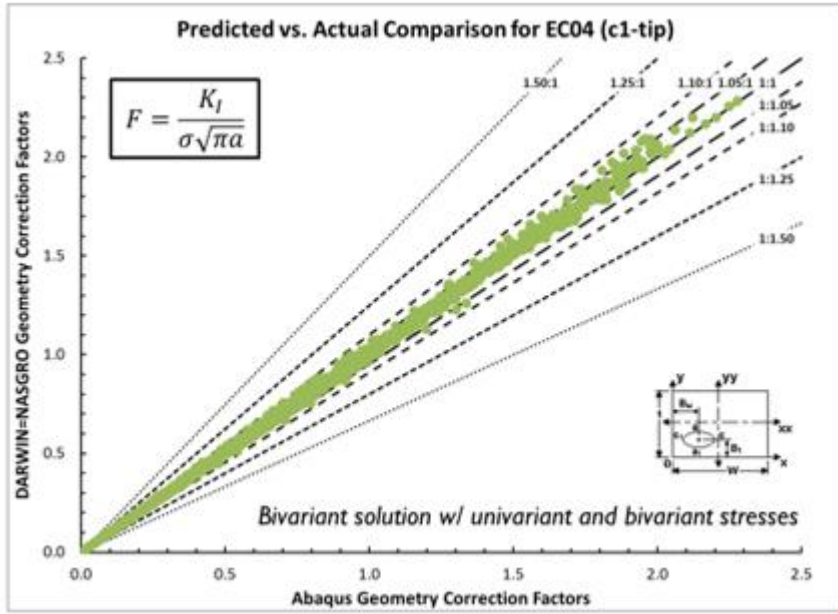


Figure B- 32. EC04 (c1-tip) geometry correction factors vs. Abaqus

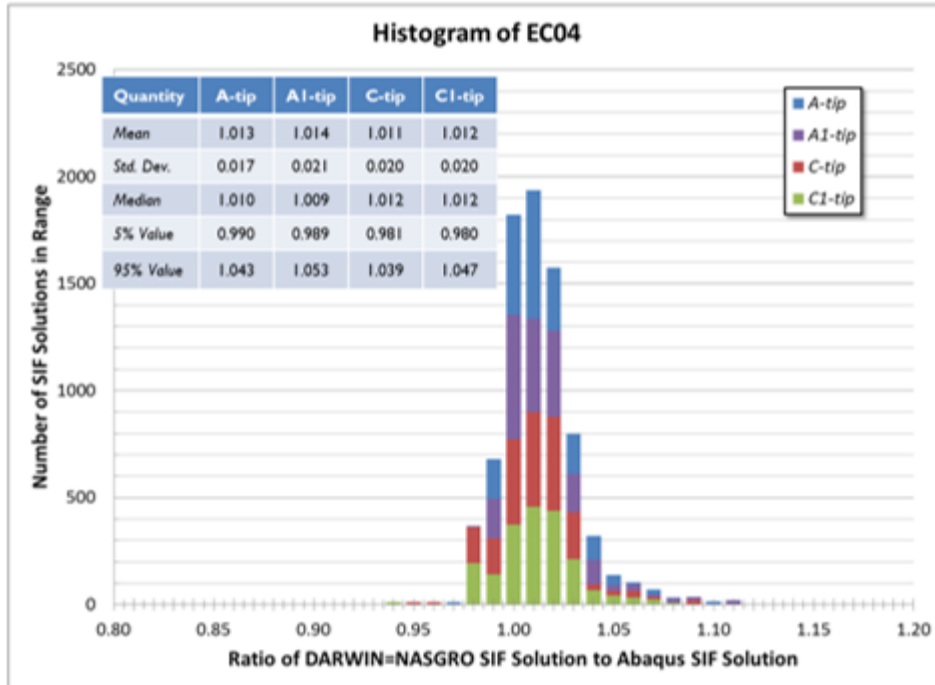


Figure B- 33. Histogram of EC04 SIFs vs. Abaqus SIFs

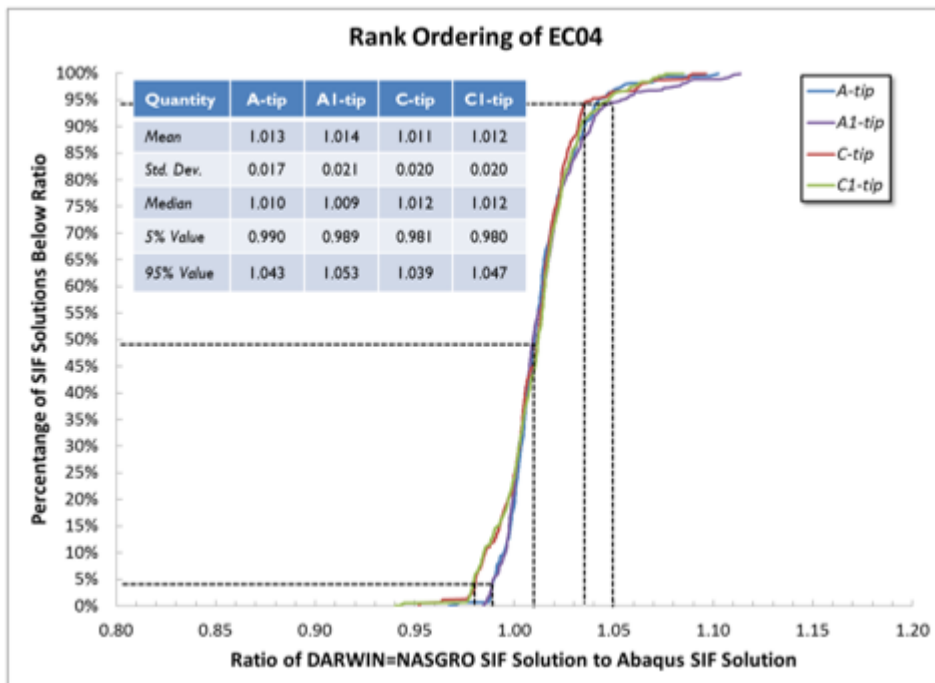


Figure B- 34. Rank ordering of EC04 SIFs vs. Abaqus SIFs.

B.11 Verification for cracks at holes- CC08 and CC10

Overview

This section provides an overview of verification efforts for the DARWIN and NASGRO SIF solutions CC08 and CC10. These solutions are weight function (WF) SIF solutions for corner cracks at holes in plates. As WF solutions, these solutions support arbitrary loading by either integrating either univariant stresses (CC08) or bivariant stresses (CC10) from the uncracked geometry over the cracked surface. SwRI originally developed these solutions in the early 2000s (Enright, et al., 2003). At that time, SwRI verified CC08 and CC10 using available methodologies. New methodologies (described in the previous section) offer a more robust verification scheme that covers the entire geometric space and lower-order, orthogonal components of the stress gradient. Results from CC10 suggested some areas for improvement. This work documents efforts to develop an improved solution, CC26. This work provides credibility for FCG predictions using CC08 and CC10. These solutions are generally slightly conservative under remote loadings and for low-order polynomial loadings.

Verification approach

This work follows earlier efforts to verify SIF solutions for elliptical embedded, surface, and corner cracks in plates.

The current work focuses on the geometry shown in Figure B- 35. This geometry features the following dimensions:

- W - plate width;
- t - plate thickness;
- B - hole offset from plate;
- D - hole diameter;
- a - depth of crack in the thickness direction; and
- c -length of crack in the width direction.

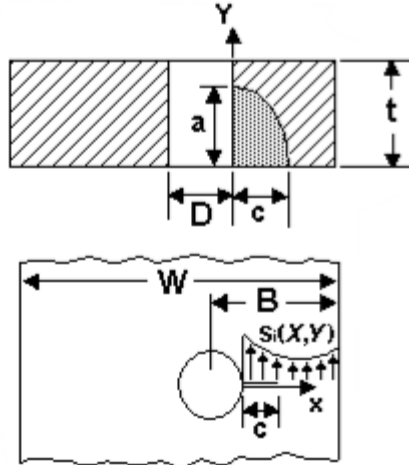


Figure B- 35. Geometry of a quarter-elliptical corner crack at a hole offset in a plate

This nomenclature reflects the NASGRO definition of a and c . DARWIN inconveniently reverses these definitions. CC08 and CC10 center the crack on the hole normal to the plate height (H). The crack plane divides the hole into two equal halves. There is no fastener in the hole, *i.e.*, it is an open hole. For all analyses, we position the crack on the short ligament side of the hole, *i.e.*, $B \leq 0.5 \times W$.

The LHS methodology (Simpson, Lin, & Chen, 2001) samples over the following geometric ranges using the capabilities implemented within the NESSUS® Response Surface Toolkit® (McFarland, Dimeo, & Bichon, 2017):

- $\alpha \in [0,1]$: α is a crack size parameter defined below;
- $\log_2(a/c) \in [-1,2]$: a/c defines the crack shape and ranges over $a/c \in [0.5,4]$;
- $\log_2(D/2t) \in [-2,1]$: $D/2t$ sets the relative diameter to thickness and ranges over $D/2t \in [0.25,2]$;
- $2B/W \in [0.2,1]$: $2B/W$ provides the relative hole offset in the plate; and
- $\log_2(D/B) \in [-3,0.5]$: D/B indicates the relative hole size to offset and ranges over $D/B \in [0.125,0.707]$.

The first two parameters define the crack size and shape. The remaining three parameters set the plate dimensions. The "log" sampling adopted here reflects that certain parameters (*i.e.*, a/c) are best treated as ratios with equally likely values above and below one. Sampling on the log-space ensures that this is not unnaturally truncated.

The crack size parameter (α) sets the crack depth a as follows:

$$a = [0.025 + \Delta \times \alpha] \times t, \quad (\text{B-11})$$

where:

$$\Delta = \min\left(0.9, \frac{9}{5} \times \frac{a}{c} \times \frac{D}{2t} \times \left(\frac{B}{D} - \frac{1}{2}\right)\right) - 0.025. \quad (\text{B-12})$$

The Δ -term ensures that the crack remains within the following limits:

$$0.025 \leq \frac{a}{t} \leq 0.9, \quad (\text{B-13})$$

$$\frac{c}{B - D/2} \leq 0.9. \quad (\text{B-14})$$

These limits ensure that the crack tips remain well-contained in the plate boundaries.

Figure B- 36 summarizes the geometries sampled by the LHS process using the Response Surface Toolkit developed at SwRI. There are 500 geometries shown here. This figure demonstrates that the LHS process leads to geometries that fill the space over multiple dimensions. Diagonal entries show the distribution of parameters across the sampled variable. Off-diagonal entries show how different parameters are related to other parameters. Geometric parameters show limited correlation with other parameters. Limited correlation provides a larger sampling of the solution space for the same number of parameters. Limited correlation also prevents clustered solutions from biasing the statistical results.

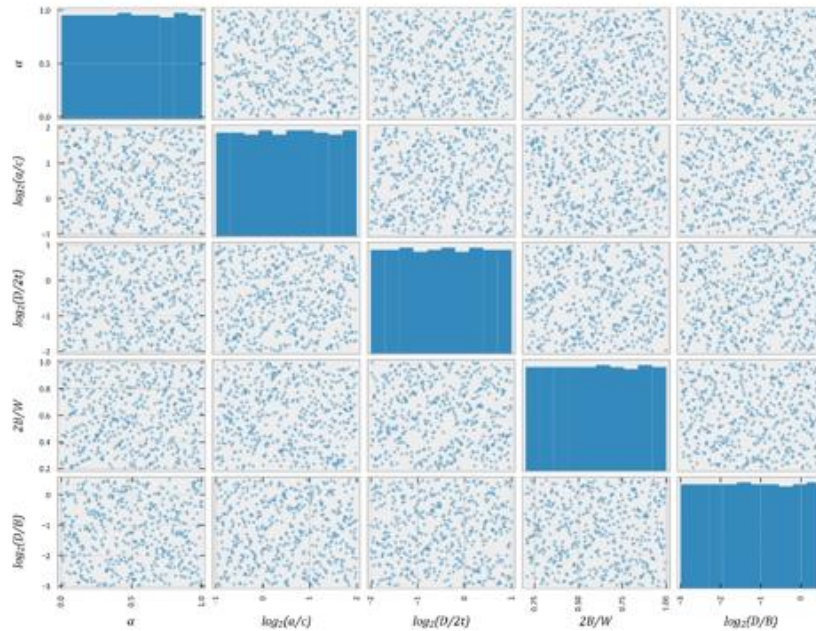


Figure B- 36. Geometries selected for this verification study by the LHS method

Applied stresses

The WF approach computes SIFs by integrating the WF ($w(x, y)$) times stresses from the corresponding uncracked geometry ($\sigma_n(x, y)$) over the cracked area (for bivariant WFs). Here, $\sigma_n(x, y)$ are the stresses normal to the cracked area. These stresses may develop due to remotely applied stresses on the far boundaries. For a simple plate with a hole, commonly applied remote stresses include:

- S_0 – uniform stress applied at far boundary;
- S_1 – linearly-varying stress across the plate thickness;
- S_2 – linearly-varying stress across the plate width.

In this geometry, these applied remote stresses result in complex and bivariant stress gradients across the uncracked plane due to the hole and 3D effects. This work investigates SIF values driven by these remote stress quantities as they provide a practical example of real stresses in engineering structures. Unfortunately, there are no closed-form expressions to provide the impact of these remote stresses on the stress gradients over the crack plane. Approximate expressions may be determined by interpolating over a database of stress gradients from computational analyses. This interpolation introduces limited errors for most geometries.

We also determine SIF error metrics for combinations of orthogonal polynomials applied to crack faces. The total error will then be the sum of errors for a stress combination times the magnitude of that stress combination from a remotely applied loading. We focus on the lowest order stress gradients that will have the largest magnitudes. We (arbitrarily) select the Legendre polynomials ($\sigma_i(\zeta)$) for this analysis with the domain $\zeta \in [0,1]$ and with $i \in \mathbb{Z}; i \geq 0$. These polynomials satisfy the following relationship:

$$\int_0^1 \sigma_m(\zeta) \sigma_n(\zeta) d\zeta = \frac{1}{2n+1} \delta_{mn}, \quad (\text{B-15})$$

where δ_{mn} is the Kronecker delta such that $\delta_{mn} = 1$ if $m = n$ and $\delta_{mn} = 0$ otherwise. In this report, we limit our analyses to the first two Legendre polynomials:

$$\sigma_0(\zeta) = 1; \quad (\text{B-16})$$

$$\sigma_1(\zeta) = 2\zeta - 1; \quad (\text{B-17})$$

Equations B-16 and B-17 provide the basis for stresses applied to the crack. We reverse the sign $\sigma_i(\zeta)$ if $\sigma_i(\zeta) \rightarrow -1$ as $\zeta \rightarrow 1$. This ensures that small cracks (as $\zeta \rightarrow 0$) have a positive driving force. Here, we define a stress polynomial term P_{ij} over the normalized domain (ξ, η) as:

$$P_{ij}(\xi, \eta) = \sigma_i(\eta)\sigma_j(\xi), \quad (\text{B-18})$$

with $\xi = x/(B - D/2)$ and $\eta = y/t$. The stresses applied in this work are shown in Table B-14.

Table B- 14. Stresses applied during FEA of corner crack at a hole by step time

Stress	Region	Description
S_0	Far Boundary	Uniform Tension
S_2	Far Boundary	In-Plane Bend
S_1	Far Boundary	Out-of-Plane Bend
P_{00}	Cracked Area	$\sigma_0(\eta) \times \sigma_0(\xi)$
P_{01}	Cracked Area	$\sigma_0(\eta) \times \sigma_1(\xi)$
P_{10}	Cracked Area	$\sigma_1(\eta) \times \sigma_0(\xi)$
P_{11}	Cracked Area	$\sigma_1(\eta) \times \sigma_1(\xi)$
S_0	Far Boundary	Uniform Tension

Analyses

During this work, we evaluated 500 geometries to compute SIF values at the *a*-tip and *c*-tip. We exploited the Python scripting capability in Abaqus/CAE to generate FEA (Sobotka & McClung, 2018). The Python interface enables user-created scripts to define the geometric configuration, apply loads, describe the material response, set meshing parameters, and create domain integral definitions. Python scripting also supports data processing and transfer, e.g., to/from Excel spreadsheets. Python also features libraries that simplify the scripting process. There are several advantages to the scripting interfaces besides the obvious efficiencies, e.g., consistent model definitions and more rigorous modeling techniques. Please refer to earlier comments in this document for details on the FEA set-up, execution, and post-processing.

B.12 Results for CC08

During this work, automated scripting capabilities generated many figures documenting discrepancies and their variability. For every (appropriate) loading and for every crack tip, figures were generated that showed differences, relative errors (linear and log scales), and absolute error (log scale) vs. eight geometric parameter combinations (e.g., *a/t*). These figures provide insight into how discrepancies vary with geometric parameters. These figures are not reproduced here due to their quantity. Instead, this section presents selected statistical graphs that demonstrate SIF solution quality.

These statistical graphs employ the geometry correction factor $F = K_I/\sigma \times \sqrt{\pi a}$, where σ is the stress magnitude set equal to one. The following figures provide the relative error metric (E_R) defined as:

$$E_R = \frac{F^{CC\#\#} - F^{FEA}}{F^{FEA}} \times 100. \quad (\text{B-19})$$

Here, E_R is defined as a percentage. These graphs censor small geometry correction values ($F < 0.1$). Small values provide a limited contribution to FCG lives and may artificially increase the relative error values due to round-off errors. Note that this definition of error differs from the error definition in the earlier sections. The current definition of error can be mapped onto the earlier definition of error (based on ratios of F) through the following expression: $0.01 \times E_R + 1$.

CC08 is a univariant WF solution for a corner crack at a hole in a plate. Stresses are assumed to vary along the width direction and are assumed constant along the thickness direction. In reality, 3D stresses are always bivariant at a hole in a plate, and so there will always be some error introduced by using a univariant solution. However, the univariant assumption is sometimes a convenient efficiency with adequate accuracy. Figure B- 37 provides relative error metrics for CC08 using NASGRO v9.2. These solutions are identical to the solutions in DARWIN v9.2. This figure provides results for remote loadings S_0 and S_2 and crack plane stresses P_{00} and P_{01} . Here, (a) shows the a -tip result and (b) shows the c -tip result.

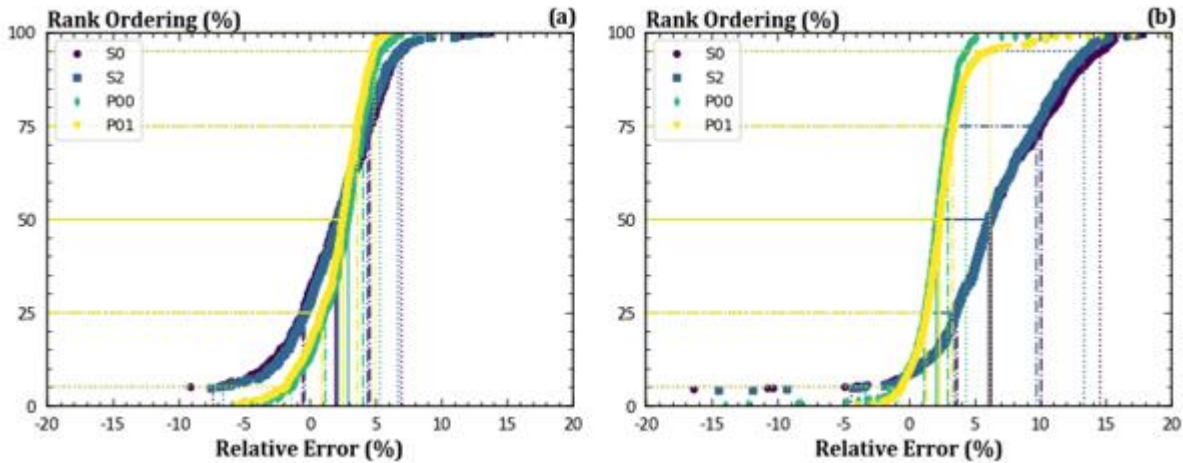


Figure B- 37. Relative error metrics for CC08 geometry correction factors

For crack plane stresses, errors are modest, and the solution is slightly conservative. Median values of relative error are between 2-3% for both crack tips. Most solutions are within 5% of the value from a detailed FEA.

In NASGRO, crack-plane stress gradients for the WF solution can also be defined by interpolating over a database of crack-plane stresses at pre-defined uncracked geometries for specific remote loadings: S_0 is uniform remote tension and S_2 is an in-plane remote linear bending stress. The database of crack-plane stresses was determined using high-fidelity analyses of the uncracked geometries. Critically, those analyses assumed a 2D plane-stress, geometric formulation and represent mid-plane stresses in a 3D plate. These 2D stresses in NASGRO are generally higher than the stresses at the free surface of a 3D plate, and the higher stresses may result in slightly more conservative SIF values at the surface. WF calculations of CC08 use the 2D stress gradients from remote loading. Results from 3D FEA set the remote loadings directly on the remote boundaries of the geometry.

For these NASGRO remote loadings, errors at the a -tip are modest with median values between 2-3%. Errors at the c -tip are much larger with median values around 6%. Many solutions at the c -tip have errors in excess of 5% from the FEA. These larger errors probably reflect issues with the univariant uncracked stresses. These particular NASGRO results are not directly relevant to DARWIN because DARWIN uses only actual crack plane stresses. Nevertheless, they are a useful reminder that using any univariant stress gradient in DARWIN will lead to some small additional errors in calculating SIF values with CC08.

To be more specific, crack plane stresses under S_0 and S_2 remote loading generally decrease slightly near the plate surface due to 3D effects close to the hole. A DARWIN CC08 analysis using a univariant stress gradient extracted away from the edge (e.g., mid-plane) may be slightly conservative compared to the actual SIF value from a 3D FEA under a remotely imposed loading that reflects the actual bivariant stress distribution on the crack plane. For example, CC08 could be the post-transition geometry for a DARWIN analysis that started with a univariant surface crack (SC18) in the bore of the hole, since the original SC18 gradient is used for the post-transition CC08. Alternatively, a DARWIN CC08 analysis using a univariant stress gradient extracted at the plate surface (which is the standard protocol in DARWIN when CC08 is the initial crack type) may be slightly non-conservative, because the actual crack plane stresses will be slightly higher away from the edge. That is, CC08 produces non-unique SIF values for identical geometries dependent on the initial crack type due to how DARWIN sets univariant stress gradients for corner cracks and surface cracks. Therefore, it is generally best practice to use the bivariant solution for a DARWIN analysis that begins as a corner crack at a hole. This principle is generally true for any univariant SIF solution; it may give inaccurate results if the actual crack plane stress distribution is significantly bivariant. Finally, these results highlight that the accuracy of any DARWIN SIF solution requires an accurate FEA to determine crack plane

stresses, even when bivariate stresses are extracted. These SIF verification exercises cannot address the potential influence of inaccurate stress inputs.

Overall, CC08 tends to be slightly conservative and contributes towards conservative crack growth life predictions when appropriate univariate stress gradients are used.

B.13 Results for CC10

CC10 is a bivariate WF solution for a corner crack at a hole in a plate. Figure B- 38 provides relative error metrics for CC10 using NASGRO v9.2. These solutions are identical to the solutions in DARWIN v9.2. This figure provides results for crack plane stresses. Figure B- 38(a) shows the *a*-tip result. Figure B- 38 (b) shows the *c*-tip result. These results suggested a conservative, but perhaps overly conservative solution for most geometries. Further investigations suggested that the original CC10 might be slightly non-conservative for vanishingly small cracks. These investigations also indicated errors for highly offset holes and long cracks.

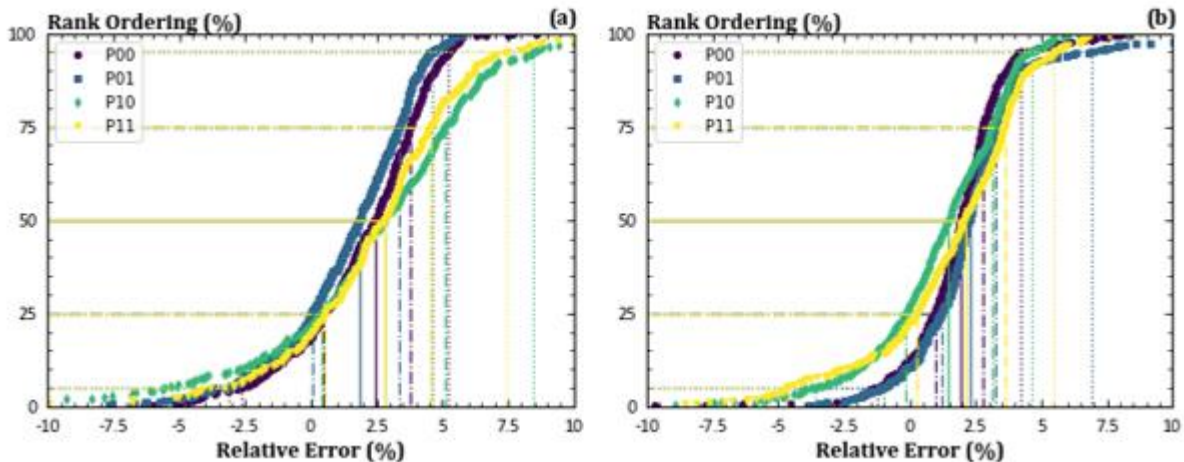


Figure B- 38. Relative error metrics for CC10 geometry correction factors

B.14 Development and verification of CC26

The results in the previous section led us to reevaluate CC10. CC10 was originally developed more than 15 years ago. At that time, we did not have capabilities to build large databases of solutions rapidly and (more or less) automatically. Consequently, CC10 was calibrated using results from only 72 geometries.

At the current time, we have developed capabilities to rapidly build, analyze, and post-process FEAs. Furthermore, computational resources have improved significantly, allowing larger

models that support more accurate solutions. These capabilities enable a new solution matrix to be built with the following geometries:

$$\frac{D}{2t} = 0.25, 1.0, 2.0 \quad (\text{B-20})$$

$$\frac{2B}{W} = 0.2, 1.0 \quad (\text{B-21})$$

$$\frac{c}{a} = 0.2, 0.4, 1.0, 2.0 \quad (\text{B-22})$$

$$\frac{c}{B - D/2} = 0.004, 0.1, 0.2, 0.4, 0.7, 0.9 \quad (\text{B-23})$$

$$\frac{a}{t} = 0.004, 0.1, 0.2, 0.4, 0.7, 0.9 \quad (\text{B-24})$$

This solution matrix features 864 new geometries. However, several of these geometries lead to extremely large or extremely small holes relative to the plate width. There are 114 geometries with $D/2B < 0.05$, and there are 140 geometries with $D/2B > 0.95$. These geometries are not realistic. Consequently, we changed the plate width to ensure that $0.05 \leq D/2B \leq 0.95$.

Vanishingly small cracks with $a/t = 0.004$ and $c/(B - D/2) = 0.004$ should not be influenced by the offset, and they are removed from the calibration matrix. Similarly, very small crack ratios in one direction (e.g., the a -tip) paired with much larger crack ratios in the alternative direction (e.g., the c -tip). This means that we eliminated crack pairs with $a/t \geq 0.7$ and $c/(B - D/2) = 0.004$ or $a/t = 0.004$ and $c/(B - D/2) \geq 0.7$. These cracks are unrealistic, and they are removed from the calibration matrix as well. (Note that when a crack is removed from the solution matrix, there is still a value for it in the WF calibration database. This number is provided by a geometrically similar crack, *i.e.*, a vanishingly small crack at a centered hole instead of an offset hole.) These considerations reduce the number of geometries needed to calibrate this geometry. There are also three reference stresses per geometry:

$$\sigma_0 = 1 \quad (\text{B-25})$$

$$\sigma_1 = 1 - x/c \quad (\text{B-26})$$

$$\sigma_2 = 1 - y/a \quad (\text{B-27})$$

These analyses were performed using the scripts built to verify CC08 and CC10. The computational analyses required about four days to complete. Pre-processing and post-processing times required more effort. The resulting SIF values were used to develop a new solution denoted CC26.

Figure B- 39 provides relative error metrics for CC26 using NASGRO v10.0. This figure provides results for crack plane stresses with Figure B- 39(a) showing the a -tip result, and Figure B- 39(b), showing the c -tip result. These results suggest a slightly conservative solution. For

these crack plane stresses, most SIF values are within 5% of the FEA. The revised solution CC26 provides tighter distributions that indicate less error relative to the original CC10 solution.

In addition to the formal verification plots, we also investigated baseline plate geometries and determined SIFs for various crack lengths and crack ratios. For the baseline geometries, we built FEAs of the uncracked models and then extracted stresses along the crack plane. These baseline geometries feature remote loadings of S_0 , S_1 , and S_2 . These results were input to CC26 to drive the SIF calculations.

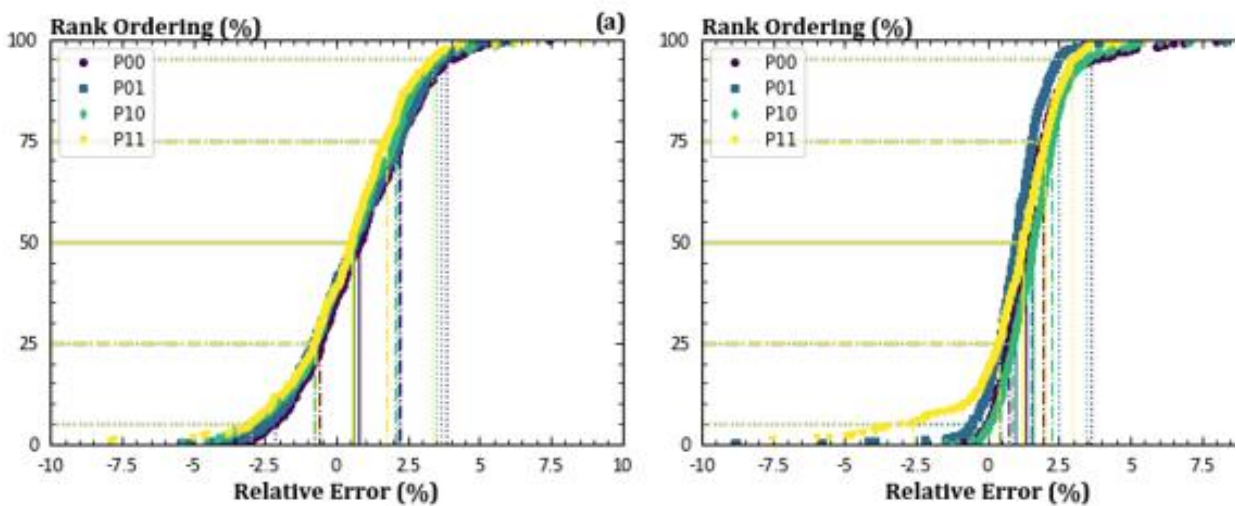


Figure B- 39. Relative error metrics for CC26 geometry correction factors

Figure B- 40 (a-tip) and Figure B- 41 (c-tip) show results from one geometry with $D/2t = 2$, $2B/W = 1$, and $D/2B = 0.25$. In these figures, all remote stress components are zero unless indicated. Here, the SIF values change with increasing crack depth and different crack shapes. In general, the CC10 solution in NASGRO v9.2 and DARWIN 9.2 contains SIF values that deviate mildly from the FEA values. The revised version of CC10 has SIF values that track more closely with the SIF values from the FEAs. Other baseline geometries lead to similar conclusions. These results suggest that replacing the CC10 solution with the revised CC26 solution in DARWIN would lead to more accurate SIF values and more reliable life predictions.

Due to these significant improvements, the new solution was implemented in NASGRO v10.0 as CC26. This new solution will also be integrated into DARWIN in the near future. The specific schedule for implementing this new solution will be decided with guidance from the project Steering Committee.

Inevitably, the new CC26 will result in some differences in FCG life predictions compared to the old CC10 solution. Calculated lives may increase or decrease depending on the geometry, loading, and initial crack size. We do not anticipate that lives will change by more than 40%, with most changes much smaller than that value. The exact change in lives will depend on the use case of the solution.

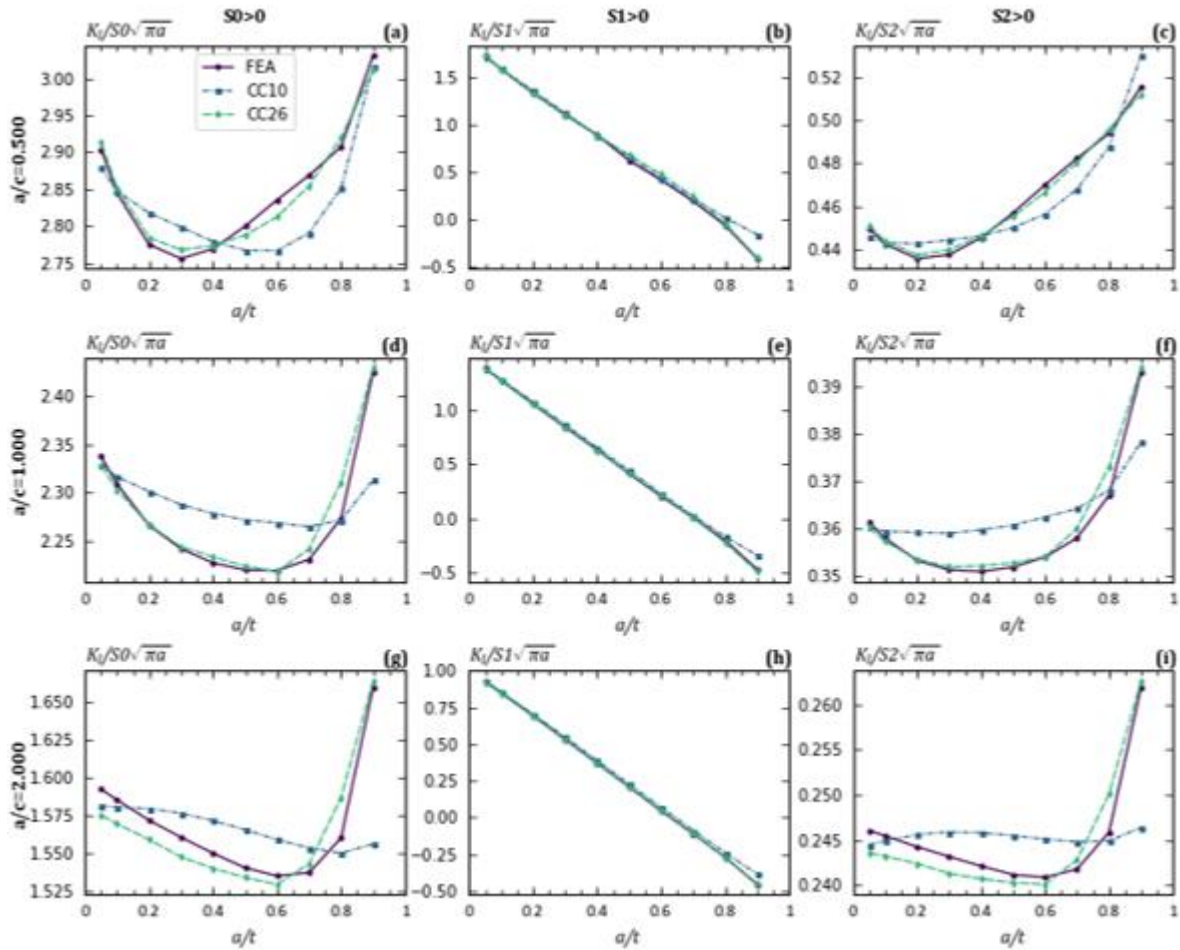


Figure B- 40. Geometric correction factors at the a -tip for CC10 as a function of crack length

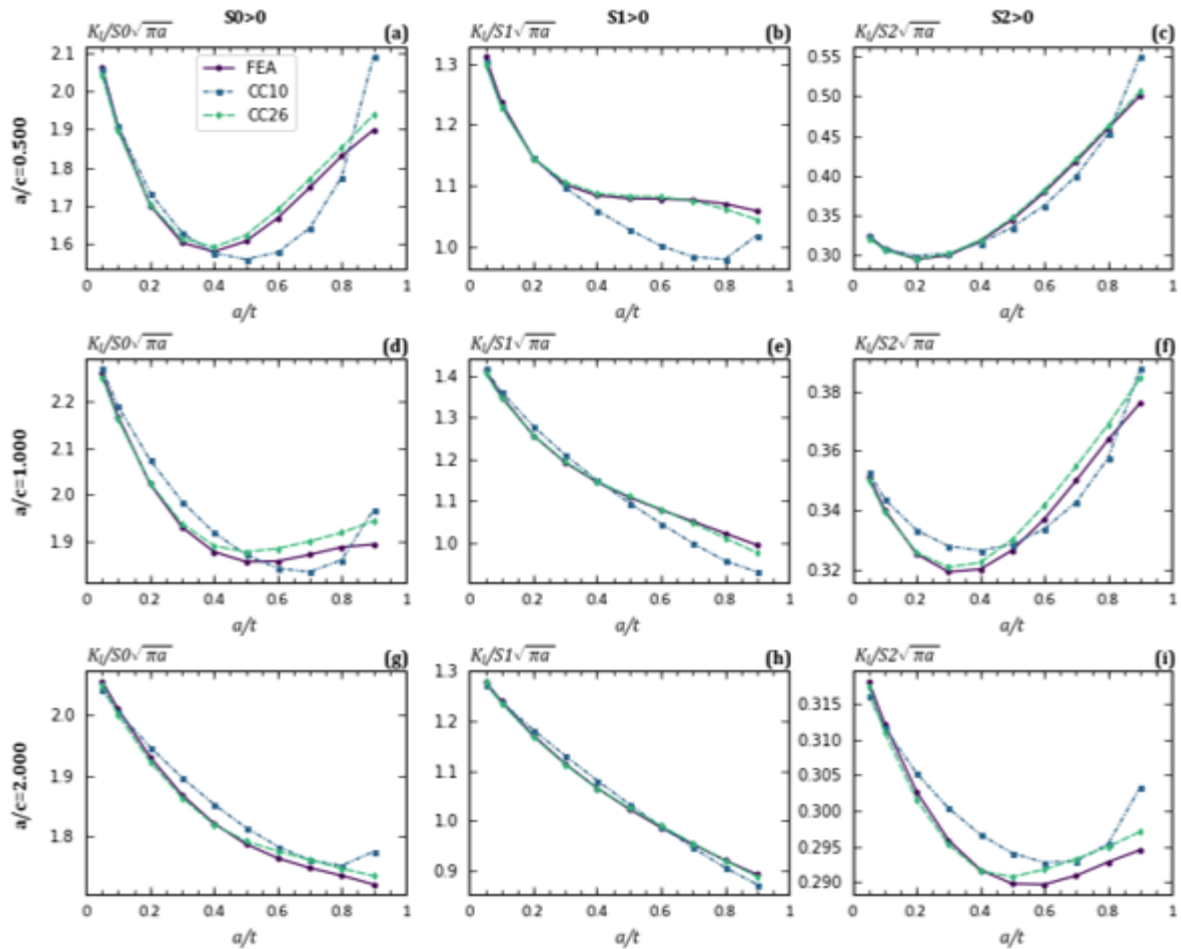


Figure B- 41. Geometric correction factors at the c -tip for CC10 as a function of crack length

B.15 Verification for a crack spanning a chamfer

Overview

Crack case CC12 models a corner crack that fully spans a 45-degree chamfer. CC12 is a bivariate weight-function solution based on the formulation for CC09. Figure B- 42 shows the geometry of this solution.

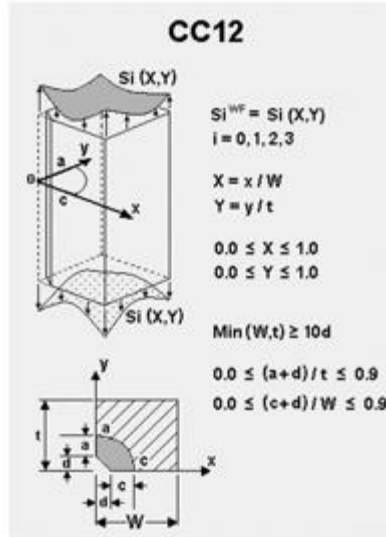


Figure B- 42. Geometry of CC12 - a corner crack spanning a chamfer in a plate

Methodology

SwRI employed the LHS technique to sample geometries from the solution space semi-randomly. Here, we selected points over the range:

$$0.01 \leq \frac{d}{t} \leq 0.1$$

$$1 \leq \frac{W}{t} \leq 10$$

$$0.2 \leq \frac{a}{c} \leq 5$$

$$0.05 \leq \frac{a}{t} \leq 0.9$$

These geometries set the dependent ratio c/W . Physical and computational constraints limit this ratio. Consequently, we only selected geometries that have $0.002 \leq c/W \leq 0.85$. Of the geometries sampled in this work, 503 geometries satisfy these criteria. These geometries were used in the verification efforts. These geometries were built using the Python scripting capabilities described in the earlier sections.

For any geometry, stresses applied to crack faces drive the SIF variation over the crack front. In this work, we focus on three stress variations that support uniform loading and bending loads:

$$S_0 = 1$$

$$S_\xi = \xi = \frac{2x}{W}$$

$$S_\eta = \eta = \frac{2y}{t}$$

Here, S_0 is uniform loading, S_ξ is a bending loading across the width, and S_η is a bending loading across the thickness. Note that S_ξ is symmetric with respect to S_η . Here, loads are set on the crack plane using a user-defined traction function. These loads are applied on the crack face based on the value at the centroid of the element's surface. For vanishingly small elements, this approach trends to the exact solution. Figure B- 43 shows Mises stresses near the crack front for these loading combinations. Here, the geometry is $W/t = 8.35$, $d/t = 0.07$, $a/c = 1.5$, $c/W = 0.04$, & $a/t = 0.45$. Smooth stresses suggest adequate refinement.

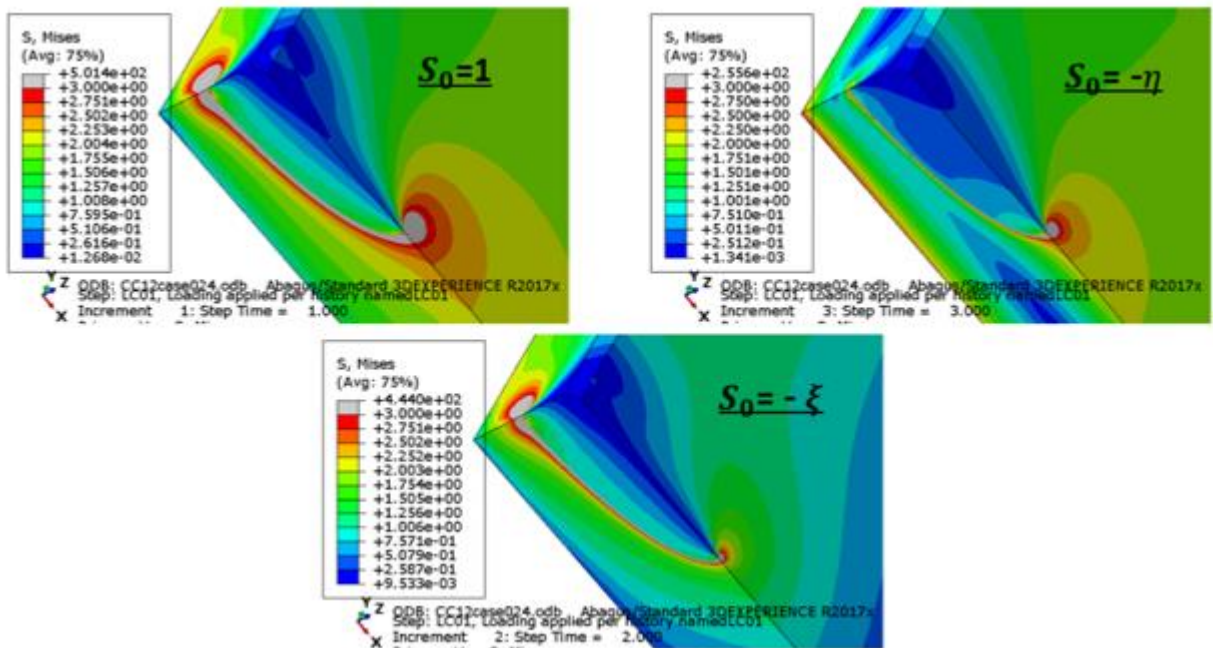


Figure B- 43. Mises stress in the crack region for three crack plane loadings

Results

Figure B- 44, Figure B- 45, and Figure B- 46 show the variation of errors for CC12 under the three loading scenarios. These figures show that for S_0 and S_ξ loading, more than 90% of the solutions have errors less than 5% compared to the FEA value. For S_η loading, most solutions are within 5% of the FEA values. However, there are long tails with errors below -5%. Further review of these solutions reveals that most errors develop for $a/c < 0.3$ coupled with $a/t > 0.6$. These cracks are non-physical and often have very small geometry correction factor values.

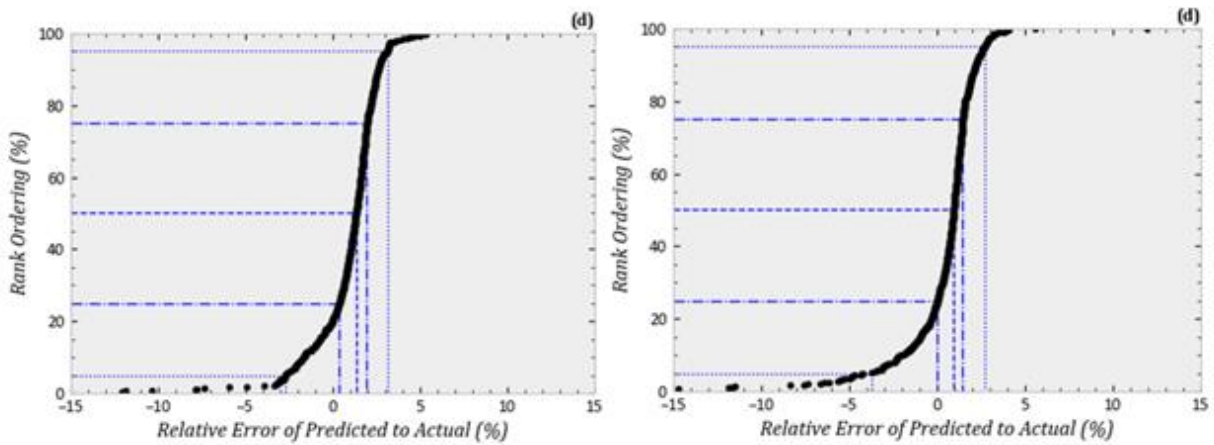


Figure B- 44. Relative error plots of CC12 under S_0 loading at the a -tip (left) and c -tip (right)

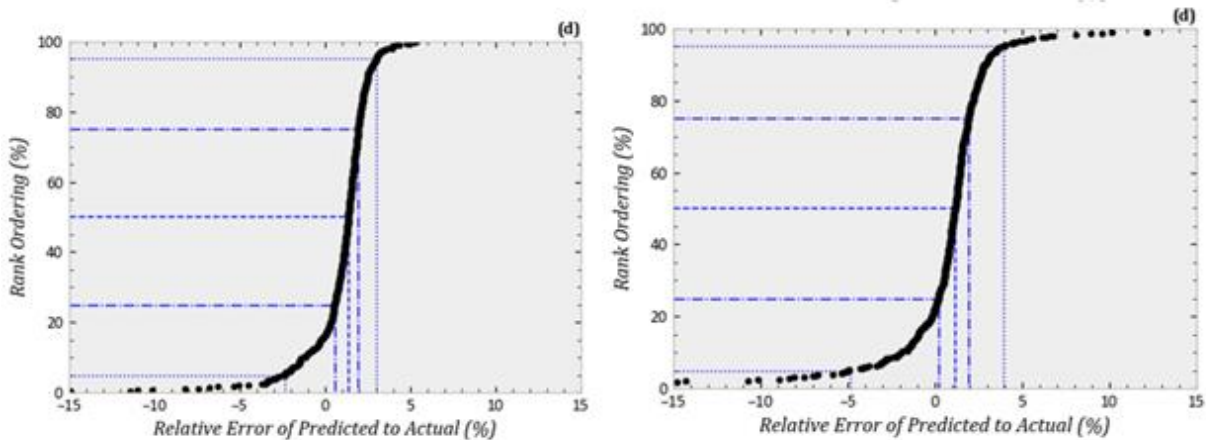


Figure B- 45. Relative error plots of CC12 under S_ξ loading at the a -tip (left) and c -tip (right)

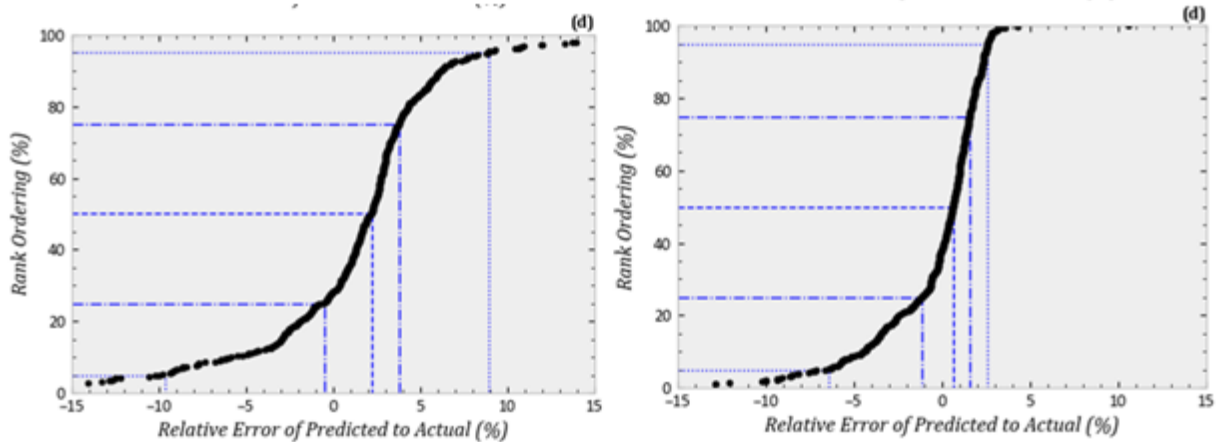


Figure B- 46. Relative error plots of CC12 under S_η loading at the a -tip (left) and c -tip (right)

B.16 Verification for external surface crack in cylinder

Overview

A SIF solution was developed in this grant for an external circumferential semi-elliptical surface crack in a hollow cylinder denoted SC34. Figure B- 47 shows the parametric idealization for this new SIF solution. The characteristic dimensions are measurable with D representing the diameter; t the thickness; a the crack depth; and c the crack half-length along the surface of the cylinder. The new solution has geometric limits defined by $4 \leq D/t \leq 256$, $0 \leq a/t \leq 0.9$, and a wide range of a/c -ratios that depend on other parameters. The new crack case is a weight function solution that employs bivariant stress gradients. It is analogous to other bivariant weight-function solutions in DARWIN, such as SC31 or CC09. Please refer to Appendix A for additional details regarding its formulation, development, and implementation. Note that in this section, we use a and c to refer to the measured crack lengths.

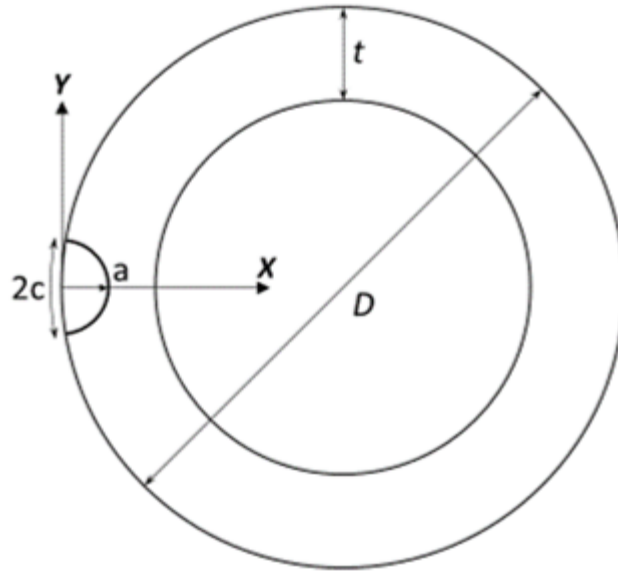


Figure B- 47. Geometric parameterization of SC34

Approach

Verification of SC34 followed the same procedure described previously. The verification process involves semi-randomly sampling geometries from the solution space using the Latin Hypercube Sampling (LHS) methodology to create a space-filling design of experiment. In this work, we selected 500 geometries from the geometric parameters as follows:

$$0.05 \leq \frac{a}{t} \leq 0.9 \quad (\text{B-28})$$

$$0.25 \leq \frac{a}{c} \leq 2 \quad (\text{B-29})$$

$$4 \leq \frac{D}{t} \leq 256 \quad (\text{B-30})$$

These geometries span the range of cracks, crack shapes, and shafts/casings relevant to practical engineering assessments. These geometries do not include very elongated crack shapes ($a/c < 0.25$). While such elongated cracks may be initially present, these crack shapes are not stable, and the crack rapidly advances into the more stable shapes investigated here.

During the LHS process, we sample a/c in \log_2 space. This log scaling ensures that LHS roughly provides the same number of points between $0.25 \leq a/c \leq 0.5$, $0.5 \leq a/c \leq 1$, and $1 \leq a/c \leq 2$. Linear scaling on a/c would sample about 33% more points in $1 \leq a/c \leq 2$ vs. $0.25 \leq a/c \leq 1$. Lower ratios of a/c develop more frequently in preliminary FCG analyses using SC34, and the linear sampling is less desirable as a result. Similar reasoning led us to

sample D/t over \log_4 space to capture thicker shafts in the analysis rather than focus on very thin casings.

This work selected two loadings relevant for shafts/casings. The loading S_0 represents a uniform tension load applied normal to the cross-sectional area. The loading S_1 represents a linear-bending load with decreasing stresses in the direction of crack advance.

SC34 was also integrated into version 9.2 of NASGRO. This implementation of SC34 is identical to the implementation in DARWIN. Consequently, we performed verification using NASGRO rather than DARWIN since it requires much less effort to develop NASGRO input files than DARWIN input files. However, SIF results using DARWIN would be identical to those obtained from NASGRO.

Formal verification was accelerated by the Python scripting capability developed to build FEAs that define the reference solution matrix. Here, we initiated the scripting process with new inputs from the LHS process and the relevant applied stresses. This process built new FEAs input files, extracted results, and processed output SIF values.

This investigation defines relative error (%) as:

$$E_R = \frac{F_{DARWIN} - F_{FEA}}{F_{FEA}} \times 100 \quad (\text{B-31})$$

Here, F is the geometry correction factor computed either by DARWIN (F_{DARWIN}) or by the FEA (F_{FEA}). The geometry correction factor provides a normalized value for the SIF as follows:

$$F = \frac{K_I}{S \times \sqrt{\pi a_m}} \quad (\text{B-32})$$

Here, S represents the normalized stress magnitude (S_0 or S_1). The SIF value can be from either the a -tip or the c -tip. Consequently, this work examines four geometry corrections factors:

- F_0^a – geometry correction factor at a -tip for S_0 loading;
- F_1^a – geometry correction factor at a -tip for S_1 loading;
- F_0^c – geometry correction factor at c -tip for S_0 loading; and
- F_1^c – geometry correction factor at c -tip for S_1 loading.

Results

Figure B- 48 shows the verification results for SC34. This figure shows relative error as function of geometry (a/t , a/c , and D/t), as a function of F , and as a PDF/CDF that visualizes overall error. Each subfigure shows relative error for the four geometry correction factors of interest. Table B- 15 provides statistics of the relative error in Figure B- 48(f).

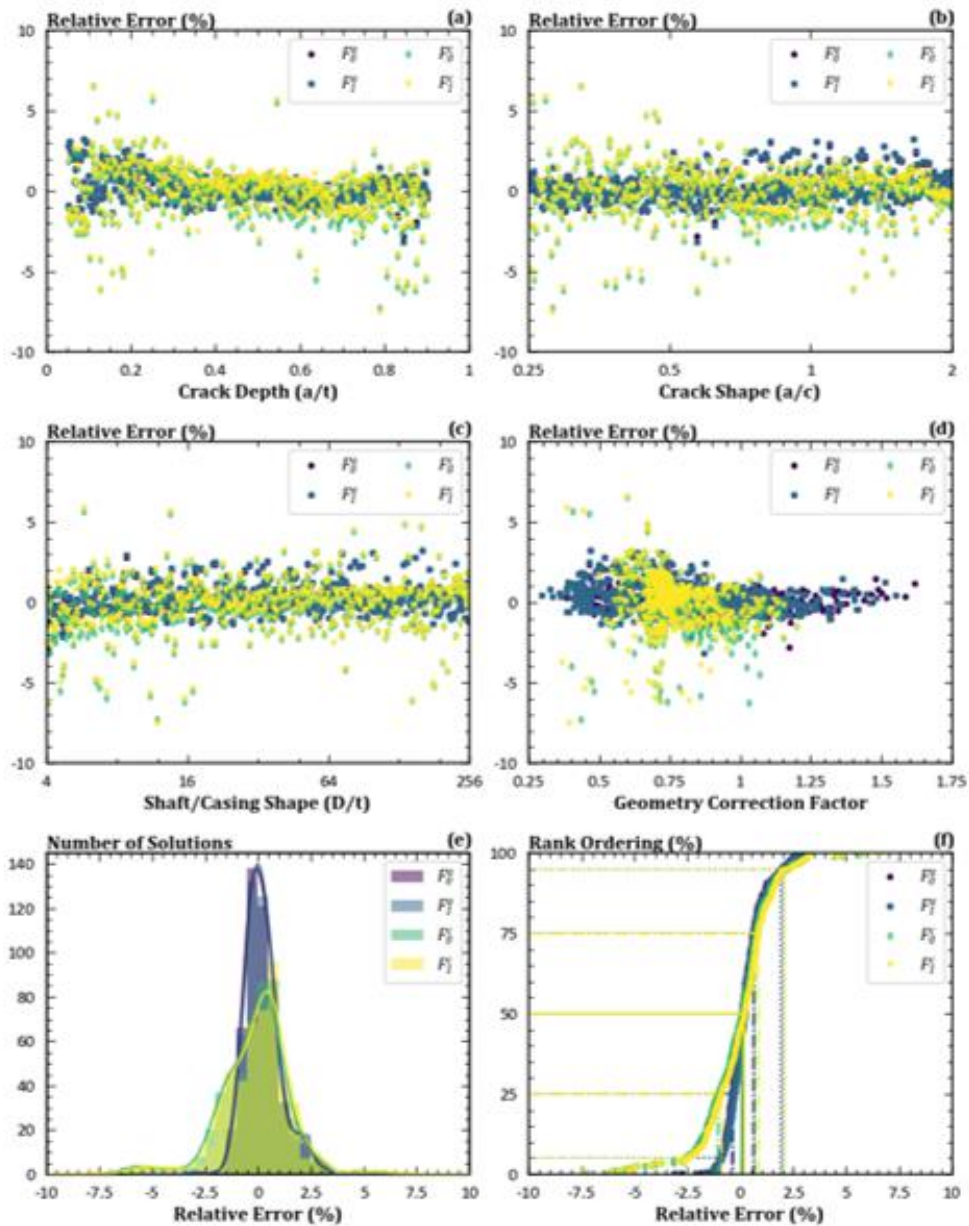


Figure B- 48. Formal verification results for SC34

Table B- 15. Relative error (%) statistics for the final implementation of SC34 with an enhanced reference solution matrix and support for small cracks

SIF	min	1%	5%	10%	25%	50%	75%	90%	95%	99%	max
F_0^a	-2.78	-1.32	-0.93	-0.71	-0.38	0.10	0.60	1.24	1.92	2.53	3.21
F_1^a	-3.14	-1.29	-0.92	-0.67	-0.31	0.17	0.66	1.31	2.05	2.57	3.22
F_0^c	-7.27	-5.79	-2.61	-1.97	-1.06	0.07	0.70	1.48	2.01	4.43	6.57
F_1^c	-7.51	-5.61	-2.47	-1.69	-0.90	0.17	0.84	1.64	2.14	4.47	6.58

These results indicate that errors never exceed 3.2% at the *a*-tip. At the *c*-tip, errors never exceed 7.5%. Most SC34 solutions are much closer to the FEA results than suggested by the minimum and maximum values shown here. For the *a*-tip, more than 90% of the solutions are between -0.93% and 2.05% of the FEA value. For the *c*-tip, more than 90% of the solutions are between -2.6% and 2.14% of the FEA value. The median values indicate a slight conservatism in the overall solution.

B.17 References

- Barsoum, R. S. (1976). On the use of isoparametric finite elements in linear fracture mechanics. *International Journal for Numerical Methods in Engineering*, 10(1), 25-37.
doi:doi.org/10.1002/nme.1620100103
- Enright, M. P., Lee, Y.-D., McClung, R. C., Huyse, L., Leverant, G. R., Millwater, H. R., & Fitch, S. K. (2003). Probabilistic surface damage tolerance assessment of aircraft turbine rotors. *Proc. 48th ASME International Gas Turbine & Aeroengine Technical Congress, Paper GT-2003-38731*. Atlanta, Georgia: ASME.
- Fawaz, S. A. (1999). Application of the virtual crack closure technique to calculate stress intensity factors for through cracks with an elliptical crack front. *Engineering Fracture Mechanics*, 59(3), 327-342. doi:doi.org/10.1016/S0013-7944(97)00126-4
- Fawaz, S. A. (1999). Stress intensity factor solutions for part-elliptical through cracks. *Engineering Fracture Mechanics*, 62(3), 209-206. doi:doi.org/10.1016/S0013-7944(99)00003-X
- Fawaz, S. A., & Andersson, B. (2004). Accurate stress intensity factor solutions for corner cracks at a hole. *Engineering Fracture Mechanics*, 1235-1254.
doi:doi.org/10.1016/S0013-7944(03)00207-8
- Ferahi, M., & Meguid, S. A. (1998). A novel approach for evaluating weight functions for cracks in finite bodies. *Engineering Fracture Mechanics*, 59(3), 343-352.
doi:doi.org/10.1016/S0013-7944(97)00091-X
- Glinka, G., & Shen, G. (1991). Universal features of weight functions for cracks in mode I. *Engineering Fracture Mechanics*, 40(6), 1135-1146. doi:doi.org/10.1016/0013-7944(91)90177-3
- Irwin, G. R. (1962). Crack-extension force for a part-through crack in a plate. *Journal of Applied Mechanics*, 29(4), 651-654. doi:doi.org/10.1115/1.3640649
- John, R., Kaldon, S. G., Johnson, D. A., & Coker, D. (1995). Weight function for a single edge cracked geometry with clamped ends. *International Journal of Fracture*, 72(2), 145-158.
doi:doi.org/10.1007/BF00042825
- Lee, Y.-D., McClung, R. C., & Chell, G. G. (2008). An efficient stress intensity factor solution scheme for corner cracks at holes under bivariate stressing. *Fatigue and Fracture of Engineering Materials and Structures*, 31(11), 1004-1016.

- McClung, R. C., Lee, Y.-D., Cardinal, J. W., & Guo, Y. (2013). The pursuit of K: Reflections on the current state of the art in stress intensity factor solutions for practical aerospace applications. *Proc. 27th Symposium of the International Committee on Aeronautical Fatigue and Structural Integrity*, (pp. 361-375). Jerusalem, Israel.
- McFarland, J. M., Dimeo, J. A., & Bichon, B. J. (2017). Gaussian process response surface modeling and global sensitivity analysis using NESSUS. *Proc. 2nd International Conference on Uncertainty Quantification in Computational Sciences and Engineering (UNCECOMP 2017)*, (pp. 225-237). Rhodes Island, Greece.
doi:doi.org/10.7712/120217.5365.16997
- McKay, M. D., Beckman, R. J., & Conover, W. J. (1979). A comparison of three methods for selecting values of input variables in the analysis of output from a computer code. *Technometrics*, *21*(2), 239-245. doi:doi.org/10.2307/1268522
- Nakamura, T., & Parks, D. M. (1988). Three-dimensional stress field near the crack front of a thin elastic plate. *Journal of Applied Mechanics*, *55*(4), 805-813.
doi:doi.org/10.1115/1.3173725
- Newman, J. C., & Raju, I. S. (1981). An empirical stress-intensity factor equation for the surface crack. *Engineering Fracture Mechanics*, *15*(1-2), 185-192. doi:doi.org/10.1016/0013-7944(81)90116-8
- Nikishkov, G. P., & Atluri, S. N. (1987). Calculation of fracture mechanics parameters for an arbitrary three-dimensional crack, by the 'Equivalent Domain Integral' method. *International Journal for Numerical Methods in Engineering*, *24*(9), 1801-1821.
doi:https://doi.org/10.1002/nme.1620240914
- Oberkampf, W. L., & Roy, C. J. (2010). *Verification and validation in scientific computing* (First ed.). New York, NY: Cambridge University Press.
doi:doi.org/10.1017/CBO9780511760396
- Oberkampf, W. L., Trucano, T. G., & Hirsch, C. (2004). Verification, validation, and predictive capability in computational engineering and physics. *Applied Mechanics Reviews*, *57*(5), 345-384. doi:doi.org/10.1115/1.1767847
- Pook, L. P. (1994). Some implications of corner point singularities. *Engineering Fracture Mechanics*, *48*(3), 367-378. doi:doi.org/10.1016/0013-7944(94)90127-9
- Rice, J. R. (1972). Some remarks on elastic crack-tip stress fields. *International Journal of Solids and Structures*, *8*(6), 751-758. doi:doi.org/10.1016/0020-7683(72)90040-6

- Shen, G., & Glinka, G. (1991). Determination of weight functions from reference stress intensity factors. *Theoretical and Applied Fracture Mechanics*, 15(3), 237-345.
doi:doi.org/10.1016/0013-7944(91)90177-3
- Shivakumar, K. N., Tan, P. W., & Newman, J. C. (1988). A virtual crack-closure technique for calculating stress intensity factors for cracked three dimensional bodies. *International Journal of Fracture*, 36(3), R43-50. doi:doi.org/10.1007/BF00035103
- Simpson, T. W., Lin, D., & Chen, W. (2001). Sampling strategies for computer experiments: Design and analysis. *International Journal of Reliability and Applications*, 209-240.
- Sobotka, J. C., & McClung, R. C. (2018). Automatic 3D crack placement using the Python API in Abaqus CAE. *Science Age Exposition*. Boston, MA.
- Tada, H., Paris, P. C., & Irwin, G. R. (1973). *The stress analysis of cracks handbook*. Hellertown, PA: Del Research Corporation.
- Wang, X., & Lambert, S. B. (1997). Stress intensity factors and weight functions for high aspect ratio semi-elliptical surface cracks in finite-thickness plates. *Engineering Fracture Mechanics*, 57(1), 13-24. doi:doi.org/10.1016/S0013-7944(97)00018-0
- Wu, X. (2019). A review and verification of analytical weight function methods in fracture mechanics. *Fatigue and Fracture of Engineering Materials and Structures*, 42(9), 2017-2042. doi:doi.org/10.1111/ffe.13073

C Benchmark fatigue crack growth testing

List of Figures

Figure C- 1. Model hierarchy for FCG lifetime calculation	C-2
Figure C- 2. Microstructure of Ti-6Al-4V forgings after heat treatment.....	C-4
Figure C- 3. Benchmarking test configuration for (a) tension and (b) bending	C-5
Figure C- 4. Ti-6Al-4V forgings.....	C-6
Figure C- 5. Base specimen configurations for tension and bending	C-6
Figure C- 6. Residual stress profiles of Ti-6Al-4V specimens.....	C-7
Figure C- 7. Example heating tinted fracture surface for a surface crack.	C-8
Figure C- 8. Crack case diagram for through crack at edge of plate	C-9
Figure C- 9. Crack case diagram for through crack [offset] in plate	C-10
Figure C- 10. Legacy TI-6Al-4V fatigue crack growth rate behavior.....	C-11
Figure C- 11. Statistical representation of FCG rate behavior.....	C-12
Figure C- 12. Comparison of SwRI and legacy FCG behavior	C-12
Figure C- 13. Statistical representation of SwRI baseline data	C-13
Figure C- 14. Crack case diagram for corner crack in plate	C-14
Figure C- 15. Crack case diagram for surface crack in plate.....	C-15
Figure C- 16. Crack case diagram for through crack at hole	C-15
Figure C- 17. Crack case diagram for corner crack at hole	C-16
Figure C- 18. Calculated and measured FCG results for edge crack specimens (tension).....	C-19
Figure C- 19. Comparison of calculated FCG results for different TC02 restraint options	C-20
Figure C- 20. Calculated and measured FCG results for center through crack specimen	C-21
Figure C- 21. Calculated and measured FCG results for corner crack specimen (tension).....	C-22
Figure C- 22. Calculated and measured FCG results for surface crack specimen.....	C-23
Figure C- 23. Calculated and measured FCG results for through crack at hole specimen	C-24
Figure C- 24. Calculated and measured FGC results for corner crack at hole specimen	C-25
Figure C- 25. Calculated and measured FCG results for through crack under bending	C-26
Figure C- 26. Calculated and measured FCG results for corner under bending.....	C-26

List of Tables

Table C- 1. Forman-Mettu Ti-6Al-4V heat tint schedule	C-8
Table C- 2. Summary of test matrix and test results.....	C-17

C.1 Introduction

The use of a predictive model such as the DARWIN[®] software for design and certification of safety-critical components requires some confidence that the model is performing as intended and that the model is an adequately accurate representation of physical reality. The formal process of generating this confidence is called model verification and validation (V&V).

Verification is the process of determining that a model implementation accurately represents the developer's conceptual description of the model and the solution to the model. Verification also confirms that the governing equations in the model are being solved correctly. Validation is the process of determining the degree to which a model is an accurate representation of the real world from the perspective of the intended uses of the model. Validation also confirms that we are solving the right equations.

Following the established paradigms of model V&V as described in ASME V&V 10-2019 (ASME, 2019), V&V is performed step-by-step in a hierarchal, building block approach. For example, a DARWIN fatigue crack growth (FCG) lifetime calculation, which is a key piece of a DARWIN fracture risk calculation, can be broken down into several major sub-models, as shown in Figure C- 1.

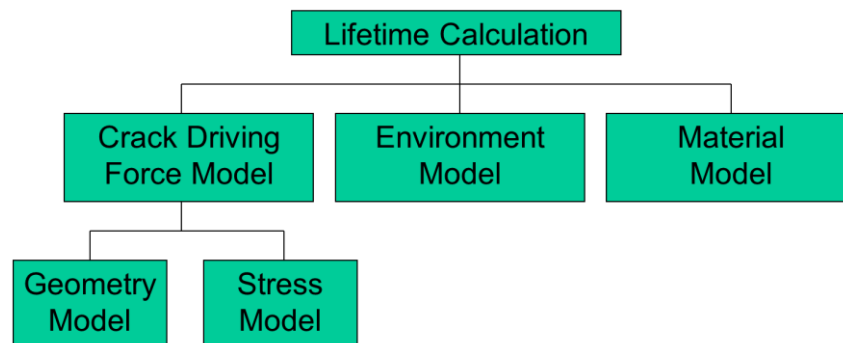


Figure C- 1. Model hierarchy for FCG lifetime calculation

Here the geometry model is the representation of the size, shape, orientation, and location of the crack, as well as the shape and dimensions of the uncracked component. The stress model describes the loads and stresses applied to the component globally as well as the local stress distribution near the crack (but in the corresponding uncracked body), along with any residual stresses or other elastic-plastic deformation. The material model includes equations and related equation parameters that describe material strength and material resistance to FCG and fracture under different conditions (including effect of temperature and chemistry), as well as the similitude of the component material to the material source used to generate material properties.

The environment model is the description of the actual temperature and chemistry in the baseline experiments and the actual application. All of these models, while having a significant influence on the accuracy of a DARWIN life calculation, are largely outside the control of DARWIN itself. They depend on factors such as structural and thermal analyses, manufacturing process control, and material test methods.

The calculation of the crack driving force model, on the other hand, is one of the primary operations in DARWIN. In particular, this sub-model involves calculation of the stress intensity factor (SIF, often denoted with the symbol K) for a given geometry and applied stresses. The main V&V challenge for DARWIN, then, is to determine if the SIF is being calculated accurately (verification) and if the resulting value can be used to calculate FCG rate and lifetime accurately (validation). The verification step is a mathematical exercise involving detailed comparisons of DARWIN SIF values against closed-form solutions or against high-resolution numerical solutions. The process of verifying DARWIN SIF solutions has been documented in Appendix B of this report. The present appendix describes the process of validating DARWIN SIF solutions.

Because the sub-models in Figure C- 1 are all interrelated and all affect the lifetime calculation, validation of SIF solutions through FCG testing is more difficult than it might first seem. It is not possible to measure the SIF directly; we can only determine its effect indirectly by measuring FCG rates and lifetimes and comparing those measurements with predictions based on the SIF solutions. Some uncertainties in this comparison can be minimized through careful experimental design. Factors such as stress, geometry, environment, and material can be carefully controlled and/or measured. However, the effects of baseline FCG properties, their uncertainties, and the FCG model used to predict growth rates cannot be fully separated from the effects of the calculated SIF. Furthermore, there are additional factors to be considered in how the SIF is used to calculate crack growth rate, such as constraint loss effects for part-through cracks, or crack transition models. For these reasons, we cannot claim rigorous “validation” of DARWIN SIF solutions from this experimental program. Instead, we will describe a set of benchmark FCG experiments, and the analysis used to draw conclusions about the suitability of the SIF solutions to provide sufficiently accurate predictions of FCG lifetime.

The FCG benchmarking activity has two key steps. The first step is to determine the baseline FCG properties (the material model in the hierarchy in Figure C- 1) for the material/environment of interest, using specimen geometries with well-established SIF solutions. Establishing this baseline and its uncertainty are essential to making conclusions about the suitability of the SIF solutions from the indirect approach employed here, where the experimental SIF is inferred from

the baseline FCG behavior. The second step is to perform FCG tests for specific crack and loading configurations and to compare those results against calculations based on the appropriate SIF solution and baseline material model in light of the baseline and experimental uncertainties. While rigorous uncertainty quantification was not used to quantify all sources of uncertainty, the uncertainty in the FCG baseline is known to be significant, and its effects were considered in the SIF validation.

Because the SIF solutions themselves are material-independent, the conclusions from this benchmarking study would ideally be material-independent as much as possible. However, the results may still be influenced somewhat by material-specific factors through the baseline testing or through other influences on the effective SIF (*e.g.*, constraint loss). The goal in this particular study was to minimize extraneous material effects through material selection.

The material chosen for the study was fine-grained Ti-6Al-4V forgings originally produced to support a large research study of high cycle fatigue (HCF) organized by the U.S. Air Force (USAF). Each forging was about 16" × 6" × 0.80." The forgings were solution-treated at 1710°F ±20°F after forging to provide a uniform microstructure. After solution treatment, the forgings were fan-cooled and mill-annealed at 1300°F ±25°F for two hours. The resulting microstructure consisted of approximately 60% primary alpha phase with the remainder lamellar-transformed beta phase. A micrograph is shown in Figure C- 2. The 0.2% yield strength (YS) and ultimate tensile strength (UTS) in the longitudinal direction were 930 MPa (134.9 ksi) and 978 MPa (141.8 ksi), respectively.

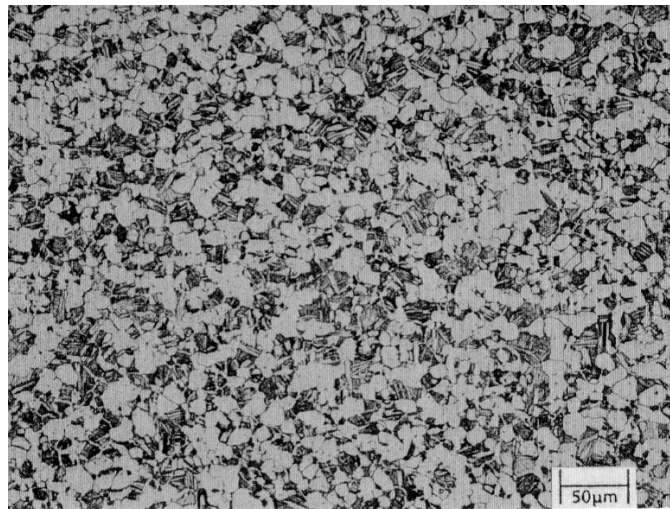


Figure C- 2. Microstructure of Ti-6Al-4V forgings after heat treatment

C.2 Experimental procedure

Fatigue crack growth (FCG) testing was performed using MTS servohydraulic test frames with MTS Flex Test 60 digital controllers. Hydraulic wedge grips were used for testing in tension and a four-point bend fixture was used for testing in bending (see Figure C- 3). For tension configurations, frame and fixture alignment was performed in keeping with ASTM 1012 to ensure bending was less than 5% (in practice, bending was found to be ~1%). For the bending configuration, a dummy specimen was strain gaged to ensure that the induced bending was within approximately 1% of the intended bending.

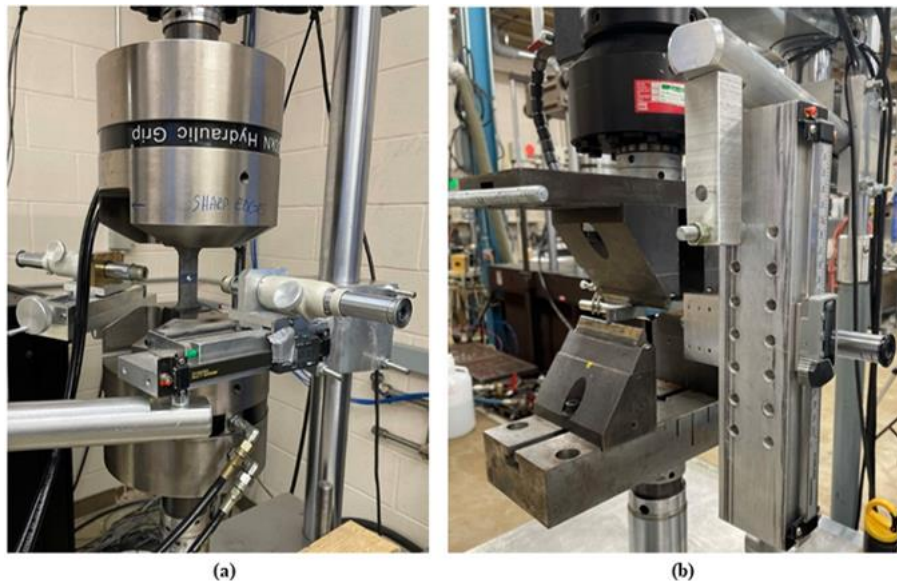


Figure C- 3. Benchmarking test configuration for (a) tension and (b) bending

Traveling microscopes on linear verniers were used to measure crack lengths as a function of applied cycles. In the case of corner crack specimen configurations, angled mirrors (calibrated against fine scribe lines at known positions) were used to measure the a-tip length of corner and bore cracks. In instances when a corner or surface crack transitioned to a through-crack, the back-face crack was also measured. Surface crack length measurements were made for each tip relative to a scribe line centered about the initial surface crack, thereby allowing for independent tracking of each surface tip to assess crack growth symmetry.

Specimens were fabricated from the Ti-6Al-4V forgings (see Figure C- 4). In all cases, specimens were excised such that testing was in the L-T orientation (corner and surface cracks were oriented such that the a-tip was in the through-thickness direction).



Figure C- 4. Ti-6Al-4V forgings

Schematics of the base specimen configurations are shown in Figure C- 5. The tensile test section was two inches long and one inch wide. The bend configuration was a simple rectangular bar, nominally 0.5 in. by 0.2 in. cross-section and five inches in length, loaded in four-point bending. The principal loading of each specimen configuration produced an in-plane stress in the forging longitudinal direction. Electro-discharge machining (EDM) was used to efficiently blank out specimens to make efficient use of the limited forgings. Conventional machining (*e.g.*, milling, drilling, reaming) was then used to machine specimens to final sizes and to add features (*e.g.*, holes), removing any potential EDM re-cast layer. Low stress milling/grinding was used for finishing passes to minimize machining-induced residual stress.

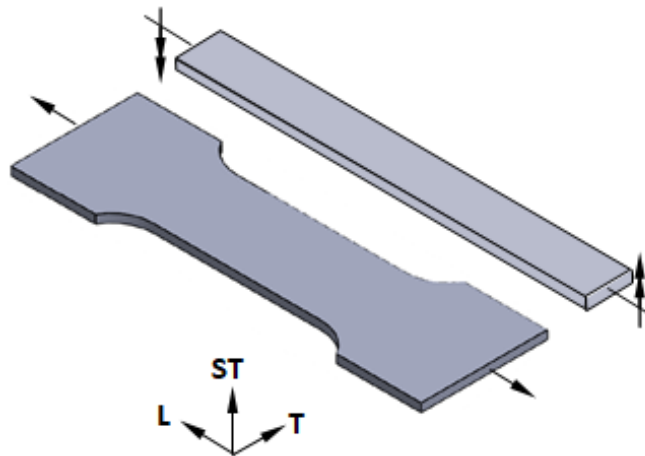


Figure C- 5. Base specimen configurations for tension and bending

Following machining, specimens were subjected to an electropolish protocol (9 vol% HF with 40 vol% HNO₃ at 120°F) to remove nominally 0.003 in. of material. X-ray diffraction was used to measure the residual stress profiles in the as-machined and electropolished conditioned,

indicating that the electropolishing protocol was sufficient in eliminating machining-induced residual stresses (see Figure C- 6).

Initial notches were introduced with EDM (wire for through- and corner cracks and plunge for surface cracks). These EDM notches were introduced after electropolish to avoid excessive blunting of the EDM notches due to the electropolish. Through cracks were oriented in the forging transverse direction. Corner and surface cracks transitioned into through cracks in the transverse direction.

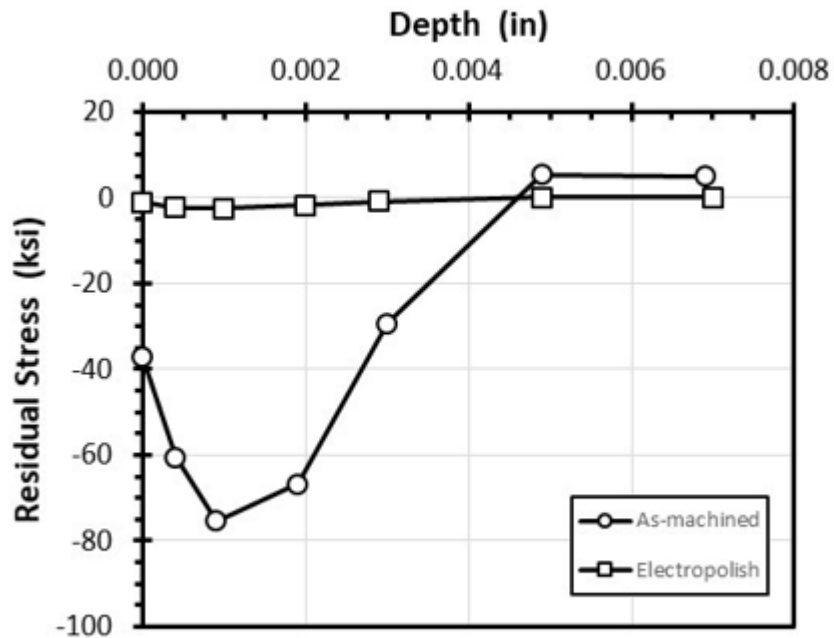


Figure C- 6. Residual stress profiles of Ti-6Al-4V specimens

Fatigue crack growth testing was performed in load control with an $R = 0.1$ (ratio of minimum to maximum load), consistent with the legacy FCG characterization of the Ti-6Al-4V forgings. Pre-cracking was performed at the same loading conditions at the test to avoid any load history effects.

Heat tinting was used to capture the crack front profile for corner and surface crack configurations and during crack transitions to through-cracks. The heat tint schedule (originally developed at National Aeronautics and Space Administration (NASA) Johnson Space Flight Center) is shown in Table C- 1. An example fractography showing the results of the full heat-tinting schedule is shown in Figure C- 7. Some of the heating tinting is subtle, particularly in the later parts of the schedule. Comparisons between specimens exposed to the heat tint schedule and those without exposure indicated no discernable difference in FCG behavior.

Table C- 1. Forman-Mettu Ti-6Al-4V heat tint schedule

Number	Temperature		Time (hrs)
	°F	°C	
1	1000	538	2
2	1000	538	1
3	900	482	2
4	801	427	2
5	700	371	2
6	601	316	2
7	399	204	2

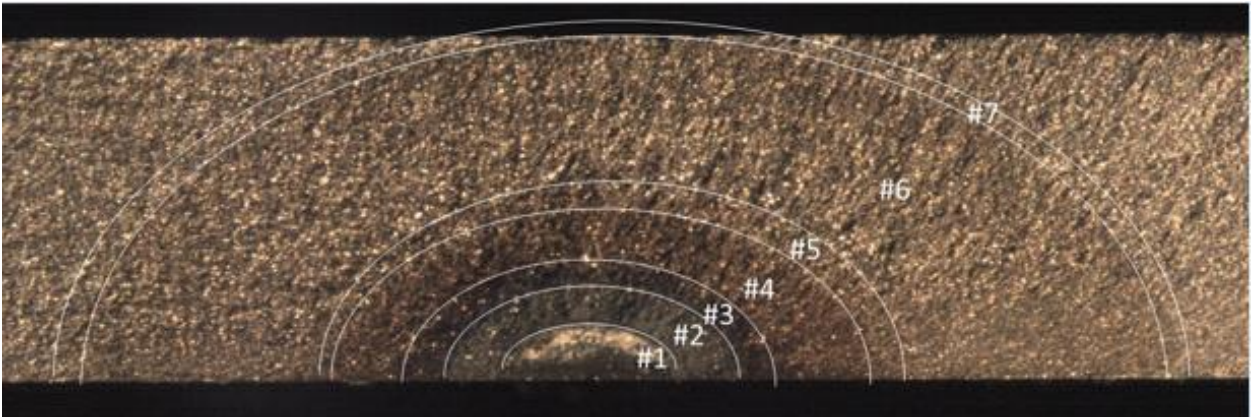


Figure C- 7. Example heating tinted fracture surface for a surface crack.

C.3 Results

Baseline data

The first analysis step in the benchmarking study was to characterize the baseline FCG properties. These properties were determined from FCG experiments using through-crack-in-plate geometries for which the SIF is well established due to the simplicity of the configuration. Both edge crack and center crack geometries were used.

It should be noted that all of the calculations of SIF, FCG rate, and FCG life in this study were performed using NASGRO[®] as an identical surrogate for DARWIN. Because DARWIN is primarily configured for the analysis of components using finite element models, and because DARWIN employs complicated binary file formats to support that configuration, it is extremely cumbersome to use for the analysis of simple specimen data. The NASGRO software is also

developed and maintained by Southwest Research Institute® (SwRI®) (in fact, the same person is the primary developer of both NASGRO and DARWIN SIF modules). The SIF solutions evaluated in this benchmarking study are the same in both DARWIN and NASGRO, and hence they give exactly the same results. The same tabular FCG property representation is also available in both codes. However, the NASGRO software is much more nimble and accessible, with direct access to all SIF solutions (no finite element intermediary) and direct access to calculated results through several different NASGRO modules. One of the NASGRO modules (NASSIF) is specifically designed to provide direct access to the SIF solution alone, and this NASSIF module was used extensively in the SIF verification study documented in Appendix B.

The two specific crack models used to establish the baseline properties were TC02 (through crack at edge of plate) and TC11 (through crack in plate). Crack case diagrams for these two models are shown in Figure C- 8 and Figure C- 9.

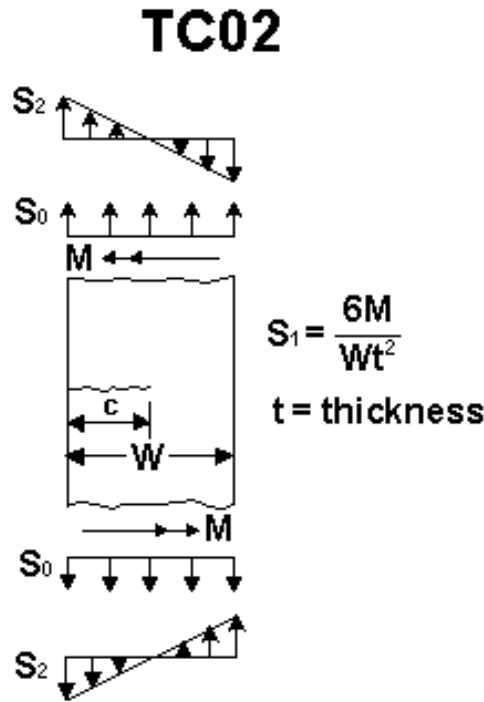


Figure C- 8. Crack case diagram for through crack at edge of plate

TC11

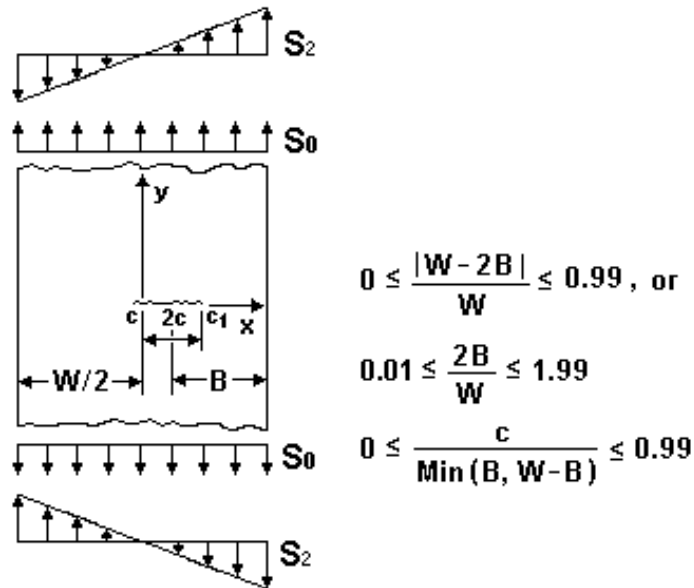
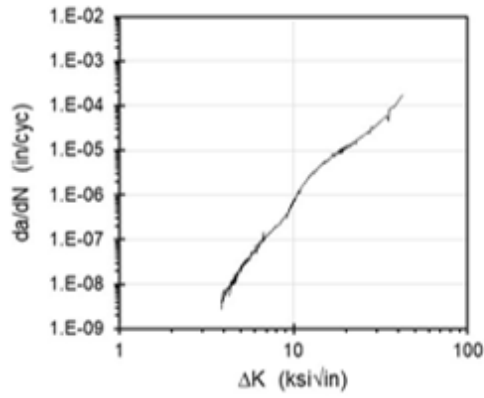


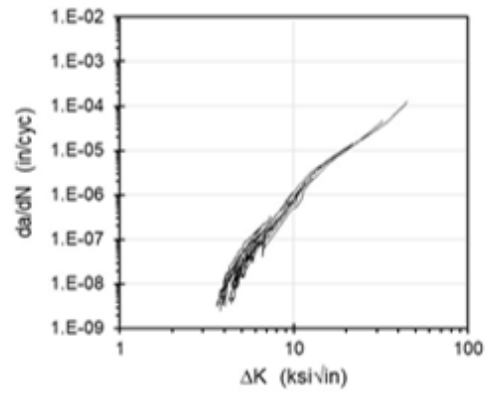
Figure C- 9. Crack case diagram for through crack [offset] in plate

Baseline FCG data at $R = 0.1$ had previously been generated on other forgings from the same material source as part of the USAF HCF project, and those data were available at SwRI. Boyce (Boyce & Ritchie, 2001) generated data from seven individual tests using middle-crack tension specimens. Pratt & Whitney (Sheldon, Bain, & Donald, 1999) generated data from eighteen tests using compact tension specimens. GE Aviation (Sheldon, Bain, & Donald, 1999) generated data from three surface-crack tension specimens. Those tests yielded data for both surface (c) and depth (a) tips. These legacy baseline data are summarized in Figure C- 10.

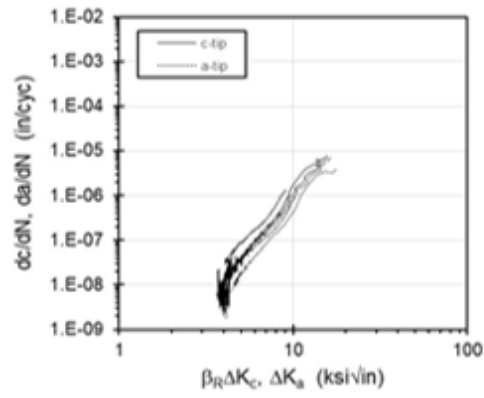
A statistical representation of the legacy FCG behavior was developed. For a discrete crack growth rate, the distribution of measured crack driving force associated with each crack growth rate was characterized by a mean and standard deviation by interpolating each dataset whose data bracketed the discrete growth rate. This statistical representation of the legacy data is shown in Figure C- 11. The upper/lower bounds capture 95% of the data (± 2 standard deviations). Note that this statistical modeling was limited to the general Paris regime and truncated at growth rates above 10^{-5} in/cycle, beyond which limited data prohibited meaningful statistical analyses.



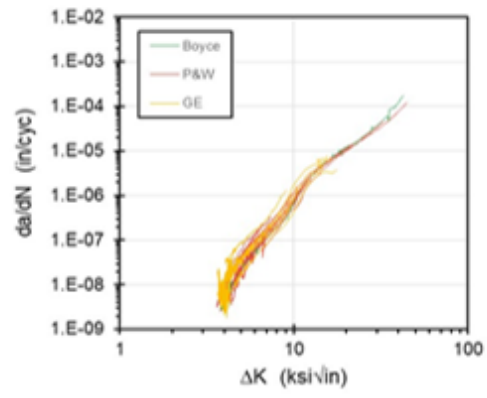
(a) Boyce data



(b) P&W data



(c) GE data



(b) combined data

Figure C- 10. Legacy TI-6Al-4V fatigue crack growth rate behavior

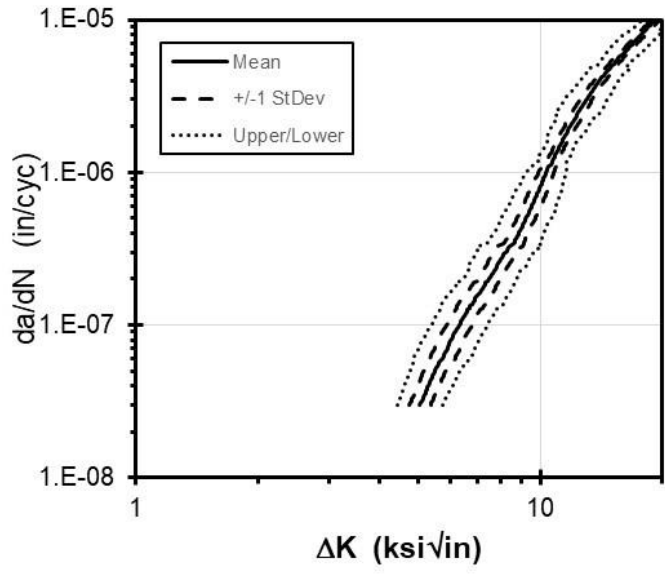


Figure C- 11. Statistical representation of FCG rate behavior

Additional baseline data were generated in the current program using two TC02 (edge crack) specimens and two TC11 (middle crack) specimens, all tested under remote tension. These new data are compared to the legacy data in Figure C- 12.

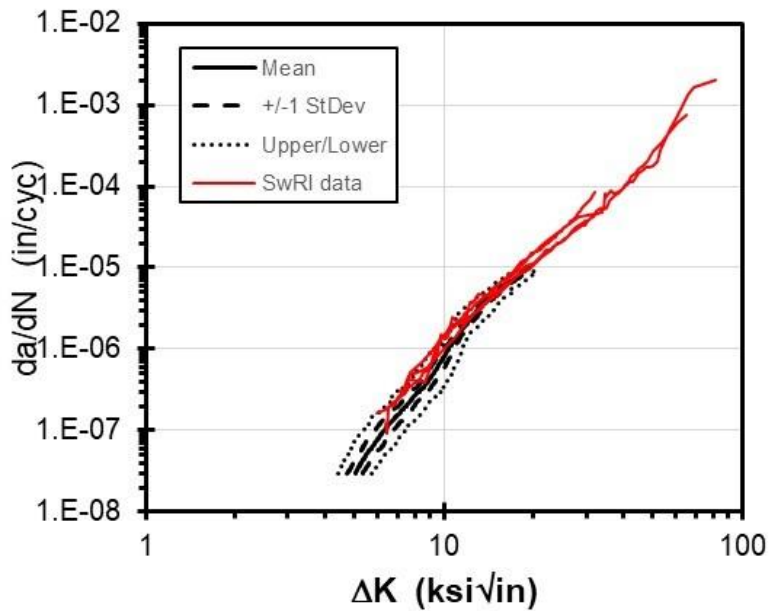


Figure C- 12. Comparison of SwRI and legacy FCG behavior

The SwRI baseline FCG results are consistent with the legacy data (they are within the confidence bounds), trending slightly towards the upper trends of the legacy FCG distribution. To eliminate the potential influence of inter-laboratory variability from the study, and to ensure that the baseline properties were based on the specific forgings used in the benchmark tests, it was decided to use only the SwRI data to generate the baseline properties. A statistical mean for the SwRI FCG data was developed. However, given the limited SwRI dataset, it was decided to employ the variation of the legacy data to represent the probable variation in the SwRI data. This combined statistical representation of the SwRI data is shown in Figure C- 13. A tabular representation of the mean and standard deviations of the SwRI data were used for the benchmarking assessments.

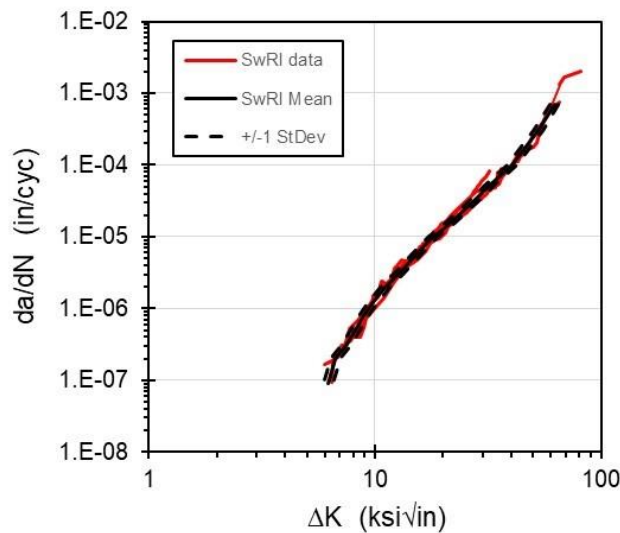


Figure C- 13. Statistical representation of SwRI baseline data

Benchmark tests

The second analysis step was to perform calculations (using these baseline properties) of FCG rate and FCG lifetime for specimens employing other crack geometries, and compare those calculated results with the measured FCG rates and lifetimes from the benchmark tests. Several different benchmark specimen configurations were evaluated. Tension-loaded configurations included corner crack in plate (CC11), surface crack in plate (SC30) through crack at hole in plate (TC13), and corner crack at hole in plate (CC08). Configurations loaded under bending included through crack in plate (TC02) and corner crack in plate (CC11).

The additional crack models considered in this study are shown in Figure C- 14 through Figure C- 17. Shown here are the crack case diagrams that appear in the NASGRO GUI.

CC11

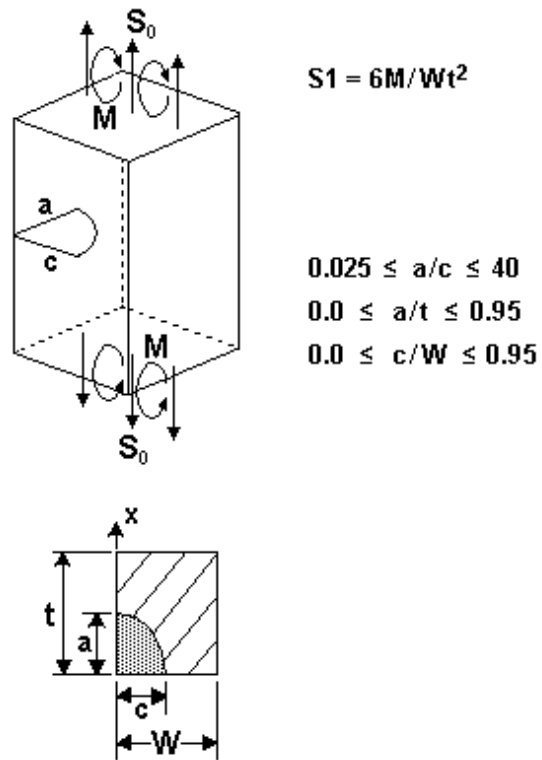


Figure C- 14. Crack case diagram for corner crack in plate

SC30

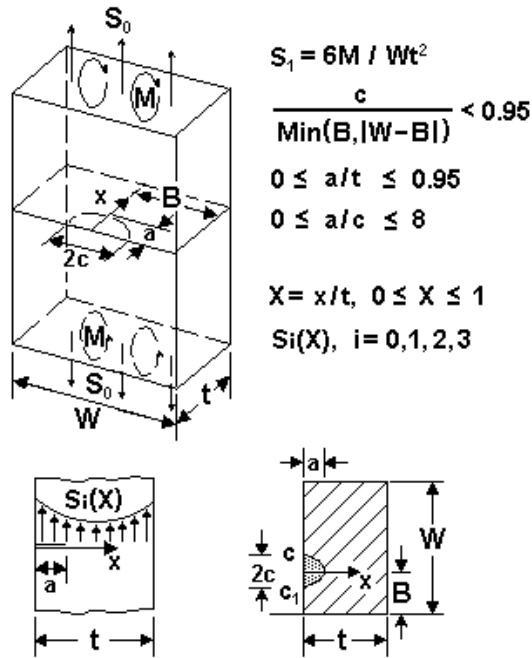


Figure C- 15. Crack case diagram for surface crack in plate

TC13

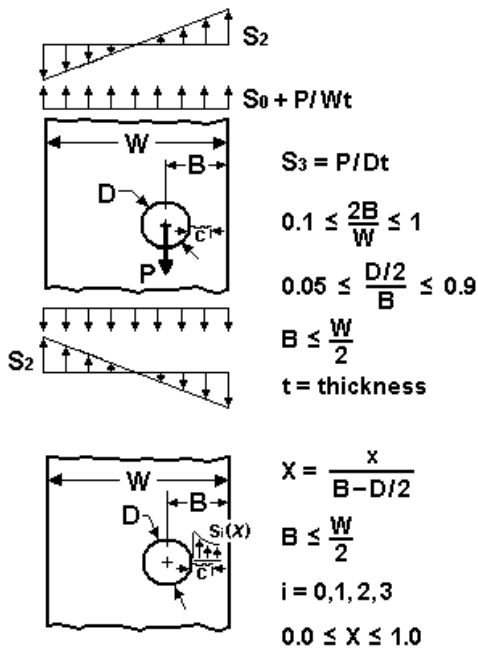


Figure C- 16. Crack case diagram for through crack at hole

CC08

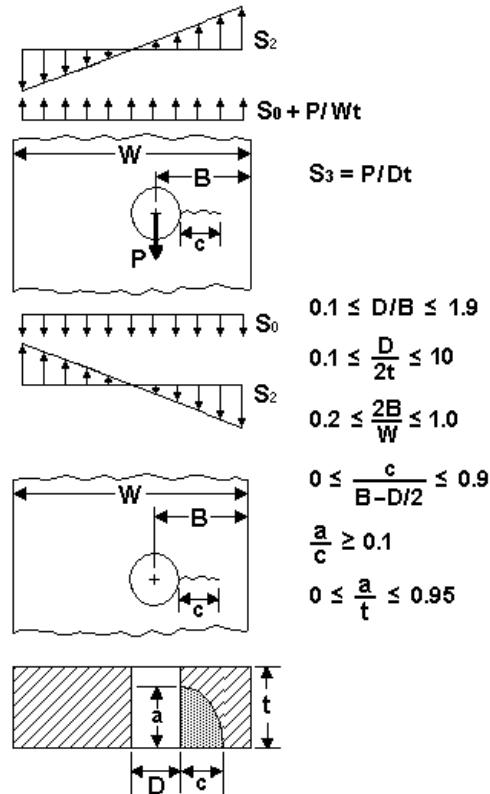


Figure C- 17. Crack case diagram for corner crack at hole

Predictions were made for each benchmark test using the average benchmark FCG properties as well as curves representing one standard deviation above and below the mean curve. These predicted crack length versus cycles curves are compared with the experimental data in the following figures. The test matrix is summarized in Table C- 2, which includes the specimen ID and applied stress for each test as well as the experimental and predicted lifetimes. The results are discussed in groups by specimen type in the following paragraphs.

Table C- 2. Summary of test matrix and test results

Geometry	Test ID	Loading Modes	Max Stress (ksi)	Actual Life (cycles)	Calculated Life (cycles)				Actual/ Mean
					Mean	+1SD	-1SD	+1SD/-1SD	
Edge Through Crack	TC02-1	Tension	22.10	154,743	146,838	184,566	115,778	1.59	1.05
	TC02-2	Tension	22.22	108,200	111,564	137,810	91,512	1.51	0.97
	TC02-3	Bend	29.61	54,298	28,112	32,455	23,769	1.37	1.93
	TC02-4	Bend	36.96	33,484	18,356	21,363	15,785	1.35	1.82
	TC02-6	Tension	23.59	66,000	57,739	69,546	48,452	1.44	1.14
	TC02-7	Tension	29.94	20,950	23,935	27,883	20,581	1.35	0.88
Center Through Crack	TC11-1	Tension	14.94	290,857	308,567	392,517	238,982	1.64	0.94
	TC11-2	Tension	15.00	217,453	216,971	268,757	176,056	1.53	1.00
Corner Cracks	CC11-1	Tension	32.32	166,400	95,265	132,483	76,042	1.74	1.75
	CC11-2	Tension	45.63	14,000	14,047	16,610	11,942	1.39	1.00
	CC11-3	Tension	31.89	160,271	101,302	129,960	80,334	1.62	1.58
	CC11-4	Tension	31.85	162,905	91,670	119,709	73,715	1.62	1.78
	CC11-5	Bend	31.38	299,000	57,027	70,596	46,735	1.51	5.24
	CC11-6	Bend	35.05	315,497	103,534	128,608	83,494	1.54	3.05
Surface Cracks	SC30-1	Tension	32.54	62,696	68,580	85,662	55,586	1.54	0.91
	SC30-2	Tension	33.12	57,000	37,564	45,605	31,359	1.45	1.52
	SC30-3	Tension	31.92	70,603	53,832	66,173	44,027	1.50	1.31
	SC30-4	Tension	47.00	83,212	55,866	68,407	45,679	1.50	1.49
Through Crack at Hole	TC13-1	Tension	15.08	84,925	80,727	78,095	109,885	1.41	1.05
	TC13-2	Tension	14.82	72,500	81,054	95,989	68,918	1.39	0.89
Corner Crack at Hole	CC08-1	Tension	15.04	193,953	109,947	133,281	91,572	1.46	1.76
	CC08-2	Tension	16.02	309,000	200,757	230,938	149,830	1.54	1.54
	CC08-3	Tension	26.56	40,500	20,708	24,050	17,914	1.34	1.96

The results for the edge crack (TC02) geometry under remote tension are shown graphically in Figure C- 18. In this figure (and the following figures), the individual data points are the experimentally measured values. The solid line is the calculated result using the mean value baseline FCG model. The dashed lines are the calculated results using FCG models representing FCG models that are one standard deviation above or below the mean baseline FCG model. The shaded region between those two lines indicates how much natural variability in the material properties influences the crack growth predictions.

Note that specimens TC02-1 and TC02-2 were baseline specimens used to generate the properties, so the calculated results for those two tests are not independent predictions. The close agreement between calculated and measured data indicates consistency. The data from specimens TC02-6 and TC02-7 were not used to generate the baseline data, so the comparisons of calculated and measured data in those two cases represent independent validation. Again, the agreement is excellent. Note that specimen TC02-7 was excised from a different forging (a second forging that was used only for this specimen and four bending tests described later).

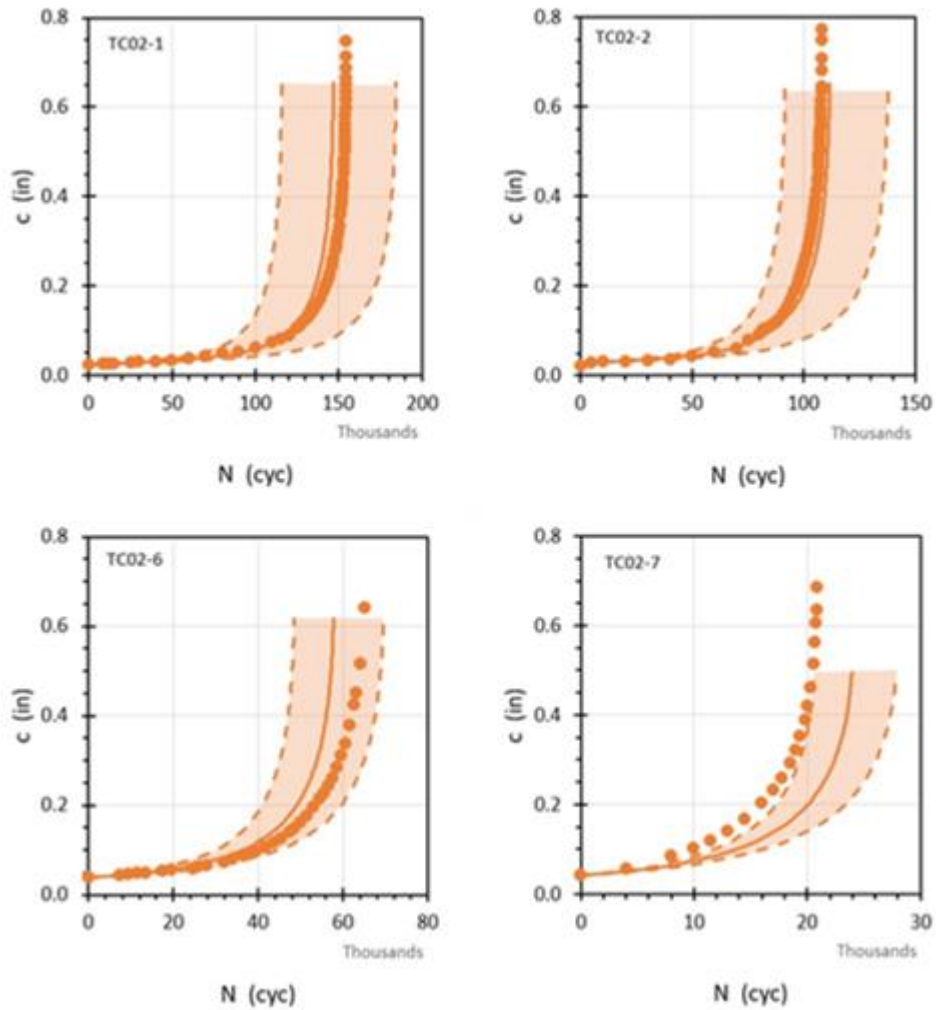


Figure C- 18. Calculated and measured FCG results for edge crack specimens (tension)

Note that the TC02 configuration in NASGRO includes two options for remote boundary conditions. The standard option does not restrain the ends against bending but allows them to rotate freely. This is the conventional form for most edge through crack SIF solutions used in engineering FCG software. NASGRO also has an alternative SIF solution option for the TC02 geometry that restrains the remote ends against in-plane bending. This is a more realistic representation of the test specimen configuration used in this study, and so that alternative solution option was used to reduce the TC02 tension-loaded data to generate the baseline properties. The solution option with end restraint reduces the SIF values for larger c/W values, compared to the unrestrained solution, but the SIF values are similar at small c/W values. The excellent agreement between the TC02 specimen data analyzed with end restraints and the TC11

data (not affected by end restraint), as seen in earlier figures, confirms that this was the correct choice.

However, DARWIN includes only the unrestrained TC02 solution. Additional calculations were performed to determine how well the unrestrained solution would predict the specimen tests. For the four TC02 tension tests considered, the calculated FCG lifetimes using the unrestrained solutions were about 15% shorter (on average) than the calculated lifetimes using the restrained solutions. One specific example is shown in Figure C- 19; here the blue line is the unrestrained calculation. This means that a DARWIN calculation would be slightly conservative compared to the actual lifetime for an edge-crack tension configuration if actual rotations were restrained in the component. The differences would be larger for larger crack sizes.

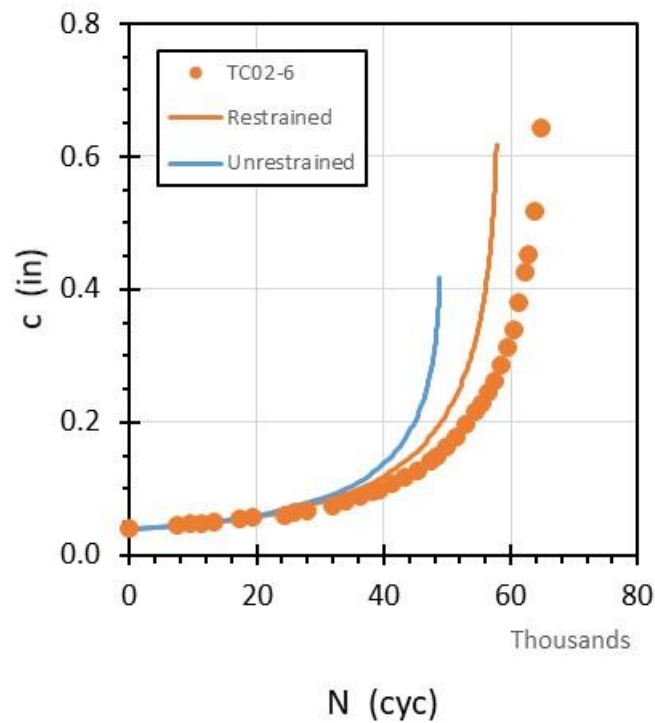


Figure C- 19. Comparison of calculated FCG results for different TC02 restraint options

The two test results for the center through crack (TC11) geometry under remote tension are shown in Figure C- 20. Both specimens were used to generate the baseline properties, so again the calculated results are not entirely independent predictions. However, the close agreement between calculated and measured results again indicates consistency.

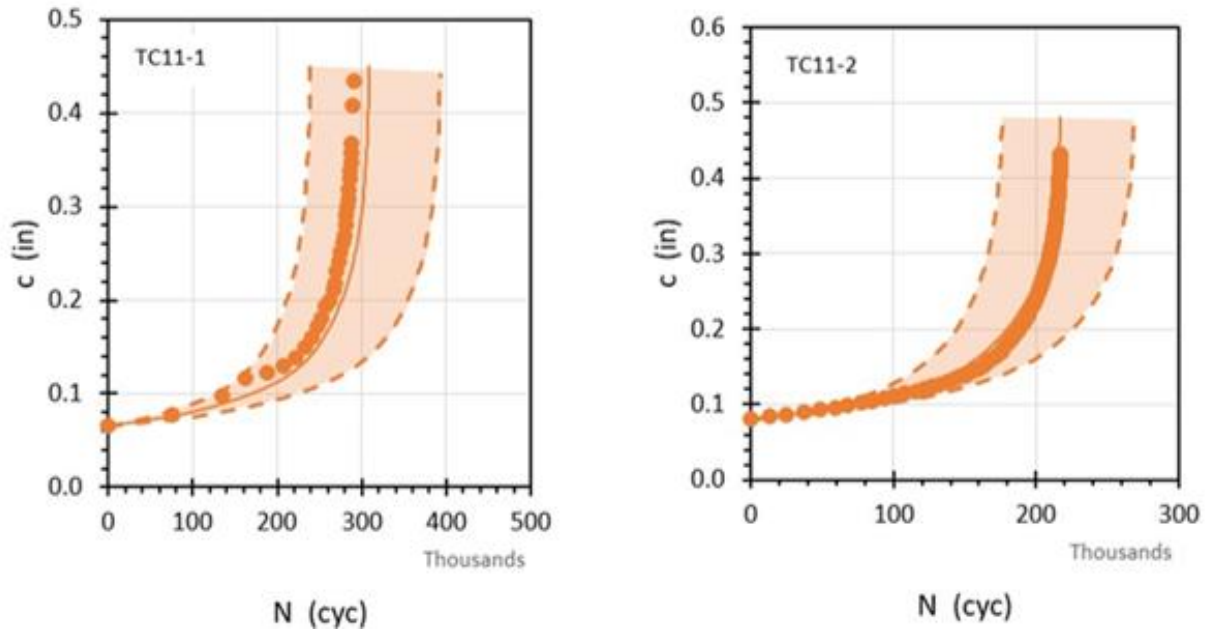


Figure C- 20. Calculated and measured FCG results for center through crack specimen

The results for the corner crack in plate (CC11) geometry under tension loading are shown in Figure C- 21. All four of the calculated results are either accurate or modestly conservative, with ratios of calculated to actual test life ranging from 1.0 to 1.78. In other words, DARWIN predictions would be either accurate or slightly conservative. The conservatism is slightly larger than would be expected from material scatter alone. Note that the data shown in these figures include both corner crack results (blue points are the crack length growing through the thickness, and orange points are the crack length growing along the front surface) and through crack results (additional orange points) after the corner crack reaches the back surface and transitions to a through crack. Some of the conservatism in the predictions may be due to a lack of end restraint against bending in the CC11 and TC02 solutions used here. The actual test specimen provides some restraint against end bending, which would reduce the SIF values and increase the calculated lifetime, as noted previously for the TC02 baseline data and calculations.

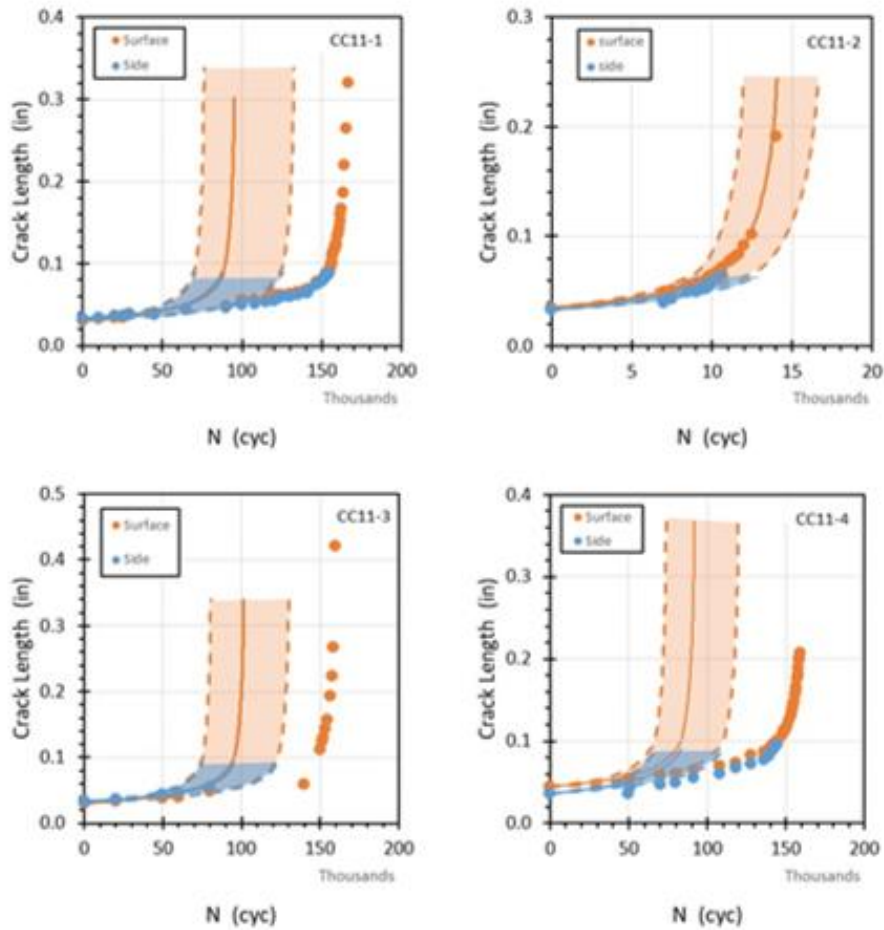


Figure C- 21. Calculated and measured FCG results for corner crack specimen (tension)

The results for the surface crack in plate (SC30) geometry under tension loading are shown in Figure C- 22. Two of these predictions fall within expected material scatter, while two of them are slightly more conservative. Ratios of calculated to actual life range from 0.91 to 1.52. The test with the most conservative prediction had ambiguous data for the initial crack size (its initial depth was not known), so those results are less reliable.

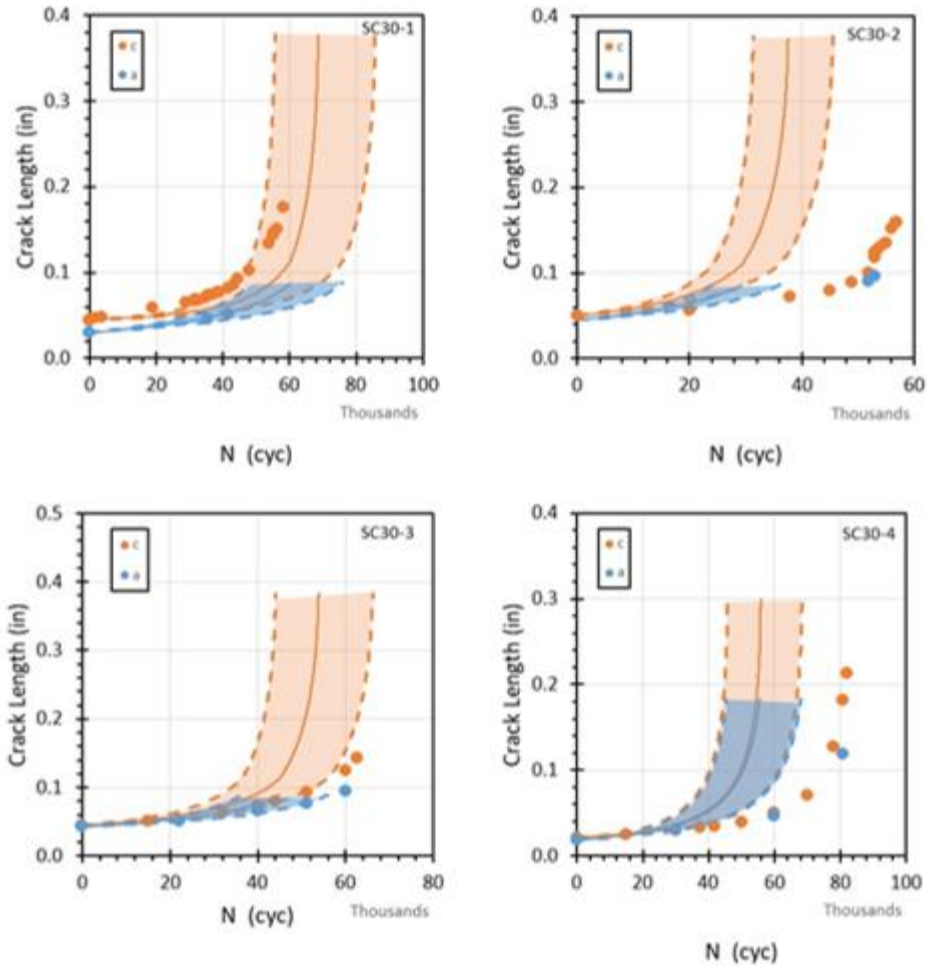


Figure C- 22. Calculated and measured FCG results for surface crack specimen

The results for the through crack at hole (TC13) geometry under remote tension loading are shown in Figure C- 23. The calculated results for these two specimens give slightly longer lifetimes than exhibited by the test data, but the differences are within the range of inherent scatter in material properties, so the disagreement is not significant.

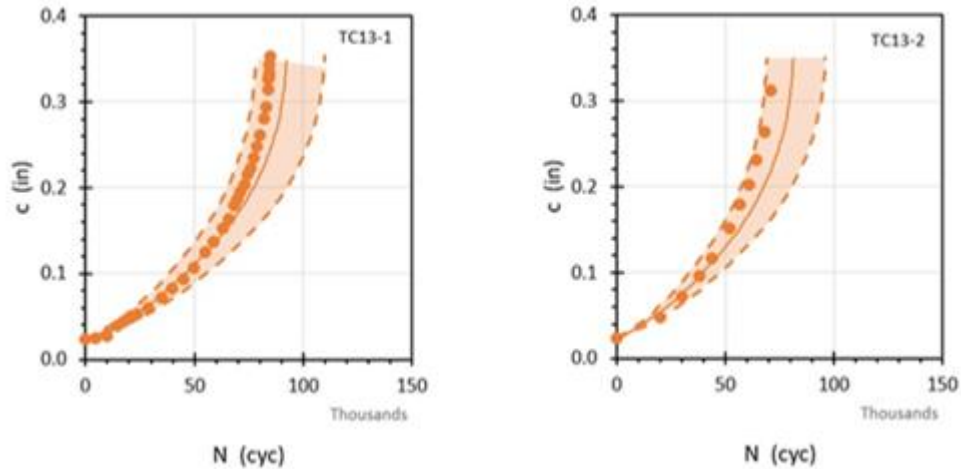


Figure C- 23 Calculated and measured FCG results for through crack at hole specimen

The results for the corner crack at hole (CC08) geometry under remote tension loading are shown in Figure C- 24. The predictions in all three cases are conservative by factors ranging from 1.54 to 1.96. This is an expected result based on the SIF solution verification studies documented in Appendix B. The CC08 solution trended conservatively, (predicted values higher than actual) due to the bivariate nature of the actual crack plane stresses. The stress gradient used in both those verification studies and these validation studies was a mid-plane stress characteristic of a 2D solution. The actual 3D stresses on the crack plane will be slightly higher at the mid-plane and slightly lower at the surface; the actual differences will be larger for a thick plate and smaller for a thin plate. As noted in Appendix B, this geometry is better suited for a bivariate solution. Verification of the DARWIN/NASGRO bivariate SIF solution for a corner crack at a hole was not completed during this grant but is being completed during a subsequent grant. Analysis of these experiments will be revisited after the additional SIF solution verification is complete.

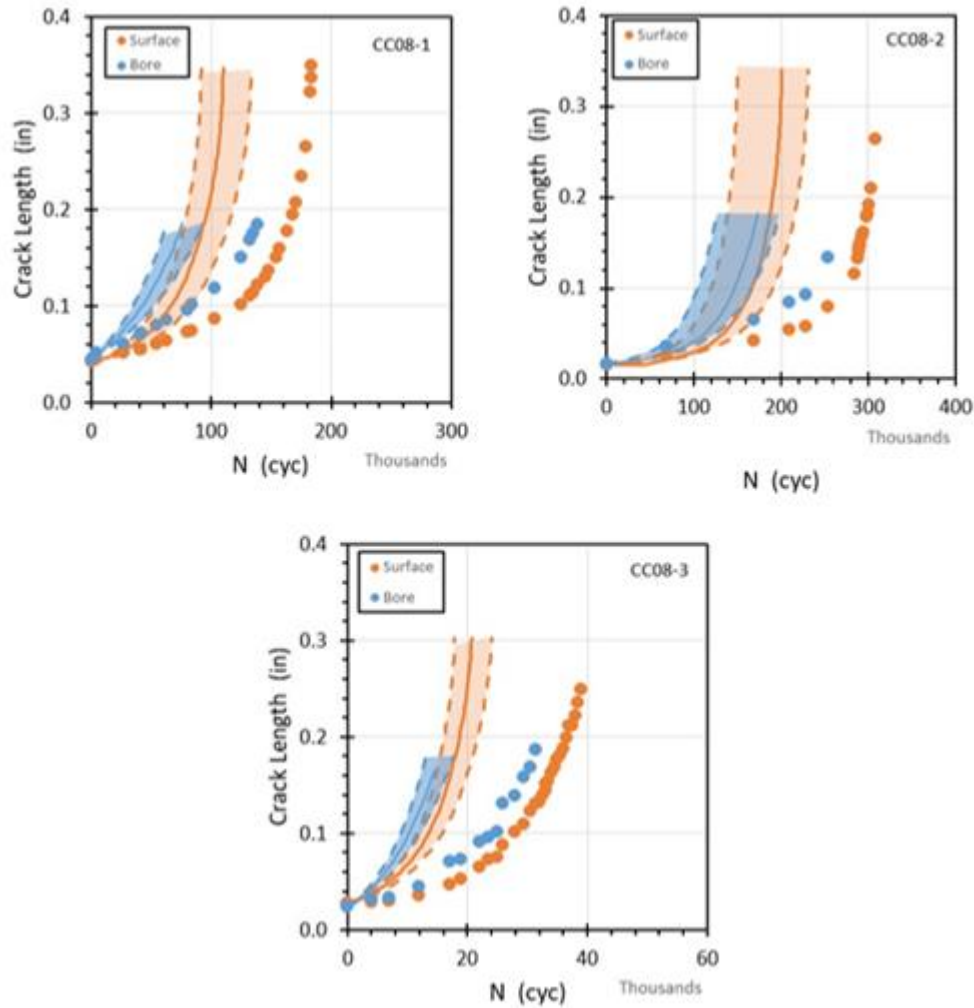


Figure C- 24. Calculated and measured FGC results for corner crack at hole specimen

A limited number of benchmark tests were performed under four-point bending, as shown previously in Figure C- 3. Only two specimen geometries were considered, through crack at edge of plate (TC02) and corner crack in plate (CC11). The results for the through crack in plate (TC02) geometry under four-point bending are shown in Figure C- 25, and the results for the corner crack in plate (CC11) geometry under four-point bending are shown in Figure C- 26. In all cases, the predicted crack growth rates and lifetimes were significantly conservative compared to the experimental results. The two through crack results had life ratios of 1.82 and 1.93, while the two corner crack results were more dramatically conservative (factors of $3\times$ to $5\times$). These results are not currently understood. The experimental and calculation methods were revisited in a search for errors or missing factors, but neither was found. Specimens were strain-gaged to compare actual and predicted strains. Three-dimensional finite element SIF calculations

under actual four-point bending configurations were completed for selected crack sizes. One possibility is that the experimental configuration introduces constraint against end rotation that is not included in the DARWIN/NASGRO SIF solution, and that this effect is more severe under bending than under tension. No definite conclusions can be drawn at this time. However, it is important to note that the predicted results are conservative relative to the observed lifetimes, so the differences do not represent a safety issue.

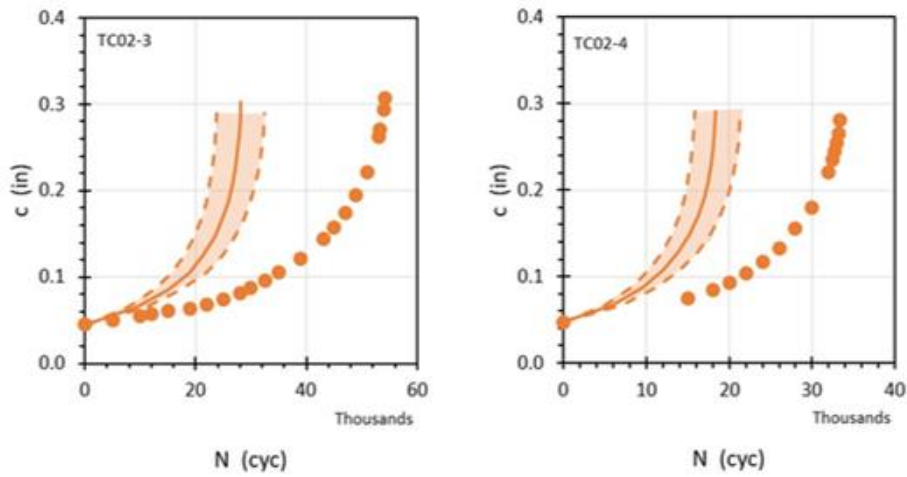


Figure C- 25. Calculated and measured FCG results for through crack under bending

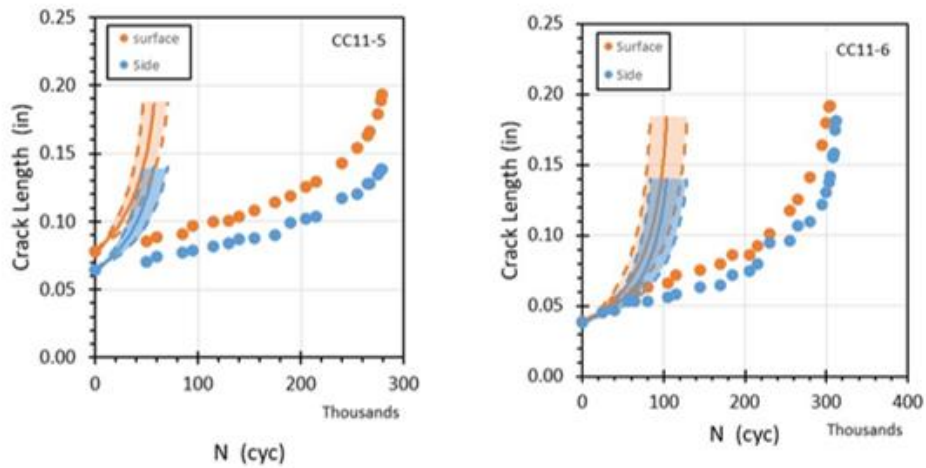


Figure C- 26. Calculated and measured FCG results for corner under bending

C.4 Discussion

As noted, because it is not possible to measure directly the SIF, the SIF models were benchmarked by comparing measured and predicted FCG. FCG predictions involve an integration of the baseline FCG property model and SIF models, which results in a compounding or accumulation of errors. Thus, it is imperative to understand the various sources of error and uncertainties when assessing the appropriateness of SIF solutions.

There are several possible reasons for differences observed between calculated curves and experimental data in all of the preceding benchmark configurations. First, as mentioned previously, there is an inherent (irreducible) scatter in the baseline material properties, and total prediction scatter cannot be smaller than the inherent FCG model scatter.

Second, there is error in the mathematical calculation of the SIF solution itself. This potential error was addressed previously in the verification study documented in Appendix B. That study noted that over 90% of the SIF solutions agreed with high-fidelity SIF solutions from 3D finite element (FE) analyses within 5%, most solutions even closer. These are relatively tight bounds, but still represent a source of some potential life variability. A consistent error of 5% in the SIF could translate roughly into a life calculation error around 15% to 20%. For one crack case (CC08), it was noted previously that the verification study had shown the SIF solution to trend more conservative, and this may explain the larger conservatism observed in calculated lifetimes.

There are other sources of uncertainty or error as well. There is epistemic (reducible) error in how the baseline FCG response is modeled. Statistically, the mean was established by treating all measurements as independent, despite being derived from a series of tests where it would be reasonable to anticipate some correlation between data within a particular test. Further, the baseline data were modeled in a piecewise linear fashion.

There may be a lack of similitude between the SIF model and the actual specimen or component. The SIF calculation may be nearly exact, but for a slightly different configuration than actually encountered. For example, the influence of boundary conditions that may restrain the ends of the specimen or component remote from the crack against rotation was mentioned earlier for a few crack cases. A SIF model for an unrestrained configuration will give conservative predictions for a restrained configuration.

Two other issues deserve brief consideration, surface correction factors and stress level effects.

Surface correction factors

One of the features of the SIF solutions in both DARWIN and NASGRO is the use of surface correction factors at the tips of part-through cracks (surface and corner cracks). Many years of experimental observations for surface cracks in plates has shown it has become common to slightly reduce the values of ΔK of the surface tips when performing FCG calculations. The method used in both NASGRO and DARWIN (Newman & Raju, 1984) employs a surface correction factor β_R that is a function of the R value. For $R > 0$, β_R is given by $\beta_R = 0.9 + 0.2R^2 - 0.1R^4$ and for $R \leq 0$, β_R is assumed to have a value of 0.9.

There have been few experimental efforts to evaluate the use of β_R for corner cracks. This is more difficult to discern by test than for a surface crack, because using β_R for a surface crack changes its shape, while using β_R for a corner crack does not change its shape--only a small reduction in the SIF value at both tips. Nevertheless, the benchmark study performed here does provide some useful evidence. All the calculated crack growth curves in this study employed the β_R factor for the surface tips, so the ΔK values at those tips were reduced by about 10%. If the β_R had not been included, the ΔK values would have been higher, and the calculated FCG lifetimes shorter. In this case, they are shorter by about 40% for all corner crack tests. The calculations for the corner crack tests were already shown to have a conservative bias, and so an additional decrease in calculated life would have rendered them rather over-conservative. Therefore, the use of the β_R factors seems appropriate.

Stress level effects

The specific stress levels employed in these experimental studies were chosen in part for experimental convenience, to focus the crack growth in the Paris regime of the baseline curves while avoiding near-threshold and plasticity effects. In principle, these FCG models should work equally well at any stress level in the small-scale yielding regime. However, maximum stress levels could nevertheless have some complicating effect on the performance of the models (for example, due to stress-driven crack closure effects). Therefore, a few tests were conducted at contrasting (higher) applied stress levels (refer again to Figure C- 3). For example, three of the corner crack in plate (tension) tests were performed with a maximum stress around 32 ksi, while one test was conducted at a maximum stress of almost 46 ksi. Surface crack tension tests were performed at maximum stresses around 32 ksi and 47 ksi. Edge crack tension maximum stresses varied from 22 ksi to 30 ksi.

These increases in maximum stress in a few tests did generally have the expected effect of significantly decreasing the test lifetimes, but there was not an obvious degradation of prediction

quality compared to the lower stresses. The only apparent bias was in the four corner-crack tension tests, where the one test at high stress was predicted very accurately, while the three tests at lower stresses gave conservative predictions.

C.5 Future work

This benchmark study is certainly not exhaustive, and some questions remain. A modest budget is available for additional benchmark testing and analysis in a subsequent grant. That additional work will follow up on some of the most significant remaining questions from the current study.

Several of these questions and issues have been mentioned in the preceding pages. The corner crack at hole geometry deserves further analysis upon completion of the corresponding verification studies for the bivariate SIF solution. The puzzling results in the bending tests may invite additional investigations. Additional stress level effect studies seem worthwhile, including tests in lower life ranges ($\sim 10^5$ cycles and below).

Other issues may also be targets for additional study. The limited amount of detailed transition data collected in the current study has not been analyzed in depth. Additional transition data could be collected: for example, offset surface cracks that transition to corner cracks before transitioning to through cracks. A new SIF solution for a curved edge through crack has been developed and implemented in NASGRO and could provide more accuracy for transition modeling. This solution has not yet been implemented in DARWIN but has been under consideration.

The current study considered six different SIF solutions. DARWIN contains several other SIF solutions, and there may be value in exploring some of these. Some (*e.g.*, bivariate surface crack at a hole) would be very difficult to investigate with enough fidelity and may not be worth the effort, given their level of usage. Embedded cracks are also extremely difficult to study and introduce several confounding effects (*e.g.*, vacuum effects on FCG properties). However, DARWIN contains a few novel SIF solutions that have not been studied previously (since they have just recently been developed) and that may be more amenable to investigation (albeit with some experimental difficulty). Two such candidates include the TC15 solution for an edge through crack in a variable thickness (*e.g.*, tapered) plate, and the CC18 solution for a corner crack at a 135 degree corner.

Other questions may arise from the industry review of this initial benchmarking study, and those will be considered in line with the available budget.

C6. Summary and conclusion

A benchmarking study was conducted to perform validation of DARWIN SIF solutions and their use for FCG life predictions using Ti-6Al-4V at room temperature. Six different crack model geometries were evaluated.

Baseline FCG tests were performed with simple through crack tension geometries to develop high quality FCG properties. These baseline tests were analyzed statistically and shown to compare favorably with legacy FCG data for the same material source. Calculated FCG curves and lifetimes were compared with the baseline tests, as well as independent tests performed with the same geometries, to validate the baseline property models.

Additional benchmark FCG experiments were performed with four other geometries as well as different loading configurations (bending versus tension). The FCG behavior of the benchmark experiments was predicted using the baseline properties. The predictions were highly accurate (within expected material scatter) or slightly conservative in all cases with tension loading. Some potential reasons for the conservatism were identified. The predictions for the bending tests were more conservative, and the reasons for this stronger bias are not yet understood.

The results to date indicate that the DARWIN SIF solutions provide accurate or conservative predictions of FCG lifetime under all conditions considered. Additional studies are planned to explore other conditions.

C7. References

ASME. (2019). Guide for verification and validation in computational solid mechanics,. New York, NY: ASME International.

Boyce, B. L., & Ritchie, R. (2001). Effect of load ratio and maximum stress intensity on the fatigue threshold in Ti-6Al-4V. *Engineering Fracture Mechanics*, 68, 129-147.

Newman, J. C., & Raju, I. S. (1984). Prediction of fatigue crack-growth patterns and lives in three-dimensional cracked bodies. *Advances in Fracture Research (Fracture 84), Sixth International Conference on Fracture, Vol. 3*, pp. 1597-1608.

Sheldon, J. W., Bain, K. R., & Donald, J. K. (1999). Investigation of the effects of shed-rate, initial k_{max} , and geometric constraint on ΔK_{th} in Ti-6Al-4V at Room Temperature. *International Journal of Fatigue*, 21, 733-741.

D Thermo-mechanical fatigue crack growth testing

List of Figures

Figure D- 1. HS718 forging material used for the test program.....	D-6
Figure D- 2. HS718 grain macro.....	D-6
Figure D- 3. Crack growth specimen geometries used in TMF tests.....	D-7
Figure D- 4. Specimen extraction and cut-up plan	D-8
Figure D- 5. TMF test cycle.....	D-9
Figure D- 6. HS718 isothermal baseline testing with no shot peen – 450°F.....	D-11
Figure D- 7. HS718 isothermal baseline testing with no shot peen – 1200°F.....	D-11
Figure D- 8. HS718 isothermal shot peen (450°F) specimen 814306-SP8 heat-tints	D-12
Figure D- 9. HS718 isothermal shot peen (1200°F) specimen 814306-SP11 heat-tints	D-13
Figure D- 10. HS718 TMF specimen (814306-SP6) heat-tints	D-14
Figure D- 11. HS718 TMF shot peen specimen 814306-SP3 heat-tints	D-16
Figure D- 12. RS profile measured on rectangular specimen 814306-RS.....	D-17
Figure D- 13. Proposed residual stress measurement locations on dovetail notch specimen – Location 1 - Notch root; Location 2 - Gage section just outside the notch	D-18
Figure D- 14. RS profile measured on notched specimen 814306-SP10 at notch root	D-19
Figure D- 15. RS profile measured on notched specimen 814306-SP10 at gage section.....	D-19
Figure D- 16. Comparison of GE design curve vs. baseline tests on log-log scale confirms that the specific material curves buy into the generic curves	D-20
Figure D- 17. TMF crack growth calculation process	D-21
Figure D- 18. Normalized gradient used to predict lives of -220 specimens	D-22
Figure D- 19. Normalized baseline residual stress profile comparing the as-measured data to the GE design data	D-22
Figure D- 20. Analysis results for isothermal shot-peened specimen (specimen 814306-SP8 450°F)	D-23
Figure D- 21. Analysis results for isothermal shot-peened specimen 814306-SP11 (1200°F)....	D-24
Figure D- 22. Analysis results for TMF unpeened specimen (specimen 814306-SP6).....	D-25
Figure D- 23. Analysis results for TMF un-peened specimen 814306-SP6 comparing the TMF method to isothermal methods	D-26
Figure D- 24. Analysis results for TMF peened specimen 814306-SP3 comparing the predictions with peening benefit turned on to the prediction with peening turned off.....	D-27
Figure D- 25. Analysis results for TMF peened specimen 814306-SP3 comparing the TMF method to isothermal methods	D-28

List of Tables

Table D- 1. HS718 isothermal shot peen (450°F) specimen 814306-SP8 heat-tints.....	D-12
Table D- 2. HS718 isothermal shot-peen specimen (1200°F) heat-tint measured crack size ..	D-14
Table D- 3. HS718 TMF unpeened specimen (814306-SP6) heat-tint measured crack size ...	D-15
Table D- 4. HS718 TMF with peen specimen (814306-SP3) heat-tint measured crack size ...	D-16
Table D- 5. Analysis results with and without peening considered.....	D-28

D.1 Introduction

Aircraft turbine-engine components operate in a complex thermo-mechanical fatigue (TMF) environment, and often the stress and thermal cycles are not completely in-phase. The stress cycles are commonly defined by the well-known “Stress Rainflow” method, such as cycle pairing methods defined in American Society for Testing and Materials (ASTM) Standard Practice E1049 (ASTM, 2005). However, temperature must also be assigned to each cycle pair to determine the appropriate material properties for fatigue crack growth (FCG) rate computation. One common approach is to use the temperature at the maximum stress time point. Alternatively, the maximum temperature among the two cycle endpoints can be used. This approach will potentially provide a more conservative result. However, both of those approaches neglect the possibility that a time point elsewhere in the mission might have a higher temperature that could adversely affect the crack growth resulting from the stress pair. This can be conservatively addressed by using properties corresponding to the maximum temperature in the mission, but this may be excessively conservative. Other approaches take a more integrated perspective for temperature effects, including the “damage rainflow” and “average da/dN ” methods. The DARWIN software offers these five options: temperature at the maximum stress time point in the stress pair, maximum temperature among the end points of the stress pair, maximum temperature in the mission, average da/dN , and damage rainflow.

The average da/dN crack growth-rate methodology is based on stress rainflow pairing. Equation D-1 computes the crack growth rates for each rainflowed stress pair derived from average FCG rates, from reference temperature at the maximum stress time point of the current stress pair, to the maximum reference temperature in the whole mission. Then, the crack growth for this load pair is computed by integrating the crack growth rates between these two bounding temperatures:

$$\text{average } da/dN = \frac{\int_{T_{\max \sigma}}^{T_{\max}} (da/dN)_T dT}{(T_{\max} - T_{\max \sigma})} \quad (\text{D-1})$$

The actual TMF approach implemented is a numerical integration scheme that discretizes the above integral in 1°F increments.

Each of these five methods have been shown in industrial practice to give reasonable or conservative results for certain materials and stress-temperature histories, and several of the methods are used routinely by one or more aircraft engine manufacturers. However, the general applicability and relative accuracy of each is unclear. Given that real engine components operate under complex missions with variable thermal and stress environments, each of these methods is at best an approximation. A universal method that addresses every scenario accurately may not exist. The phrase commonly attributed to statistician George E. P. Box, “all models are wrong, but some methods are useful,” may be applicable here. While individual manufacturers have generally adopted a preferred method and generated appropriate validation experience (which usually remains proprietary), there has been interest in developing additional data to support industry discussion. For example, thermo-mechanical FCG data were generated in the Turbine Rotor Material Design Phase II grant (McClung, et al., 2008).

Many aircraft engine turbine-components employ some surface treatment (*e.g.*, shot peening) that imparts a compressive residual stress (RS) layer on the surface. This practice generally results in improved fatigue life. While previous studies have explored the TMF effect on crack growth or the RS effect on crack growth, very little effort has been spent to understand the complex interaction of RS and thermo-mechanical effects for FCG.

A very limited exploratory study was conducted at GE Aviation to understand the interaction of RS and TMF effects. The objective of this effort was not to fully characterize the complex interaction (potentially a major focus topic for a future research contract), but rather to build some limited understanding and key insights with a handful of benchmark experimental data that can be shared with industry and researchers. This small common dataset will hopefully form the basis for additional exploration of different TMF models and a more comprehensive effort to characterize this important effect in the future. The widely used high temperature, high-strength alloy Inconel 718 was chosen for this investigation. Specimens were machined from remnant material contributed by GE Aviation.

With these objectives in mind, the following task scope was developed:

- Conduct isothermal FCG rate tests (unpeened) to establish baseline FCG rate properties at 450°F and 1200°F, including replicate tests at each temperature.
- Conduct isothermal residual life FCG tests at 450°F and 1200°F for specimens that have been shot peened to a prescribed intensity (Almen 7A).

- Conduct a residual life FCG test for a representative out-of-phase TMF history between 450°F and 1200°F with an unpeened specimen to establish the baseline TMF effect without RS.
- Conduct up to two residual life crack-growth tests for the same representative TMF history and the same shot peening intensity as above. Unfortunately, due to program budget constraints, the duplicate specimen was machined and peened, but the testing could not be completed.
- Perform heat tinting as part of residual life tests to aid with interpretation and analysis of test results (approximately three heat tints per test).
- Measure shot peening RS gradient (X-ray diffraction with layer removal) for the same shot peening intensity. One set of measurements will be performed on a coupon that has not been tested, and another set of measurements will be performed on a coupon at the end of a TMF test. The RS measurement planned at the end of the test was pulled back due to programmatic budget constraints, but the test specimen is available and archived if this effort needs to be revisited.
- Predict FCG lifetime for all TMF tests, including RS effects as appropriate.

D.2 Materials and processing

The test material for this program was High Strength 718 (HS718). It was obtained from a production-forging ring used on a compressor rotor spool provided by GE Aviation, as shown in Figure D- 1. The forging pedigree is summarized as Supplier Serial No. EGG0912/AFPV1912, Heat No. 814306_2A.



Figure D- 1. HS718 forging material used for the test program

The forging was solution treated between 1725°F and 1875°F for one hour. Following the solution treatment, the material was aged at 1325°F for eight hours, followed by another age at 1150°F for eight hours. Figure D- 2 shows the microstructure from the forging. The grain size was estimated to be ASTM GS 10 average with as large as (ALA) 7.5. The 1200°F 0.2% average yield strength was 144.8 ksi.

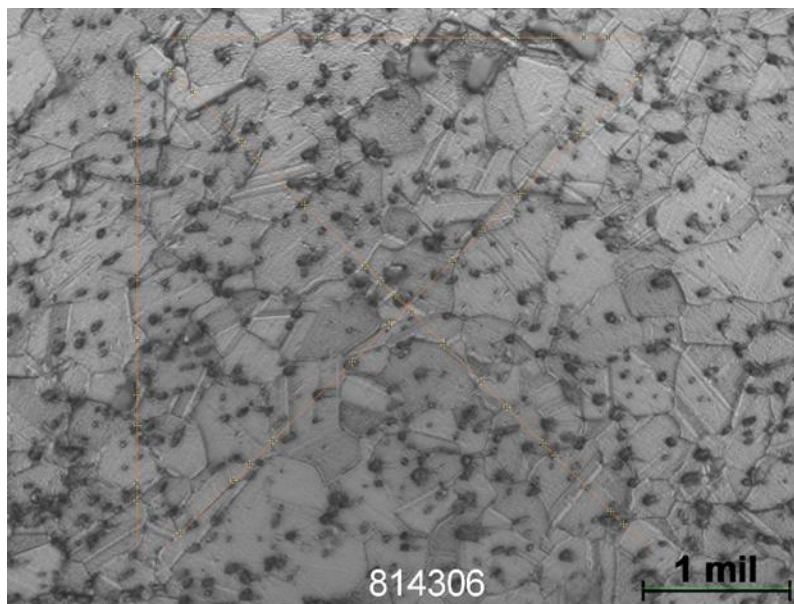
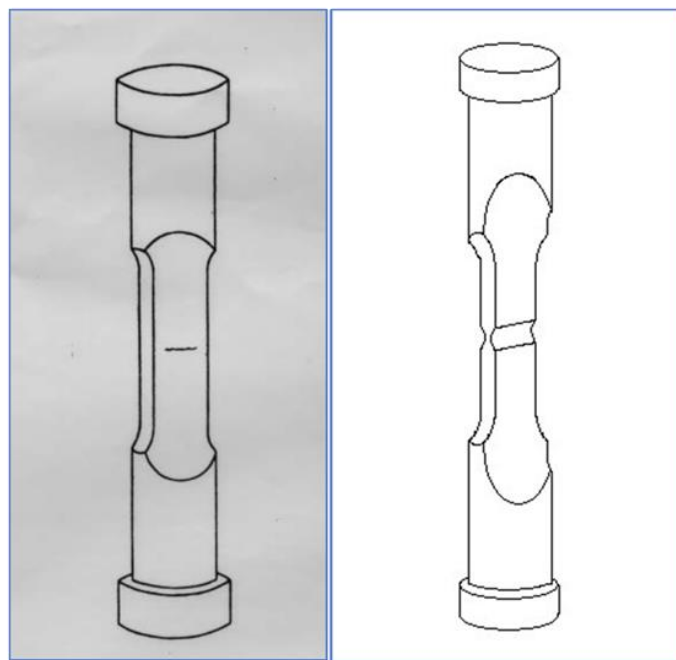


Figure D- 2. HS718 grain macro

The specimens that were peened had 100% coverage over the entire gage section to an intensity of 7A. The medium was CW14. The impingement angle was set at 45 degrees.

D.3 Specimen geometry and test methods

FCG specimens were extracted from the ring forging described in the previous section. The corresponding cut-up plan is shown in Figure D- 3. FCG testing was performed using a combination of Kb specimens and dovetail notch specimens (see Figure D- 4). The Kb bar (GE - 402 specimen geometry) has a semicircular flaw in the center of the gage dimension, and the crack grows along the flat of the gage section as well as through the thickness. The dovetail notch specimen (GE -220 specimen geometry, used on peened tests) has a semicircular flaw in the center of the notch, and crack growth occurs along the notch surface as well as from the bottom of the notch through the thickness towards the notch on the other side. The selection of the dovetail notch specimen for peened tests was based on the requirement to get small cracks to grow in a peened residual stress field, but also avoid net-section yielding. GE has previously compared un-peened crack growth results between the two configurations and ensured consistency.



Kb bar specimen

Dovetail notch

Figure D- 3. Crack growth specimen geometries used in TMF tests

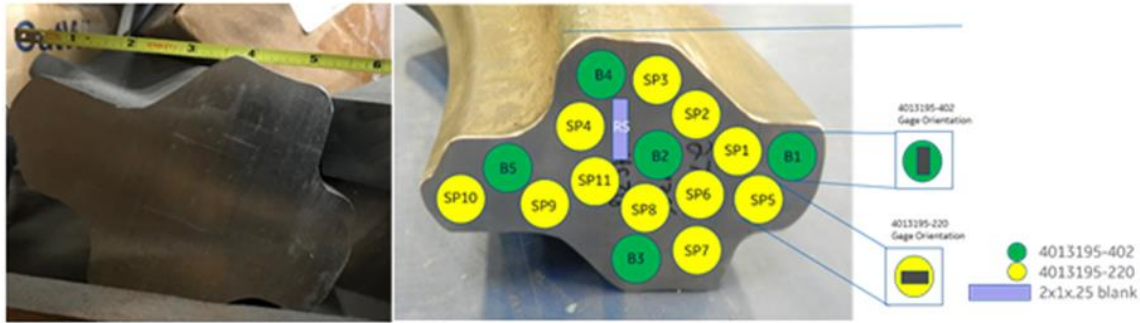


Figure D- 4. Specimen extraction and cut-up plan

D.4 TMF test matrix

An out-of-phase TMF cycle was selected for this study. The TMF cycle was designed to balance key considerations, including: (1) mission cycle is somewhat representative of actual engine cycles; (2) cycles have significantly different lives than comparable isothermal cycles; (3) temperature cycling is slow enough to avoid excessively high transient thermal stresses; and (4) test is fast enough that total test time would keep program costs within budget. Based on these considerations, the typical duration of a single TMF cycle was selected as 221.5 seconds. The details of the test conditions are listed below and are depicted pictorially in Figure D- 5

- 1.5 second ramp from 0 to 100 ksi (net section stress); temperature at 450°F
- 80 second ramp from 100 ksi to 0 ksi; temperature ramps from 450°F to 1200°F
- 140 second ramp from 1200°F to 450°F; stress at 0 ksi

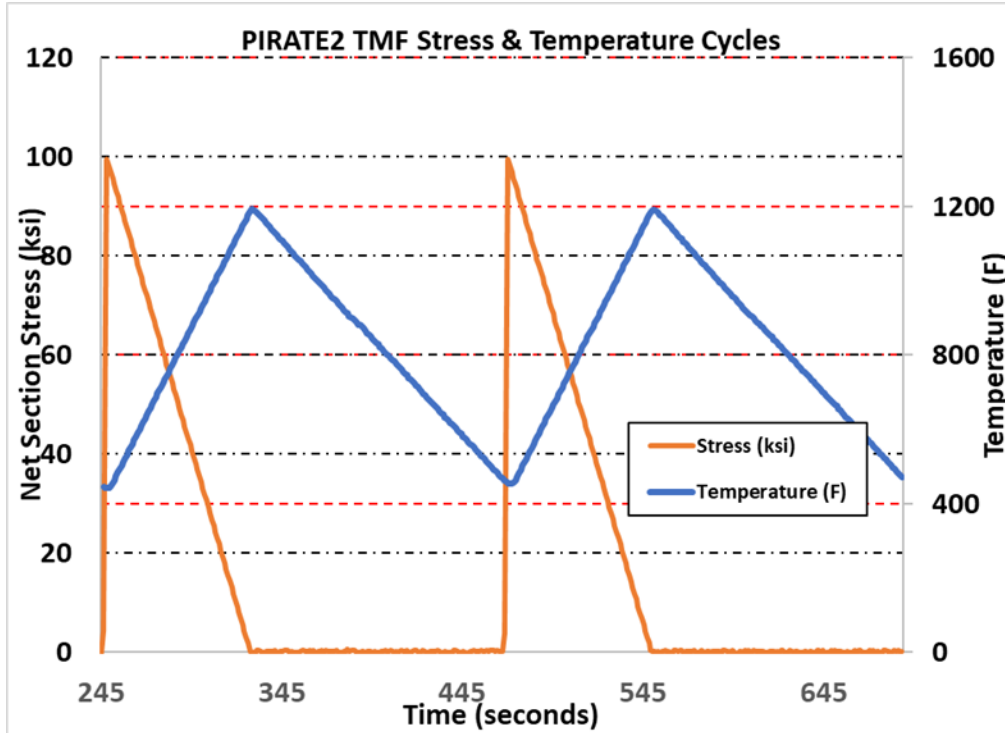


Figure D- 5. TMF test cycle

D.5 Experimental procedure and results

Before getting into the experimental procedures and results, some basic definitions and nomenclature used to describe the results is in order.

K_{eff} - Mean stresses can have a significant influence on cyclic FCG rates. For LEFM crack growth, it is useful to define the mean stress model in terms of *K* instead of stress. In this work, the effect of mean stress is incorporated using a Walker mean stress (Walker, 1970) model. For a cyclic *K*, the values of *K* at the minimum and maximum of a cycle are combined with various material specific data to identify an effective Walkerized value of *K* (*K_{eff}* or *K_{bar}*).

The *R*-ratio is defined as:

$$R = K_{min}/K_{max}$$

For a zero-max-zero cycle, *R* is zero. Otherwise, the sign of *R* is the sign of the minimum stress or *K*.

\bar{K} or *K_{eff}* is defined by the Walker equation:

$$K_{eff} = K_{max} (1-R)^m = \Delta K (1-R)^{m-1}$$

ΔK is the difference between K_{max} and K_{min} .

Here, we utilize a dual Walker exponent model where:

$$m = m+ \text{ when } R \geq 0$$

$$m = m- \text{ when } R < 0$$

The different exponents are required for the different R ratios because of the large amount of crack closure present when the minimum stress is compressive.

Isothermal no-peen crack growth test

To characterize the fracture mechanics properties of the baseline material fully, isothermal crack growth tests were conducted at 450°F and 1200°F, respectively. The corresponding results (using Kb bar specimens) are shown in Figure D- 6 and Figure D- 7. Baseline specimens were cycled using a 20 cycles per minute (cpm) triangle waveform (3 second cycle). The baseline isothermal crack growth tests were run at R=0 and 90 ksi maximum stress for the 1200°F test and 120 ksi maximum stress for the 450°F test.

Isothermal crack growth test with shot peening

Shot-peened specimen 814306-SP8 was tested at an isothermal temperature of 450°F using a 20 cpm (3 second cycle) triangle waveform. The net section stress was cycled from 0 ksi to 100 ksi, resulting in a maximum concentrated stress in the notch root of about 170 ksi. Net section stress refers to the unconcentrated stress in the notched portion of test bar and corresponds to the average stress in the minimum cross-section of the bar.

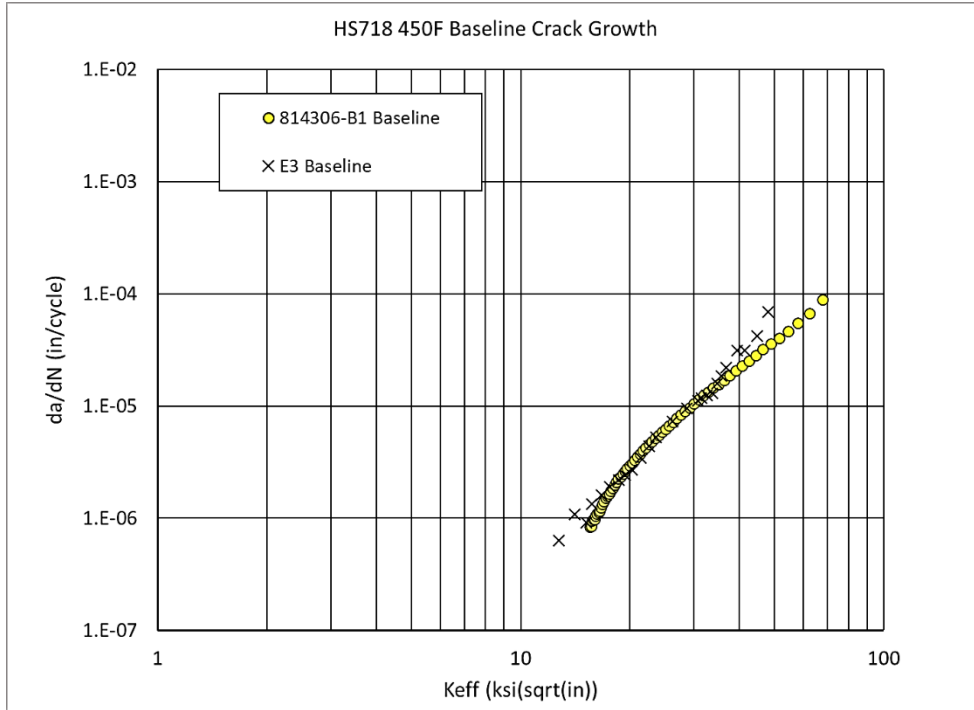


Figure D- 6. HS718 isothermal baseline testing with no shot peen – 450°F

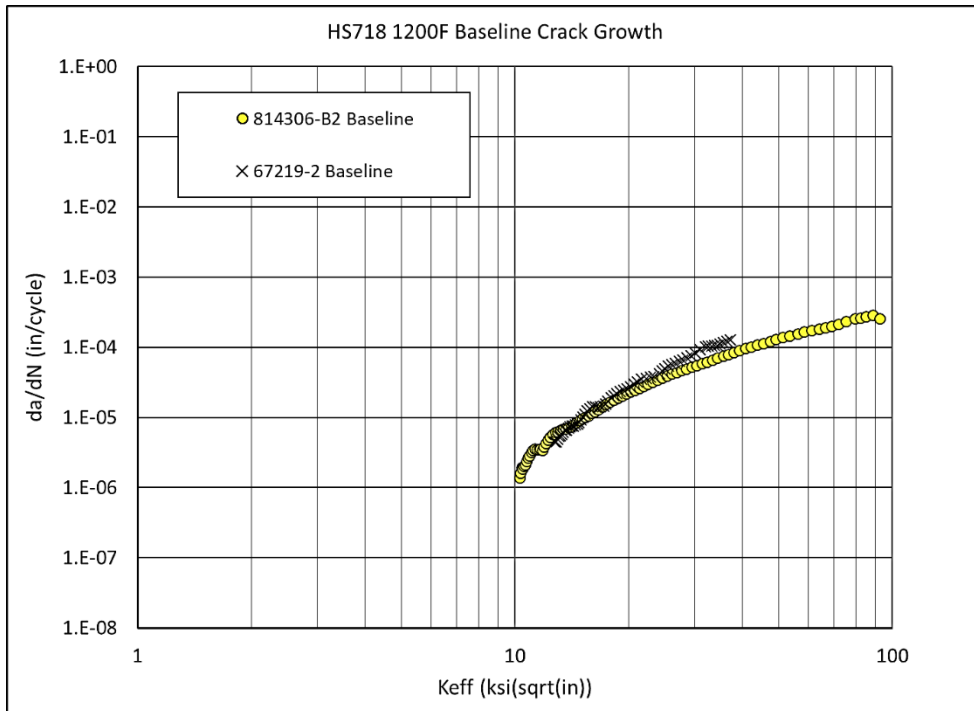


Figure D- 7. HS718 isothermal baseline testing with no shot peen – 1200°F

One heat tint was applied after the specimen was pre-cracked but before the FCG test started. Three heat tints were applied during the test according to the following schedule.

- Pre-test heat tint 1200F/16 hours
- Heat tint 1 @ 12,060 cycles (1225F/four hours)
- Heat tint 2 @ 20,160 cycles (1225F/two hours)
- Heat tint 3 @ 24,300 cycles (1225F/one hour)

Final fracture occurred at 26,780 cycles. The fracture surface with the heat tints is shown in Figure D- 8. Measured crack dimensions (inches) are summarized in Table D- 1.

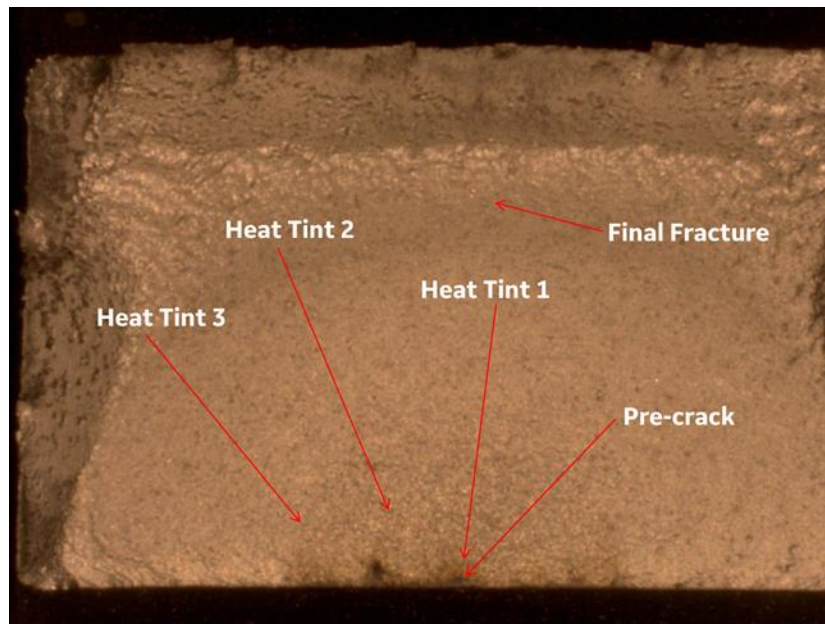


Figure D- 8. HS718 isothermal shot peened (450°F) specimen 814306-SP8 heat-tints

Table D- 1. HS718 isothermal shot peened (450°F) specimen 814306-SP8 heat-tints

Cycles	Measured a (inch)	Measured c (inch)
0	0.0056	0.00975
12060	0.0161	0.0187
20160	0.1419	0.0420
24300	0.0855	0.09775
26780	0.2174	0.2246

Shot-peened specimen 814306-SP11 was tested at an isothermal temperature of 1200°F using a 20 cpm (three second cycle) triangle waveform. The net section stress was cycled from zero ksi to 100 ksi, resulting in a maximum concentrated stress in the notch root of about 170 ksi.

One heat tint was applied after the specimen was pre-cracked but before the FCG test commenced. Three heat tints were applied during the test, according to the following schedule.

- Pre-test heat tint 1200°F/16 hours
- Heat tint 1 @ 1,820 cycles (1225°F/four hours)
- Heat tint 2 @ 2,740 cycles (1225°F/two hours)
- Heat tint 3 @ 3,460 cycles (1225°F/one hour)

Final fracture occurred at 4,200 cycles. The fracture surface with the heat tints is shown in Figure D- 9. Measured crack dimensions (inches) are summarized in Table D- 2.

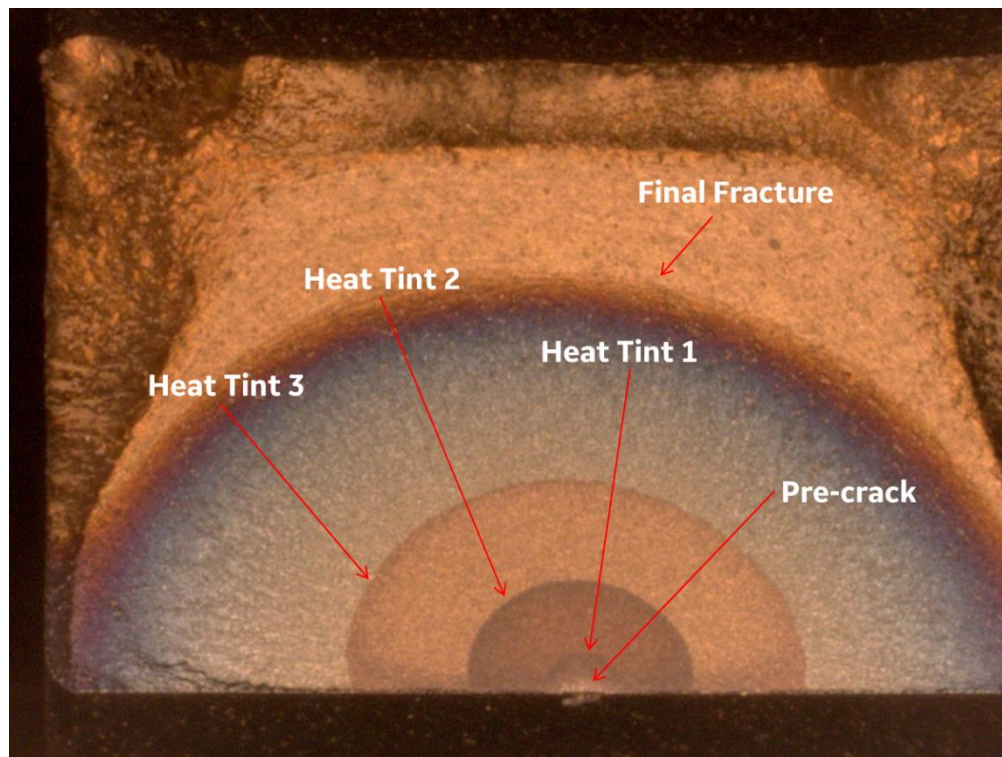


Figure D- 9. HS718 isothermal shot peen (1200°F) specimen 814306-SP11 heat-tints

Table D- 2. HS718 isothermal shot-peen specimen (1200°F) heat-tint measured crack size

Cycles	Measured a (inch)	Measured c (inch)
0	0.0071	0.0119
1820	0.0190	0.01935
2740	0.0529	0.0527
3460	0.1001	0.1072
4200	0.1970	0.2306

Unpeened TMF crack growth test

Unpeened specimen 814306-SP6 was tested using an out-of-phase TMF cycle (221.5 second cycle) as defined in Figure D- 10. The heat-tinting schedule was as follows.

- Pre-test heat tint 1200°F / 16 hours
- Heat tint 1 @ 1,200 cycles (1225°F / 4 hours)
- Heat tint 2 @ 2,400 cycles (1225°F / 2 hours)
- Heat tint 3 @ 3,600 cycles (1225°F / 1 hour)

Final fracture occurred at 6,662 cycles. The fracture surface with the heat tints is shown in Figure D- 10. Measured crack dimensions (inches) are summarized in Table D- 3.

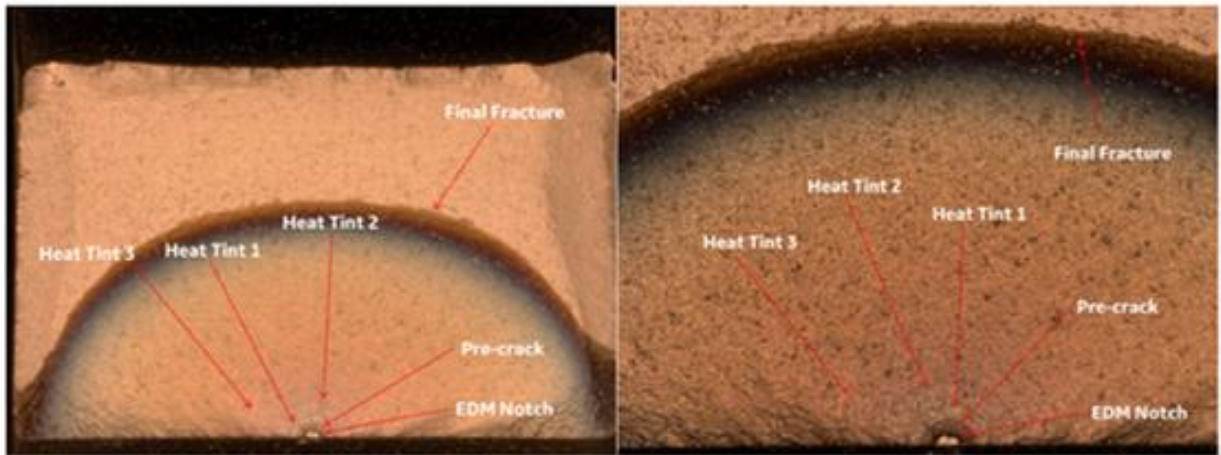


Figure D- 10. HS718 TMF specimen (814306-SP6) heat-tints

Table D- 3. HS718 TMF unpeened specimen (814306-SP6) heat-tint measured crack size

Cycles	Measured a (inch)	Measured c (inch)
0	0.0117	0.0127
1200	0.0204	0.02015
2400	0.0301	0.03185
3600	0.0471	0.05045
6662	0.196	0.24515

Shot-Peened TMF Crack Growth Test

Specimen 814306-SP3 was tested using the same defined out-of-phase TMF cycle but was shot-peened to 7A intensity. The dovetail notch geometry was used for this test specimen geometry. One heat tint was applied prior to test and two heat tints were applied during the test, as follows:

- Pre-test heat tint 1200°F/16 hours to mark pre-crack
- Heat tint 1 @ 5,000 cycles (1225°F/four hours)
- Heat tint 2 @ 10,000 cycles (1225°F/two hours)

The test bar failed at 13,058 cycles. The fracture surface with the heat tints is shown in Figure D-11. Measured crack dimensions (inches) are summarized in Table D- 4. The heat tint at 5000 cycles was not clear enough to permit a confident measurement of crack size.

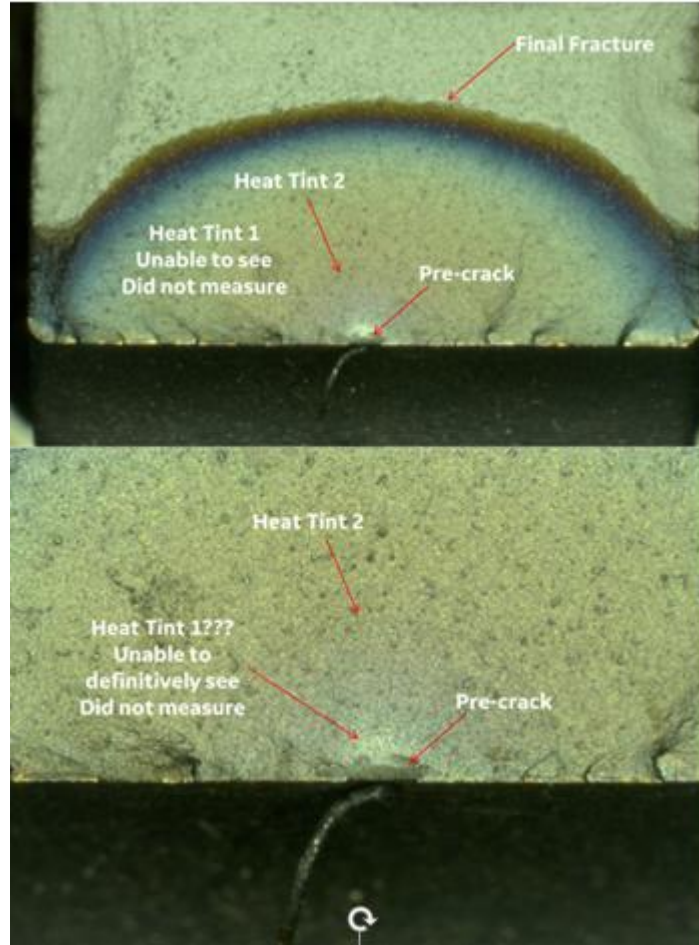


Figure D- 11. HS718 TMF shot peen specimen 814306-SP3 heat-tints

Table D- 4. HS718 TMF with peen specimen (814306-SP3) heat-tint measured crack size

Cycles	Measured a (inch)	Measured c (inch)
0	0.0006	0.0112
5000	Difficult to read heat tint – not measured	
10000	0.0536	0.0582
13058	0.185	0.2478

D.6 Residual stress measurement

One of the main objectives of this effort was to investigate the interaction between RS and thermo-mechanical effects in crack growth. Obtaining a good measurement of RS imparted on the test specimens is essential for building this knowledge. Towards this end, the following RS measurements were conducted. All RS measurements were completed by Lambda[®] Research.

Residual stress measurement on rectangular panel

A rectangular HS718 coupon (1"×0.25"×2", Panel-ID: 814306-RS) shot-peened to the same specifications as the TMF samples was used to obtain RS measurements at the following depths: 0 (Surface), 0.5, 1, 2, 3, 4, 5, 7.5, 10, and 15 mils depth. The resulting RS profile is shown in Figure D- 12.

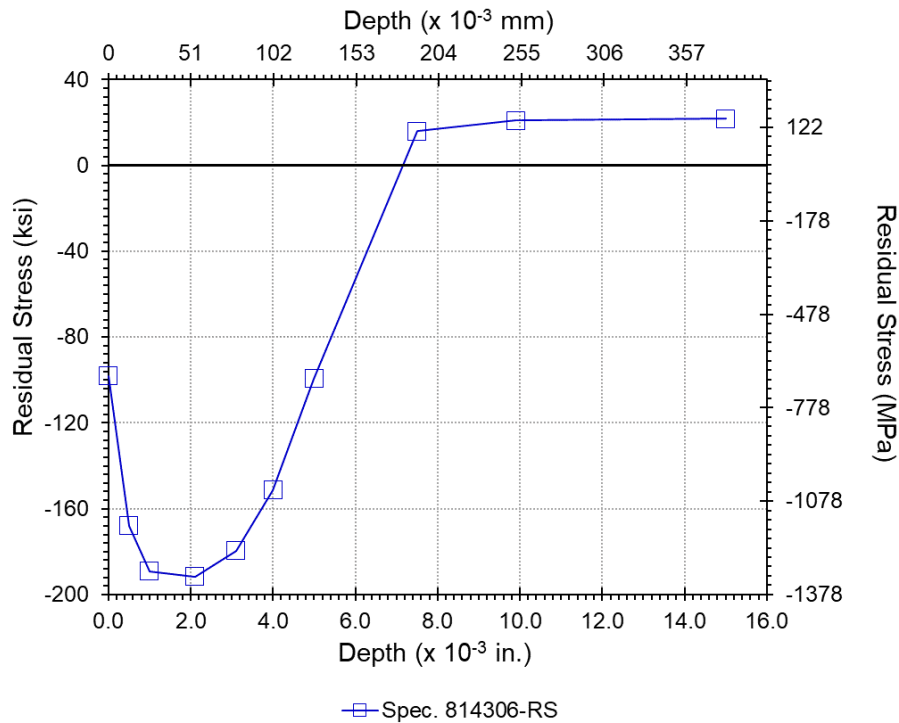


Figure D- 12. RS profile measured on rectangular specimen 814306-RS

Residual stress measurement on untested dovetail notch specimen

To understand the difference in RS between a flat coupon specimen and a notched specimen, residual stresses were measured on an untested dovetail notch as shown in Figure D- 13. The locations included the notch root and another on the gage section just outside the notch. The purpose of selecting these locations was to compare how the RS varies within the flat section and contoured section of the same specimen and benchmark this against the RS of the rectangular coupon specimen shown in Figure D- 14. The difference would also exist in rotor components with flat or contoured surfaces. The dovetail specimen was peened and had some oxidation due to heat-tint at 1200°F for 16 hours. The heat-tint was intentionally done for consistency with the starting condition of the test specimens after heat tinting to mark the pre-crack. Measurements were taken at 0 (surface), 0.5, 1, 2, 3, 4, 5, 7.5, 10, and 15 mils depth. The resulting RS profiles are shown in Figure D- 14 and Figure D- 15. The comparisons of these plots indicate that there is no RS at the surface in the notched geometry and that the magnitude of the RS in the depth is reduced in the notched geometry compared to that in the rectangular coupon specimen up to a depth of about four mils. The heat tint prior to the measurement could explain this amount of relaxation but based on the test results of the peened specimens this amount of relaxation seems unreasonable. The crack should have grown faster along the surface if the residual stress was completely relaxed. It would be interesting to measure the RS in the tested specimen to see how it compares to these notched specimen results.

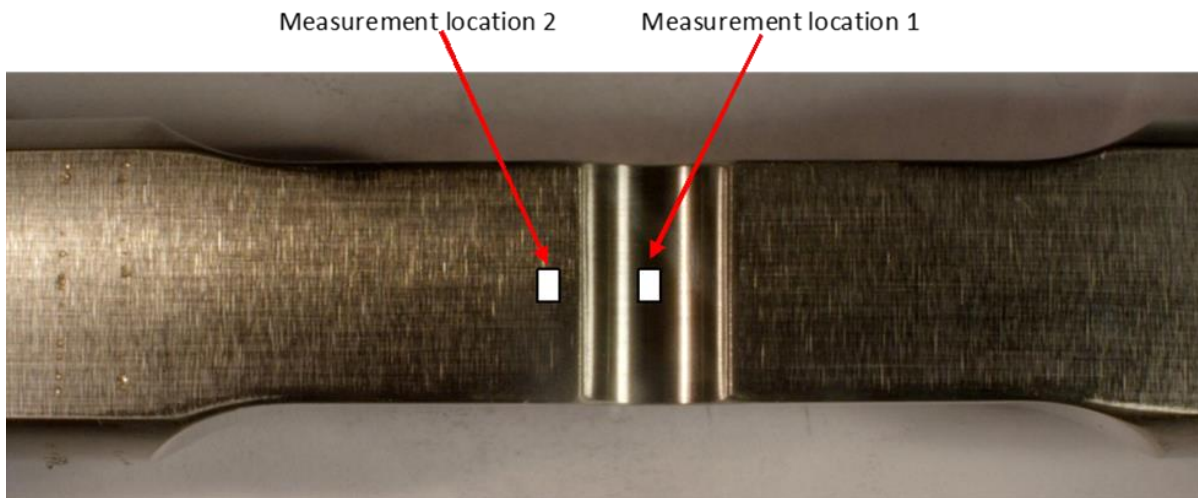


Figure D- 13. Proposed residual stress measurement locations on dovetail notch specimen – Location 1 - Notch root; Location 2 - Gage section just outside the notch

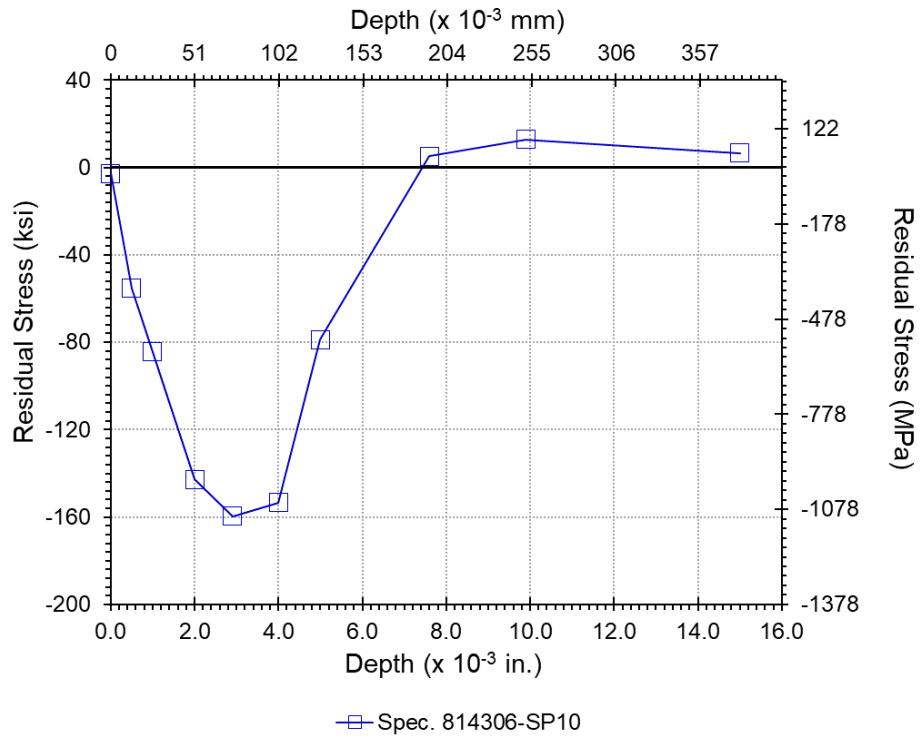


Figure D- 14. RS profile measured on notched specimen 814306-SP10 at notch root

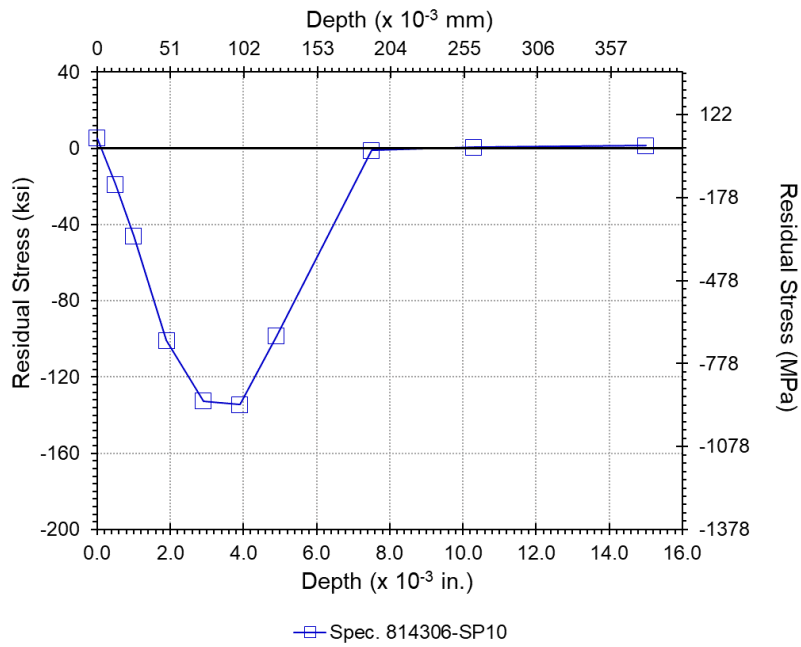


Figure D- 15. RS profile measured on notched specimen 814306-SP10 at gage section

D.7 Analysis results

The FCG tests were back-predicted using the GE Aviation Residual Life Program, PROPLIFE. The GE Aviation production crack-growth curves for HS718 at 450°F and 1200°F were used to predict the crack growth rate. Isothermal baseline tests conducted as part of this program were compared against GE design curves (see example normalized comparison shown at 450°F in Figure D- 16) to confirm that the specific material data did buy into the generic design curves for this material. Since the GE design curves are based on extensive testing well outside the scope of this limited test program (~50 tests covering the 450-1200 °F temperature range, which include a good distribution of $R = 0$, $R < 0$ and $R > 0$ tests to account for mean-stress effects); it was considered prudent to verify “buy-in” and then use the GE design curves for the analysis effort. Note that the GE design curves are somewhat conservative at higher K_{eff} . However, from a crack-growth life standpoint, this regime accounts for a very small percentage of the overall propagation life. As such, additional details associated with these design curves (or underlying tests) are considered GE proprietary and will not be made available as part of this report.

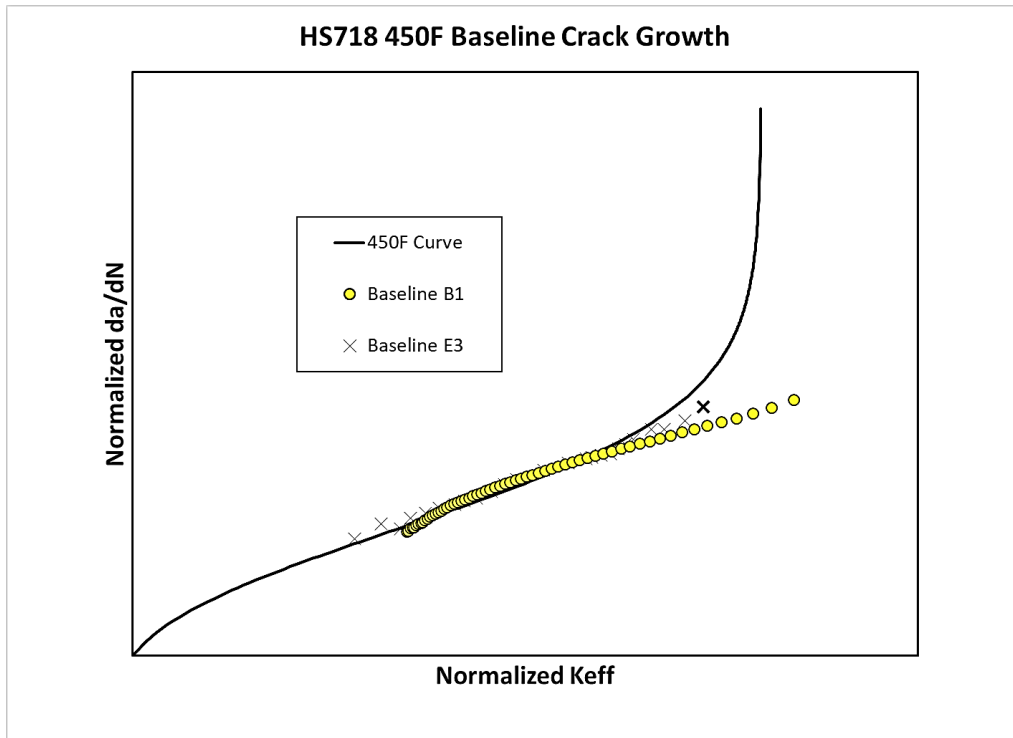


Figure D- 16. Comparison of GE design curve vs. baseline tests on log-log scale confirms that the specific material curves buy into the generic curves

Figure D- 17 outlines the TMF crack-growth calculation procedure, including a simple superposition approach to account for peen residual stress effects. The elastic gradient for the dovetail notch (-220 specimen geometry) specimens was obtained from a finite element model of the specimen. That gradient, normalized to a stress of 1.0 at the surface, is shown in Figure D-18. The weight function method is used to calculate the stress intensity factors.

The production HS718 7A intensity peen model was used to account for the effect of the RS due to peening and any relaxation of the residual stress for those specimens that were peened. Figure D- 19 shows the normalized baseline residual stress profile comparing the as-measured residual stress profile of the peened test bar against the GE production HS718 peen model. This confirms that the peening residual stress imparted adequately matches the production peen models. The initial crack dimensions used in the analyses were taken from the heat tint measurements at cycle zero. All analyses were run to failure. Termination was due to the calculated maximum K_{eff} value exceeding 96% of the toughness value contained in the crack growth curve.

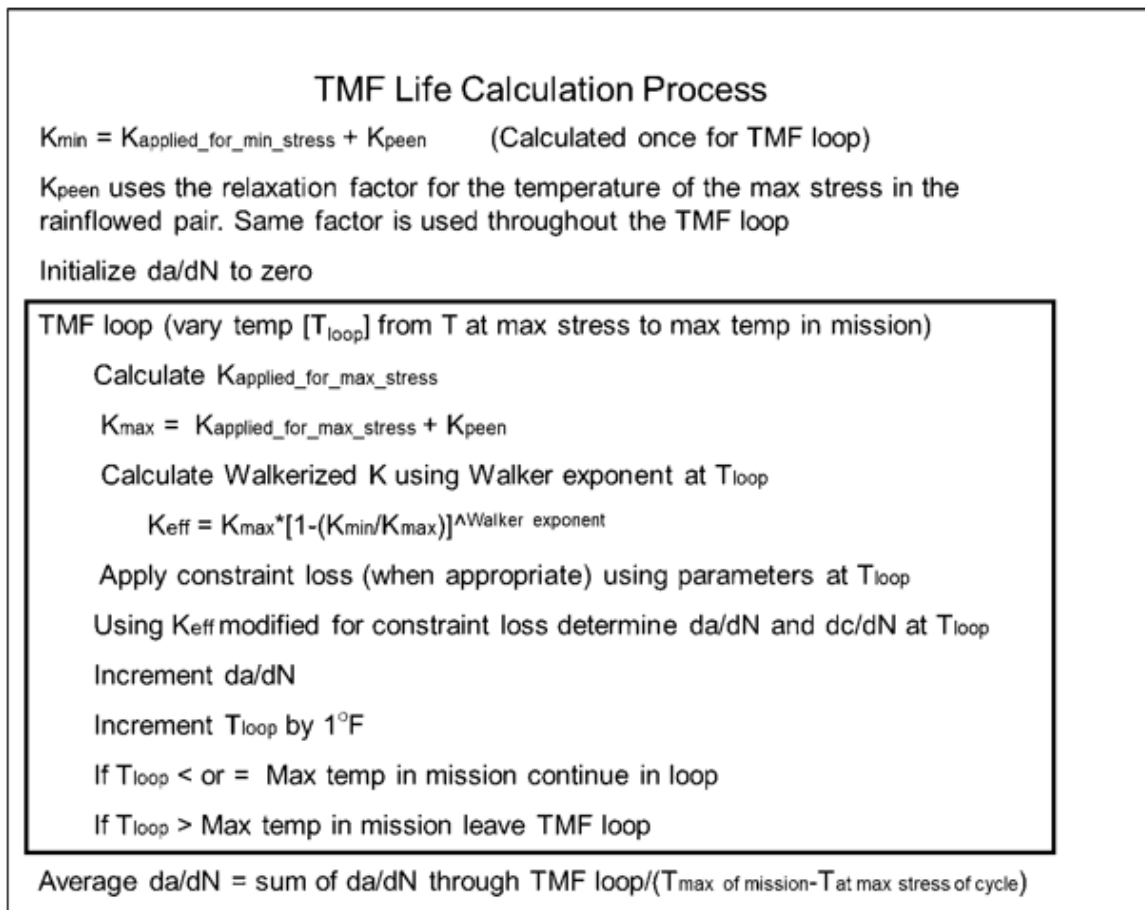


Figure D- 17. TMF crack growth calculation process

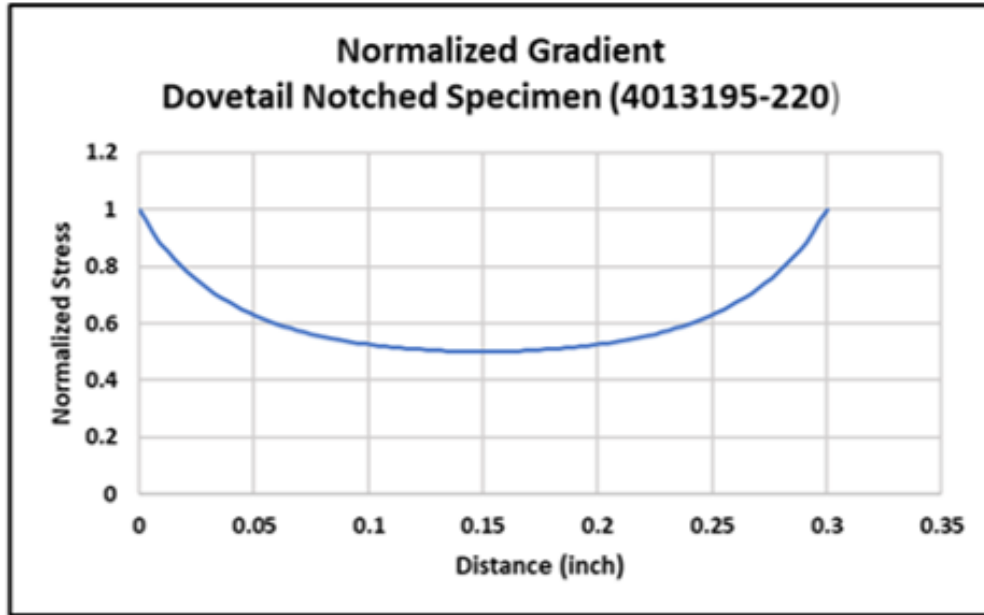


Figure D- 18. Normalized gradient used to predict lives of -220 specimens

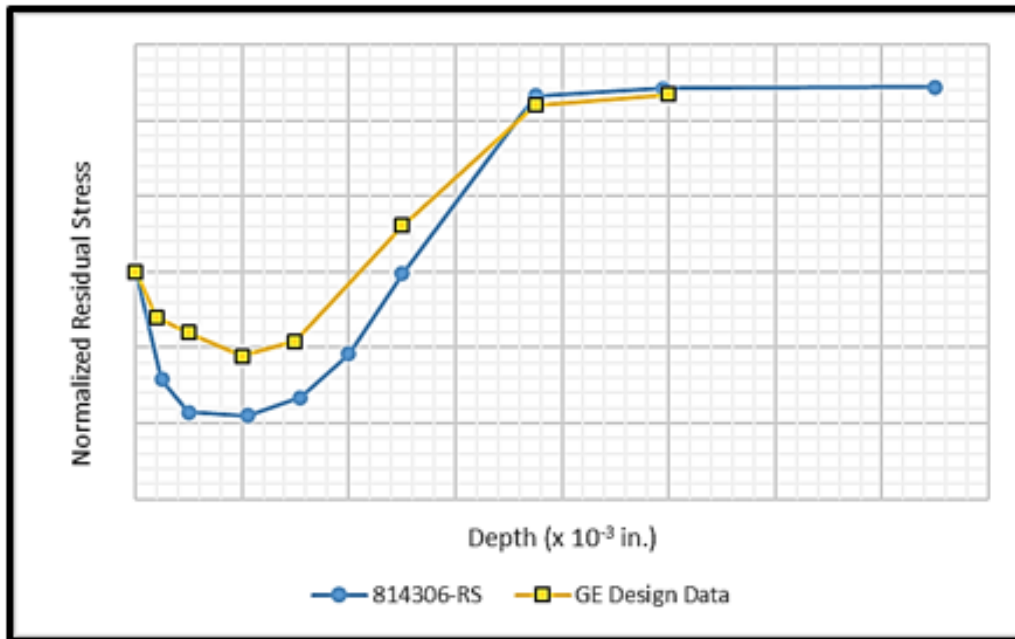


Figure D- 19. Normalized baseline residual stress profile comparing the as-measured data to the GE design data

Specimen 814306-SP8 analysis results are shown in Figure D- 20. This specimen was run isothermally at 450°F and was peened. The results are shown for predictions both with and without peening. The peening results were run with both the GE Aviation RS profile and the RS profile measured from the plate geometry as a part of this program. Refer to Figure D- 20. In both peened predictions, the relaxation parameter was assumed the same as that used in the GE Aviation model. For this specimen the predictions including peening are slightly non-conservative. The initial crack growth rate correlates well with the experimental results, but as the crack gets deeper and longer, the predicted rate is slower than observed in the tests. Adjusting the relaxation factor would result in better correlation, but this factor was appropriate for the tests included in the GE Aviation design model.

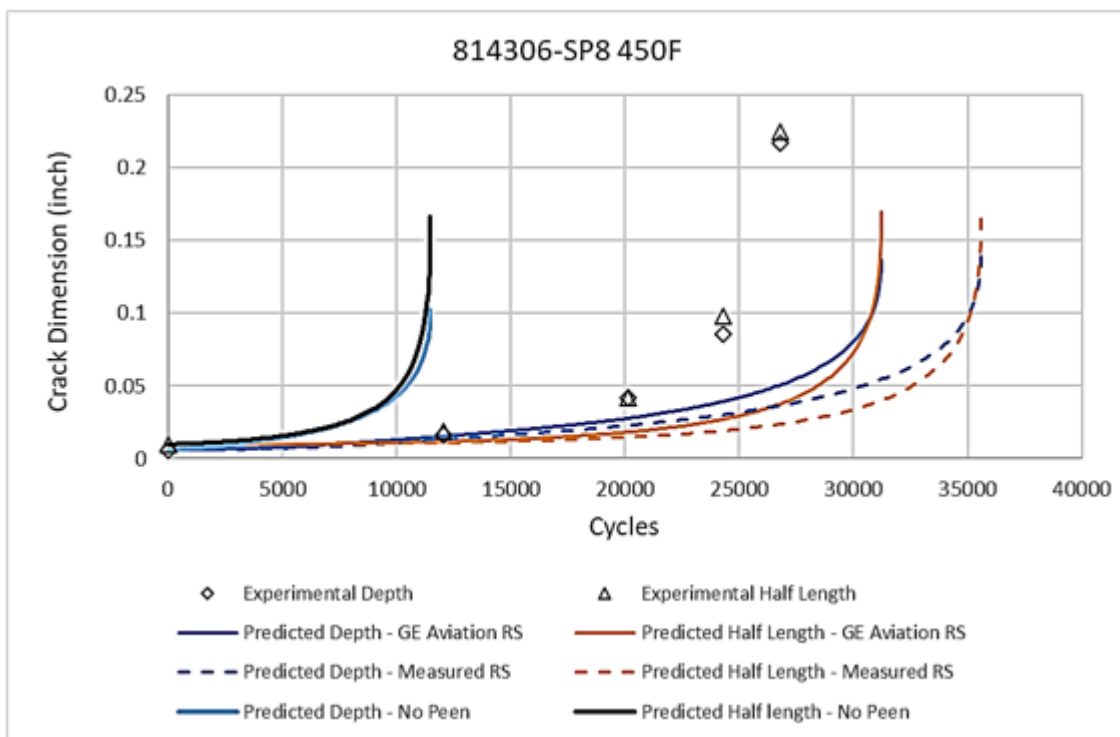


Figure D- 20. Analysis results for isothermal shot-peened specimen (specimen 814306-SP8 450°F)

Figure D- 21 shows the analysis results for Specimen 814306-SP11. This specimen was peened, and the test was run isothermally at 1200°F. The results are shown for predictions both with and without peening. For this specimen the predictions with peening turned on are slightly conservative. Notice that the prediction using the measured RS and the GE Aviation relaxation factor is basically the same as that using the GE Aviation RS and relaxation factor. The initial predicted crack growth rate is faster than in the experiment even with peening turned off, but the cycle count and crack dimensions correlate well at the second heat tint when the peening effect is included. The final growth rate in the test is slower than the predicted one.

Based on the comparisons of the predictions of these two peened isothermal tests the RS profile and relaxation factor used in the GE Aviation peen model were appropriate to use for the prediction of the peened TMF test.

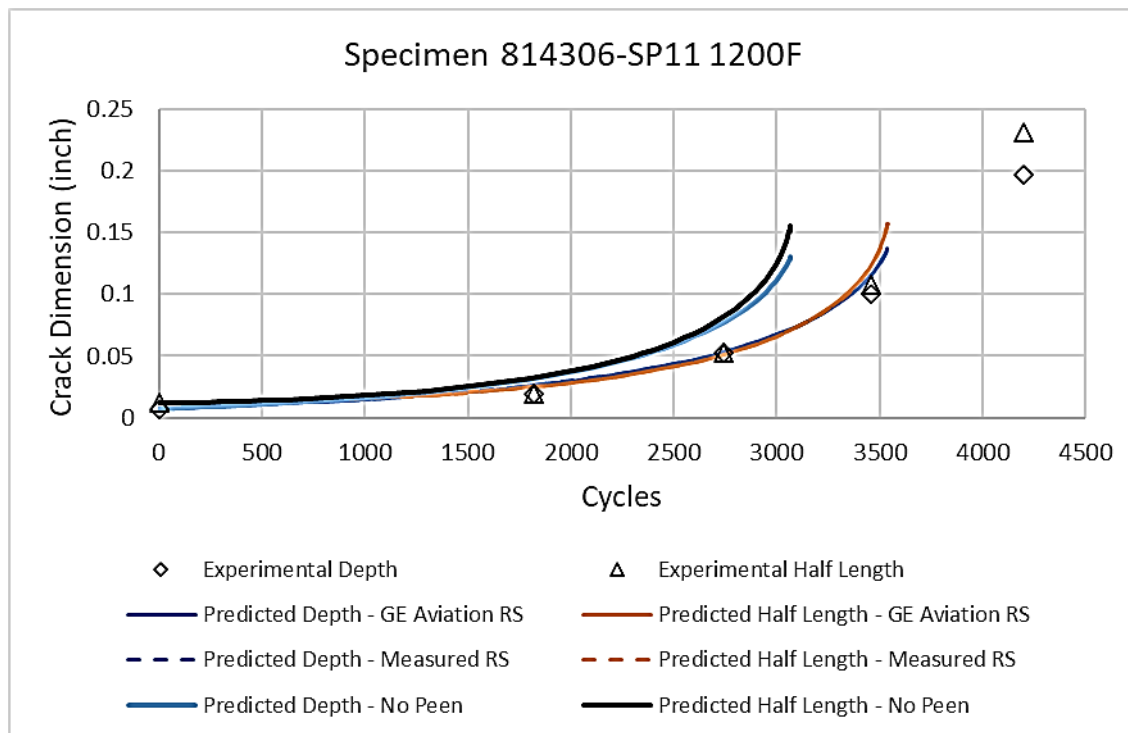


Figure D- 21. Analysis results for isothermal shot-peen specimen 814306-SP11 (1200°F)

The first TMF test, Specimen 814306-SP6, was not peened. The prediction method used for this specimen was that the stress intensity was calculated for the max stress point at 450°F but the crack growth rate was the integrated average rate between 450°F and 1200°F. See Figure D- 22 for the results. The prediction tracks the rate of growth well for the first three heat tints. However, the predicted failure occurs sooner and at smaller crack dimensions than observed in

the test. This could be attributed to the faster growth rate in Region III of the GE Aviation crack growth curves. Refer to Figure D- 21.

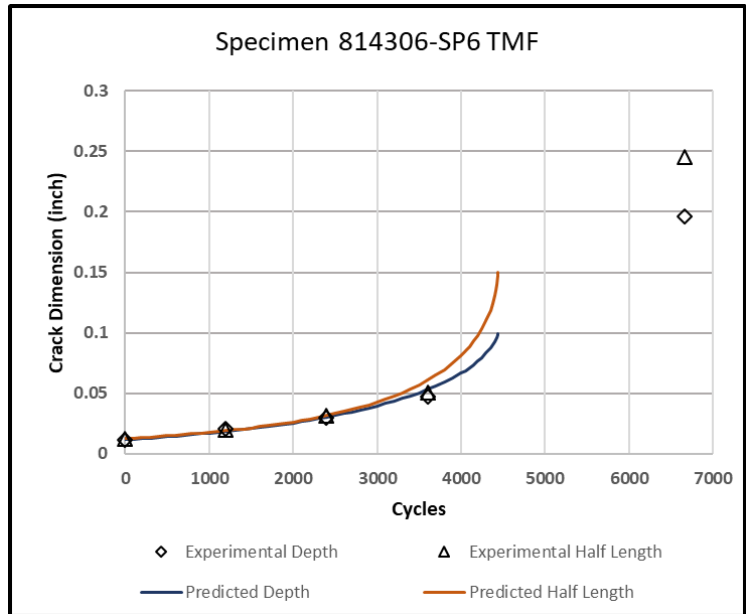


Figure D- 22. Analysis results for TMF unpeened specimen (specimen 814306-SP6)

Figure D- 23 shows the results using either the 450°F or 1200°F crack-growth rate properties to predict the life. These results bracket the actual life of the test specimen, but the TMF method yields a more accurate result.

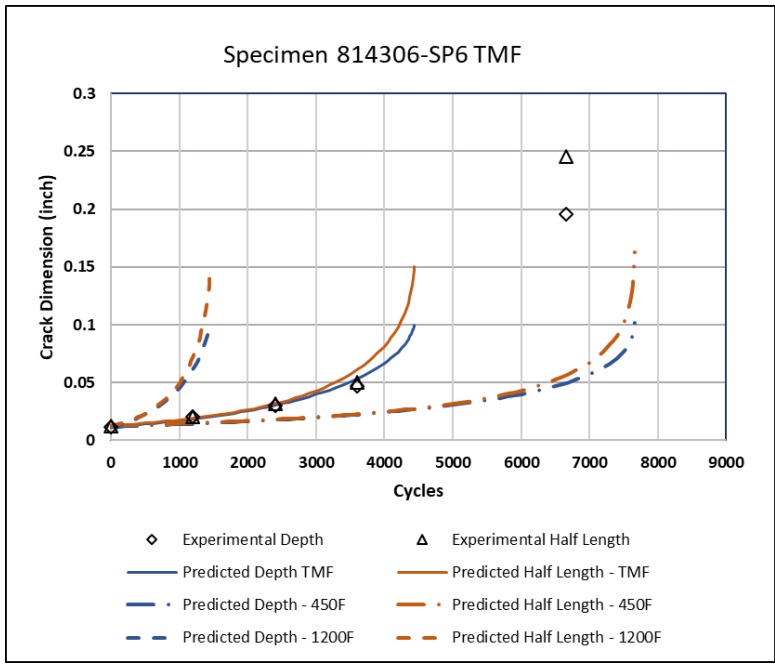


Figure D- 23. Analysis results for TMF un-peened specimen 814306-SP6 comparing the TMF method to isothermal methods

Specimen 814306-SP3 was also a TMF test and was peened to 7A intensity. The prediction method used was that the stress intensity (calculated for the max stress point at 450°F) and the crack growth rate was the integrated average rate between 450°F and 1200°F. The amount of relaxation used was based on the 450°F value in the production shotpeen model and is consistent with the GE recommendation (relaxed residual stresses correspond to the temperature at the maximum stress). This assumption may be challenged and is potentially a focus topic for a more extensive TMF validation effort.

Figure D- 24 displays the results. The prediction including the peening benefit tracks the rate of growth well.

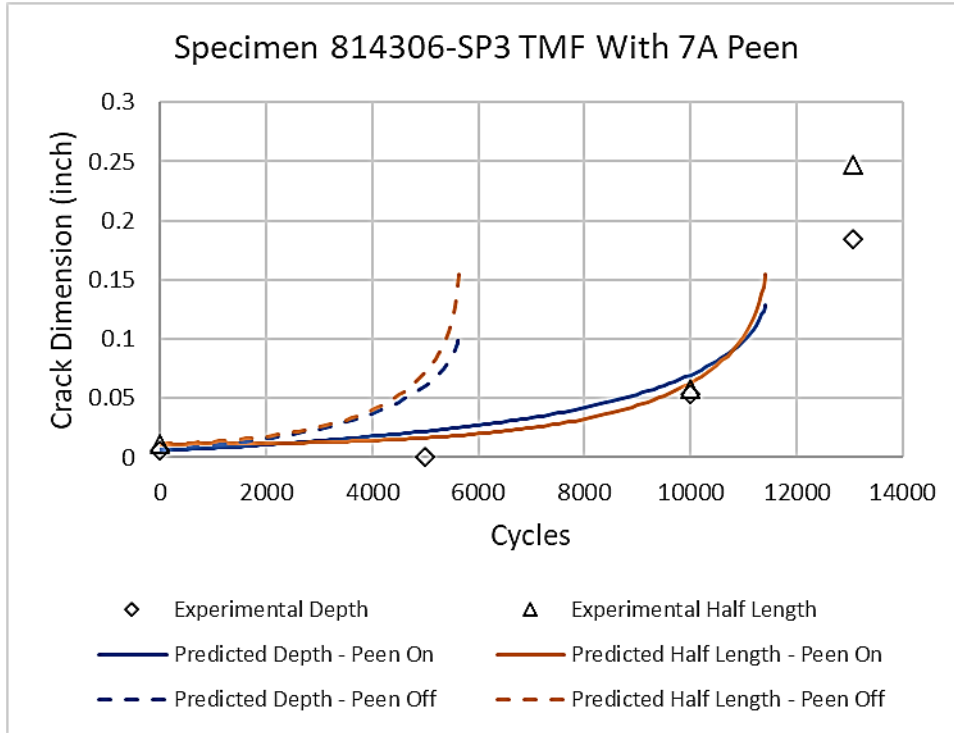


Figure D- 24. Analysis results for TMF peened specimen 814306-SP3 comparing the predictions with peening benefit turned on to the prediction with peening turned off

For this specimen, predictions were also performed using either the 450°F crack-growth rate curve and the 450°F shotpeen model or the 1200°F crack-growth rate curve and the corresponding shotpeen model. Those predictions are shown in Figure D- 25. The TMF method of average crack- growth rate between the temperature of the max stress and the max temperature of the mission correlates much better with the experimental results.

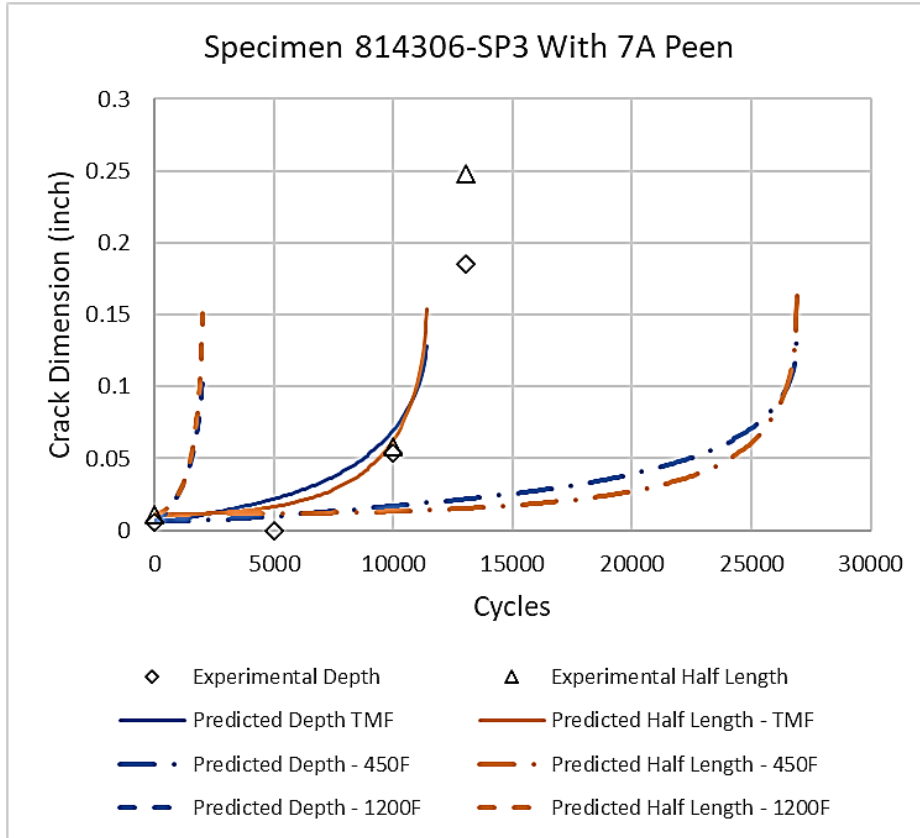


Figure D- 25. Analysis results for TMF peened specimen 814306-SP3 comparing the TMF method to isothermal methods

The analysis results for the cases with peening turned off and peening turn on are summarized in Table D- 5. The predictions for the TMF tests were made using the average TMF method. When peening was turned on, the relaxation factor was that associated with the temperature of the maximum stress in the cycle.

Table D- 5. Analysis results with and without peening considered

Specimen	Test description	Experimental life (cycles)	Peen off predicted life (cycles)	Peen off pred / exp	Peen on predicted life (cycles)	Peen on pred / exp
814306	Isothermal (450°F) peened	26780	11485	0.429	31236	1.17
814306-SP11	Isothermal (1200°F) peened	4200	3068	0.730	3539	0.84
814306-SP6	TMF test unpeened	6662	4440	0.666	—	—
814306-SP3	TMF test peened	13058	5637	0.432	11404	0.87

D.8 Conclusions

This limited exploratory study indicated that, for the single set of test conditions considered, the “average da/dN ” method predicted experimental results reasonably well and was more accurate than the maximum temperature or temperature at maximum stress approaches. Although the analysis was not run using a damage rainflow approach specifically, using the standard stress rainflow and the crack growth rate of the maximum temperature in the mission would yield similar results to the damage rainflow method. This is due to the simple cycle that was used for the TMF tests. The predictions using the TMF method usually compared more closely earlier in the test but deviated as final fracture approached. The GE team believes that the fracture toughness estimates used in the design curves are conservative and this was a significant contributor to the near-fracture deviation of the experiment versus predictions. There is potential for additional influence from the uncertainty around residual stress relaxation in an actual specimen versus what is modeled in the analysis. More work is necessary to understand these effects further. This testing effort also highlighted the need for good intermediate heat-tints during benchmark crack-growth testing in order to correlate with post-test analysis. While this adds an incremental cost to the testing efforts, the benefits may out-weigh the effort.

While this limited experimental work highlighted some key observations, additional testing is needed to explore some of these trends further and to quantify uncertainty. TMF effects in crack growth is a complex and interesting topic, and future work could consider several issues, including in-phase versus out-of-phase TMF cycles, realistic missions, and combinations of over peak retardation effects with TMF and RS effects. Exploring damage rainflow approaches would also be interesting.

D.9 References

- ASTM. (2005). *Standard practices for cycle counting in fatigue analysis, ASTM Book of Standards, ASTM E1049-85(2005)*. West Conshohocken, PA: ASTM International.
- McClung, R. C., Leverant, G. R., Enright, M. P., Huyse, L., Lee, Y.-D., Waldhart, C. J., . . . Srivatsa, S. K. (2008). *Turbine rotor material design—Phase II, DOT/FAA/AR-07/13, Grant No. 99-G-016*. Final Report, Federal Aviation Administration.
- Walker, K. (1970). The effect of stress ratio during crack propagation and fatigue for 2024-T3 and 7075-T6 aluminum. In *Effects of Environment and Complex Load History on Fatigue Life, ASTM STP 462* (pp. 1-14). Philadelphia, PA: ASTM.

E Wrought nickel anomaly low cycle fatigue testing

List of Figures

Figure E- 1. Four-point bend specimen	E-3
Figure E- 2. Anomaly specimen prior to peening demonstrating unequal width chamfers	E-4
Figure E- 3. Four-point bend equation to determine applied load	E-5
Figure E- 4. Calibrated specimen temperatures at three locations.....	E-6
Figure E- 5. Four point bend span	E-6
Figure E- 6. Four point bend test set up.....	E-7
Figure E- 7. S-N plot of IN-718 four point bend fatigue specimens (anomaly specimen in gold)	E-8
Figure E- 8. Illustration of failures opposite a loading pin	E-10
Figure E- 9. MTU IN-718 baseline #2 specimen.....	E-11
Figure E- 10. MTU IN-718 baseline #4 specimen.....	E-11
Figure E- 11. MTU IN-718 baseline #6 specimen.....	E-11
(b) EDX analysis identifying Nb carbide Figure E- 12. MTU IN-718 Baseline #2 Specimen .	E-12
Figure E- 13. MTU IN-718 Baseline #4 Specimen	E-13
Figure E- 14. MTU IN-718 Baseline #6 Specimen	E-14
Figure E- 15. Anomaly specimen failed from a cluster of Nb and Ti carbides	E-15
Figure E- 16. Anomaly Specimen.....	E-16
Figure E- 17. Sectioned anomaly location	E-17
Figure E- 18. SEM image of the sectioned area	E-17
Figure E- 19. No chemical difference between the area below anomaly and IN-718	E-18

List of Tables

Table E- 1. Four point bend test results	E-9
--	-----

E.1 Introduction

Historically, wrought nickel (Ni) alloy disk fractures from melt anomalies have had a very low incidence rate. This is especially true for triple-melt wrought Ni alloys, which is the predominant melt practice for recent rotating engine hardware designs. Furthermore, melt practices have improved over time, reducing the observed melt anomaly occurrence rate over the last two decades. The low incidence rate of wrought Ni melt anomalies is beneficial for the flying fleet, but poses a problem in developing a probabilistic damage tolerance methodology due to the lack of available data.

The Rotor Integrity Steering Committee (RISC) previously investigated the fatigue initiation and propagation of embedded wrought Ni melt anomalies. Under the Turbine Rotor Material Design, Phase II (TRMD-II) grant, eight double melt IN-718 billet sections (mults) were found to have nine ultrasonic indications (McClung, et al., 2008). These mults were forged into cylinders 16” in diameter and 2.9” thick, typically called pancake forgings, with the intent of creating specimens with anomalies in the gage section. After forging, only three anomalies were found. Specimens were machined around these anomalies and fatigue tested under the “Probabilistic Design for Rotor Integrity” (PDRI) grant. These fatigue tests demonstrated that significant initiation life is possible for wrought Ni anomalies (McClung, et al., Probabilistic Design for Rotor Integrity, DOT/FAA/TC-18/6, Grant No. 2005-G-005, SwRI Project 18.11481, 2018). This test program also highlighted the difficulty of obtaining specimens with embedded melt anomalies. At the conclusion of this activity, RISC decided to pause work on wrought Ni melt anomalies to give more attention to other high priority risks to rotating engine hardware.

In October 2016, a wrought Ni high-pressure turbine (HPT) disk fractured from a subsurface anomaly was not detected by inspections performed at manufacture. This accident emphasized the need to develop enhanced melting, inspection, and design methods. As a result of this accident, the Federal Aviation Administration (FAA) tasked RISC in November 2019 to develop a probabilistic assessment approach for Ni material anomalies in rotating engine hardware.

Based on the previous TRMD-II and PDRI experience, RISC recognized the difficulty of collecting fatigue initiation and crack propagation data from wrought Ni melt anomalies. RISC made a request to member original equipment manufacturers (OEM)s to attempt to intercept any wrought Ni anomalies found during manufacturing with the intent of turning the material into test bars. MTU Aero Engines (MTU) found such an anomaly during an etch process of forged material of an IN-718 part. This report describes the test program used to define a potential low cycle fatigue debit due to the presence of an anomaly, the results of those tests, and the conclusions drawn from the test program.

All data generated under this effort will be made publicly available. A summary of the data generated under the FAA grant is provided in this report. All testing discussed in this report was performed by Pratt & Whitney (P&W) in East Hartford, CT. P&W was chosen to perform this testing since they had an established relationship with MTU and were a subcontractor on the current PIRATE grant.

E.2 Objective

The objective of this task was to characterize the potential low-cycle fatigue-initiation life debit due to the presence of a naturally occurring wrought Ni anomaly. To determine the life debit, a specimen containing the anomaly as well as six baseline specimens without any known anomalies were machined out of the same part and then tested in fatigue. Testing of the six baseline specimens established a typical low cycle fatigue response for the tested material in comparison with the response of the anomaly specimen.

E.3 Test specimen

Because the anomaly was found on the surface of the part, it was not possible to create a conventional tensile fatigue specimen. A four-point bend specimen was the only test specimen that was compatible with the available material where the anomaly was found.. The test specimen geometry used for the four-point bend testing was developed by MTU. Specimen blanks were provided by MTU and then machined to the final dimensions shown in Figure E- 1. The as-received surface finish on the intended tension side of the sample was maintained throughout the finish machining process. The surface roughness of the as-received surface ranged from 70Ra to 90Ra. Two chamfers were machined along the length of the sample and then shot peened to 4A-7A. These measures were taken to ensure that the tension side of the sample would fail away from the edges.

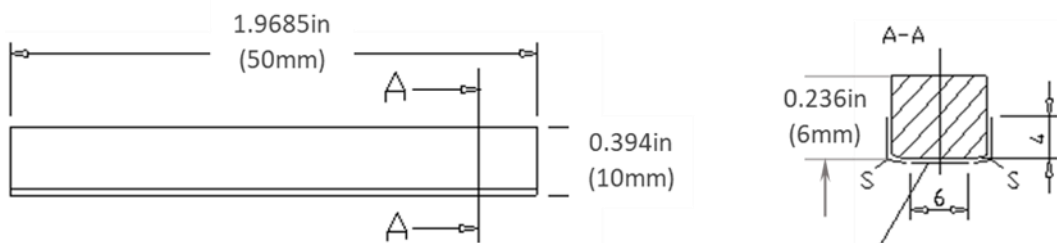


Figure E- 1. Four-point bend specimen

The anomaly sample was etched to identify the location of the anomaly prior to finish-machining the sample. The grain size of the specimen was measured to be ASTM 8.5 while the anomaly had a grain size of ASTM 5.0. Unfortunately, the specimen with the anomaly was mis-

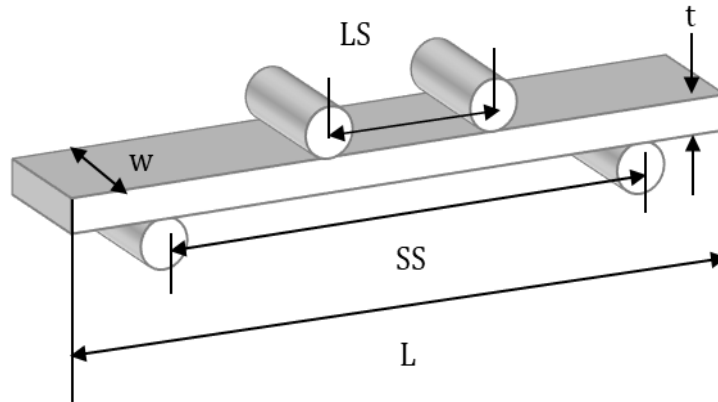
machined with a larger than specified chamfer on one side of the specimen. This specimen is the only specimen that had a mis-machined chamfer. This is shown in Figure E-2. As seen in the picture, the bottom chamfer was roughly twice the size of the top chamfer. It is not believed that the asymmetry of the chamfers affected the results of the test. The anomaly was preferentially located to one side of the specimen, which affected how the chamfers for this specimen were peened. While all the baseline specimens had the entire chamfer peened, the specimen with the anomaly was left unpeened for a small region near the tensile surface. Approximately 20 mils of the chamfer was left unpeened to avoid providing beneficial peening to the anomaly.



Figure E- 2. Anomaly specimen prior to peening demonstrating unequal width chamfers

E.4 Test method

Four-point bend fatigue tests were performed on 20 kilopound (kip) loading capacity servo hydraulic test frames. Tests were performed in load control, utilizing MTS Flex Test 40 controllers for closed loop control. The load to apply for a requested stress condition was determined by the equation in .



LS = Loading Span
 SS = Support Span
 L = Length
 t = Thickness
 w = Width
 ρ = Load
 σ = Stress

$$\rho = \frac{w * t^2 * \sigma}{3 * \left(\frac{SS}{2} - \frac{LS}{2} \right)}$$

Figure E- 3. Four-point bend equation to determine applied load

Resistive heating with the use of thermocouples placed along the length of the specimen were used to control and maintain a constant temperature along the specimen length within +/- 5°F throughout the test, as well as maintain test target temperature to within +/- 5°F, as shown in Figure E- 4. The temperatures recorded were part of the pre-test calibration procedure. Figure E- 4 shows that the steady-state temperatures met the requested test temperature as well as the temperature gradient across the specimen. The tests were conducted in lab air.

As shown in Figure E- 5, the upper span was 0.625 inches, and the lower span was 1.725 inches. The loading pin diameters were 0.25 inches. Due to the low minimum stress, a specimen constraint was implemented into the test setup to limit the movement of the specimen during the test (Figure E- 6). The specimen shifts during the test due to the specimen nearing zero load at the minimum stress. Control limits were set in both load and displacement to ensure the sample was not overloaded during the test as well as indicate a failure. At the test temperature, it is not expected that the loading pins are free to rotate due to differences in thermal expansion. It is

likely that the pins are seized in the fixture at the testing temperature. It does not appear that fixed loading pins were problematic for the test.

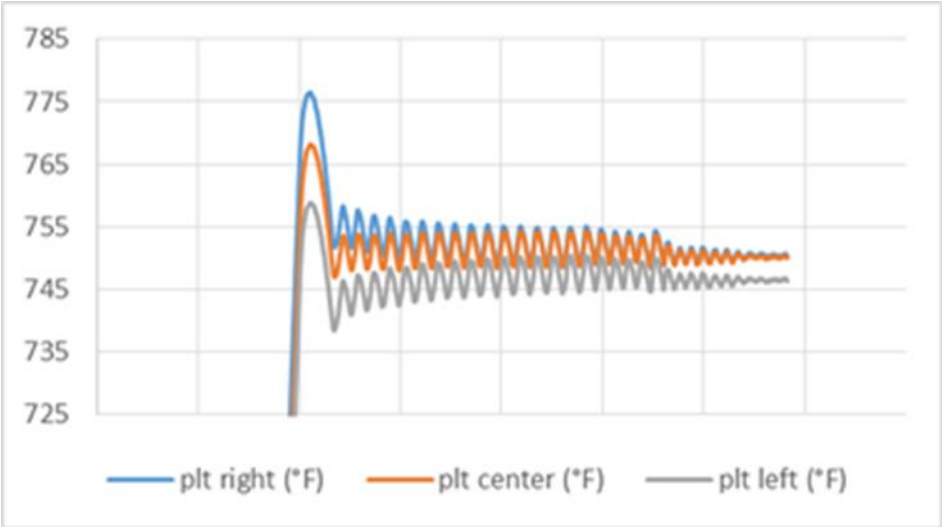


Figure E- 4. Calibrated specimen temperatures at three locations

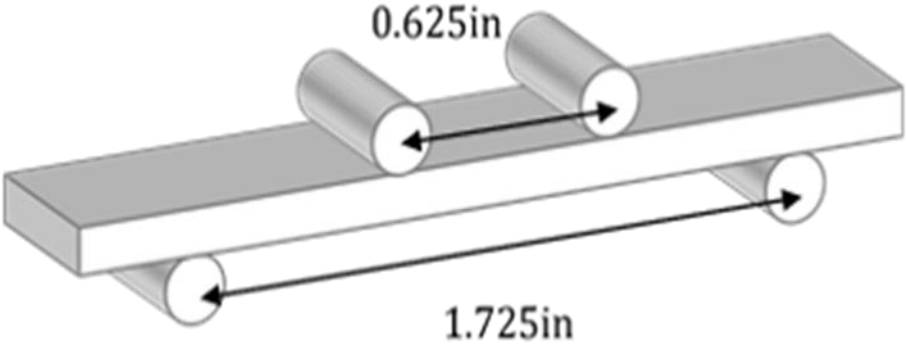


Figure E- 5. Four point bend span

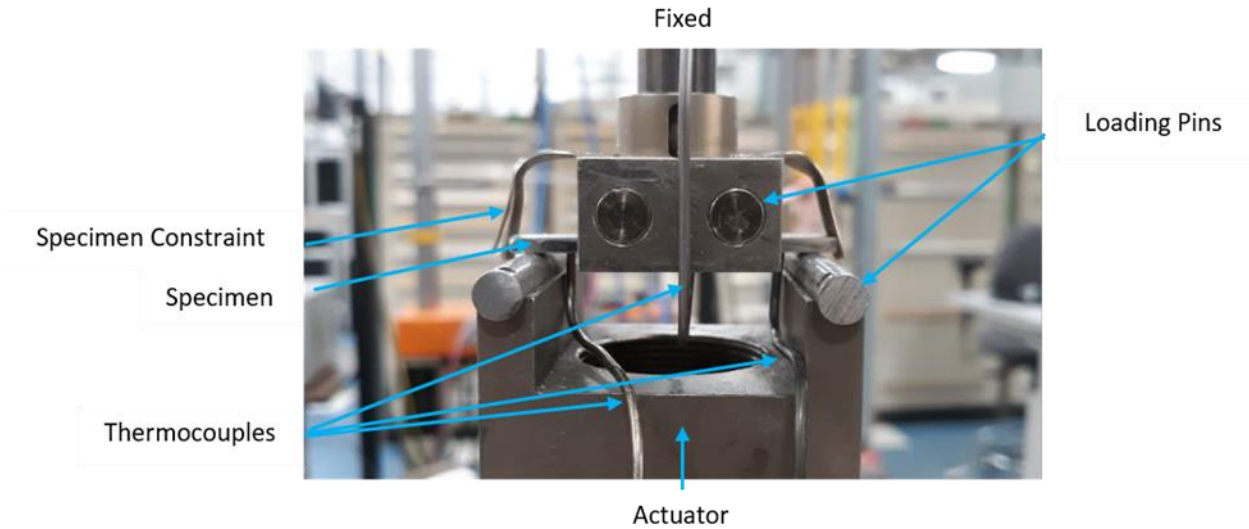


Figure E- 6. Four point bend test set up

E.5 Test conditions

Initially, MTU proposed testing at a constant temperature of 572°F with a maximum stress of 152 ksi and R = 0.01, since MTU had previous experience testing at those conditions. Both P&W and MTU had successful experience testing at frequencies between 1 Hz and 5 Hz for four-point bend testing. P&W and MTU decided to begin testing at 1 Hz.

RISC recommended specific parameters to minimize the number of conditions tested in a larger, coordinated, data generation effort and to facilitate the pooling of data across OEMs. . Due to this request, changing the temperature to either 400°F or 750°F was considered. A third temperature, 1000°F, was also an option. However, neither P&W nor MTU had four-point bend experience near this highest temperature, so it was not considered.

It is common practice for IN-718 low cycle fatigue specimens to have the surface peened to avoid surface and near-surface carbide-initiated cracks, especially at the temperatures considered for this test program. Because the tensile surface of the four-point bend specimen was not going to be peened due to the presence of the melt anomaly, there was a concern about failing from carbides at the lower temperatures, both 400°F and 572°F. It was decided to test at 750°F to try to avoid carbide-initiated failures.

E.6 Results

This test program consisted of seven four-point bend fatigue tests: six baseline specimens and one specimen with the melt anomaly. All specimens were extracted from the same part serial

number. Figure E- 7shows these test results on an S-N diagram. Table E- 1 summarizes the test conditions and lives for each of the specimens tested.

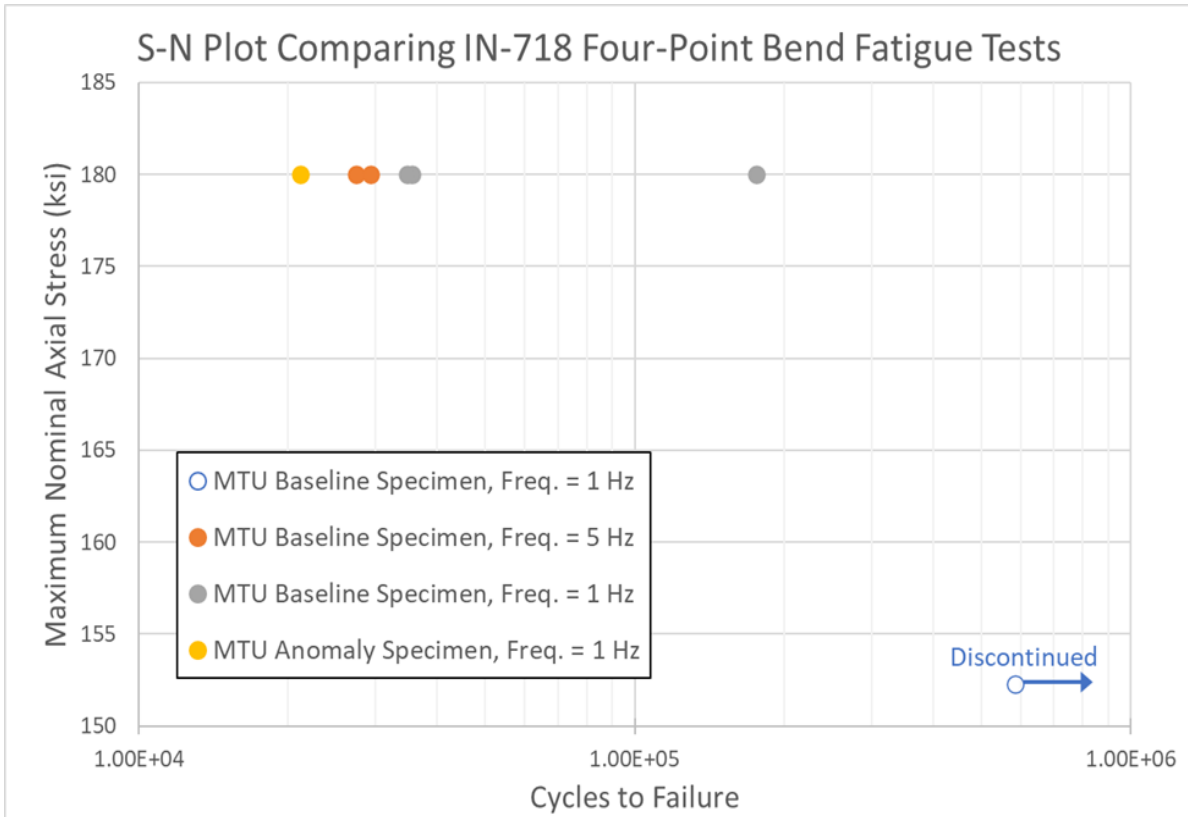


Figure E- 7. S-N plot of IN-718 four point bend fatigue specimens (anomaly specimen in gold)

Table E- 1. Four point bend test results

Specimen ID	Test Temp.(F)	Max Nominal Axial Stress (ksi)	R Ratio	Frequency	Status	Cycles to Failure
MTU INCO718 Baseline #1	750	152.3	0.01	1 Hz	Discontinued	5.85E+05
MTU INCO718 Baseline #2	750	180	0.01	5 Hz	Failed	2.93E+04
MTU INCO718 Baseline #3	750	180	0.01	5 Hz	Failed	2.74E+04
MTU INCO718 Baseline #4	750	180	0.01	1 Hz	Failed	1.76E+05
MTU INCO718 Baseline #5	750	180	0.01	1 Hz	Failed	3.56E+04
MTU INCO718 Baseline #6	750	180	0.01	1 Hz	Failed	3.48E+04
MTU INCO718 with Anomaly	750	180	0.01	1 Hz	Failed	2.12E+04

Six specimens were tested in load control at $R = 0.01$ and 750°F . The initial sample was tested at 152 ksi, which resulted in a nonfailure (runout) test that was halted at 585,000 cycles. This test condition was assessed in P&W’s low cycle-fatigue prediction tool, and it corroborated the long life of the first test. RISC requested that test conditions should target test lives no greater than 100,000 cycles. As a result, the maximum stress was increased to 180 ksi to reflect a more representative stress and to decrease the life. As the expected life was still high, it was also decided to increase the frequency of the testing to 5 Hz to expedite testing.

Specimens 2 and 3 were tested at the higher stress of 180 ksi and the higher frequency of 5 Hz. It was observed that these specimens failed on the tension side opposite to an upper loading pin span. To ensure that loading frequency was not playing a role in the failure location, the frequency was reduced back down to 1 Hz. All the remaining baseline specimens as well as the specimen with the anomaly were all tested at 1 Hz. No fretting was observed on either the 1 Hz or the 5 Hz specimens and no effect on life was observed by changing the frequency. Most of the test samples failed on the tension side of the specimen opposite to an upper loading span pin, as shown in Figure E- 8.

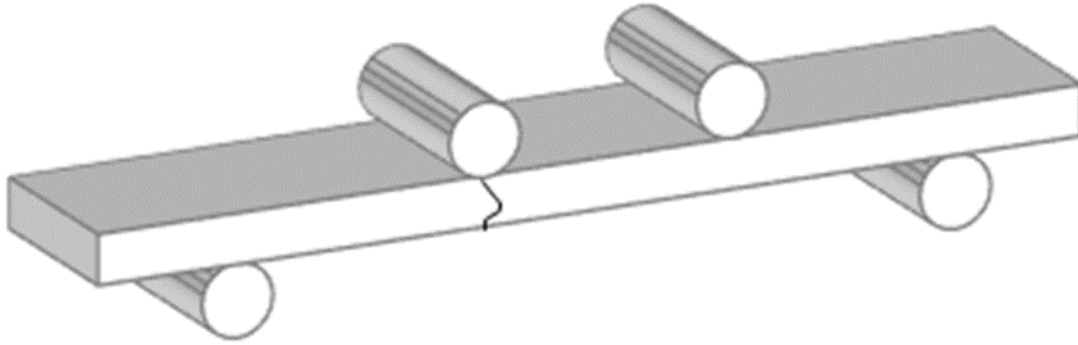


Figure E- 8. Illustration of failures opposite a loading pin

To understand these failures, scanning electron microscope (SEM) and energy dispersive X-ray spectroscopy (EDX) analyses were made on representative specimens to determine if failures were driven by the test setup or were metallurgically driven.

The representative samples were specimens #2, #4 and #6. See Figure E- 9, Figure E- 10, and Figure E- 11. Specimen #2 and # 4 failed preferentially opposite to a loading pin. Specimen #4 failed almost a decade longer in cycle count than Specimen #2. Specimen #6 failed in the center of the specimen. When assessed under SEM and EDX, the primary crack-initiation failure mechanism in all three specimens was identified as surface carbides. See Figure E- 12 thru E-14.



Figure E- 9. MTU IN-718 baseline #2 specimen



Figure E- 10. MTU IN-718 baseline #4 specimen

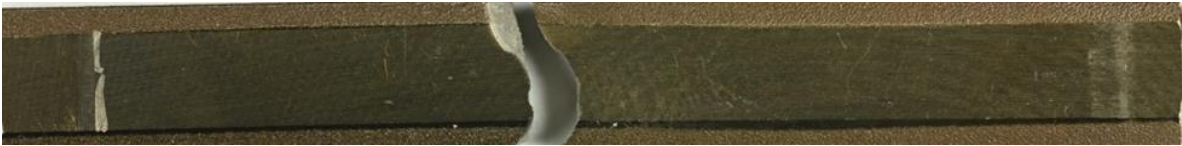
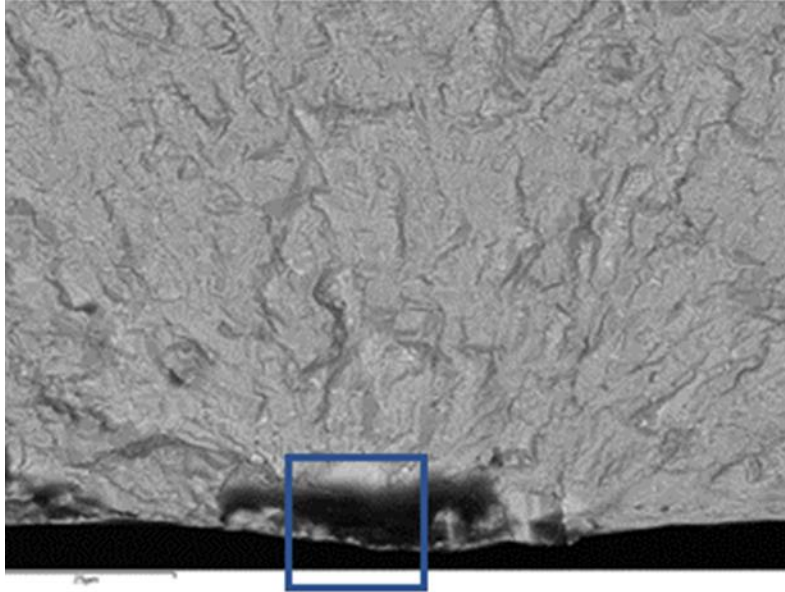
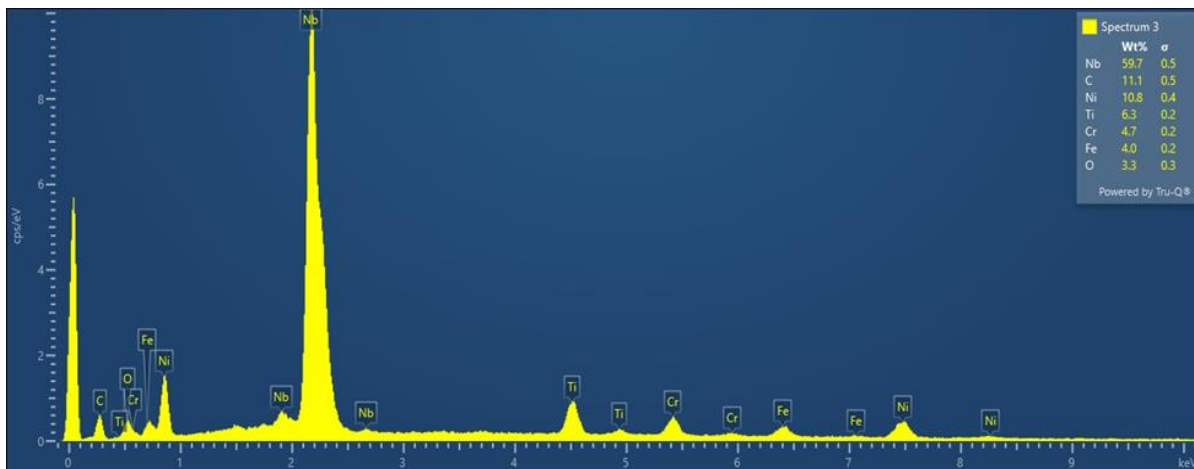


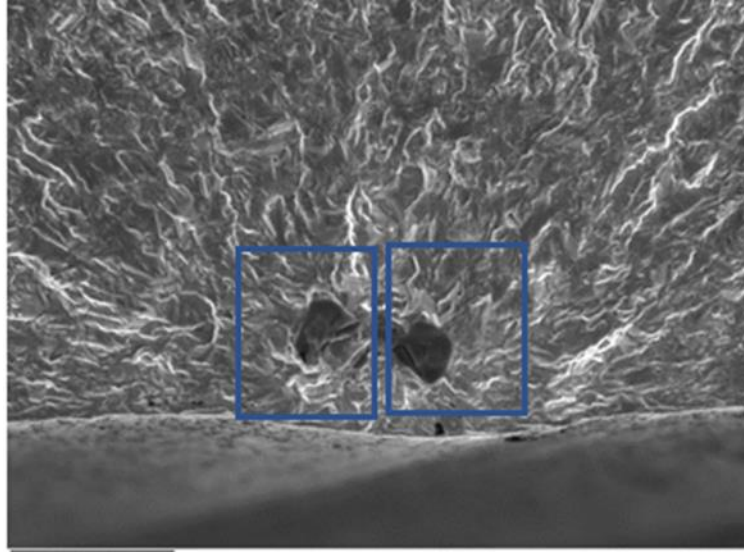
Figure E- 11. MTU IN-718 baseline #6 specimen



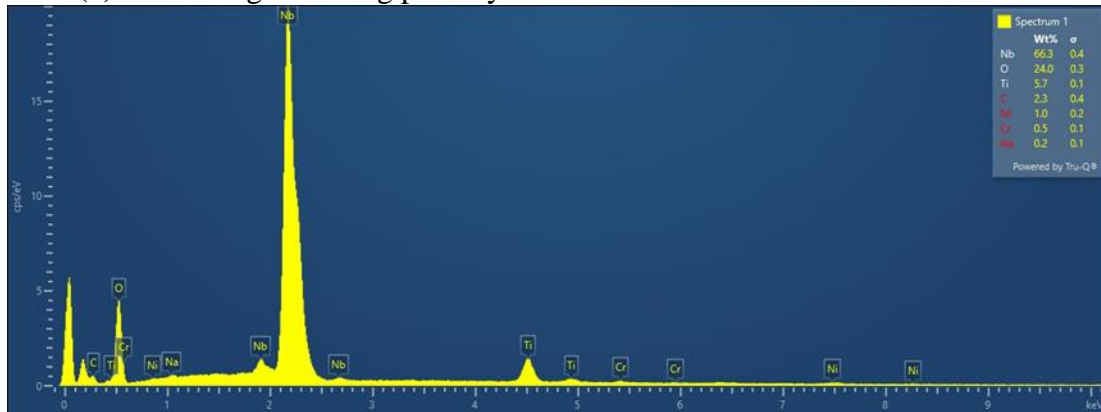
(a) SEM image showing primary crack initiation from surface carbides



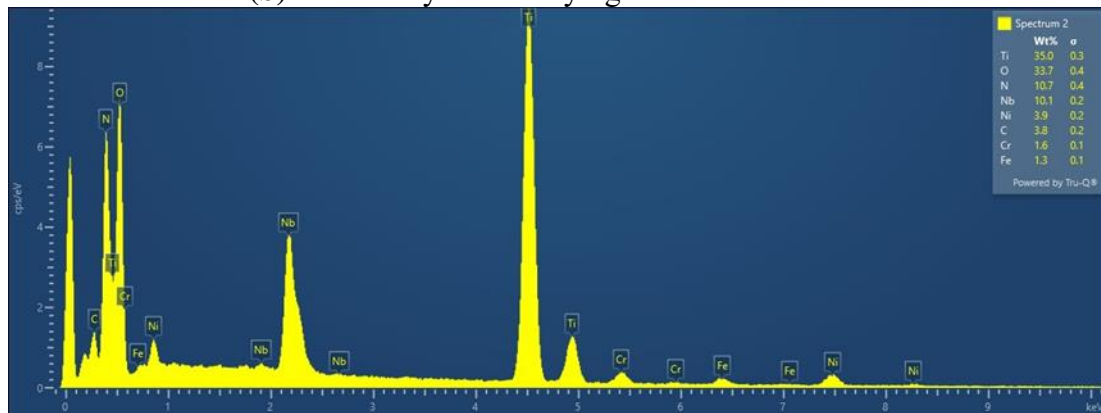
(b) EDX analysis identifying Nb carbide Figure E- 12. MTU IN-718 Baseline #2 Specimen



(a) SEM image showing primary crack initiation from surface carbides

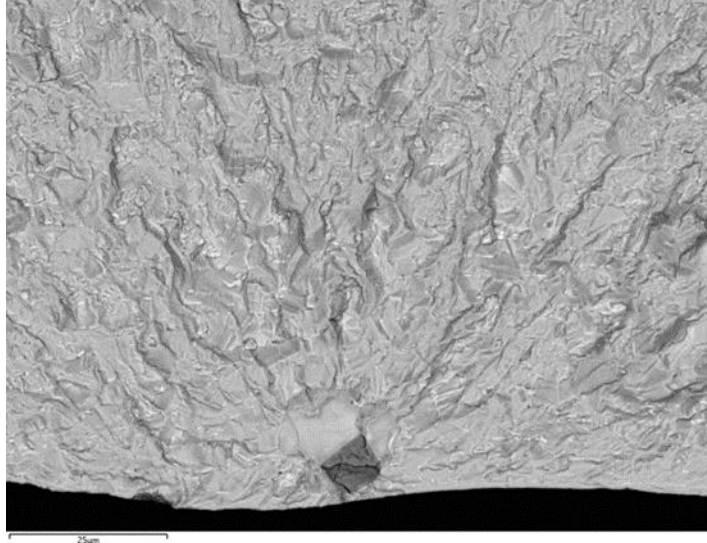


(b) EDX analysis identifying Nb carbide

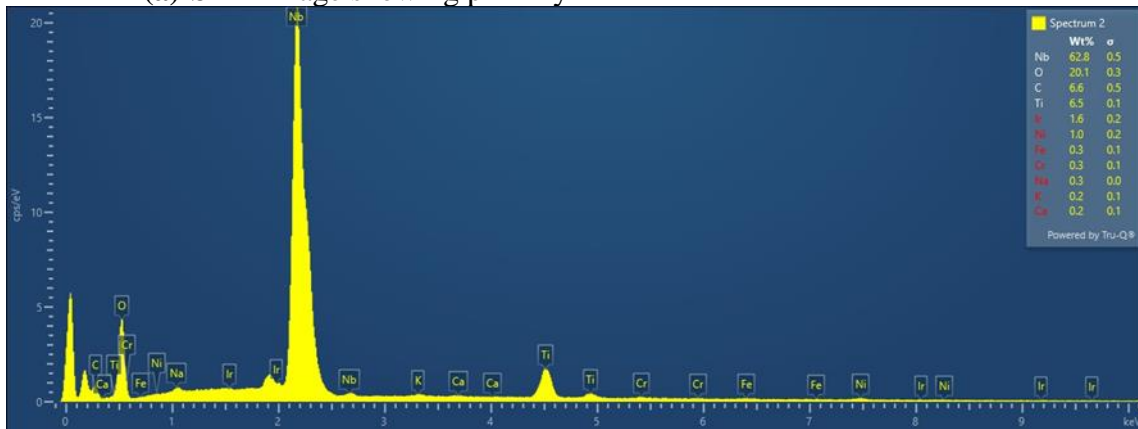


(c) EDX analysis identifying Ti carbide

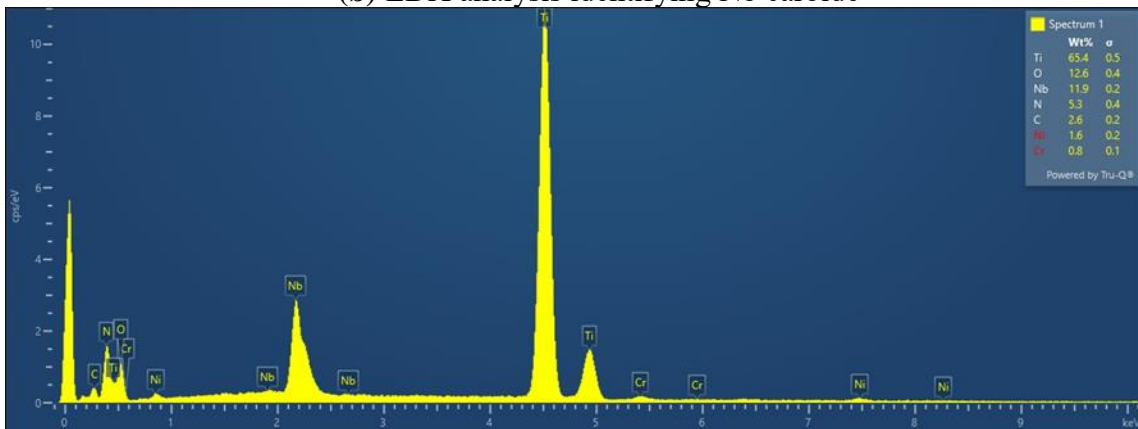
Figure E- 13. MTU IN-718 Baseline #4 Specimen



(a) SEM image showing primary crack initiation from surface carbides



(b) EDX analysis identifying Nb carbide



(c) EDX analysis identifying Ti carbide

Figure E- 14. MTU IN-718 Baseline #6 Specimen

The test anomaly specimen did not fail from the melt anomaly. The top picture in Figure E-15 shows the specimen with the anomaly with the tensile side of the bar visible. The blue box in the picture highlights the melt anomaly location. The failure location of this specimen coincided with the opposite side of the loading pin, consistent with most of the other baseline specimen failures.

The lower right picture in Figure E-15 is a closer look at the melt anomaly, which is classified as a dirty white spot. The lower left picture in Figure E-15 is a magnified image of the fracture surface where carbides are seen. Figure E-16(a) shows these carbides in more detail. Figure E-16(b) and (c) show the EDX analysis identifying a Ti carbide as well as Nb carbide at the initiation site.

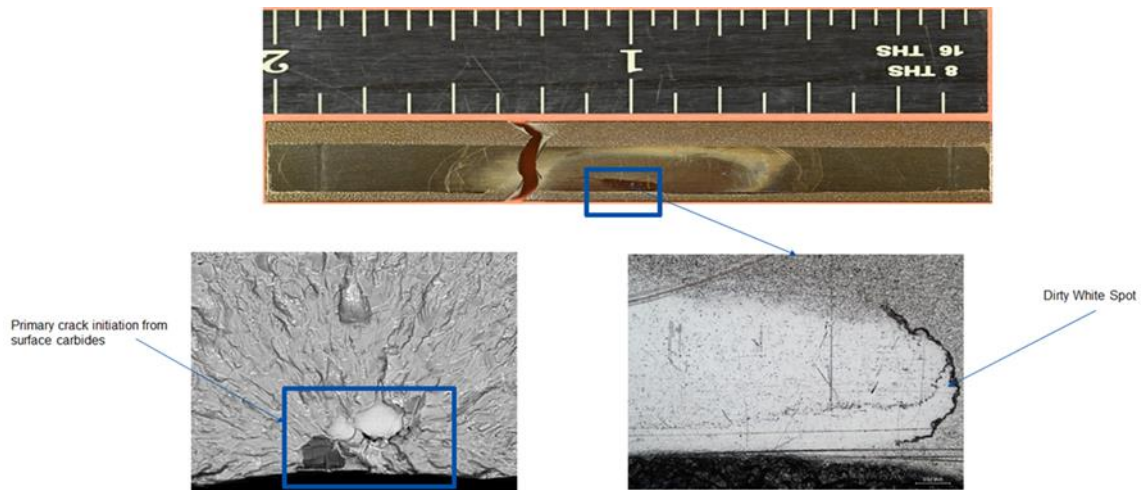
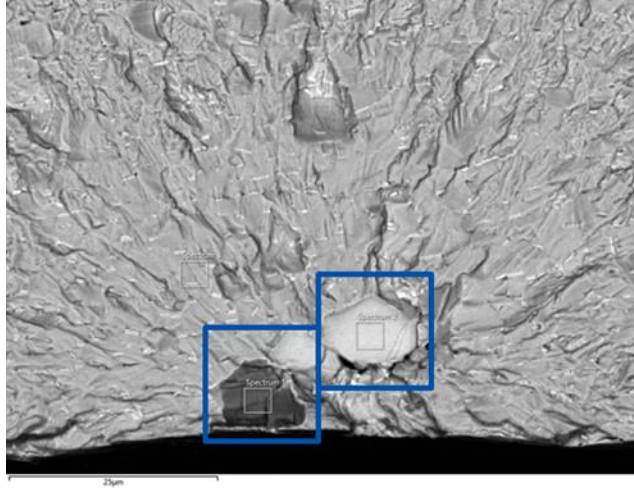
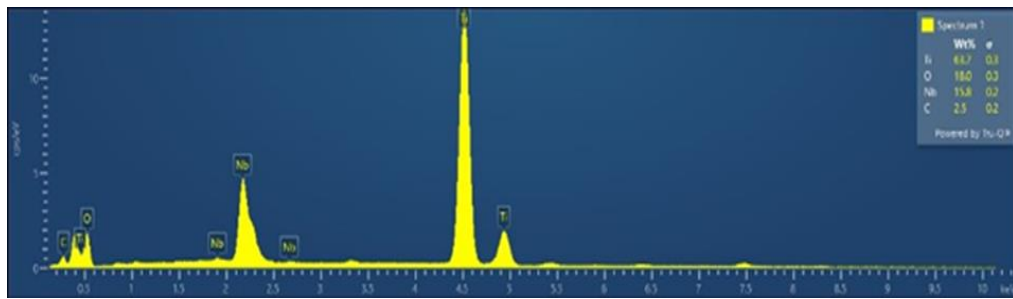


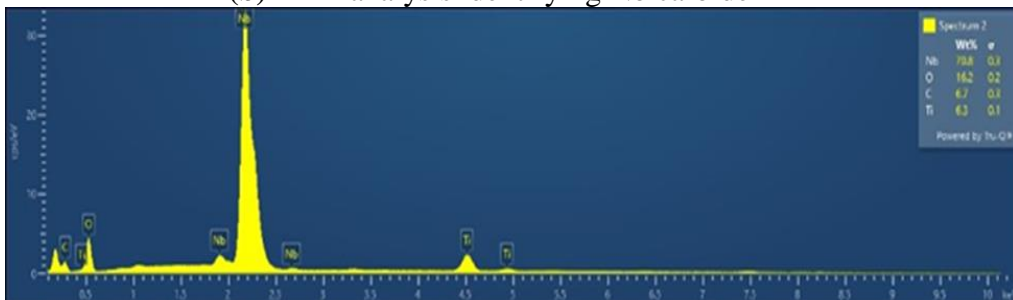
Figure E- 15. Anomaly specimen failed from a cluster of Nb and Ti carbides



(a) SEM image showing primary crack initiation from surface carbides



(b) EDX analysis identifying Nb carbide



(c) EDX analysis identifying Ti carbide

Figure E- 16. Anomaly Specimen

E.7 Detailed anomaly assessment

The anomaly was further interrogated to determine if it was more than a surface feature. The anomaly was sectioned through the center as illustrated in Figure E- 17. The initial micrographs of the anomaly appear to have some depth. When analyzed under the SEM, there is a dark band of coarse grains as shown in Figure E- 18. EDX analysis in Figure E- 19(a) through Figure E- 19(d) showed no difference in chemistry between the sectioned area below anomaly and typical IN-718. The anomaly appears to be a dirty white spot discrete coarse grain region associated with non-metallic inclusions. Images were taken using a Nikon Eclipse MA200 and Amray 1910 FESEM was used to more in-depth metallography. The anomaly was additionally etched with AG-21 (IN-718).

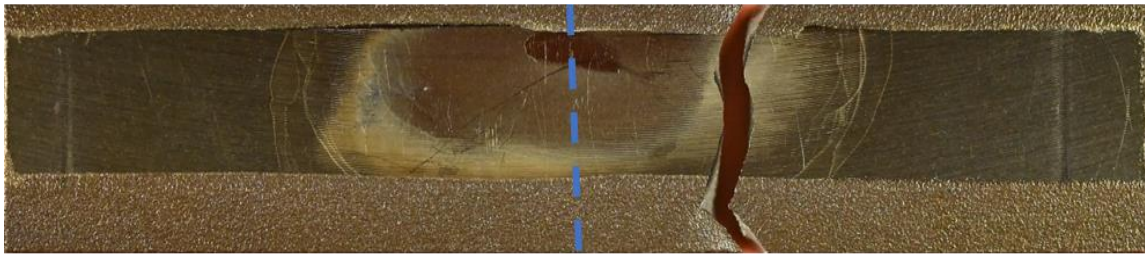


Figure E- 17. Sectioned anomaly location

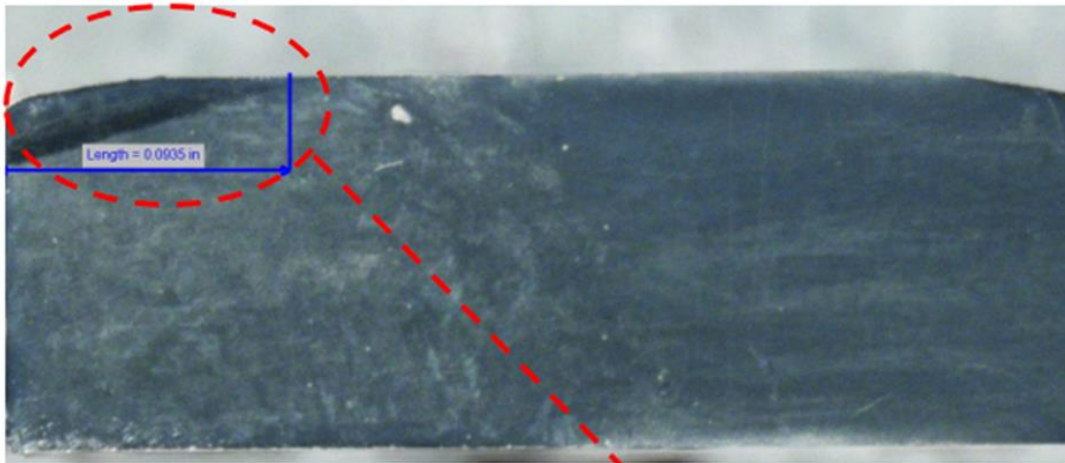
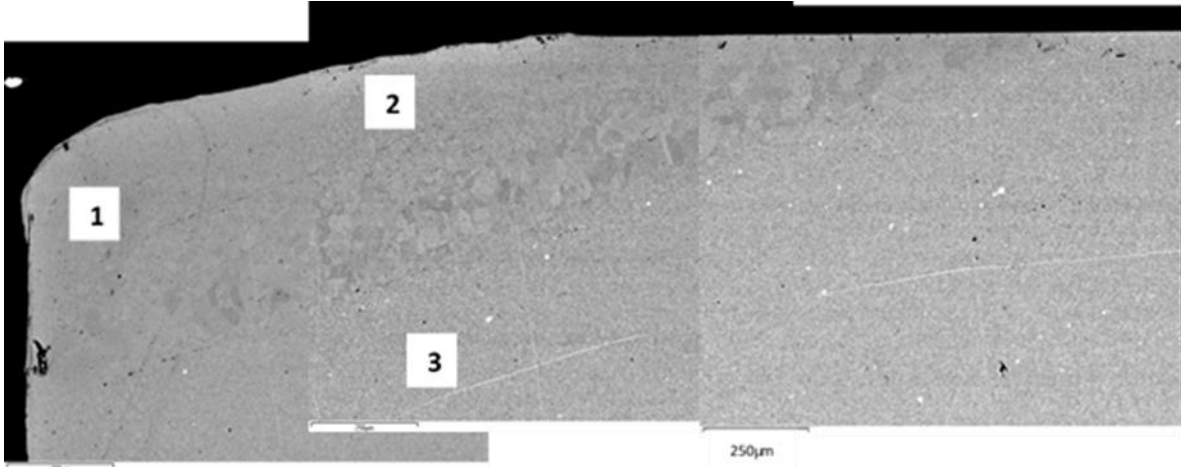
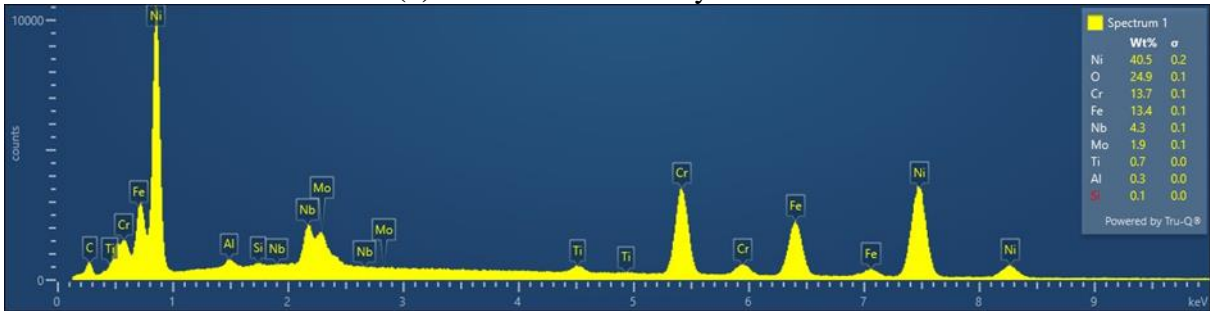


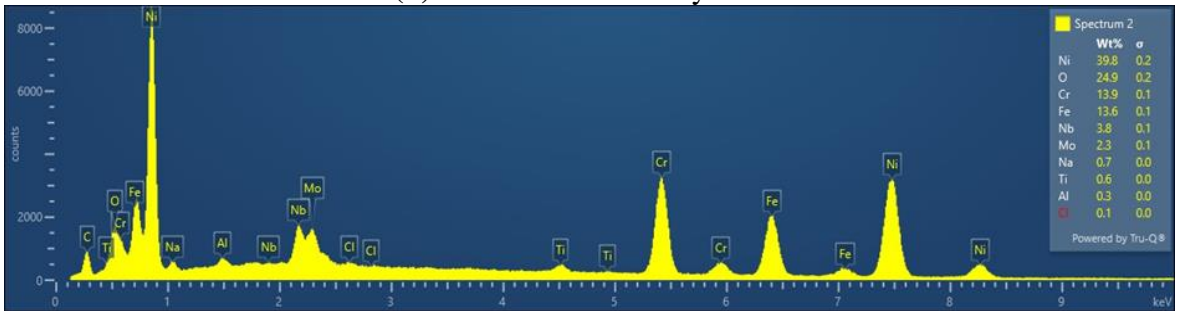
Figure E- 18. SEM image of the sectioned area



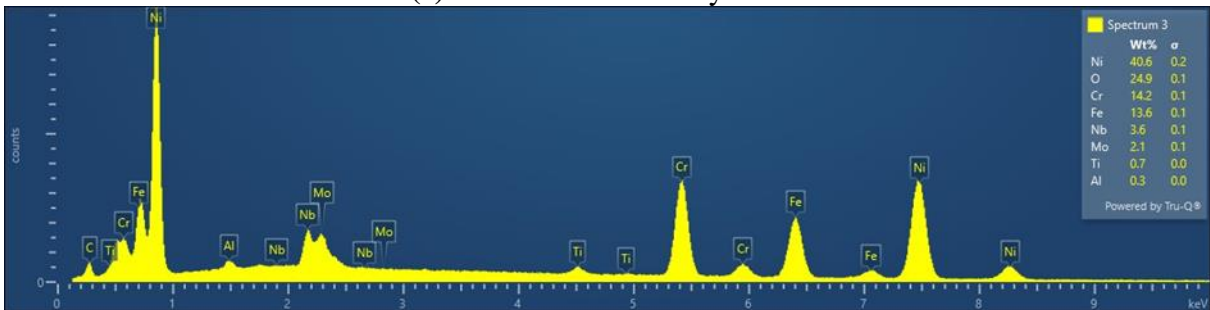
(a) EDX chemical analysis locations



(b) EDX chemical analysis Area 1



(c) EDX chemical analysis Area 2



(d) EDX chemical analysis Area 3

Figure E- 19. No chemical difference between the area below anomaly and IN-718

E.8 Discussion of results

Since the failure crack in the specimen with the anomaly initiated from a carbide, it is not possible to determine a low cycle fatigue debit from the presence of the anomaly. All that can be observed was that the anomaly was not as limiting as the carbide. While all test specimens evaluated with fractography failed from a carbide, failures from carbides at these temperatures in unpeened material are not uncommon and not the goal of this test program.

While there was prior concern about failure from a carbide at these temperatures, it was originally thought that 750°F would be a high enough temperature to suppress carbide-initiated cracks and to observe a debit due to a melt anomaly. Testing at the highest temperature that RISC requested, 1000°F, would more likely have avoided these carbide failures, but P&W does not have four-point bend IN-718 test experience at those temperatures.

Standard procedure for low cycle fatigue specimens is to peen the entire surface to suppress carbide-initiated cracks. The tensile surface was not peened for this test program as it was thought that peening the tensile surface where the anomaly was located would also suppress any debit associated with the anomaly. If the tensile surface was peened and no low cycle fatigue debit was observed, it would not be clear if the lack of a debit was due to the anomaly being benign or if the peening suppressed the debit due to the anomaly.

The results from this test program call into question the ability to test surface connected wrought Ni anomalies at temperatures where carbides are active. It will be difficult to get reliable results for surface connected anomalies without peening to suppress the impact of carbides that are naturally occurring in IN-718. Based on this limited testing, it appears that carbides may still be the limiting failure for unpeened material.

Ideally, subsurface anomalies would be tested so that the specimen surfaces could be peened to suppress carbide initiations. This has several benefits. It allows for testing at all requested temperatures. It also tests anomalies in a condition more like the type of anomaly that caused the accident in 2016. Unfortunately, it will be difficult to test these subsurface anomalies since they are very difficult to find with current inspection methods.

E.9 References

McClung, R. C., Enright, M. P., Lee, Y.-D., Liang, W., Moody, J., Fitch, S. K., Peralta, A. D. (2018). *Probabilistic design for rotor integrity, DOT/FAA/TC-18/6, Grant No. 2005-G-005, SwRI Project 18.11481*. Final Report, Federal Aviation Administration.

McClung, R. C., Leverant, G. R., Enright, M. P., Huyse, L., Lee, Y.-D., Waldhart, C. J., Srivatsa, S. K. (2008). *Turbine rotor material design—Phase II, DOT/FAA/AR-07/13, Grant No. 99-G-016*. Final Report, Federal Aviation Administration.

F DARWIN® model quality checks

F.1 Motivation and overview

Over the years, DARWIN development team members have noticed that fatal errors during a DARWIN assessment can often be traced back to errors in the finite element (FE) model. That is, the error is not ultimately a DARWIN issue. These errors tend to be time-consuming for the DARWIN team and frustrating for DARWIN users. The major lesson learned from verification exercises performed with original equipment manufacturer (OEM) models is the need to screen models by performing model quality checks (MQCs) prior to loading the models into DARWIN. MQCs are designed to catch most issues responsible for DARWIN run-time errors.

To prevent these run-time errors, the DARWIN development team introduced MQCs for the FE model into the DARWIN FE model translator FE2NEU. FE2NEU can evaluate model quality either at the time the model is converted to the HSIESTA file format or after conversion. Once the checks are performed, FE2NEU inserts a digital signature into the *.fea file indicating the status of the checks. If a model fails one or more of the MQCs, FE2NEU reports the checks that failed to the FE2NEU output console and stores the results in the *.fea file. Beginning in DARWIN 9.4, all FE models imported into DARWIN require a digital signature indicating that the MQCs were performed.

F.2 Summary

As a result of this development activity, FE2NEU now performs the following MQCs:

- All nodes must be connected to an element. Orphan nodes are prohibited.
- All nodes must have stresses and temperatures assigned to them for all loadcases.
- All nodes must have unique locations. Coincident nodes are not supported.
- All elements must conform to the list of elements supported by the HSIESTA file format.
- All elements must have a positive volume. Negative volumes are prohibited.
- All element faces must have a positive area. Collapsed faces are prohibited.
- All element edges must have a positive length. Collapsed edges are prohibited.
- Models may only contain one component.
- Models must have a conforming mesh. Tied edges/faces are prohibited.

- Duration times for loadcases must be consistent, *i.e.*, all defined, or none defined.

MQCs represent known issues that lead to non-recoverable errors in DARWIN. For example, elements with a negative volume are elements for which DARWIN cannot process stresses. MQCs cannot be easily resolved by FE2NEU without potentially corrupting the model. Users are responsible for resolving MQCs. Enforcing MQCs may reduce, but not eliminate, the number of errors users encounter during a DARWIN analysis. SwRI will modify the list of additional MQCs as necessary to improve the robustness of the code.

The list of MQCs represents experience gained by the DARWIN design team over several years. This list reflects errors that occurred in some OEM models investigated under the current PIRATE-II grant. MQCs do not reflect bugs or limitations of the Autoplate code. MQCs reflect known issues with input FE models that prevent Autoplate from determining an appropriate plate. They are unrecoverable by Autoplate and can only be resolved by correcting errors in the FE model. At present, those issues are handled by the node skipping capability.

FE2NEU also determines model quality metrics (MQMs). MQMs indicate deviations from ideal elements or potential unit conversion errors. They may lead to Autoplate errors. However, firm suggestions about limits for MQMs are currently not available. FE2NEU can report the following information from the MQMs:

- Maximum and minimum internal edge angles;
- Maximum and minimum element aspect ratios;
- Maximum and minimum element edge lengths;
- Maximum and minimum element Jacobians;
- Maximum and minimum stress values;
- Maximum and minimum temperature values.

For the maximum and minimum values, FE2ENU reports the top and bottom ten values.

Further research may require certain upgraded MQMs to MQCs based on threshold values; (e.g., if internal edge angles above a certain limit cause Autoplate to fail). This can be decided by comparing MQMs with error messages produced by Autoplate.

F.3 Modifications to FE2NEU

This capability was first implemented into FE2NEU version 7.0 in DARWIN 9.4. The enhanced version of FE2NEU enables users to convert ANSYS or Abaqus result files into the HSIESTA file format. In addition to this previous capability, FE2NEU 7.0 is supplemented by new routines to evaluate MQCs and MQMs. These new routines read the HSIESTA file built by FE2NEU and check it automatically. FE2NEU digitally signs the file after completing the checks. FE2NEU also reads existing HSIESTA files that were possibly created by an earlier version of FE2NEU or by third-party routines.

Modifications to the DARWIN graphical user interface (GUI) check the digital signature of the HSIESTA file. This is like recent work to protect anomaly exceedance curves and material input files. HSIESTA files without a digital signature or with the wrong digital signature trigger an error message in DARWIN 9.4. The DARWIN GUI prohibits users from loading this file into the GUI. This approach protects users who employ the GUI to build DARWIN input decks.

The DARWIN GUI includes the FE MQC Results Viewer. This tool enables users to view a summary of MQCs in the FE model. This tool is always available.

DARWIN Risk Assessment Code (RAC) modifications check the digital signature of the HSIESTA file. HSIESTA files without a digital signature or with the wrong digital signature trigger an error message in DARWIN 9.4. The DARWIN RAC prohibits the analysis from continuing. This approach protects users who build DARWIN input decks without the GUI, i.e., using the DARWIN Python model.

F.4 Usage of FEA MQC Results Viewer

The FEA MQC Results Viewer tool is always available in the GUI. To view MQC results of an FEA file in the FEA MQC Results Viewer tool, the FEA file must be converted in FE2NEU 7.0 FEM Converter or a later version. The FE2NEU 7.0 (and later versions) FEM Converter performs MQCs during the FEM conversion. The converter writes out MQC results in the FEA file.

The FEA MQC Results Viewer tool is accessed from the **Tools > FEA MQC Results Viewer** menu. In the FEA MQC Results Viewer tool, use the **Browse** button to locate the FEA file of interest. Once the user selects the FEA file, the tool shows MQC results of the FEA file, as shown in Figure F-1.

FEA MQC Results Viewer

square-4elem.us.fea

Description	Entity	Result	# Failures
Nodes not connected to elements	NODE	FAILED	1
Multiple components	COMPONENT	PASSED	0
Inconsistent loadstep times	LOADSTEP	PASSED	0
Missing temperatures at any loads...	NODE	PASSED	0
Unsupported element types	ELEMENT	PASSED	0
Non-unique locations	(x,y,z)	FAILED	1
Missing stresses at any loadsteps	NODE	PASSED	0
Elements with negative area	ELEMENT	PASSED	0

Figure F-1. FEA MQC Results Viewer showing MQC results of an example FEA file

The tool has the following columns:

- **Description** – Provides a short description of the model quality check.
- **Entity** – Specifies the entity (node, element, or loadstep *etc.*) associated with the model quality check.
- **Result** – Specifies if the entity passed or failed the model quality check in the entire FE model.
- **# Failures** – Specifies the number of failure instances in the model quality check of the entire FE model.

G DARWIN® Python module usage cases

G.1 Introduction

The DARWIN Python Module (DPM) is a Python module that enables users to build DARWIN input files and to process DARWIN output files. Here, users write Python 2.7 code that sets projects, missions, properties, cracks, and autozoning routines for a DARWIN input file. After executing the input decks, users can then employ similar routines to extract data from the output file and output to some other data file format. These routines support the automation activities performed by the original equipment manufacturer (OEM) to explore the sensitivity of DARWIN to their inputs. That is, users can build multiple input files and use Python to analyze them without interacting with the graphical user interface (GUI). This capability is extremely helpful for multiple analyses that involve only small changes that would be tedious to accomplish manually.

The DPM was originally developed by SwRI to support verification testing of large numbers of analyses. After learning about it, the engine company partners asked that this capability be extended to support their activities. Consequently, the DPM was formalized and distributed with DARWIN. It is now available with recent releases of DARWIN in the program files folder. This folder contains example Python files that highlight the DPM. At this writing, the DPM is limited to only a few project modes:

- User-defined crack life assessments for 2D anomalies in 2D FE models
- User-defined crack life assessments for 2D anomalies in 3D FE models
- General inherent risk assessment for 2D anomalies in 2D FE models
- General inherent risk assessment for 2D anomalies in 3D FE models

More project modes are anticipated in the future, based on user interest.

G.2 Usage

Overview

The DARWIN Python Module (DPM) is a Python package for managing DARWIN software projects. It does so by providing methods for editing and accessing DARWIN project files (*.dhf). With these methods, DARWIN users can modify existing, create new, and execute projects, as well as query project definitions and results.

Incorporating DPM into a user's Python script requires the application of four basic steps.

Step 1: Import the DARWIN Python Module into a Python script

```
import darwin93
```

Step 2: Initialize a DARWIN project object

```
projectObj = darwin93.Project()
```

Step 3: Import an existing DARWIN project file or create a new DARWIN project file

Import an existing DARWIN project file:

```
projectObj.open_project(path_to_dhf_file)
```

Create a new DARWIN project file

```
projectObj.create_project(path_for_new_dhf_file,project_code)
```

Step 4: Interact with the DARWIN project as desired using the provided methods

Requirements

The DPM requires the following programs:

- Python (Python 2.7 recommended): A high-level programming language.
- PyTables: A Python package for managing HDF5-formatted files such as DARWIN project files (*.dhf). For more information visit the PyTables website (<http://www.pytables.org>).

Capabilities

The DPM supports the project types highlighted in green in Table G- 1. Note that only a few project codes are currently available.

Table G-1. Overview of Project Codes

Code	Objective	Geometry Mode	Anomaly Characterization	Zoning Mode	Supported?
1012	User-Defined Crack Life Assessment	1D Stress Profiles	2D	N/A	No
1022		2D FE Model	2D	N/A	Yes
1023		2D FE Model	3D	N/A	No
1032		3D FE Model	2D	N/A	Yes
1222	Crack Growth Contour Life Assessment	2D FE Model	2D	N/A	No
1232		3D FE Model	2D	N/A	No
20121	General Surface Damage Risk Assessment	1D Stress Profiles	2D	Manual	No
20221		2D FE Model	2D	Manual	No
20321		3D FE Model	2D	Manual	No
22121	Circular Hole Feature Surface Damage Risk Assessment	1D Stress Profiles	2D	Manual	No
22321		3D FE Model	2D	Manual	No
24220	General Inherent Risk Assessment	2D FE Model	2D	Auto	Yes
24221		2D FE Model	2D	Manual	No
24231		2D FE Model	3D	Manual	No
24320		3D FE Model	2D	Auto	Yes
24321		3D FE Model	2D	Manual	No
26220	Titanium Hard Alpha Risk Assessment	2D FE Model	2D	Auto	No
26221		2D FE Model	2D	Manual	No

The DPM enables users to define the core information including the project title and description. It also enables users to configure the analysis by setting the unit system, anomaly type, analysis method, analysis mode, and geometry mode. It supports the following optional features: cyclic crack growth, time dependent crack growth, rainflow, shakedown, user formation module, multiple anomalies per zone, propagation life multipliers, zone size multipliers, cyclic retardation, and static retardation. Users can define the following global parameters: service life, TMF method, probabilistic method, number of probabilistic samples, and the probabilistic seed. A single mission is defined by importing load steps from a finite element model. Important property regions are defined, including regions for materials, anomalies, and zone multipliers.

Individual cracks are defined by providing the coordinate of the crack in the finite element model.

The DPM also enables users to extract results from the model. These results include information on the fatigue crack growth history at a single point: crack size, crack area, driving force, and cycles to fracture. For risk analyses, the DPM enables users to extract information on zone risk and disk risk.

The DARWIN user manual contains the complete details on usage of the DPM. Please refer to it for complete information on the methods in use.

G.3 Example scripts

The following examples demonstrate how to employ the DPM. These examples are taken from the DPM example script directory distributed with DARWIN.

Case 1022

```
#!/usr/bin/env python

# Developed by Southwest Research Institute
# Last Modification Date: July 25, 2017

#####
...
This script demonstrates how the DARWIN Python Module (DPM) may be used to
create, execute, and process projects for 2D User-Defined Crack Life Assessment
analyses.

To execute this script, update the variable named exeFilePathGlobal with the
full file path to the DARWIN executable file (darwin.exe). Next, execute this
script from the command line or from a Python IDE (e.g., Spyder). No command line
arguments are required.

...

#####
#####
#####

import os, sys

# DPM main directory
scriptPath = os.path.realpath(__file__)
scriptDirectoryGlobal = os.path.dirname(scriptPath)

# Add path to Python source code (for internal testing purposes only)
sys.path.append(scriptDirectoryGlobal + os.sep + '..' + os.sep + '..' + os.sep + '..' + os.sep + '..' + os.sep)

import darwin93 as darwin

#####

# FEM file path
feaFilePath = scriptDirectoryGlobal + os.sep + 'auxiliaries' + os.sep + 'fea' + os.sep + 'impneu.us.fea'

# Material properties file path
matFilePath = scriptDirectoryGlobal + os.sep + 'auxiliaries' + os.sep + 'mat' + os.sep + 'NASGRO_none.us.mat'
```

```

# Crack properties
evaluatedNodes = [64,212,228,240]
initRadius = 0.05 # Initial crack radius (a=c)

#####

def define_project(dhffFilePath):

    # FEA file name
    feaBaseName = (os.path.basename(feaFilePath)).replace('.fea','')

    # Open a DARWIN file object
    # if exe path was not given at runtime use the default path.
    if len(sys.argv) > 1:
        projectObj = darwin.Project(exeFilePath=sys.argv[1])
    else:
        projectObj = darwin.Project()

    # Initialize the DARWIN project
    projectObj.create_project(dhffFilePath,1022,overwrite=True)

    # Project Title
    projectObj.title = 'DPM-Generated 2D User-Defined Crack Life Assessment'

    # Project Description
    feaBaseName = (os.path.basename(feaFilePath)).replace('.fea','')
    projectObj.description = 'FEA File Name: ' + feaBaseName + '.fea'

    # Unit System
    projectObj.unitSystem = 'US'

    # Global Parameters
    projectObj.tmfMethod = 'TEMP_MAX_STRESS'

    # Finite Element Model
    projectObj.geometry = feaFilePath

    # Properties
    props = darwin.Properties()
    props.add_material('ALL',matFilePath)
    projectObj.properties = props

    # Mission Profile
    msn = darwin.Mission()
    msn.add_all_fea_steps(feaFilePath)
    projectObj.missions = msn

    # Optional Features
    projectObj.cyclicCrackGrowth = 'FLIGHT_LIFE'
    projectObj.rainflow = 'STRESS'
    projectObj.shakedown = True

    # Crack model definition
    crk = darwin.Cracks()
    for nodeID in evaluatedNodes:
        crk.add_crack(title='Node ' + str(nodeID),location=nodeID,size=[initRadius,initRadius])
    projectObj.cracks = crk

    return projectObj

def main():

    print(' Creating the project file')
    dhffFilePath = scriptPath.replace('.py','.dhf')
    projectObj = define_project(dhffFilePath)

    print(' Executing the project')
    projectObj.execute(np=4)

    print(' Processing the project results')
    resultsObj = projectObj.results
    propLife = resultsObj.zone_fractureResult('cycles',cycle="LAST")

```

```

print('\n      Cycle To Failure')
for zoneID in propLife.keys():
    print('          ' + zoneID + ': ' + str(propLife[zoneID]))
print('      CPU Time (sec): ' + str(resultsObj.cpuTime))
print('      Wall Time (sec): ' + str(resultsObj.wallTime))

# Close the DHF file
projectObj.close()

if __name__ == "__main__":
    main()

```

Case 1032

```
#!/usr/bin/env python
```

```
# Developed by Southwest Research Institute
# Last Modification Date: July 25, 2017
```

```
#####
```

```
...
```

This script demonstrates how the DARWIN Python Module (DPM) may be used to create, execute, and process projects for 3D User-Defined Crack Life Assessment analyses.

To execute this script, update the variable named exeFilePathGlobal with the full file path to the DARWIN executable file (darwin.exe). Next, execute this script from the command line or from a Python IDE (e.g., Spyder). No command line arguments are required.

```
...
```

```
#####
#####
#####
```

```
import os, sys
```

```
# DPM main directory
scriptPath = os.path.realpath(__file__)
scriptDirectoryGlobal = os.path.dirname(scriptPath)
```

```
# Add path to Python source code (for internal testing purposes only)
sys.path.append(scriptDirectoryGlobal + os.sep + '..' + os.sep + '..' + os.sep + '..' + os.sep + '..' + os.sep)
```

```
import darwin93 as darwin
```

```
#####
```

```
# FEM file path
feaFilePath = scriptDirectoryGlobal + os.sep + 'auxiliaries' + os.sep + 'fea' + os.sep + 'full_bore_model.us.fea'
```

```
# Material properties file path
matFilePath = scriptDirectoryGlobal + os.sep + 'auxiliaries' + os.sep + 'mat' + os.sep + 'NASGRO_none.us.mat'
```

```
# Crack properties
evaluatedNodes = [5830,6214]
initRadius = 0.05 # Initial crack radius (a=c)
```

```
#####
```

```
def define_project(dhffFilePath):
```

```
    # FEA file name
    feaBaseName = (os.path.basename(feaFilePath)).replace('.fea','')
```

```
    # Open a DARWIN file object
```

```

# if exe path was not given at runtime use the default path.
if len(sys.argv) > 1:
    projectObj = darwin.Project(exeFilePath=sys.argv[1])
else:
    projectObj = darwin.Project()

# Initialize the DARWIN project
projectObj.create_project(dhfFilePath,1032,overwrite=True)

# Project Title
projectObj.title = 'DPM-Generated 3D User-Defined Crack Life Assessment'

# Project Description
feaBaseName = (os.path.basename(feaFilePath)).replace('.fea','')
projectObj.description = 'FEA File Name: ' + feaBaseName + '.fea'

# Unit System
projectObj.unitSystem = 'US'

# Global Parameters
projectObj.tmfMethod = 'TEMP_MAX_STRESS'

# Finite Element Model
projectObj.geometry = feaFilePath

# Properties
props = darwin.Properties()
props.add_material('ALL',matFilePath)
projectObj.properties = props

# Mission Profile
msn = darwin.Mission()
msn.add_all_fea_steps(feaFilePath)
projectObj.missions = msn

# Optional Features
projectObj.cyclicCrackGrowth = 'FLIGHT_LIFE'
projectObj.rainflow = 'STRESS'
projectObj.shakedown = True

# Crack model definition
crk = darwin.Cracks()
for nodeID in evaluatedNodes:
    crk.add_crack(title='Node ' + str(nodeID),location=nodeID,size=[initRadius,initRadius])
projectObj.cracks = crk

return projectObj

def main():

    print(' Creating the project file')
    dhfFilePath = scriptPath.replace('.py','.dhf')
    projectObj = define_project(dhfFilePath)

    print(' Executing the project')
    projectObj.execute(np=4)

    print(' Processing the project results')
    resultsObj = projectObj.results
    propLife = resultsObj.zone_fractureResult('cycles',cycle="LAST")

    print('\n Cycle To Failure')
    for zoneID in propLife.keys():
        print(' ' + zoneID + ': ' + str(propLife[zoneID]))
    print(' CPU Time (sec): ' + str(resultsObj.cpuTime))
    print(' Wall Time (sec): ' + str(resultsObj.wallTime))

    # Close the DHF file
    projectObj.close()

if __name__ == "__main__":
    main()

```

Case 24220

```
#!/usr/bin/env python

# Developed by Southwest Research Institute
# Last Modification Date: August 11, 2017

#####

'''
This script demonstrates how the DARWIN Python Module (DPM) may be used to
create, execute, and process projects for 2D General Inherent Risk Assessment
analyses using automatic zone setup.

To execute this script, update the variable named exeFilePathGlobal with the
full file path to the DARWIN executable file (darwin.exe). Next, execute this
script from the command line or from a Python IDE (e.g., Spyder). No command line
arguments are required.

'''

#####

import os, sys

# DPM main directory
scriptPath = os.path.realpath(__file__)
scriptDirectoryGlobal = os.path.dirname(scriptPath)

# Add path to Python source code (for internal testing purposes only)
sys.path.append(scriptDirectoryGlobal + os.sep + '..' + os.sep + '..' + os.sep + '..' + os.sep + '..' + os.sep)

import darwin93 as darwin

#####

# FEM file path
feaFilePath = scriptDirectoryGlobal + os.sep + 'auxiliaries' + os.sep + 'fea' + os.sep + 'impneu.us.fea'

# Material properties file path
matFilePath = scriptDirectoryGlobal + os.sep + 'auxiliaries' + os.sep + 'mat' + os.sep + 'NASGRO_none.us.mat'

# Exceedance curve file path
distFilePath = scriptDirectoryGlobal + os.sep + 'auxiliaries' + os.sep + 'dist' + os.sep +
'aia.post95.2fbh.1fbh.dist'

#####

def define_project(dhfFilePath):

    # FEA file name
    feaBaseName = (os.path.basename(feaFilePath)).replace('.fea','')

    # Open a DARWIN file object
    # if exe path was not given at runtime use the default path.
    if len(sys.argv) > 1:
        projectObj = darwin.Project(exeFilePath=sys.argv[1])
    else:
        projectObj = darwin.Project()

    # Initialize the DARWIN project
    projectObj.create_project(dhfFilePath,24220,overwrite=True)

    # Project Title
    projectObj.title = 'DPM-Generated 2D General Inherent Risk Assessment using Automatic Zone Setup'

    # Project Description
    feaBaseName = (os.path.basename(feaFilePath)).replace('.fea','')
    projectObj.description = 'FEA File Name: ' + feaBaseName + '.fea'
```

```

# Unit System
projectObj.unitSystem = 'US'

# Global Parameters
projectObj.serviceLife = 10000
projectObj.tmfMethod = 'TEMP_MAX_STRESS'
projectObj.probMethod = 'MONTE_GPM'
projectObj.probSeed = 12345
projectObj.probSamples = 50000

# Finite Element Model
projectObj.geometry = feaFilePath

# Properties
props = darwin.Properties()
props.add_material('ALL',matFilePath)
props.add_anomaly('ALL',distFile=distFilePath)
projectObj.properties = props

# Mission Profile
msn = darwin.Mission()
msn.add_all_fea_steps(feaFilePath)
projectObj.missions = msn

# Optional Features
projectObj.cyclicCrackGrowth = 'FLIGHT_LIFE'
projectObj.rainflow = 'STRESS'
projectObj.shakedown = True

# Autozoning Properties
autoProps = darwin.Autozone()
autoProps.set_zone_refinement_criteria(convThreshold=5.0)
projectObj.autozone = autoProps

return projectObj

def main():

    print('    Creating the project file')
    dhfFilePath = scriptPath.replace('.py','.dhf')
    projectObj = define_project(dhfFilePath)

    print('    Executing the project')
    projectObj.execute(np=4)

    print('    Processing the project results')
    resultsObj = projectObj.results
    diskRisk = resultsObj.disk_uncondRisk('probFractureWithOutInspection',cycle='SERVICE')

    print('\n        Disk Risk w/o Inspections @ Service Life: ' + str(diskRisk))
    print('        CPU Time (sec): ' + str(resultsObj.cpuTime))
    print('        Wall Time (sec): ' + str(resultsObj.wallTime))

    # Close the DHF file
    projectObj.close()

if __name__ == "__main__":
    main()

```

Case 24320

```

#!/usr/bin/env python

# Developed by Southwest Research Institute
# Last Modification Date: August 11, 2017

#####

'''
This script demonstrates how the DARWIN Python Module (DPM) may be used to

```

create, execute, and process projects for 3D General Inherent Risk Assessment analyses using automatic zone setup.

To execute this script, update the variable named exeFilePathGlobal with the full file path to the DARWIN executable file (darwin.exe). Next, execute this script from the command line or from a Python IDE (e.g., Spyder). No command line arguments are required.

...

```
#####
#####
#####

import os, sys

# DPM main directory
scriptPath = os.path.realpath(__file__)
scriptDirectoryGlobal = os.path.dirname(scriptPath)

# Add path to Python source code (for internal testing purposes only)
sys.path.append(scriptDirectoryGlobal + os.sep + '..' + os.sep + '..' + os.sep + '..' + os.sep + '..' + os.sep)

import darwin93 as darwin

#####

# 3D FEM file path
feaFilePath = scriptDirectoryGlobal + os.sep + 'auxiliaries' + os.sep + 'fea' + os.sep + 'full_bore_model.us.fea'

# Material properties file path
matFilePath = scriptDirectoryGlobal + os.sep + 'auxiliaries' + os.sep + 'mat' + os.sep + 'NASGRO_none.us.mat'

# Exceedance curve file path
distFilePath = scriptDirectoryGlobal + os.sep + 'auxiliaries' + os.sep + 'dist' + os.sep + 'aia.post95.2fbh.1fbh.dist'

#####

def define_project(dhfFilePath):

    # FEA file name
    feaBaseName = (os.path.basename(feaFilePath)).replace('.fea','')

    # Open a DARWIN file object
    # if exe path was not given at runtime use the default path.
    if len(sys.argv) > 1:
        projectObj = darwin.Project(exeFilePath=sys.argv[1])
    else:
        projectObj = darwin.Project()

    # Initialize the DARWIN project
    projectObj.create_project(dhfFilePath,24320,overwrite=True)

    # Project Title
    projectObj.title = 'DPM-Generated 3D General Inherent Risk Assessment using Automatic Zone Setup'

    # Project Description
    feaBaseName = (os.path.basename(feaFilePath)).replace('.fea','')
    projectObj.description = 'FEA File Name: ' + feaBaseName + '.fea'

    # Unit System
    projectObj.unitSystem = 'US'

    # Global Parameters
    projectObj.serviceLife = 10000
    projectObj.tmfMethod = 'TEMP_MAX_STRESS'
    projectObj.probMethod = 'MONTE_GPM'
    projectObj.probSeed = 12345
    projectObj.probSamples = 50000

    # Finite Element Model
```

```

projectObj.geometry = feaFilePath

# Properties
props = darwin.Properties()
props.add_material('ALL',matFilePath)
props.add_anomaly('ALL',distFile=distFilePath)
projectObj.properties = props

# Mission Profile
msn = darwin.Mission()
msn.add_all_fea_steps(feaFilePath)
projectObj.missions = msn

# Optional Features
projectObj.cyclicCrackGrowth = 'FLIGHT_LIFE'
projectObj.rainflow = 'STRESS'
projectObj.shakedown = True

# Autozoning Properties
autoProps = darwin.Autozone()
autoProps.set_prezone_method('GRID',10,False)
autoProps.set_zone_refinement_criteria(convThreshold=5.0)
projectObj.autozone = autoProps

return projectObj

def main():

    print(' Creating the project file')
    dhfFilePath = scriptPath.replace('.py', '.dhf')
    projectObj = define_project(dhfFilePath)

    print(' Executing the project')
    projectObj.execute(np=4)

    print(' Processing the project results')
    resultsObj = projectObj.results
    diskRisk = resultsObj.disk_uncondRisk('probFractureWithOutInspection',cycle='SERVICE')

    print('\n      Disk Risk w/o Inspections @ Service Life: ' + str(diskRisk))
    print('      CPU Time (sec): ' + str(resultsObj.cpuTime))
    print('      Wall Time (sec): ' + str(resultsObj.wallTime))

    # Close the DHF file
    projectObj.close()

if __name__ == "__main__":
    main()

```

Case results-2d.py

```

#!/usr/bin/env python

# Developed by Southwest Research Institute
# Last Modification Date: July 25, 2017

#####
"""
This script demonstrates the DARWIN Python Module can be used to retrieve
life results from a DARWIN project that contains results.

To execute this script, update the variable named exeFilePathGlobal with the
full file path to the DARWIN executable file (darwin.exe). Next, execute this
script from the command line (python minLife.py) or from a Python IDE
(e.g., Spyder). No command line arguments are required.

"""
#####

```



```

import os, sys

# DPM main directory
scriptDirectoryGlobal = str(os.path.dirname(os.path.realpath(__file__)))

# Add path to Python source code (for internal testing purposes only)
sys.path.append(scriptDirectoryGlobal + os.sep + '..' + os.sep + '..' + os.sep + '..' + os.sep + '..' + os.sep)

import darwin93 as darwin

#####

def main():

    # Open a DARWIN file object
    # if exe path was not given at runtime use the default path.
    if len(sys.argv) > 1:
        projectObj = darwin.Project(exeFilePath=sys.argv[1])
    else:
        projectObj = darwin.Project()

    projectObj.open_project(scriptDirectoryGlobal + os.sep + '2d-risk-general-inherent2d.dhf')

    # Retrieve the DARWIN project results
    resultsObj = projectObj.results
    defectAreaResults = resultsObj.zone_fractureResult('defectArea', cycle="Last")

    # Print the results
    print("\n%10s %25s" % ('Zone ID', 'Defect Area @ Failure'))
    print("%10s %25s" % ('-----', '-----'))
    for zoneID, defectArea in defectAreaResults.items():
        print("%10s %25.5e" % (zoneID, defectArea))

    # Close the project object
    projectObj.close()

if __name__ == "__main__":
    main()

```

H PIRATE/DARWIN® publications and presentations (2016–present)

Significant results from this research program were disseminated to a much broader audience in the gas turbine engine community or the international technical community. These included disciplines such as fracture mechanics or reliability through presentations at conferences and symposia or publications in archival technical journals. A number of additional publications and presentations during the term of this grant were derived from DARWIN-related research funded primarily by non-FAA sources, but based on the broad foundation of our previous FAA-funded research. This appendix lists all of these publications and presentations during the designated term, whether derived directly or indirectly from the research in this grant or its predecessor grants. Both lists are presented in chronological order.

H.1 Publications

Chan, K. S. (2016). Mechanistic modeling of time-dependent fatigue crack growth in Ni-based superalloys. *Materials at High Temperatures*, 33(4-5), 425–438.

Chan, K. S., Enright, M. P., Moody, J., & Fitch, S. H. K. (2016). Mitigating time-dependent crack growth in Ni-base superalloy components. *International Journal of Fatigue*, 82, 332–341.

Chan, K. S., Enright, M. P., Moody, J. P., & Fitch, S. H. K. (2016). Physics-based modeling tools for predicting type II hot corrosion in Ni-based superalloys. In: Hardy M, Huron E, Glatzel U, Griffin B, Lewis B, Rae C, Seetharaman V, Tin S, editors. *Superalloys 2016*. New Jersey: Wiley, 917–25.

Chan, K. S., & Moody, J. P. (2016). A hydrogen-induced decohesion model for treating cold dwell fatigue in Ti-based alloys. *Metallurgical and Materials Transactions A*, 47A, 2058–2072. doi: 10.1007/s11661-016-3367-0.

Enright, M. P., McClung, R. C., Chan, K. S. McFarland, J., Moody, J. P., & Sobotka, J. C. (2016). Micromechanics-based fracture risk assessment using integrated probabilistic damage tolerance analysis and manufacturing process models, Paper GT2016-58089, *ASME Turbo Expo Conference*, Seoul, Korea.

Enright, M. P. Moody, J. P., & J. C. Sobotka. (2016). Optimal automated risk assessment of 3D gas turbine engine components,” Paper GT2016-58091, *ASME Turbo Expo Conference*, Seoul, Korea.

- McClung R. C., & Bhamidipati, V. (2016). An investigation of small-crack effects in various aircraft engine rotor materials. *Materials at High Temperatures*, 33(4-5), 452-464.
- McClung, R. C., Wawrznyek, P., Lee, Y.-D., Carter, B. J., Moody, J. P., & Enright, M. P. (2016). An integrated software tool for high fidelity probabilistic assessments of metallic aero-engine components, Paper GT2016-57877, *ASME Turbo Expo Conference*, Seoul, Korea.
- Enright, M. P., Moody, J. P., & Sobotka, J. C. (2017). Optimal automated fracture risk assessment of 3D gas turbine engine components. *Proceedings of the 12th International Conference on Structural Safety and Reliability (ICOSSAR)*, Vienna, Austria.
- McClung, R. C., Enright, M. P., Moody, J. P., Lee, Y.-D., Sobotka, J. C., Bhamidipati, V., & McClure, J. W. (2017). A comprehensive framework for probabilistic damage tolerant design of aerospace components. *29th ICAF Symposium, International Committee on Aeronautical Fatigue and Structural Integrity*, Nagoya, Japan.
- McClung, R. C., Enright, M. P., Moody, J. P., Lee, Y.-D., Sobotka, J. C., Bhamidipati, V., & McClure, J. W. (2017). A general framework for probabilistic fracture mechanics analysis of components. *14th International Conference on Fracture (ICF14)*, Rhodes, Greece.
- Enright, M. P., R. McClung, R. C., Sobotka, J. C., Moody, J. P., McFarland, J., Lee, Y.-D., Gray, J., & Gray, I. (2018). Influences of non-destructive inspection simulation on fracture risk assessment of additively manufactured turbine engine components. *ASME Turbo Expo Conference*, Oslo, Norway. ASME Paper GT2018-77058, pp. V07AT32A013; 9 pages; doi:10.1115/GT2018-77058.
- McClung, R. C., Lee, Y.-D., Sobotka, J. C. Moody, J. P., Bhamidipati, V., Enright, M. P., Guseman, D. B., & Thomas, C. B. (2018). Some recent advances in engineering fracture modeling for turbomachinery. *ASME Turbo Expo Conference*, Oslo, Norway. ASME Paper GT2018-75400, pp. V07AT31A002. 10 pages; doi:10.1115/GT2018-75400.
- Sobotka J. C., & McClung, R. C. (2018). Automatic 3D crack placement using the Python API in Abaqus/CAE. *Science in the Age of Experience*, Boston, MA.
- McClung, R. C., Lee, Y.-D., Sobotka, J. C., Moody, J. P., Bhamidipati, V., Enright, M. P., Guseman, D. B., & Thomas, C. B. (2019). Some recent advances in engineering fracture modeling for turbomachinery. *ASME Journal of Engineering for Gas Turbines and Power*, 141(2). Paper No: GTP-18-1378. doi: 10.1115/1.4040901.

- Sobotka, J. C., Enright, M. P., & McClung, R. C. (2019). Application of critical distances to fatigue at pores. *Fatigue and Fracture of Engineering Materials and Structures*, 42(8), 1646-1661. doi.org/10.1111/ffe.13004.
- Sobotka J. C., & McClung, R. C. (2019). Verification of stress-intensity factor solutions by uncertainty quantification. *ASME Journal of Verification, Validation, and Uncertainty Quantification*, 4(8). doi: 10.1115/1.4044868.
- Chan, K. S., Burns, J. T., Enright, M. P., Moody, J. P., & Goodrum, W. (2020). Validation of hot corrosion and fatigue models in HOTPITS. *Journal of Engineering Materials and Technology*, 142, 031001. https://doi.org/10.1115/1.4045910.
- Chan, K. S., Enright, M. P., Moody, J. P., Thomas, C., & Goodrum, W. (2020). HOTPITS: The DARWIN approach to assessing risk of hot corrosion induced fracture in gas turbine components. *Engineering Fracture Mechanics*, 228, 106889.
- Sobotka J. C., & McClung, R. C. (2020). Characterization of stress fields near pores and application to fatigue lives. in *Structural Integrity of Additive Manufactured Parts* (ASTM STP 1620), ed. N. Shamsaei, S. Daniewicz, N. Hrabe, S. Beretta, J. Waller, and M. Seifi (West Conshohocken, PA: ASTM International, 2020), 367-380. doi: 10.1520/STP162020180141. Originally presented at *ASTM Symposium on Structural Integrity of Additive Manufactured Parts*, Washington, D.C., November 8, 2018.

H.2 Presentations (no manuscript)

- Enright, M. P., McClung, R. C., Chan, K. S., McFarland, J., Moody, J. P., & Sobotka, J. C. (2016). *Micromechanics-based fracture risk assessment using integrated probabilistic damage tolerance analysis and manufacturing process models*. *Propulsion Safety and Sustainment Conference*, Grapevine, TX.
- Enright, M. P., Moody, J. P., & Sobotka, J. C. (2016). *Optimal automated fracture risk assessment of 3D gas turbine engine components*. *Propulsion Safety and Sustainment Conference*, Grapevine, TX.
- Gray, J., Gray, I., Enright, M. P., McClung, R. C., McFarland, J., & Moody, J. P. (2016). Integration of simulated NDE POD curves with structural reliability assessments. *Aircraft Airworthiness and Sustainment Conference*, Grapevine, TX.

- McClung, R. C. (2016). Fracture mechanics and nondestructive evaluation modeling to support rapid qualification of additively manufactured parts. *ASTM Workshop on Mechanical Behavior of Additive Manufactured Components*. San Antonio, TX.
- McClung, R. C. (2016). Structural integrity assessment for aviation parts with inherent or induced material or manufacturing anomalies. *Joint FAA – Air Force Workshop on Qualification / Certification of Additively Manufactured Parts*, Dayton, OH.
- McClung, R. C. (2016). Predicting fatigue crack growth in forgings with bulk residual stress. Metals Affordability Initiative Workshop on *Incorporation of Residual Stress Modeling into Next Generation Design, Manufacturing, and Sustainment for Advanced Airframe Structures*. Dayton, OH.
- Enright, M. P. (2017). Integrating non-destructive inspection simulation with fracture risk assessment of additively manufactured turbine engine components. *Propulsion Safety and Sustainment (PS&S) Conference*, Phoenix, AZ.
- Sobotka J. C., & McClung, R. C. (2017). A verification process for surrogate models: applications to stress intensity factors. *ASME Verification and Validation Symposium*, Las Vegas, NV.
- Sobotka, J. C., Enright, M. P., Chan, K. S., McClung, R. C., McFarland, J. & Moody, J. P. (2017). Propagating stochastic manufacturing processes into risk predictions for gas-turbine engines. *U.S. National Congress on Computational Mechanics*, Montreal, Canada.
- Enright, M. P., McClung, R. C., Lee, Y.-D., Moody, J. P., Bhamidipati, V., McFarland, J., Sobotka, J. C., Gray, J., & Gray, I. (2018). An evolving framework for probabilistic damage tolerance assessment of additively manufactured turbine engine components. *Propulsion Safety and Sustainment (PS&S) Conference*, Jacksonville, FL.
- McClung, R. C. (2018). Integration of non-destructive inspection simulation with fracture risk assessment of additively manufactured components. *ASTM Symposium on Fatigue and Fracture of Additive Manufactured Materials and Components*, Atlanta, GA.
- McClung, R. C., Lee, Y.-D., Sobotka, J. C., Moody, J. P., Enright, M. P., & Bhamidipati, V. (2018). Practical fatigue crack growth modeling for aircraft engines: Recent enhancements. *Propulsion Safety and Sustainment (PS&S) Conference*, Jacksonville, FL.

- Sobotka J. C. & McClung, R. C. (2018). Application of residual stress in design and product performance. *Residual Stress Workshop, Thermal Processing in Motion Conference and Exposition*, Spartanburg, SC.
- McClung, R. C. (2018). Zone-based probabilistic damage tolerance methods for additive manufacturing. *Joint FAA-EASA Workshop on Qualification/Certification of Metal Additively Manufactured Parts*, Wichita, KS.
- Sobotka, J. C. (2018). A verification process for stress intensity factor solutions. *ASTM Subcommittee E08.04 on Structural Applications*, Washington, DC.
- McClung, R. C. (2019). Zone-based probabilistic damage tolerance methods for additive manufacturing. *America Makes Technical Review and Exchange (TRX) Meeting*, San Antonio, TX.
- McClung, R. C., Lee, Y.-D., Enright, M. P. McFarland, J., J., Moody, J. P., Bhamidipati, V., Sobotka, J. C., & Thomas, C. B. (2019). Incorporating residual stress into practical damage tolerance assessments. *Propulsion Safety and Sustainment (PS&S) Conference*, Washington, D. C.
- Enright, M. P., McClung, R. C., Sobotka, J. C., Chan, K. S., & Moody, J. P. (2019). Recent advances in probabilistic damage tolerance assessment for additively manufactured turbine engine components. *Propulsion Safety and Sustainment (PS&S) Conference*, Washington, D. C.
- McClung, R. C., Sobotka, J. C., & Enright, M. P. (2020). Probabilistic damage tolerance methods for structural integrity of additively manufactured parts. *ASTM International Conference on Additive Manufacturing*, Virtual | On-Demand.
- Sobotka, J. C. McClung, R. C., & Enright, M. P. (2020). Micromechanics-based effect of defects models for ellipsoidal anomalies. *TMS 2020 Annual Meeting and Exhibition*, San Diego, CA.
- Sobotka, J. C., McClung, R. C., Enright, M. P. Moody, J. P., Lee, Y.-D., & Bhamidipati, V. (2020). A zone-based, probabilistic damage tolerance framework for AM components. *TMS 2020 Annual Meeting and Exhibition*, San Diego, CA.